# Integrated Energy Operation Solution Customized for Floating Offshore Wind Power Characteristics

Lingte Chen

Submitted in fulfilment of the requirements for the

Degree of Doctor of Philosophy (Ph.D.)

James Watt School of Engineering
College of Science and Engineering
University of Glasgow

May 2024

# Declaration

I hereby declare that the work presented in this thesis has not been submitted for any other degree or professional qualification, and that it is the result of my own independent work.

---

Full Name Goes Here (Candidate)

**Lingte Chen**

---

Date

**24/04/2024**

# Abstract

Amidst global efforts towards carbon neutrality and energy transition, offshore wind power has emerged as a critical source of clean energy, attracting significant attention from governments and investors worldwide. This thesis provides an in-depth exploration of Floating Offshore Wind Turbines (FOWTs), focusing on their dynamic performance and power quality under varying wind and wave conditions. The overarching goal is to optimize the design, operation, and integration of FOWTs into renewable energy systems, thereby enhancing their contribution to sustainable energy generation.

By integrating mechanical and electrical models, this research deepens our understanding of FOWT dynamics, facilitating more accurate power system analysis. The study introduces fully coupled mathematical models that address existing research gaps, particularly in the context of Wind Power Ramp Events (WPREs). The investigation highlights the distinctive dynamic responses of FOWTs, which are markedly different from those of conventional bottom-fixed turbines, due to their floating nature. These findings underscore the importance of considering wave-induced loading and pitch motion in FOWT design and operation, as these factors significantly influence power output and operational stability.

In addition, the research tackles the challenges associated with the low-frequency power fluctuations and reduced power generation efficiency in FOWTs. A novel bus extension scheme is proposed, incorporating a sea wave band stop filter and a Hybrid Energy Storage System (HESS) under Real-Time Coordinated Control (RTCC). This approach maximizes the potential of energy storage systems, improves power quality, and ensures better compliance with grid dispatch commands. The study's innovative control strategies, particularly the dynamic adjustment of Kalman filter parameters, offer significant advancements in mitigating WPREs and optimizing FOWT performance.

Furthermore, the thesis explores the integration of wind and solar power on a novel catamaran FOWT platform. Through dynamic simulations and control strategies, the study demonstrates the platform's robust dynamic stability and its ability to maintain consistent power generation under adverse sea conditions. The research also delves into the effectiveness of various wind-solar capacity ratios and PV system configurations, highlighting their potential to enhance power quality and energy complementarity. These insights pave the way for the development of integrated renewable energy systems, particularly in coastal environments.

In conclusion, this thesis makes significant contributions to the understanding of FOWT dynamics, the optimization of power quality, and the integration of wind and solar energy on floating platforms. The findings provide valuable guidance for policymakers, researchers, and industry stakeholders, driving the advancement of offshore renewable energy technologies. As the world continues its transition towards sustainable energy, the insights and innovations presented in this research will play a crucial role in shaping the future of offshore wind power and its integration with other renewable energy sources.

# Publications associated with this research

- L. Chen, J. Yang, and C. Lou, "Hydrodynamic Frequency Analysis based Floating OWT Power Quality Mitigation," in *2023 IEEE Sustainable Power and Energy Conference (iSPEC)*, 2023, pp. 1–6, doi: 10.1109/iSPEC58282.2023.10403087.
- L. Chen, J. Yang, and C. Lou, "Characterizing ramp events in floating offshore wind power through a fully coupled electrical-mechanical mathematical model," *Renew. Energy*, vol. 221, p. 119803, Feb. 2024, doi: 10.1016/J.RENENE.2023.119803.
- L. Chen, J. Yang, and C. Lou, "Real-Time Coordinated Control of Hybrid Energy Storage Systems for Floating Offshore Wind Turbine Power Quality Mitigation," in *2024 7th International Conference on Energy, Electrical and Power Engineering (CEEPE)*, 2024, pp. 612–619. doi: 10.1109/CEEPE62022.2024.10586586.
- L. Chen, J. Yang, and C. Lou, "Floating wind-integrated PV system yield analysis considering AHSE dynamics & solar azimuth effects," *Energy Convers. Manag.*, vol. 315, p. 118799, Sep. 2024, doi: 10.1016/J.ENCONMAN.2024.118799.

# Acknowledgements

Completing this thesis marks the culmination of a transformative journey that began in October 2020, amid the challenging backdrop of the COVID-19 pandemic. Boarding that flight to Glasgow was a pivotal decision, one that has since enriched my life with invaluable experiences and personal growth.

First and foremost, I extend my deepest gratitude to my supervisor, Dr. Jin Yang, and my esteemed colleague, Dr. Chengwei Lou. Their unwavering support, expert guidance, and constructive feedback have been instrumental from the inception of my PhD dissertation proposal to the refinement of the final draft. Their mentorship, coupled with boundless patience, has not only honed my academic skills but also instilled in me the ability to identify innovation points within my research. I am equally indebted to Prof. Changhong Deng of Wuhan University for his invaluable insights, which have broadened my scholarly horizons.

I owe a profound debt of gratitude to my parents, whose unconditional support and encouragement have been the bedrock of my academic journey. Their selfless sacrifices and unwavering belief in my abilities have enabled me to pursue my passion for academia without reservation. To them, I owe my deepest gratitude and utmost respect.

Additionally, I am immensely grateful to my beloved girlfriend, Haoyue Lan, whose unwavering companionship has illuminated even the darkest moments of my PhD journey. Her steadfast presence and boundless love have been a source of immeasurable joy and strength, enriching my life in ways I never thought possible.

I extend my heartfelt appreciation to the faculty and staff of the University of Glasgow, whose support and assistance have been invaluable throughout my academic pursuit. Special thanks to the staff of the James Watt School of Engineering for their assistance in facilitating my attendance at international conferences.

To my friends and roommates who shared in both the mundane and momentous occasions, I am grateful for your companionship and support, particularly during festive seasons when your presence made a world of difference.

Every experience, both triumphant and challenging, has shaped me into the person I am today. I embrace each obstacle as an opportunity for growth and self-improvement, and I am profoundly grateful for the resilience and strength they have instilled within me.

As I embark on the next chapter of my journey, I carry with me the lessons learned and the memories cherished. May our paths be illuminated with success, and may we all stride confidently towards a future filled with promise and fulfillment.

# Abbreviations

| | |
|---|---|
| **AHSE** | Aero-Hydro-Servo-Elastic |
| **ANN** | Artificial Neural Network |
| **BEM** | Blade Element Momentum |
| **BTLCD** | Bidirectional Tuned Liquid Column Damper |
| **CFD** | Computational Fluid Dynamics |
| **CSI** | Critical Success Index |
| **DFIG** | Double Fed Induction Generator |
| **DLL** | Dynamic Link Library |
| **DoF** | Degree of Freedom |
| **DTEF** | Deformable Trailing Edge Flap |
| **EMD** | Empirical Mode Decomposition |
| **ESS-E** | Energy Storage System with high specific Energy |
| **ESS-P** | Energy Storage System with high specific Power |
| **F2A** | FAST to AQWA |
| **FCMEDM** | Fully coupled Mechanical-Electrical Detailed Model |
| **FOWT** | Floating Offshore Wind Turbine |
| **FSF** | Floating Solar Farm |
| **FSI** | Fluid–Structure Interaction |
| **FVW** | Free Vortex Wake |
| **GAST** | General Aerodynamic and Structural numerical Tool for wind turbine |
| **GDW** | General Dynamic Wake |
| **GSC** | Grid Side Converter |
| **HAWT** | Horizontal Axis Wind Turbine |
| **HESS** | Hybrid Energy Storage System |

| | |
|---|---|
| **HVRT** | High-Voltage Ride-through |
| **IEC** | International Electrotechnical Commission |
| **IPMSG** | Interior Permanent Magnet Synchronous Generator |
| **IoT** | Internet of Things |
| **LCOE** | Levelized Cost of Electricity |
| **LVRT** | Low-Voltage Ride-through |
| **MEX** | MATLAB Executable |
| **MPP** | Multi-Purpose Platform |
| **MPPT** | Maximum Power Point Tracking |
| **MSC** | Machine Side Converter |
| **NREL** | The National Renewable Energy Laboratory |
| **O&M** | Operation and Maintenance |
| **OC** | Offshore Code Comparison Collaboration |
| **OpSDA** | Optimized Swinging Door Algorithm |
| **OWC** | Oscillating Water Column |
| **OWT** | Offshore Wind Turbine |
| **PE** | Power Electronics |
| **PES** | Power Energy Systems |
| **RBM** | Rigid Body Motion |
| **RTCC** | Real-Time Coordinated Control |
| **RTDS** | Real Time Digital Simulator |
| **SCADA** | Supervisory Control and Data Acquisition |
| **SOC** | State of Charge |
| **TIR** | Turbulent Inflow Realization |
| **TMD** | Turned Mass Damper |
| **PMSG** | Permanent Magnet Synchronous Generator |

| | |
|---|---|
| **PNN** | Probabilistic Neural Network |
| **PVGIS** | Photovoltaic Geographical Information System |
| **PWM** | Pulse Width Modulation |
| **VAWT** | Vertical Axis Wind Turbines |
| **WECC** | Western Electricity Coordinating Council |
| **WECS** | Wind Energy Conversion Systems |
| **WTG** | Wind Turbine Generator |
| **WP** | Wind Process |
| **WPRE** | Wind Power Ramp Events |
| **WPP** | Wind Process Pattern |

# Table of contents

# List of figures

# List of tables



Table 2.1 Floating structure and mooring system properties in common research models . 19

Table 2.2 Common research AHSE models of FOWT ..... 22

Table 2.3 Characteristics of floating offshore wind farms operating around globe ..... 23

Table 2.4 Novel AHSE coupled modelling codes ..... 25

# Chapter 1: Introduction

In the context of the global push towards carbon neutrality and energy transition, wind power has emerged as a key player, garnering significant attention from governments and investors worldwide. In 2019, wind power accounted for more than 8% of the total global power generation, second only to hydropower in renewable energy power generation [1]. In response to the challenge of global warming and climate change, there has been a significant surge in renewable energy production worldwide. Among these renewable options, wind energy stands out as one of the most efficient choices due to its widespread accessibility across the globe [135]. In addition, wind energy potential in deep water at offshore locations is up to 1.9 times that of onshore sites [136], leading to a notable increase in the deployment of offshore wind farms on available water bodies, particularly in nations with extensive deep coastlines. However, the increasing penetration of wind power poses significant challenges for grid operators in maintaining a safe, reliable, and cost-effective power system, owing to the uncertainty and variability associated with wind energy [137].

While onshore wind power has reached a level of maturity and cost competitiveness with traditional energy sources, offshore wind power has seen rapid development in recent years, driven by abundant and high-quality wind resources at sea. Major economies like the European Union, the United States, and China have set ambitious targets for offshore wind capacity expansion, recognizing its potential as a crucial component of the renewable energy landscape. Traditional fixed-bottom offshore wind turbines have been deployed extensively in shallow waters, while floating turbines have emerged to tap into deeper offshore wind resources, offering expanded geographical possibilities and potentially higher and steadier wind characteristics. However, the floating turbine technologies are still in their developing stages, with limited knowledge and simulation tools available, particularly in integrating detailed mechanical and electrical models. This has led to wind farm operators having a limited or even underestimated understanding of the impact of dynamics

on the power output of floating offshore wind turbines (FOWTs), which further affects optimization decisions under wave and wind conditions. Addressing this gap is critical to reducing uncertainty and risks in power generation from FOWTs.

## 1.1 Motivation and Knowledge Gaps

Until the finish of this PhD thesis (May 2024), for the far offshore in Europe, there are still few commercial cases of floating wind farms. Limited notable instances of offshore floating wind power projects include the Hywind Scotland [2], which is recognized as the inaugural offshore wind farm located in the North Sea, and the WindFloat Atlantic [3], a 25.2MW floating offshore wind initiative situated off the coast of Portugal in the vicinity of Aguçadoura. Despite the indisputable advantages such as larger unit capacity and lower material and installation costs [4], there is still limited mass adoption of FOWTs for large scale applications.

One of the major factors is the complex dynamic characteristics of FOWTs under harsh wind and wave conditions [5] and power performance in conditions characterized by high wind speeds and wave intensities [6]. It was initially found that the power output of a FOWT is significantly different compared to a bottom-fixed offshore wind turbines (OWT) due to the added complexity of the floating platform and the harsh offshore environment in which they are installed [7]. It is noteworthy that, the impact of wind turbine aero-hydro-servo-elastic dynamics on the output power quality represents a crucial performance indicator for power systems that cannot be disregarded [8]. In general, this is related to two aspects of dynamic analysis of FOWTs, aerodynamics and hydrodynamics.

For FOWT aerodynamics, [9] emphases that periodic power pulsations can be attributed to various wind turbine aerodynamic factors, including wind speed, wind turbulence, wind shear, and tower shadow effects. Since this aspect of the dynamics has been comprehensively studied on onshore bottom-fixed wind turbines, the corresponding compensation and optimization strategies have been widely discussed and practiced [10]. A

number of studies [11][12] have already demonstrated the efficacy of implementing generator torque control on a per-turbine basis as a means of mitigating power oscillations.

For FOWT hydrodynamics, the motion of the floating platform, caused by waves and currents can affect the mechanical loading on the turbine and its foundation, which can also in turn significantly impact the electric power output of these turbines [13]. Within existing literature, considerable attention has been devoted to exploring protective measures aimed at countering the deleterious effects of wave impact and enhancing the stability of floating structures. On the one hand, spar-type [14], semi-submersible [15], barge-supported [16][17] FOWTs have been proposed as optimized designs which obtained improved stable hydrodynamic characteristics. On the other hand, the incorporation of wave energy converters (WECs) into a floating wind platform has been found reducing maximum horizontal force and pitch moment, leading to the development of a hybrid system [18]. Additionally this combination proves to be attractively economical and grid-complementary [19]. To date, however, it appears that no grid-connected operational standard specifically tailored for FOWTs has been established. Even for fixed OWTs, the utility grid connection standards are contingent upon the grid specifications and unique to each country [9]. Moreover, research efforts in investigating the performance of FOWTs under conditions of high wind and wave, particularly with regard to satisfying the power quality requirements of power systems, have been limited as far as the author is aware.

Based on the above review, it can be concluded that the characteristics of FOWTs under a full range of wind and wave conditions require research effort to ensure confident and mass applications. The following aspects of academic research require attention:

1. To improve theoretical yield analysis of FOWTs: both wind and wave conditions should be fully investigated for the turbines and their floating platforms. By simulating the power quality and characteristics of FOWTs under different wind

and wave conditions, researchers can gain a better understanding of how these factors affect the performance of the turbine and the floating platform.

2. To identify and address potential issues that may affect the stability and supply quality of the generation systems as well as that of the connected power grid. Understanding the power quality and characteristics of FOWTs under different wind and wave conditions can help to identify and address any potential issues that may affect the stability of the power grid [20], ensuring the smooth integration of floating offshore wind energy into the power grid and avoid disruptions to the power supply.
3. The simulation platform facilitates the seamless exchange of spatial-physical data between a FOWT and the Internet of Things (IoT) infrastructure. This exchange of data contributes to the intelligent and sustainable development of Power Energy Systems (PES). It is crucial to address the substantial fluctuations in FOWT aero-hydro-servo-elastic dynamics to prevent potential risks to the power output and ensure grid stability. The power grid can gain comprehensive insights into the spatial-physical state and characteristics of various FOWT dynamics. By intelligently collaborating with energy storage systems and other power sources, the grid can significantly enhance its stability and improve the overall power utilization rate of large-scale access to floating wind farms.

Studies toward these new knowledge gaps could help researchers optimize the design and operation of FOWTs with improved efficiency and reliability. By optimizing the design and operation of FOWTs based on simulations of their power quality and characteristics under different wind and wave conditions, it may be possible to reduce the costs associated with their construction, operation, and

maintenance [21]. This can make floating offshore wind energy more economically viable and help to accelerate its deployment.

## 1.2 Research Objectives

In response to the above, first of all, this PhD study focused on the development of a comprehensive simulation model to evaluate the dynamic performance of large-scale FOWTs under varying wind and wave conditions. The full model consists of an FOWT dynamics module and a Permanent Magnet Synchronous Generator (PMSG) featured Type 4 wind turbine generator (WTG) and converter module [22]. Real-time dynamic performance and electrical power outputs were obtained through extensive testing. The impact of FOWT on power quality was assessed in relation to varying wind and wave conditions.

Based on the established coupled model of FOWTs, the second step involves conducting comprehensive tests to address various knowledge gaps regarding the characteristics of floating offshore power. Key questions include understanding the differences between the output power of FOWTs and bottom-fixed OWTs, elucidating the relationship between floating wind power and platform motion, and assessing the quality of floating wind power. These inquiries necessitate answers obtained through simulation experiments.

Upon confirming the primary characteristics of floating wind power, the third step shifts research focus towards designing a targeted energy storage control scheme. Challenges arise due to the presence of ultra-low-frequency harmonic components in the output power that cannot be effectively separated by low-pass filters. Additionally, strategies must be devised to address disparities between the actual output power and

dispatch commands. Real-time coordinated control schemes must confront these potential challenges and address corresponding knowledge gaps.

Finally, to fully harness energy resources in remote offshore areas, the thesis will conduct comprehensive tests on the integration of floating wind energy with solar energy. This endeavour will address a research gap by evaluating the power characteristics of solar energy systems integrated onto spar-type FOWTs and optimizing tilt control strategies for the integrated floating wind-solar systems.

## 1.3 Thesis structure

The remaining parts of this thesis are organised as follows:

**Chapter 2 - Background and Literature Survey**

The integration of complex dynamics within FOWTs necessitates a comprehensive approach in electrical engineering analysis. Alongside the development of detailed electrical models, the establishment of intricate mechanical models is equally imperative. While fully coupled models for FOWTs remain scarce in current research literature, the requisite elements for constructing such models are present. Significant strides in mechanical modelling for FOWTs' AHSE dynamics have been made possible through codes refined over a decade of exploration. Simultaneously, the evolutionary trajectory of electrical design in FOWTs closely mirrors that of bottom fixed OWTs, allowing for the adaptation of electrical models from the latter. This chapter offers a comprehensive examination of research advancements in relevant fields applicable to detailed modelling of FOWTs, focusing on both mechanical and electrical aspects. Finally, this chapter consolidates and discusses the state-of-the-art advancements in the development of fully coupled mechanical-electrical models for FOWTs.

**Chapter 3 - Characterizing ramp events of Floating Offshore Wind Power**

Building upon the groundwork laid in Chapter 2, this chapter delves into the dynamic response of FOWTs, particularly focusing on wind power ramp events (WPREs). The developed fully coupled FOWT model integrates mechanical and electrical factors to analyse the impact of wind and wave loads on power stability and reliability. Results indicate that FOWTs exhibit a notable nonlinear low-frequency dynamic response during various wind-wave scenarios, leading to significant WPREs. Unlike bottom-fixed OWTs, FOWTs experience a supplementary decline in power output during these events, highlighting the critical role of pitch motion and wave load impact. This chapter underscores the importance of understanding and mitigating WPREs for ensuring grid stability and reliability in FOWT operations.

**Chapter 4 - Optimized Real-Time Coordination Control of Hybrid Energy Storage Systems for Floating Offshore Wind Power**

Addressing the challenges identified in Chapter 3, this chapter proposes a novel control scheme for managing power quality and dispatch disparities in FOWTs through Hybrid Energy Storage Systems (HESS). Leveraging Kalman filters and parameter optimization design, the developed control system aims to enhance power output quality and match dispatch commands in real-time. Experimental data demonstrate significant improvements in power quality under Real-Time Coordinated Control (RTCC). Additionally, recommendations are provided for optimizing Kalman filter parameters to address multi-objective optimization challenges. This chapter highlights the potential of HESS-based control systems in optimizing power output and quality in FOWTs.

**Chapter 5 - Optimal Control for Enhancing Power Quality in Floating Wind Turbines Integrated with Photovoltaic Power Plants**

Building upon the concepts introduced in Chapter 4, this chapter explores the potential of co-locating Floating Solar Farms (FSFs) with FOWTs to enhance overall power generation reliability. A novel design combining a barge-type FOWT with a compact solar

farm is proposed, facilitating wind-solar power complementarity across various motion states of the platform. Through comprehensive investigations, the study demonstrates the effectiveness of the proposed approach in fostering high levels of wind-solar coupling and ensuring overall output power reliability. This chapter offers insights into the operation of co-located wind-solar power generation systems, suggesting avenues for enhancing sustainable energy production.

**Chapter 6 - Conclusions and Future Work**

In the final chapter, the main research findings and contributions are outlined, followed by conclusions and suggestions for future research. This chapter synthesizes the insights gained from the preceding chapters, highlighting the significance of integrated mechanical-electrical modelling, understanding wind power ramp events, and optimizing control strategies for enhancing power quality and reliability in FOWTs. Suggestions for future research directions are provided, emphasizing the importance of continued exploration in advancing floating offshore wind technology.

# Chapter 2: Literature review

## 2.1 Introduction

In recent years, the massive consumption of fossil energy and the environmental problems caused by climate change have caused human society to try to change the energy structure, from fossil fuel-based to renewable clean energy. As the cost rapidly fallen into a competitive level [23], wind energy is currently considered to be an ideal renewable energy source for achieving global emission reduction targets, and it is also the main driving force for the growth of renewable energy. In 2019, wind power accounted for more than 8% of the total global power generation [1]. The rapid expansion of the global wind power market has driven the continuous advancement of wind turbine technology. Variable-speed operation instead of constant-speed operation [24], variable pitch instead of fixed pitch [25], etc. have become the general development trend of wind turbines. The emergence of FOWT placed on floating platforms allows human society to capture more abundant wind energy resources in the far offshore [26].

Compared with traditional fossil energy power generation and hydropower generation, the cost of offshore wind power is still at a high level [27]. In 2022, the fixed-bottom offshore wind estimate is $95/MWh, and the floating substructure reference project estimate is $145/MWh. In order to prove the technical feasibility of the proposed FOWT, three methods are usually used, including onsite measurements, scaled model test and numerical analysis. Relatively speaking, although field measurement and scale model testing could obtain more reliable data of FOWT operation, these approaches usually require a lot of money and time. In addition, most of these experimental projects rely heavily on industrial investment, which prevents ordinary researchers from obtaining valuable measurement data. In contrast, the numerical analysis method of FOWT based on mathematical model is cheaper, faster and more convenient. Therefore, after modelling the dynamics and response of the floating wind turbine platform in a fully and fully integrated manner, the design and manufacturing of FOWT can be more optimized and cost-effective [28].

The main contributions to the knowledge gap in FOWT numeral modelling is summarized as follows:

(1) In most current investigations, due to different research purposes and the function simplifications of single software, the FOWT model is simplified when simulating for specific research topics, including mechanical model and electrical model. As a result, these simplified models built cannot fully consider all of the factors such as aerodynamics, hydrodynamics, mechanical transmission, and electromagnetic transient response in FOWTs, which causes certain limitations during simulation [7]. The end of this chapter proposes a method to develop the fully coupled mechanical-electrical detailed model (FCMEDM). Through cross-software co-simulation, high-precision FOWT system dynamics can be obtained at a lower computational cost, so it is easier to extend to O&M research.

(2) For all types of OWT, including FOWT, the field of control theory is mainly used by researchers to model the electrical and electronic dynamics of wind turbines. However, the application research field of this FOWT modelling scheme and the research significance in the power system are very limited. From an O&M perspective, there is a great need to model all aero-hydro-elastic-servo (AHSE) aspects of FOWT. This review The FCMEDM proposed in this article focuses on the O&M stage and is the first review that discusses the mechanical model and the electrical model in a highly correlated manner.

(3) Although there are projects represented by The Offshore Code Comparison Collaboration (OC3) dedicated to verifying the technical feasibility of FOWT numerical tools [29], due to the scarcity of FOWT test data to the public, detailed code to experimental comparisons are still relatively few [30]. Summarizing the modelling scheme will help researchers in this field understand the dynamic theory of coupled FOWT, and promote the development, integration and optimization of FOWT numerical codes.

The remainder of this chapter is organized as follows. Section 2 provides the majority research results of bottom fixed wind turbine modelling that can be inherited during FOWT modelling, including modelling theories and solutions related to AHSE models and wind energy conversion system (WECS) models. Section 3 introduces the coupling scheme of the mechanical model and electrical model of the wind turbine and related simulation research cases. Section 4 summarizes and proposes the state of the art in feasible FOWT FCMEDM modelling scheme. Section 5 summarizes findings in the sections above, proposes the limitations of the current modelling program, and proposes ideas and prospects for future research. The Graphic outline is summarized in Fig. 2.1 Compared with vertical axis wind turbines (VAWT), horizontal axis wind turbine (HAWT) has more advantages on floating platforms [31]. As a result, all the wind turbines mentioned in the article are contained in HAWT.

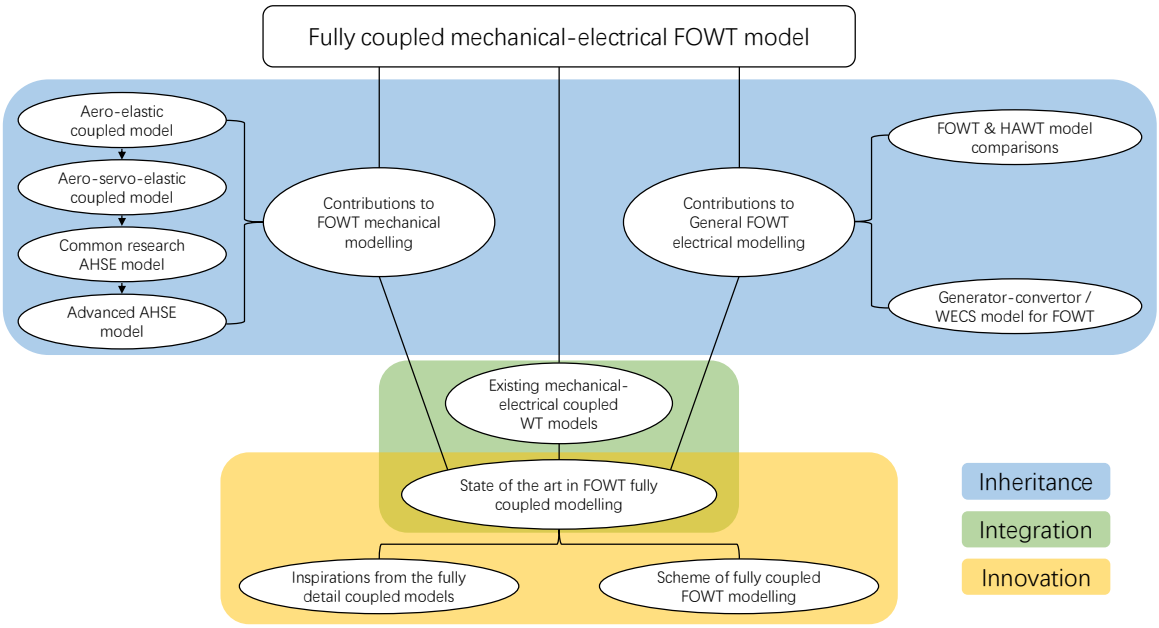


*Fig. 2.1 Graphic outline of the review*

## 2.2 General FOWT model design developments & achievements

From the modelling point of view, a FOWT is a multi-scale and multi-coupled complex dynamic system. It includes the mechanical vibration part of the large time scale (ms level time step) and the electromagnetic transient part of the small time scale (μs level time step). The modelling of FOWT is mainly divided into a mechanical model reflecting the dynamic state and an electrical model reflecting the operating state of the power system. In previous early studies on bottom fixed wind turbines, the two fields of mechanics and electrical are independently considered and analysed when modelling and simulating.

On the one hand, scholars have established fully coupled AHSE models to investigate the force of each module of the HAWT in detail. These studies often have limited connections with the electrical characteristics, so only a minimalist induction generator model is included in the mechanical model [32]. The simplified model of induction generator is based on (2.1)- (2.3), which simplifies the relationship between electromagnetic torque $T_e$ and slip rate $s$ to a proportional relationship, that is, the slope $k$ of the function in the linear region of Fig. 2.2. This equivalent method can efficiently simulate the wind turbine in normal steady-state operation, but it also means that the generator model cannot be accurately calculated outside the linear region within Fig. 2.2. This significantly affects the reliability of this type of model simulation under extreme operating conditions.

$$s = \mathrm{GBR} \cdot \Omega_{lss} - \Omega_s \tag{2.1}$$

$$T_e = k \cdot s \tag{2.2}$$

$$P_e = T_e \cdot \Omega_s \cdot \eta \tag{2.3}$$

where $s$ represents induction generator slip ratio; GBR represents gearbox ratio; $\Omega_{lss}$ is angular speed of low-speed shaft; $\Omega_s$ is rotor angular speed; $T_e$ is generator electrical torque and $\eta$ is generator efficiency.

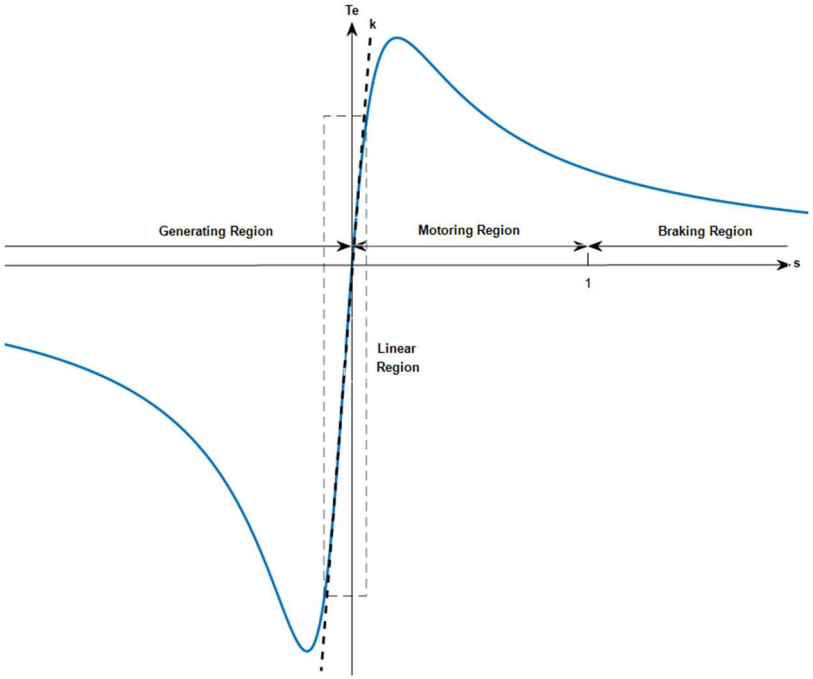


*Fig. 2.2 The torque-slip characteristic of induction generator*

On the other hand, scholars have established detailed WECS models to explore the steady-state and transient characteristics of wind turbines or wind farms, and control strategies in response to grid dispatching requirements during operation. Because towards the bottom fixed HAWTs, the mechanical modules have only a limited impact on the research in the field of power systems, a large number of studies often only establish a very simplified power coefficient ($C_p$) equivalent aerodynamic model, based on (2.4)- (2.7). $C_p$ represents the conversion efficiency of wind turbines converting wind energy into electrical energy, which is a function of the wind turbine tip speed ratio $\lambda$ and the pitch angle $\beta$. With power coefficient $C_p$, blade sweeping radius $R$ and average wind speed $V_v$, the absorbed mechanical power from the wind $P_t$ can be calculated. With the deepening of research and the iteration and update of simulation codes, a series of fully detailed models based on bottom fixed HAWTs have emerged, which includes a detailed Aero-Servo-Elastic mechanical model commonly used in the dynamic analysis and a detailed WECS model that reflects the electrical characteristics of the generator and convertor.

$$P_t = \frac{1}{2}\rho\pi R^2 V_v^3 \cdot C_p \tag{2.4}$$

$$C_p = k_1\left(\frac{k_2}{\lambda_i} - k_3\beta - k_4\beta^{k_5} - k_6\right)e^{\frac{k_7}{\lambda_i}} \tag{2.5}$$

$$\lambda_i = \frac{1}{\lambda + k_8} \tag{2.6}$$

$$\lambda = \frac{R\Omega_{lss}}{V_v} \tag{2.7}$$

In general, the aerodynamics, elastic dynamics, control strategies and generator models in the FOWT model are all developed based on the OWT model [33]. For the design of the FOWT FCMEDM, it is mandatory to absorb and transform the design scheme of the OWT model.

### 2.2.1 Development & contributions to AHSE modelling

#### *2.2.1.1 Aero-elastic coupled model*

In the early stage of research, the analysis theory of each mechanical module of the wind turbine was relatively simplified, while the academic circle has not formed a unified consensus on the design standard of the mechanical model of the wind turbine. Therefore, in the related research, the rotor/tower coupling dynamics modelling of the large HAWT was based on the improved model of helicopter coupled rotor/fuselage systems and tilt prop/rotor systems [34].

The aerodynamics of the rotor and the elastic dynamics of the tower are the first two components to be coupled. The earliest research on the coupling of wind turbine modules can be traced back to Friedmann around 1980, who discussed the aero-elastic modelling method [35] and aero-elastic coupling problem of the rotor/tower system [36] in considerable detail, based on Blade Element Momentum (BEM) theory for aerodynamic analysis and Euler-Bernoulli beam theory for elastic analysis. Based on this modelling

method, a large number of aero-elastic coupled HAWT models have been established and used for scientific research purposes. Hansen did in-depth model analysis [37] and refinements [38] on the issue of aero-elastic coupled methods and developed a model for the use of HAWT aero-elastic stability analysis. In his study, new theories FEM and multi-body formulation (predecessor of MBS) are used to analyse elastic dynamics [39]. These theories are still widely used in the latest codes and models. The versatility of the model is very good as the eigenvalues and eigenvectors can be computed at any operation condition. Chattot [40] made further improvements to the aero-elastic model. When modelling, the aerodynamic model uses the Goldstein vortex model, while implicitly coupling the aerodynamic equations and structural equations through the modal decomposition method. This novel vortex model considering blade flexibility is compared with the National Renewable Energy Laboratory (NREL) experimental data, and the results show that the code can simulate the dynamics of the coupled fluid structure with low computational cost and high accuracy. Matha et al. [41] proposed a comprehensive high-fidelity aeroelastic MBS methodology. Compared with the model based on the traditional MBS theory, the aero-elastic model based on the improved MBS theory has lower blade deflections and bending moments in the statistical results of IEC DLC 1.3. Jørgensen [42] used the AHSE code Flex5 to validate an aero-elastic model and coupled a gearbox model with detailed design and visualization. Pedersen et al. [43] extracts inflow information from the measurement database and uses it for HAWT aeroelastic simulation. The results show that the simulation based on HAWC2 can predict the measured flaps and tower-bottom load scatter well.

Turbulent inflow realization (TIR), that is, the turbulent structure in the flow field is an important source of uncertainty in the model output prediction [44], which will cause the aeroelastic wind turbine model to have random/uncertain output, which is one of the main difficulties in establishing aeroelastic wind turbine model. Murcia et al. [45] defined and proved the polynomial alternative model of DTU 10 MW RWT, which could be used to

characterize the overall performance of the aeroelastic HAWT model under multiple uncertain turbulent flow parameters.

As of today, in all mainstream simulation codes for HAWT dynamic modelling [29], aerodynamic calculations are based on BEM or General Dynamic Wake (GDW) theory, while elastic dynamics are based on FEM or MBS. The bottom fixed HAWT model based on these theories has high simulation accuracy and low calculation cost. However, currently in some situations, using BEM or GDW method does not seem to be accurate enough to analyse the aerodynamics under extreme conditions on FOWT. Therefore, more advanced aerodynamic analysis methods are then introduced into coupled modelling. In order to study the more complex motion of the rotor more accurately, from 2014, Tran and Kim [46] became the first research team to publish the research outcome on unsteady aerodynamics of FOWT platform motion using a computational fluid dynamics (CFD) model. The Computational fluid dynamic with rigid body motion (CFD-RBM) method proposed in the article is compared with the results obtained by the FAST code, showing good correlation, and can be used to accurately analyse the general horizontal and vertical axis FOWT models [47]. Lienard et al. [48] investigated the effect of typical pitch and surge motion on aerodynamic performance and wind turbine wake through CFD modelling. The CFD computations are performed using elsA CFD package [49], provided by ORENA. The effect of surge on the thrust of a floating turbine was investigated by Kyle et al. [50] with the open source CFD software OpenFOAM for conditions favourable to propeller and vortex ring state. Leroy et al. [51] introduced a new novel method Free Vortex Wake (FVW) to consider aerodynamic loads by coupling hydro dynamics code InWave [52] and aerodynamics code CACTUS [53]. Compared with FAST based on traditional BEM theory, the preliminary conclusions obtained show that FVW solver in CACTUS will obtain more accurate results in high TSR situations. Sayed et al. [54] even used the Fluid–Structure Interaction (FSI) coupling approach to introduce a CFD solver to calculate the aerodynamic blade loads in HAWT aeroelastic analysis. It is acknowledged that the many methodologies

applied above requires a very high computational resource and can therefore not be developed into a tool to simulate many wind turbines in an array for the many wave and wind conditions experienced by an installation. However, it serves to develop a better understanding of the specific aerodynamic behaviour and help develop the parameterization of these effects in a more realistic modelling framework.

However, despite the shortcomings of the most traditional and common method - BEM, it has low computational cost and can give acceptable accuracy in many cases when compared with CFD methods [48]. The actuator disc model by Mikkelsen [55] has been lately adapted by de Vaal et al. [56], Micallef and Sant [57] to model FOWT aerodynamics. The research results show that in the overall dynamics analysis of FOWT, the wake dynamics engineering model based on the traditional analysis theory represented by BEM seems to have enough ability to deal with the additional unsteady surge motion of the wind turbine rotor. Sant [58] evidenced that BEM can obtain good accuracy in the research of some other specific situations if some corrective measures are used to compensate it. Fernandez-Gamiz et al. [59] developed an improved BEM-based solver to verify the NREL 5MW wind turbine and determined the bending moment and thrust force in the blade root. Pirrung et al. [60] proved that the extended aerodynamic model based on BEM can simulate HAWT under static conditions. This overcomes the problem that BEM cannot simulate HAWT dynamics in a steady state because it assumes that the rotor can be approximated by a disk. The simulation results of this aeroelastic model agree with the results from the NREL/NASA Phase VI unsteady experiment. The above efforts have lent a hand to BEM to gain wider applicability and higher accuracy.

#### *2.2.1.2 Aero-elastic coupled model*

Based on the mature aero-elastic coupled modelling theory, many subsequent studies coupled more models of mechanical components during modelling. In 2000, NTUA developed a general aero-servo-elastic HAWT model named "General Aerodynamic and Structural numerical Tool for wind turbines" (GAST) [61]. At that period of time, the

establishment of this code serves a Greek national research activity to find wind turbine control strategies that optimize fatigue loads in complex terrain. It was the first time that the control system (servo dynamics) composed of pitch control and variable speed control is coupled with the areo-elastic model, and this modelling scheme has finally become the main mode of modelling rigid foundation HAWT in contemporary research. Riziotis et al. [62] designed a control system composed of a pitch controller coupled with an aeroelastic model to realize closed-loop operation. Compared with the aeroelastic model, the natural frequency and damping characteristics of the aero-servo-elastic model in certain structural modes will greatly change. Mauricio et al. [63] Proposed added a controller into the generator control system, which can quickly change the electromagnetic torque under gust conditions through auxiliary signals to reduce the torsional force. The research is based on an aero-servo-drivetrain model, which has detailed design control system and drive train model. However, the model ignores the elastic dynamics of the tower, uses a 6-mass model to analyse the aerodynamics of the rotor. Ahlström [64] developed a finite element aero-elastic model with a simplified but comprehensive control system for simulation of the dynamic response of HAWT. Although the model shows acceptable accuracy during the verifications with measurements, it shows the limitations of simulation in extreme situations due to the small blade deflection. Jin et al. [65] established a flexible aero-elastic-drivetrain model of wind turbine blades and towers in the universal multi-body simulation calculation software ADAMS, built a BEM-based aerodynamic model and a drivetrain model in MATLAB and performed joint simulations. However, the design method of each mechanical module of this model is relatively simplified as well as the coupling level is poor. The computational efficiency of the model is very low, and there are a number of errors in the simulation results. NREL integrates the modelling methods and coupling schemes of various mechanical components. In 2005, NREL released the standard definition and modelling method of the 5MW wind turbine model based on FAST [32], and then released the version for OWT in 2009 [66]. In addition to the drivetrain, the modelling

solution includes detailed design solutions for all mechanical modules, including aerodynamics, elastic dynamics and servo dynamics. This leads to a mainstream solution for load analysis of HAWT with traditional rigid-fixed support structures using highly coupled aero-elastic-servo detailed mechanical models.

#### *2.2.1.3 Common research AHSE model*

Compared with bottom fixed wind turbine modelling, there is more attention to hydrodynamics and mooring dynamics when modelling FOWT, that is, the movement of the floating platform. The results of a systematic comparative study of multiple wind turbine dynamic codes emphasized that the floating platform and mooring system present a much more complicated force situation and movement than bottom fixed wind turbines [29]. In addition, the FOWT control system requires a specifically design to improve responsiveness and an effective mechanism to deal with the negative damping caused by pitching motion compared to classical OWTs.

In the earliest research on FOWT dynamics, the coupling model of Hydro dynamics and mooring line dynamics was designed and discussed extensively. Among them, several "Floating platform & Mooring line" designs and definitions represented by Spar [67], Semi-submersible [68], ITI barge [67], TLP [69] and V-shape [70] have been widely recognized, and extensive hydro-mooring coupled dynamic studies have been carried out on these common research models [71][15]. Properties of these common research models are summarized in Table 2.1.

*Table 2.1 Floating structure and mooring system properties in common research models*

| Parameters | OC3-Hywind Spar Buoy | OC4-DeepCwind Semisubmersible | MIT/NREL TLP | ITI Barge | V-shaped Semisubmersible |
|---|---|---|---|---|---|
| **Total draft (m)** | 120 | 20 | 47.89 | 4 | 28 |
| **Water** | 8029.21 | 13433 | 12179 | 6000 | 10014 |

| | | | | | |
|---|---|---|---|---|---|
| **displacement ($m^3$)** | | | | | |
| **Platform mass (kg)** | $7.466\times10^6$ | $1.3473\times10^7$ | $8.6\times10^6$ | $5.452\times10^6$ | $9.503\times10^6$ |
| **Number of mooring lines** | 3 | 3 | 8 | 8 | 3 |
| **Line diameter (m)** | 0.09 | 0.0766 | 0.127 | 0.0809 | 0.138 |
| **Line mass density (kg/m)** | 77.71 | 113.35 | 116.03 | 130.4 | 117 |
| **Line extensional stiffness (N)** | $3.84\times10^8$ | $7.536\times10^8$ | $1.5\times10^9$ | $5.89\times10^8$ | $3\times10^9$ |

Based on the mature OWT coupled dynamics model, these FOWT-specific mechanical components are tried to be coupled into partially coupled dynamic models of FOWT. Karimirad et al. [72] used hydro-elastic code USFOS/vpOne and HAWC2 code to build a hydro-elastic model of tension leg spar FOWT for coupled hydro-elastic stochastic time-domain analysis. During the simulation, HAWC2 undertook wind turbine dynamic response analysis while USFOS/vpOne did dynamic response analysis of offshore structures. It is worth noting that this analysis is limited to the response caused by waves. Fylling et al. [73] conducted research on FOWTs using a aero-hydro-elastic coupled model, in which SIMO is used to simulate structural dynamics and hydrodynamics, and RIFLEX is used to model mooring lines with FEM technology. Withee [74] applies the ADAMS and the aerodynamic, hydrodynamic and mooring system subroutines to perform coupling calculations in the time domain through dynamic link library technology to simulate the dynamic response behaviour of FOWT. Similarly, Matha et al. [75] used the general multi-body simulation calculation program SIMPACK, combined with the subprograms AeroDyn, HydroDyn and the self-developed mooring-line subprogram, to study and analyse the dynamic characteristics of FOWT in the time domain. Cheng et al. [76] developed a fully coupled

aero-hydraulic dynamics solver FOWT-UALM-SJTU, introduced CFD analysis method to establish a FOWT aero-hydro coupled model.

However for FOWT, the platform floating motion indeed includes 6 degrees of freedom (DOFs) [77], enabling a great variety of sophisticated motion state. During the operation, FOWT bears complex environmental loads. The load is highly coupled with the basic motion, structural vibration and control system, which shows that its numerical simulation requires high-precision fully integrated calculation.

Therefore, the establishment of the FOWT mechanical coupling model has concentrated the cooperation and efforts of the world's best research units, enterprises and universities. In 2007, Jonkman from NREL rewritten the simulation software FAST for FOWTs, and added the self-developed hydrodynamic and mooring-line subprograms, so that the FAST software has the ability to calculate FOWT [77], as shown in Fig. 2.3. The model established through FAST can perform loads analyses for a variety of rotor-nacelle assembly, tower, support platform and mooring system configurations, and has surprising accuracy in verification exercises. In his publication [78], Jonkman named this fully coupled FOWT model “aero-hydro-servo-elastic model”, also known as AHSE model. In addition to NREL's FAST, some research institutions and scholars in the academic circle also developed a number of calculation software based on their own research results and different modelling theories to build a general AHSE model, and have used this as a research platform to carry out research in related fields, such as GH Bladed, HAWC2, SIMA, etc [28].

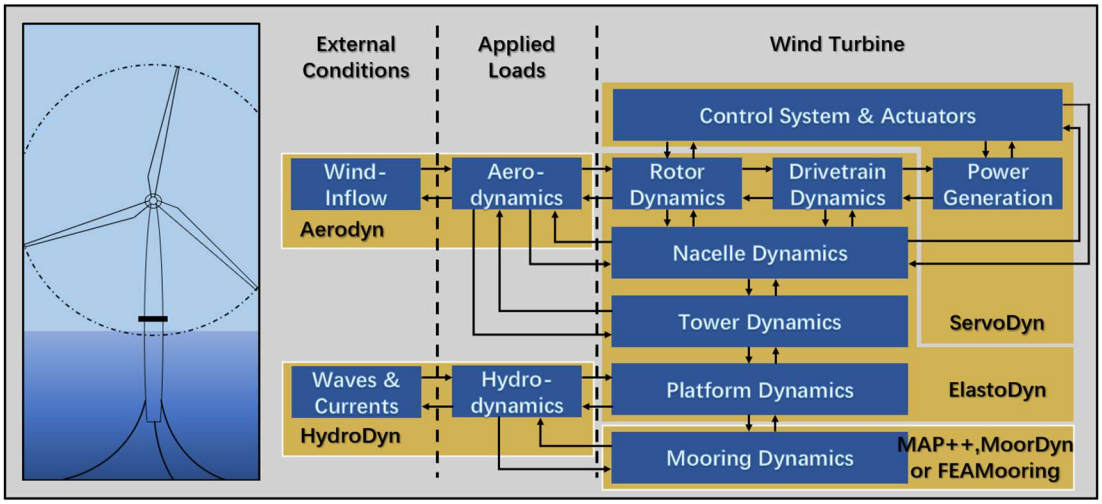


*Fig. 2.3 Program flow of FAST software*

The five models in Table 2.2 are all mainstream simulation design forms that can be traced in the literature. OC3-Hywind is regarded as a classic sample, which has made a great contribution to the establishment of AHSE model of spar type FOWT [29]. A number of research on spar buoy FOWT commonly choose to develop on this basis. AHSE modelling codes that have also been benchmarked and verified are OC4-DeepCwind [79] and OC5-DeepCwind [80], with semisubmersible floating structures.

*Table 2.2 Common research AHSE models of FOWT*

| Common research AHSE models | First appear | Code | Floating platform | Turbine |
|---|---|---|---|---|
| **OC3-Hywind** | 2010 | OC3 participants | OC3-Hywind spar buoy | NREL 5MW OWT |
| **MIT/NREL TLP FOWT** | 2010 | FAST | MIT TLP | NREL 5MW OWT |
| **OC4-DeepCwind** | 2014 | OC4 participants | OC4-DeepCwind semisubmersible | NREL 5MW OWT / DTU 10MW RWT |
| **V-shaped semisubmersible** | 2015 | FAST | V-shaped semisubmersible | NREL 5MW |

| | | | | |
|---|---|---|---|---|
| **FOWT** | | | | OWT |
| **Barge-Supported FOWT** | 2019 | FAST | ITI Energy barge | NREL 5MW OWT |

As of the year 2021, with the help of massive contributions of research carried out on scaled-down experimental models and mechanical simulation codes, two offshore floating wind farms have been successfully on the grid for power generation. The basic characteristics of these wind farms are summarized in Table 2.3.

*Table 2.3 Characteristics of floating offshore wind farms operating around globe*

| **Floating offshore wind farms** | **Year of operation** | **Location** | **Depth (m)** | **FOWT type** | **Floating Structure** | **Capacity (MW)** |
|---|---|---|---|---|---|---|
| **Hywind Scotland** | 2017 | Scotland | 120 | Siemens Wind Power SWT-6.0-154 | OC3-Hywind | 5 x 6.0 |
| **Windfloat Atlantic** | 2020 | Portugal | Around 100 | MHI Vestas V164-8.4MW | Windfloat Semisubmersible | 3 x 8.4 |
| **Hywind Tampen** | 2022 | Norway | | | | |

As for FOWT aero-hydro-servo-elastic models with other types of floating structure and mooring system, although there are limited international cooperation compared to OC3-Hywind and OC4-DeepCwind model, some scientific research organizations and individuals still tried to develop their AHSE models. Based on the updated version of FAST, Matha and Jonkman [81], Ramachandran and Vasanta [82] presented the AHSE modelling method with the TLP-type floating structure by different codes. Karimirad and Michailides [70] proposed the concept of V-shaped semisubmersible FOWT and used the tool “Simo-Riflex-Aerodyn” to establish an AHSE coupling model. He also specifically discussed the

impact of this special FOWT in the face of misaligned wave and wind [83], further proving the feasibility of this innovative solution. Qinwei [16] designed the Barge-Supported FOWT AHSE model based on FAST，in which the floating structure refers to NREL's ITI 5MW barge design scheme[78]. These modelling methods still have room for improvement as little codes has been able to adopt the most refined theory in each sub-dynamic module, and imperfect coupling effects have resulted in additional errors. Thus, accuracy and effectiveness of the modelling codes need to be further proven.

With certified and widely recognized mainstream codes such as FAST, HAWC2, and Bladed as benchmarks, more newly developed codes have simple and feasible verification and optimization methods. Based on the modelling theory of [84], Lemmer [85] developed an efficient AHSE reduced-order model SLOW. This model has only two DOFs, and pitch control is coupled into the aerodynamics model as the only part of servo dynamics. Compared with the AHSE model with the same properties run by FAST, the model with a full-module reduced-order design has a computational speed that is hundreds of times faster. Jiahao et al. [30] developed the code DARwind based on the coupled aero-hydro-servo-elastic method and has passed the verification exercises. However, its improved aerodynamic model has inaccurate simulation results when violent motion occurs under severe sea conditions, and the performance of the control system does not meet the expectations at the beginning of the design. Y. Yang[86] developed a novel framework F2A based on OpenFAST and AQWA, which shows a high degree of consistency in comparison with OpenFAST. And compared to OpenFAST, F2A has the ability to simulate fully coupled FOWT supported by multiple floats connected by flexible elements and has the ability to obtain dynamic responses through decoupling methods. M. Leimeister [87] established an OC3-Hywind model based on the MoWiT Library to verify the accuracy and reliability of the code in AHSE simulation. All these novel simulation codes are summarized in the Table 2.4.

*Table 2.4 Novel AHSE coupled modelling codes*

| Refs | Code | Methods | | | | Verification model | | |
|---|---|---|---|---|---|---|---|---|
| | | **Aero** | **Hydro** | **Servo** | **Elastic** | **Platform** | **Turbine** | **Contrast** |
| [85] | Concept-level SLOW | BEM | Airy +ME | UD | FEM/Modal+MBD | INNWIND.EU TripleSpar platform | DTU 10MW RWT | FAST |
| [88] | DARwind | BEM Correction + DS | LPF + SWF + ME | UD | FEM/Modal+MBD | OC4-DeepCwind semi-submersible ExpMdl | | FAST + ExpMdl |
| [86] | F2A | BEM/GDW + DS | Airy+ ME+ UD | DLL, UD, SM | FEM+MBD+ABM | OC3-Hywind spar buoy | NREL 5MW | FAST |
| [87] | MoWiT | BEM/GDW + DS | Airy+ WS+ ME/MCF | DLL, UD | FEM/Modal+MBD | OC3-Hywind spar buoy | NREL 5MW | FAST |

#### *2.2.1.4 Advanced AHSE model*

Due to the satisfactory accuracy and adaptability of the internationally recognized OC3-Hywind, OC4-Deepcwind framework codes shown in the research report [67][79], they have become the reference samples for scholars to model when conducting dynamic analysis of FOWT. At the same time, new or improved codes/models are designed to overcome the code-related problems that were originally pointed out in the project report. Therefore, these internationally recognized old codes have also become comparison objects in the verification process with new models with advanced concepts or detailed single-module designs.

First of all, with the improvement of hydrodynamic research, the AHSE model is no longer exclusive to FOWT. Some studies have also begun to apply the AHSE model to OWT modelling. Research team from DTU[89] presents a novel aero-hydro-servo-elastic coupling framework, MIRAS-HAWC2. A solver based on multi-body vortex particles is used to predict the aerodynamics of the rotor, which increases the fidelity of the model compared to the traditional BEM method. Z. Lin[90] has extensively designed, verified and compared a series of reduced-order AHSE-DT models that specialize in offshore wind turbine O&M. The results show that some models capture the dynamics of the turbine for a specific failure well and have improved calculation efficiency, which are more suitable for application in wind field models.

As for FOWT, with a full understanding of the theory of OC3-Hywind modelling, Karimirad [91] proposed a method to build a simplified AHSE model, which not only has acceptable accuracy, but also greatly reduces the amount of calculation required for simulation. For researchers working under wave-only cases, as well as for the wave- and wind-induced cases, this model can save a lot of time. Under the OC5 framework, Beardsell[92] improved the Bladed-based AHSE model, and fixed the problem that the low-frequency excitation was not fully captured when the Bladed was used for numerical simulation. The results show that the advanced OC5-Deepcwind model has significantly improved the prediction of tower foundation shear force. Sethurama[93] designed a fully coupled AHSE model for spar buoy direct drive FOWT, which is characterized by coupling with a detailed direct-drive shaft model validated by FEA. In the analysis of FOWT structural dynamics, Okpokparoro [94] added uncertainty modelling to make the computational result more accurate using FEA.

In addition to the above research on the comprehensive update of the modeling theory, there are many studies that supplement the common research AHSE coupled models illustrated in user's manual of mainstream codes such as OpenFAST [95], HAWC2 [96] and GH Bladed [97]. In order to further control and optimize the operation of FOWT, many

scholars have enriched the control system (servo dynamics) based on the typical AHSE model mentioned in Section 2.1.3 and added advanced control strategies for wind turbines. Qinwei [16] equipped a TMD on nacelle to control the barge FOWT generator to improve its stability, and the results show that the stability has been significantly improved. Mingming [98] designed an internal closed-loop deformable trailing edge flap (DTEF) control system based on the principle of smart rotor control and set the AHSE model of typical TLP-type FOWT on FAST [69] as the control object. The results show that the systematic implementation of intelligent DTEF control on the fatigue load of FOWT can effectively suppress the fluctuating load and relative movement of key components, and the fatigue load of turbine components. Wakui et al. [20] designed a new FOWT generator system feedback control in FAST servo dynamic module to reduce platform shaking and generator output power fluctuations. The main variables controlled by this study are blade pitch and generator torque. However, the generator model uses the first-order steady-state equivalent model, and the research in the electrical field only stops at the generator output power itself. In 2018, Tong et al. [17] teamed up with FAST and Simulink to explore the passive vibration control of FOWT AHSE models, because flexible turbine modelling and control can be performed in the Simulink environment. A bidirectional tuned liquid column damper (BTLCD) electrical model was built in Simulink to suppress the pitch and roll motion of the barge. This research only focuses on the hydrodynamic model of the floating structure and does not specifically design the aerodynamic model and electrical model. In the electrical field, only the change in the rotor speed and output power of the BTLCD itself are explored. All contributions mentioned in this section are summarized in the Table 2.5.

*Table 2.5 Contributions to advanced AHSE models*

| Refs | Codes | Structure type | Turbine | Modified module | Achievements |
|---|---|---|---|---|---|
| [89] | MIRAS, | rigid foundation, the | NREL 5MW | Aerodynamics | A novel aerodynamic analysis |

| | | | | | |
|---|---|---|---|---|---|
| | HAWC2 | tripod and the jacket | OWT/ DTU 10MW RWT | | method with higher precision |
| [90] | FAST | rigid foundation | NREL 5MW OWT | AHSE | Reduced-order model applied to O&M research of offshore wind farms |
| [91] | FAST | OC3-Hywind spar buoy | NREL 5MW OWT | AHSE | A simplified model with high computational efficiency |
| [92] | Bladed | OC5-DeepCwind semisubmersible | NREL 5MW OWT | AHSE | low-frequency excitation is able to be fully captured |
| [93] | HAWC2 | OC3-Hywind spar buoy | NREL 5MW OWT | Servo dynamics, drivetrain | Control scheme and detailed drivetrain model for PMSG |
| [94] | FAST | OC3-Hywind spar buoy | NREL 5MW OWT | Elastic dynamics | A methodology for capturing uncertainties to improve the accuracy of elasticity analysis |
| [98] | FAST, Simulink | MIT TLP-type | NREL 5MW OWT | Servo dynamics | An internal closed-loop DTEF control system |
| [16] | FAST, Simulink | ITI barge | NREL 5MW OWT | Servo dynamics | A nacelle-based TMD method generator control |
| [20] | FAST, Simulink | OC3-Hywind spar buoy | NREL 5MW OWT | Servo dynamics | A new designed generator system feedback control |
| [17] | FAST, Simulink | ITI barge | NREL 5MW OWT | Servo dynamics | Adding a BTLCD control to suppress the pitch and roll motion of the platform |

### 2.2.2 Development & contributions to WECS modelling

#### *2.2.2.1 Bottom-fixed OWT & FOWT model comparisons*

The bottom-fixed OWT electrical model describe in detail the dynamic and transient characteristics of its WECS and provide convenience for the research on issues such as grid connection and converter control design. In the model, Generator, converter and control system are the core parts of the wind turbine electrical model. The generator-converter model of FOWT can be inspired by the generator-converter model of traditional rigid

foundation OWTs as they share the same design principles. However, due to the floating characteristics of the supporting structure, the stable operation of the FOWT requires a very comprehensive control strategy, including the mechanical and electrical fields. As shown in the Fig. 2.4, the variable speed wind turbine has different control strategies in different operating regions. Therefore, Type III and Type IV wind turbines are able to meet the requirements because these types of wind turbines can operate at variable wind speeds and result in improved power quality.

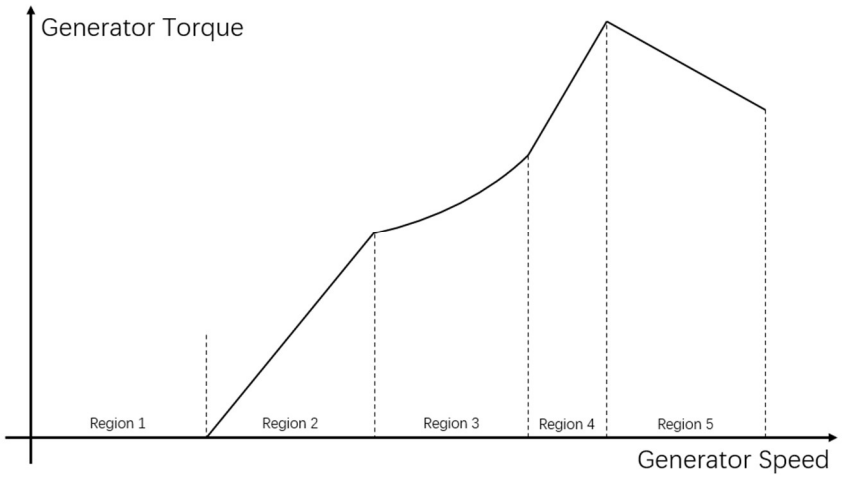


*Fig. 2.4 Operating region of the variable speed wind turbine*

In addition, the capacity of a single FOWT tested or operated is commonly larger than that of the traditional rigid foundation wind turbines [99]. The reasons are as follows: ①the environment of open seas is not restricted by many objective factors like inland or offshore. ②wind resources in the further offshore are much more abundant than inland or offshore, and higher average wind speeds are matched with more powerful wind turbines ③the FOWT with larger capacity per tower is more economical in construction and maintenance. Therefore, the generator-converter model of the FOWT can get inspired from generic type III and IV wind turbines with large single-unit capacity, which is being controlled by a more advanced control strategy.

#### *2.2.2.2 Generic WECS model for FOWT*

The detailed design of generator and converter models adapted to the research needs of power systems, also known as WECS models. Such coupling models have been established in large quantities because of the demand for wind turbine research in the field of electrical engineering, and the purpose of simulation is often the study of pure power systems such as power system steady-state analysis, transient analysis, LVRT/HVRT, power control etc. A number of studies on bottom-fixed wind turbines could simplify dynamic modelling, which means only considering aerodynamics and directly linking active power to rotor speed. The design requirements of the wind turbine model corresponding to each research topic are summarized in the Table 2.6.

*Table 2.6 Common single HAWT modelling schemes for different research subjects*

| Research Subject | Dynamics | Drivetrain | Generator & Converter | Grid |
|---|---|---|---|---|
| **Steady-state analysis** | Simplified | Simplified | Simplified | Infinity bus |
| **Transient analysis** | Detailed | Detailed | Detailed | Infinity bus |
| **O&M** | Detailed | Detailed | Detailed | Infinity bus |
| **LVRT/HVRT** | Omitted | Detailed | Detailed | Detailed |
| **MPPT** | Omitted | Omitted | Detailed | Infinity bus |
| **Yaw/pitch Control** | Simplified | Simplified | Simplified | Infinity bus |
| **Power Control** | Simplified | Simplified | Detailed | Infinity bus |
| **Power transmission** | Omitted | Omitted | Detailed | FACT/HVDC |
| **Hydrogen Production** | Simplified | Simplified | Detailed | Omitted |

According to different WECS designs, a total of four types of wind turbines are officially defined and widely used. They can be classified into fixed speed wind turbines (Type 1, Type2) and variable speed wind turbines (Type 3, Type4) according to the characteristics of whether they can change the speed of the impeller.

Fixed speed wind turbines are a relatively old type of wind turbine. Their models have very simple designs and use very limited and simple control methods. They have been

installed in large numbers because of their high economic advantages, but with the decline in the manufacturing cost of variable speed wind turbines and the lack of controllability, they gradually began to withdraw from the market [24]. For the electrical model of variable speed wind turbine, the current research can mainly divide it into detailed model, reduced-order model, and steady-state model. The detailed model is generally a fifth-order model to reflect the electromagnetic transient characteristics of the wind turbine. The reduced-order model ignores the electromagnetic changes of the stator flux linkage and is generally a third-order model. The steady-state model further ignores the electromagnetic transient characteristics on the basis of the reduced-order model and is generally a first-order model.

For type 3 wind turbines, both the stator and rotor can exchange power with the grid, as it shown in Fig. 2.5(a). And power electronics (PE) converters control the active power, reactive power, and power factor output by the wind turbine. The converter control strategies of doubly fed wind turbines mainly include vector control, direct power control and direct torque control. The current technologies are relatively mature. Among them, vector control is relatively simple to implement, with high precision and robustness, and is the most widely used. J. Liu and Z Liu [100], Xu et al. [101], Yang et al. [102][103] and López's [104] research all established detailed WECS models. Ma [105] established a reduced order model suitable for small signal stability analysis. The common feature of these reduced-order models is that they significantly reduce the amount of calculation during simulation, but the accuracy is not high. Arachchige et al. [106] simplified the design of PE converters and built an average model with simulation speed 5 times faster than that of general detailed model. But when the system is unbalanced, the RMS bus voltage calculated by the model is slightly off.

Type 4 wind turbines rectify and invert the electrical energy from the generator and connect to the grid, as it shown in Fig. 2.5(b). At present, there are two mainstream designs, and their inversion process is realized by grid side converter (GSC). One design of the rectifier is diode rectifier and boost converter. The rectification process cannot be controlled,

and the active power generated by the generator is adjusted by controlling the duty cycle of the switch of the Boost circuit. Sirichai[107] established a detailed model of the rectifier plus boost circuit. Another design of the rectifier is the machine side converter (MSC), which can effectively control the electromagnetic torque of the generator, and then effectively perform MPPT. Mohsen established a reliable detailed model, focusing on in-depth stability analysis and operation control.

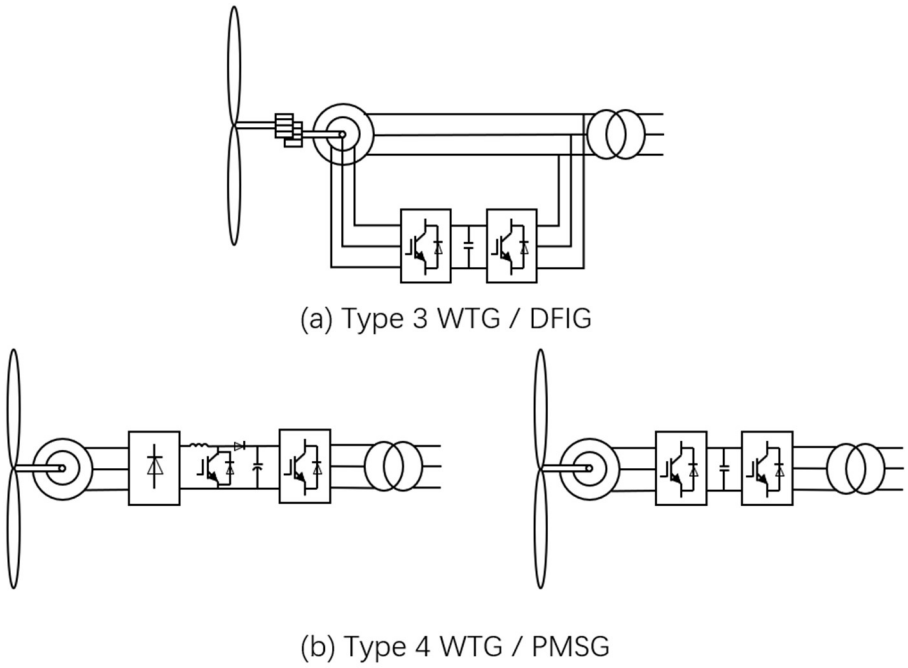


*Fig. 2.5 Variable speed WTG design*

The detailed electrical models of all four types of wind turbines contained in the Simscape Electrical library of Simulink have been summarized by NREL[108], which comprehensively introduces the theory based on the design of the generator model, the characteristics of the model and the existing problems. In order to compare the ferromagnetic resonance modes of the four types of wind turbines under overvoltage levels, Akinrinde et al. [109] designed detailed models of all four types of wind turbines. Honrubia-Escribano et al. [22] summarized the results obtained by the IEC and WECC working groups in the process of studying all four forms of Generic dynamic wind turbine

models. This article comprehensively reviewed the Generic dynamic wind turbine models used to analyse the stability of the power system. The aerodynamic, drivetrain and electrical components of the coupled model have a detailed summary. However, this review still only includes the efforts of electrical engineers. The aerodynamic and mechanical models summarized are simplified from the perspective of mechanical engineers.

It is worth noting that although these electrical models also include mechanical modules and operates in grid, they are classified as simplified models. The mechanical model design method is usually: input the average wind speed to establish the power coefficient ($C_p$) model and equivalently calculate the mechanical torque and connect to the detailed design generator-converter through the classic one-mass or two-mass drivetrain model. This is understandable, because not only the impact of mechanical models can be ignored in some electrical related studies, but also a partially detailed model could help researchers save calculation costs and resources. As for the grid design of the models, a step-up transformer and a terminal bus are commonly included [110]. Some single OWT models have coupled compensator, grounding transformers, long transmission line modules and protection circuit, to get the model be able to undertake LVRT/HVRT and power transmission related research.

### 2.2.3 Scaled FOWT model experiments

FOWT model experiments started as early as 2009 in Japan[111], in a 1/22.5 scale. As of the end of 2015, as many as 9 experimental scaled-down models have been installed, and all these early experimental models have been summarized by Gordon Stewart[112]. Early model experiments mostly used disc equivalent wind wheels, mainly based on the simulation of aerodynamic thrust, but this method ignored the aerodynamic characteristics of the wind wheel system such as torque and gyro torque. Started from 2011, some model experiments[113] gave up the similar wind speed setting and adjusted the wind speed to match the aerodynamic load of the model. However, this method cannot guarantee non-

rotating substance, such as a pneumatic load and the water flow field state more similar to the platform and the tower. But soon, the mainstream research direction abandoned the geometric similarity of the blades and redesigned the model to adapt to the blade airfoil with low model Reynolds number, such as Fowler[114], Duan[115], Chen[88], etc. However, these scaled-down models did not adequately consider the same material, construction methods, or deployment method as the full-scale system[116], which leads to limited accuracy. In particular, a scaled-down model experiment in a wave basin inherently has limitations on the simultaneous satisfaction of both Froude and Reynolds scaling laws[117][118]. An experiment on a FOWT is usually more expensive than a sophisticated design tool, which is preferred for cost-effective solutions during the design process. So that the purpose of many latest experiment models built subsequently has become focusing on validating tools (code-to-data comparisons)[119] or start a real-time hybrid model test with simulation software[120], thus significantly helped improving the accuracy of the design models.

## 2.3 Wind turbine mechanical-electrical coupled modelling

Due to the limitations of a single simulation software or code, existing literature has proposed a cross-platform co-simulation strategy for wind turbine modelling. Hemeida et al. [121] respectively established electromechanical coupling models of direct drive PMSG with converters, but they did not verify the accuracy of the simulation results of this model. Shariatpanah et al. [122] built a 10kW PMSG fully coupled AHSE model with high accuracy. Ochs et al. [123] comprehensively designed and verified the electromechanical coupling model of the permanent magnet direct drive wind turbine, which is the first coupled direct drive PMSG model that includes high-detail, high-precision mechanical, and electrical parts. Malik and Mishra [124][125] even applies information processing systems including Probabilistic Neural Network (PNN), Artificial Neural Network (ANN) and

Empirical Mode Decomposition (EMD) to the wind turbine electromechanical co-simulation model to verify the performance of wind turbine condition monitoring. However, the study only reached a preliminary conclusion, and the monitoring system could not identify the type of unbalanced fault.

In 2008, from the perspective of electrical engineering, Fadaeinedjad et al. [110] summarized the modelling scheme of all aspects of the detailed model of the FAST+Simulink co-simulation platform. Subsequently, this co-simulation scheme quickly became the mainstream choice for building WECS models. Chen [126] applied the interaction between FAST and Simulink to identify the mechanical parameters of DFIG wind turbines that have been running for many years. In the simulation platform she built, FAST outputs source code MEX files written in C or Fortran language, and MEX can be called in Simulink in the form of s functions, so simple offline co-simulation can be realized. In 2014, the developer of FAST, NREL, published a guide [108] to the use of FAST and Simulink co-simulation wind turbine generator, which comprehensively introduced the four generator models in Simulink and the electromechanical co-simulation method. Yang [127] uses the co-simulation platform to in-depth study of pitch control and drivetrain load suppression strategies. Literature [128] compiles the electrical and control model built by Simulink into a DLL (Dynamic Link Library) file and performs co-simulation with Bladed. However, a new DLL must be regenerated and embedded in Bladed every time the working conditions are switched, which is cumbersome. Wang [129] writes s-functions in MATLAB and uses interface technology to establish data transmission with DLL files, which effectively solves the defects in Literature [128], but only explores the changes in rotor speed and output power, and the electrical model is still not detailed enough. Literature [130] establishes a refined wind turbine model based on Real Time Digital Simulator (RTDS) and Bladed. However, the communication interface of this platform uses analog signal channels, which limits the amount of interactive data. Miao [131] used Simulink to call FAST compiled files to realize co-simulation. On the one hand, based on the demo in the

Simpowersystem library in Simulink, a motor model based on the dq axis, and a converter control model are established. On the other hand, FAST has established models that include blades, towers, and drive shafts. Here FAST also communicates data with Simulink through the S function. However, due to the limitations of computer performance, the design of converters and transformers has been simplified.

With the deepening of research, more technical recognized power system analysis software or platform than Simulink is introduced into real-time simulation. These software or platforms not only have higher performance, but many are compatible with Simulink, such as RTDS, RT-LAB. This means that the models in Simulink can be converted to these professional power system simulation tools in simple steps. Li [132] proposed a joint real-time simulation platform based on FAST and RTDS that meets the requirements of fine wind turbine modelling. Digital communication is realized through RTnet, which has a greater cost advantage than traditional analog communication interfaces. Diao [133] promoted the technology disclosed by Bing and built a real-time simulation platform for wind farms composed of four DFIG wind turbines, including the precise modelling and simulation of wind farms based on RT-LAB and FAST, and electric power system electromechanical systems including wind farms. Electromagnetic hybrid simulation and wind farm SCADA system. However, the wind speed model of the wind farm model does not consider the wake effects and time lag effects between wind turbines, nor can it simulate faults on the electromechanical side.

The characteristics of all the aforementioned co-simulation platforms are summarized in Table 2.7.

*Table 2.7 Fully coupled co-simulation platforms in existing bottom fixed wind turbine research*

| Refs | Year | Turbine Capacity | Electrical Characteristics | | Mechanical Characteristics | | | Research Significance |
|---|---|---|---|---|---|---|---|---|
| | | | Model | Modelling tool | Aerodynamic Method | Structural Dynamic Method | Modeling tool | |
| [110] | 2008 | 1.5 MW | Type III WTG Reduced-order Model | Simulink | BEM | $FEM^{P+}$ (Modal /MBS) | FAST | Testing the performance of controller, investigate the influence of electrical disturbances on mechanical components |
| [128] | 2009 | 3 MW | Type III WTG Reduced-order Model | Simulink | BEM | FEM | Bladed | Certificate the voltage ride through capabilities of a 3 MW Alstom-Ecotècnia wind turbine |
| [126] | 2012 | 2 MW | Type III WTG Reduced-order Model | Simulink | BEM | $FEM^{P+}$ (Modal /MBS) | FAST | Identify the mechanical parameters of wind turbines that have been in operation for years |
| [122] | 2013 | 10 kW | Type IV WTG Reduced-order Model | Simulink | BEM | $FEM^{P+}$ (Modal /MBS) | FAST | The first fully coupled simulation platform designed for type 4 wind turbines, and includes a comprehensive yaw control strategy |
| [123] | 2014 | 10 kW & 5 MW | Type IV WTG Detailed Model | Simulink | BEM | $FEM^{P+}$ (Modal /MBS) | FAST | The first fully coupled detailed model for PMSG |
| [108] | 2014 | \ | All types of WTG Reduced-order Model | Simulink | BEM/GDW | $FEM^{P+}$ (Modal /MBS) | FAST | Gave a comprehensive introduction to the co-simulation method of WTG models of all 4 types in Simulink with FAST |
| [129] | 2015 | 2 MW | Type III WTG Reduced-order Model | Simulink | BEM | $FEM^{P+}$ (Modal /MBS) | Bladed | The impact of LVRT on the wind turbine |

| | | | | | | | | |
|---|---|---|---|---|---|---|---|---|
| [127] | 2015 | 1.5 MW & 2 MW | Type III WTG Detailed Model | Simulink | BEM | FEM$^{P+}$ (Modal /MBS) | FAST | Active control strategies and characteristic of dynamic loads of wind turbine generation systems |
| [131] | 2015 | 1.5 MW | Type III WTG Simplified Model | Simulink | BEM | FEM$^{P+}$ (Modal /MBS) | FAST | Suitable for steady-state analysis, fully coupled Type 3 wind turbine model with detailed drive shaft model |
| [124][125] | 2015, 2017 | 10 kW | Type IV WTG Detailed Model | Simulink | BEM | FEM$^{P+}$ (Modal /MBS) | FAST | Application of PNN and ANN of Fault Diagnosis on a fully coupled PMSG model |
| [132] | 2020 | 5 MW | Type III WTG Detailed Model | RTDS | BEM | FEM$^{P+}$ (Modal /MBS) | FAST | Could carry out electromagnetic transient related research with higher accuracy |
| [133] | 2020 | 1.5 MW | Type III WTG Detailed Model | RT-LAB | BEM | FEM$^{P+}$ (Modal /MBS) | FASTv8 | A wind farm model consisting of four mechanical-electrical fully coupled wind turbines |
| [134] | 2023 | 5MW | Type IV WTG Detailed Model | Simulink | BEM | FEM$^{P+}$ (Modal /MBS) | FASTv8 | RC resonant circuit design for FOWT power quality mitigation at wave frequency |
| [33] | 2024 | 5MW | Type IV WTG Detailed Model | Simulink | BEM | FEM$^{P+}$ (Modal /MBS) | FASTv8 | Floating wind power ramp events characterization |

## 2.4 Coupled FOWT modelling Framework

### 2.4.1 Inspirations from the existing coupled models

At present, there is little research to build a fully coupled FOWT mechanical-electrical model. The model established by Wakui [20] in the study does include a FAST mechanical model, a drive shaft model and a complete Type 3 (DFIG) WTG model. But because its research topic is control strategy, WTG models built based on this research purpose are often first-order simplified models. The design of the generator model is very briefly mentioned in this journal, and this journal only draws preliminary conclusions in the field of power systems. It can be said that the true FOWT fully coupled model has not yet appeared.

But at present, the mechanical models for FOWT and the OWT electrical models are mature and reliable. Moreover, it is technically feasible to directly couple these two models into a mechanical-electrical fully coupled model. For the mechanical coupling modelling of FOWT, a lot of research has contributed to building a detailed and accurate AHSE model, and there are a small number of drivetrain model design schemes for reference. For the FOWT electrical model, it seems acceptable to use the existing generator-converter model applied to OWT's power system stability study.

In the research of bottom fixed HAWTs, a large number of co-simulation platforms including fully coupled dynamic models and detailed electrical models have been designed, summarized in Table 7. Except for hydro dynamics and mooring dynamics, all mechanical and electrical modules are included in these models. This is undoubtedly the most direct inspiration and guidance for FOWT mechanical-electrical fully coupled modelling and simulation.

Regarding the issue of cross-software coupled modelling and co-simulation, external DLL can be used to establish a channel with professional power system analysis software, and DLL is available in all mainstream FOWT mechanical simulation codes summarized in Table 8. Surprisingly, OpenFAST and HAWC2 have designed an interface with Simulink,

which greatly simplifies the difficulty of coupling between the mechanical model and the electrical model of FOWT. At present, many studies have used this scheme to establish a full-detail model of the rigid foundation wind turbine, which inspired the development of FOWT's mechanical-electrical fully coupled model and simulation platform. In addition, some advanced power system simulation tools such as RT-LAB and PSCAD allow the model in Simulink to be converted to its platform for simulation in simple steps. This means that more professional mechanical-electrical fully coupled FOWT models based on platforms such as FAST-RTLAB can also be expected.

*Table 2.8 Overview of simulation capabilities of major aero-hydro-servo-elastic codes*

| **ADAMS** | **Bladed** | **FAST** | **HAWC2** | **GAST** | **Flex** | **3DFloat** |
|---|---|---|---|---|---|---|
| **Developer** | | | | | | |
| MSC+NREL | DNV | NREL | DTU | NTUA | DTU | IFE |
| **Aerodynamics** | | | | | | |
| (BEM/GDW) + DS | (BEM/GDW) + DS | (BEM/GDW) + DS | (BEM/GDW) + DS | (BEM/3DFW) + DS | (BEM/GDW) + DS | BEM/GDW |
| **Hydrodynamics** | | | | | | |
| (Airy+ / UD) + ME | (Airy+ / Stream) + ME | (Airy+ / UD) + ME | (Airy+ / UD) + ME | $Airy^{str}$ + PF or Stream + ME | $Airy^{str}$ + PF or Stream + ME | $Airy^{str}$ + PF/UD Stream + ME |
| **Servo Dynamics** | | | | | | |
| DLL, UD | DLL | DLL, UD, SM | DLL, UD, SM | DLL, UD | DLL, UD | UD |
| **Elastic Dynamics** | | | | | | |
| MBS | $FEM^{P}$+ (Modal/MBS) | $FEM^{P}$+ (Modal/MBS) | MBS/FEM | MBS/FEM | Modal/FEM /Modal + FEM | FEM |
| **Comprehensive test involved** | | | | | | |
| OC3 | OC3, OC4, OC5 | OC3, OC4, OC5 | OC3, OC4, OC5 | OC4 | OC3, OC4 | OC4, OC5 |

| Open Accessibility | | | | | | |
|---|---|---|---|---|---|---|
| √ | √ | √ | × | × | √ | √ |

### 2.4.2 Proposed modelling solution

For establishing a FOWT mechanical-electrical fully coupled model, the main work is to integrate the existing mechanical model and electrical model. A very good AHSE fully coupled mechanical model can be built in the dynamic simulation software. Similarly, a detailed fully coupled WECS model can be built in the power system simulation software. Realization of co-simulation relies on external DLL including in all mainstream dynamic simulation software; or FAST, HAWC2's unique direct connection module with Simulink. It is also easy to replace Simulink with more advanced power system software, and there have been successful cases published in the academic community. The block diagram of the FOWT mechanical-electrical full-detailed coupling model under the co-simulation platform is shown in the Fig. 2.6.

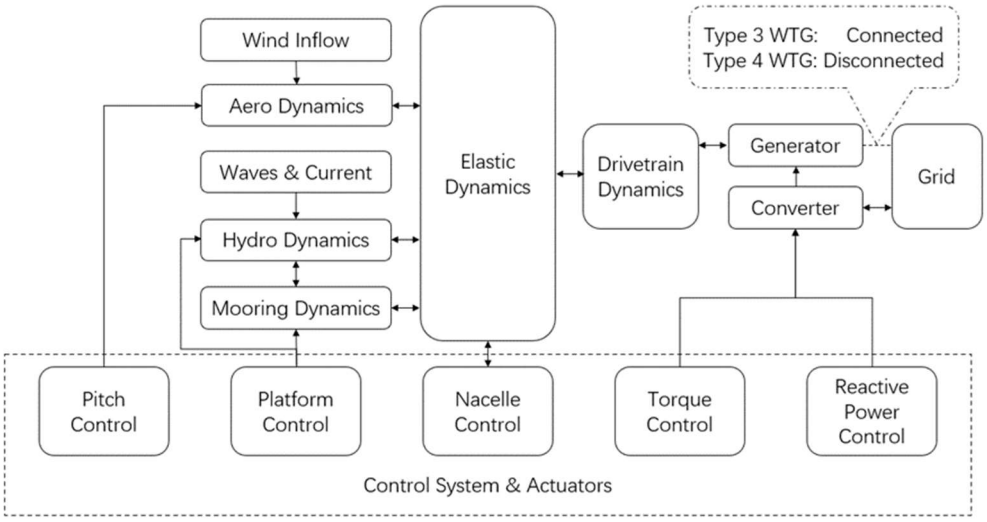


*Fig. 2.6 Block diagram for fully coupled FOWT model*

For FOWT, the dynamic analysis method of the coupled dynamic analysis code is still in the process of research and improvement, and it has been emphasized that it will obtain limited accuracy in extreme motion situations. Therefore, when using this co-simulation platform, researchers should better not involve the research of FOWT under too extreme motion conditions for the time being.

As for the control system, the design and integration method need to be reconsidered. As for FOWTs, there is no unified and comprehensive control strategy that thinks from a mechanical and electrical perspective, so the early mechanical-electrical fully coupled model built in the future may still be based on the design of the OWT control system and modified according to the research towards to FOWT control in specific areas. And how to cooperate with the control strategy of OWT and the control strategy of floating platform will be an interesting theme.

## 2.5 Conclusion to this chapter

This chapter comprehensively reviews the mechanical-electrical model established during a comprehensive and detailed study of FOWTs from the perspective of mechanical and electrical engineers. In the early days of wind power research, researchers in the mechanical and electrical fields conducted independent research in their respective fields, and the models built did not overlap. In recent years, research in the electrical field has begun to pay attention to the impact of wind & waves on OWTs and power systems. In recent years, researchers have introduced detailed mechanical models of wind turbines, with higher orders, more complete control strategies and more accurate dynamic analysis methods. It can be said that the joint model allows electrical engineering researchers to enter a more accurate and detailed new level of research on the operation status of the wind turbine power system. This makes future research on the power system analysis of wind

turbines no longer just a simple process of modelling the mechanical part, and there will be more studies using electromechanical joint models to conduct research.

After more than ten years of co-simulation exploration, the use of FAST+Simulink is currently a friendly approach for building FCMEDM for FOWTs. Open-source software, efficient calculations and good accuracy are the main driving factors. In order to carry out comprehensive and detailed research in power system steady state and transient response, more advanced and accurate simulation platform has replaced Simulink for research, represented by RTDS and RT-LAB.

At present, the research on the use of co-simulation is still in the early stage, and the research focus of scholars in the field is mainly on the detailed modelling and reduction processing of a single wind turbine. With the in-depth research on the operation characteristics of wind power grid-connected and the continuous expansion of installed capacity, large-scale wind farms have an increasing impact on the power grid. Therefore, the dynamic characteristics of wind farms have gradually attracted the attention of scholars. A small number of electromechanical joint models of wind farms composed of multiple wind turbines have been built and applied to the steady state and transient state of the power system, which has obviously become a new research direction in the field of wind turbine electrical.

In addition, the research on establishing the co-simulation model of FOWT is limited. On the one hand, there are few applications for floating wind turbines. This makes it difficult to verify the validity of the simulation model established by the researchers. It is foreseeable that in future research, a FOWT co-simulation platform with detailed models of all mechanical and electrical components will be established, which can more effectively quantify the power characteristics of FOWT and provide targeted control through pitch angle control, yaw control, generator torque control, converter control, additional electrical component coupling control, etc

# Chapter 3: Characterizing Ramp Events of Floating Offshore Wind Power

## 3.1 Introduction

The abrupt power fluctuations, characterized by substantial magnitudes and brief durations, that manifest during the operation of wind turbines and wind farms are typically attributed to intricate physical processes and atmospheric phenomena, including thunderstorms, gusts, cyclones, and low-level jets [138]. These phenomena are collectively referred to as Wind Power Ramp Events (WPREs). A key approach to address this challenge involves the quantification of WPREs, encompassing their intensity and frequency characteristics, as it aids in power system planning by providing crucial information for predicting necessary control measures [139]. In accordance with the findings of Reference [140], a power-ramp rate limit control was devised within the context of a wind-solar system. This control mechanism was designed to alleviate the impacts stemming from distinct fluctuations in power, specifically those attributable to wind, solar, and load dynamics of a substantial nature. Reference [141] studied the optimal daily peak-load scheduling for cascaded hydropower stations with consideration of wind energy uncertainty based on WPRE research. In a separate study [142], flexibility requirements based on WPRE analysis were employed to investigate cases involving energy storage and flexible power generation. Moreover, the accuracy of WPRE detection is pivotal in ensuring the reliability of wind power forecasting. Reference [143] introduced a range of data sampling techniques aimed at enhancing the accuracy of ramp alerts for wind power events by effectively addressing the issue of class imbalance. Reference [144] introduced pattern recognition to probabilistic forecasting, leading to improved reliability and sensitivity of wind power predictions. Reference [145] improved prediction accuracy by employing precise wind process (WP) and wind process pattern (WPP) delineation in the pattern recognition stage. However, existing achievements have been primarily based on onshore or bottom-fixed Offshore Wind Turbine (OWT) types, leaving a research gap in WPRE studies

related to Floating Offshore Wind Turbines (FOWT), as platform motions could result in elevated power output fluctuations and deteriorate the overall generating performance significantly [20].

Presently, only 3 grid-connected floating wind farms are in operation worldwide [2][3][146], making it challenging to directly reference and analyse open-access operational data. As an alternative approach, modifications could be made based on reliable mathematical models of wind turbines [123]. In the generic dynamic Wind Energy Conversion System (WECS) modelling developed by widely recognized International Electrotechnical Commission (IEC) and Western Electricity Coordinating Council (WECC) working groups, power characteristics are simplified and correlated with wind speed [22]. Such approaches, incorporating linearized aerodynamic models, consider the limited knowledge background of grid operators in dynamic analysis [9]. Despite the proven reliability of generic WECS models over the past decade [132][103][10][109][11], they cannot be directly applied as references for FOWT modelling, as they suffer from three crucial limitations:

(1) The simplified aerodynamic models fail to capture the significant variations in FOWT power characteristics [20][147].

(2) Research on FOWT power characteristics through FAST represented dynamic simulation codesare commonly based on the first-order induction generator provided by the code by default [148], while the research on synchronous generators with large inertia and low speed ratio is limited [149].

(3) The generic WECS models completely disregard the influence of wave loads on FOWT power, a factor that could potentially play a pivotal role in the emergence of WPREs [5][150].

Hence, there is a need for a comprehensive aero-hydro-servo-elastic (AHSE) dynamic model coupled with the WECS model. Therefore, in this chapter, an interdisciplinary study

is proposed to explore a mechanical-electrical fully coupled model to investigate real-world grid-connected scenarios involving WPRE cases, with a careful consideration of input wind and waves. The graphic outline of the entire study is logically summarized in Fig. 3.1. Initially, a standard AHSE model was developed using the open-source FAST software, while a detailed high-order WECS model was created using Simulink. The dynamic analysis was performed using FAST, and the DLL interface was employed to establish a connection between the WECS model and the generator, enabling the exchange of critical parameters such as electrical power and mechanical speed. This achieved a precise electromechanical coupling for the FOWT. Subsequently, adjustments were made to the hydrodynamically influenced FOWT equivalent power curve, accurately representing its electrical energy generation under real operational conditions. Optimized Swinging Door Algorithm (OpSDA) has conducted successful and impactful research in conventional wind farms by effectively combining "bumps" displaying diverse directional changes into neighbouring slope segments, resulting in significant enhancement of detection precision [138], and is chosen to serve as a foundation for floating offshore WPRE data analysis. In this study, the OpSDA was tailored and optimized to suit the specific considerations of hydrodynamics, facilitating thorough data processing and analysis in the context of WPRE assessment.

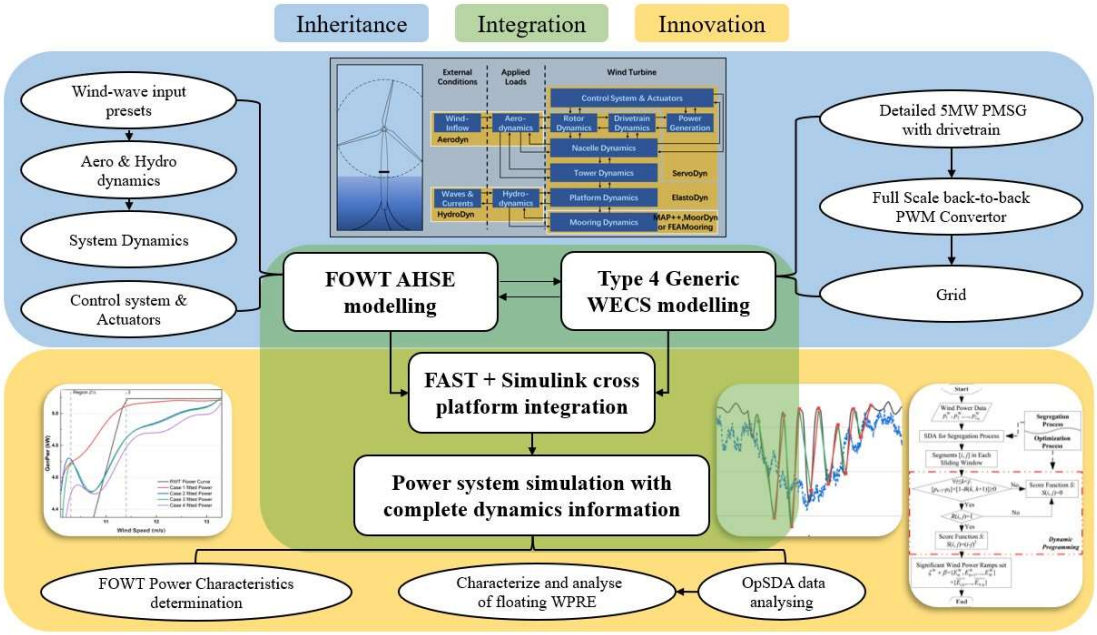


*Fig. 3.1 Graphic Outline of floating offshore WPRE research*

The chapter is organized as follows: Section 2 outlines the mathematical model formulation. Section 3 presents details of the flowchart-based simulation model setup based on Fig. 3.1. In Section 4, the relationship between hydrodynamic characteristics and power is examined under various wind and wave conditions, with detailed simulation results provided for a full range of conditions. Finally, Section 5 presents the conclusion.

## 3.2 Complete system mathematical model formulation

The fully coupled model developed in this chapter includes two distinct aspects of the complete system: modelling of the FOWT dynamics and that of the energy conversion system.

### 3.2.1 TurbSim-based Wind speed modelling

The wind speed on the swept surface of the impeller includes two parts: random process and periodic process. Stochastic processes generally refer to turbulent winds that vary continuously in time and space. The periodic process is mainly caused by wind shear and tower shadow effects. According to the requirements of the wind turbine load

calculation standard IEC61400-1:2019 [151], TurbSim simulates the turbulence, wind shear and tower shadow effects of wind speed when modelling wind speed.

#### *3.2.1.1 Turbulent Wind Modelling*

TurbSim uses the Kaimal model to simulate turbulent wind. The random signal generated by this model is filtered by the Kaimal filter [152], and the obtained random wind speed model conforms to the Kaimal spectrum distribution, as shown in (3.1).

$$\omega_T S_v(\omega_T) = \frac{\frac{\omega_T x_L}{V_{mean}}\sigma_v^2}{(1+1.5(\frac{\omega_T x_L}{V_{mean}}))^{\frac{5}{3}}} \tag{3.1}$$

where $V_{mean}$ is the average wind speed; $\omega_T$ is the frequency of the turbulent wind; $x_L$ is the turbulent scale; $\sigma_v$ is the standard deviation of the turbulent wind speed sequence; $S_v(\omega_T)$ is the power spectral density of the turbulent wind.

#### *3.2.1.2 Wind Shear Modelling*

Wind shear is the vertical increase in wind speed with height. The reasons for this phenomenon include dynamic factors and thermal factors. The dynamic factor is mainly related to the vertical stability of the near-surface atmosphere, while the thermal factor mainly comes from the friction effect of the offshore surface, that is, the roughness of the sea surface. TurbSim considers the influence of wind shear effect and describes the relationship between wind speed and height [153] as:

$$V(h) \approx V_{hub}\left(\frac{H+z}{H}\right)^{\alpha} = V_{hub}\left(1+\frac{z}{H}\right)^{\alpha} \tag{3.2}$$

where $V_{hub}$ is the wind speed at the hub; $H$ is the height of the hub center; $\alpha$ is the wind shear coefficient, which usually takes a constant value of 0.2; $z$ is the vertical height of the blade, that is:

$$z = -r\sin\varphi \tag{3.3}$$

In the above equation, $r$ is the distance between the blade element and the hub center; $\varphi$ is the position angle of the blade element. Combined with Fig. 3.2, the specific designation of the parameters in the equation can be intuitively understood.

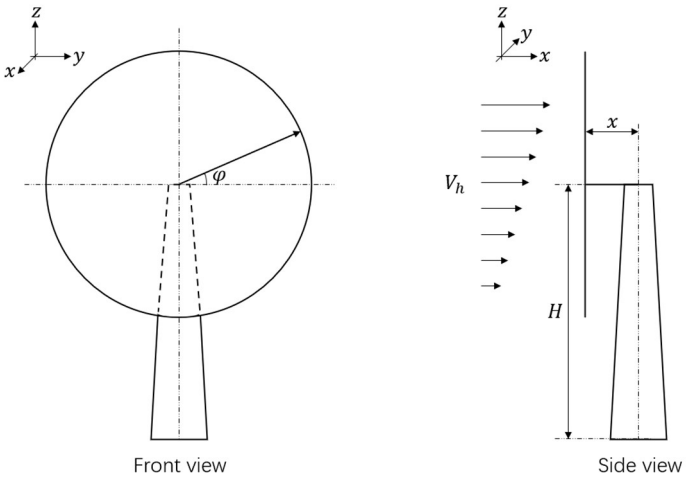


*Fig. 3.2 Wind shear of the turbine hub*

### *3.2.1.3 Tower Shadow Effect Modelling*

For an upwind three blade HAWT, wind speed expression applied in TurbSim considered the tower shadow effect, which is:

$$V(y,x) \approx V_h + v_t(y,x) \tag{3.4}$$

$$v_t(y,x) = V_{mean} r_t^2 \frac{y^2 - x^2}{y^2 + x^2} \tag{3.5}$$

where $V_{mean}$ is the spatial average wind speed; $V_h$ is the radius of the tower; $y$ is the distance from the blade element to the y-axis of the tower; $x$ is the distance from the blade element to the x-axis of the tower, that is, the overhang distance; $v_t(y,x)$ is the variation disturbance exerted by the tower shadow effect on the wind speed.

It is worth emphasizing that different reference wind speeds are used in the wind shear and tower shadow effect calculations. The wind shear adopts the custom $V_h$ at the hub

height $H$, while the spatial average wind speed $V_{mean}$ is used in the calculation of the tower shadow effect [154]. The relationship between these two wind speeds is:

$$V_{mean} = \left[1 + \frac{\alpha(\alpha-1)R^2}{8h^2}\right] V_h \tag{3.6}$$

### 3.2.2 FOWT Dynamic modelling

AHSE model is a mathematical model that describes the dynamic behaviour of a FOWT in response to environmental loads, such as wind and waves. In the study of this thesis, we utilized FAST code to implement AHSE modelling for FOWT, adopting the widely tested OC3-Hywind platform and set reasonable wind and wave conditions. The model considers the interactions between the FOWT's structural, hydrodynamic, and aerodynamic components, as well as the control system used to stabilize the turbine in operation.

The FOWT model is used to predict the performance and stability of an FOWT under different operational conditions, such as different wind and wave conditions, which is used to design the control system for the FOWT. The model can also be used to optimize the design of the FOWT, such as selecting appropriate size, shape, and materials, to achieve required performance with reduced costs [28].

The FOWT model typically consists of several sub models, each representing a different aspect of the FOWT's behaviour. The structural sub model represents the mechanical properties of the FOWT's structure, including its stiffness, mass, and damping. The hydrodynamic sub model represents the forces acting on the FOWT due to wave load, wave current, and added mass effects. The aerodynamic sub model represents the forces acting on the FOWT due to the motion of the air, including the lift and drag forces on the turbine blades. The control sub model represents the control system used to stabilize the FOWT, such as the mooring system or the blade pitch control. Thus, the model of the

FOWT is shown in Fig. 3.3, which corresponds to the parameters of the AHSE dynamics and the complete WECS model.

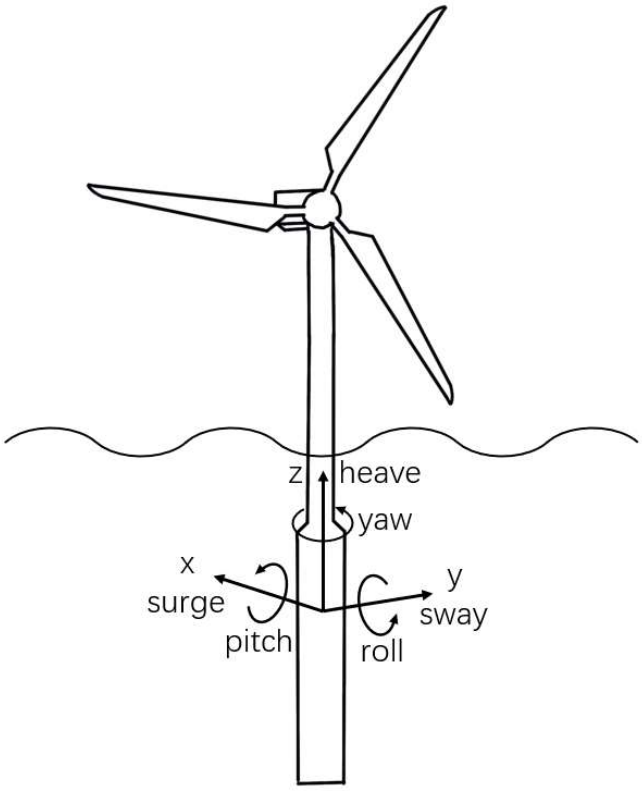


*Fig. 3.3 The 6 degrees of freedom of fully coupled FOWT model*

The FOWT model is typically solved using computational methods, such as the finite element method or the boundary element method [92]. These methods allow the model to be solved quickly and accurately for a wide range of operational conditions, making it a valuable tool for the design and analysis of FOWTs.

### 3.2.3 WECS modelling

AHSE model of the FOWT can be established in detail through FAST, where it only uses a generator model to simulate the operating characteristics of the generator [31]. This simplified WECS model does not fully reflect the transient characteristics of the generation system. Therefore, this chapter establishes a detailed PMSG system in MATLAB/Simulink

through the interface of MATLAB/Simulink and FAST. This section will describe the modelling of the control strategy of PMSG and its back-to-back PWM converter.

#### *3.2.3.1 Specification of the reference direction*

Using the motor convention, looking towards the motor, the voltage and current will follow the cross-reference direction. The reference direction of the current and the reference direction of the magnetic flux produced by it follow a right-handed spiral relationship. The magnetic flux is in a right-handed spiral relationship with the induced electromotive force generated by itself.

#### *3.2.3.2 Generator voltage equation and flux equation*

When the positive directions of the stator, rotor voltage and current adopt the motor convention, the voltage equation and flux linkage equation of the PMSG in the rotating synchronous coordinate system are (3.7) and (3.8), respectively

$$v_s = R_s i_s + \frac{d(L_s i_s)}{dt} + \frac{d}{dt}\left(\Psi_f e^{j\theta_e}\right) \tag{3.7}$$

$$\begin{cases} \Psi_d = L_d i_d + \Psi_f \\ \Psi_q = L_q i_q \end{cases} \tag{3.8}$$

where $v_s$ is the stator terminal voltage vector of the generator, $R_s$ is the resistance of the stator winding of the generator, $i_s$ is the stator current vector, $L_s$ is the stator inductance, $\theta_e$ is the electrical angle rotated by the rotor, and $\Psi_f$ is the flux linkage obtained by the interlinkage between the magnetic field generated by the permanent magnet and the stator winding. $L_d$ and $L_q$ are the self-inductances in the stator d-q axis, as shown in (3.9).

$$\begin{cases} L_d = L_{dm} + L_{\sigma s} \\ L_q = L_{qm} + L_{\sigma s} \end{cases} \tag{3.9}$$

where $L_{dm}$, $L_{qm}$ are the excitation inductance of the stator d-q axis, respectively. $L_{\sigma s}$ is the leakage inductance of the stator phase winding.

In the synchronous rotation coordinate system, the positive direction of the d-axis is the positive direction of the direct axis of the rotor magnetic pole, and the positive direction of the q-axis is the direction ahead of the d-axis by 90 degrees of electrical angle. The d-q axis rotates with the rotation of the rotor magnetic poles, then in the $dq$ coordinate system, the stator voltage equations can be expressed as:

$$v_d = R_s i_d + L_d \frac{di_d}{dt} + \frac{d\Psi_f}{dt} - \omega_e L_q i_q \tag{3.10}$$

$$v_q = R_s i_q + L_q \frac{di_q}{dt} + \omega_e (L_d i_q + \Psi_f) \tag{3.11}$$

where $v_d$, $v_q$ are the d-q axis components of the PMSG stator terminal voltage; $i_d$, $i_q$ are the d-q axis components of the stator current, respectively.

#### *3.2.3.3 Generator torque equation*

The electrical torque of the generator $T_e$ depends on its flux linkage $\Psi_s$ and current vector $i_s$, which is illustrated in the following equations:

$$T_e = \frac{3}{2} n_p \Psi_s \times i_s \tag{3.12}$$

$$\Psi_s = \Psi_d + j\Psi_q \tag{3.13}$$

$$i_s = i_d + j i_q \tag{3.14}$$

where $n_p$ is the generator pole pair number. Thus generator $T_e$ can be further derived by (3.8), (3.13), and (3.14).

$$T_e = \frac{3}{2} n_p (\Psi_f i_q + (L_d - L_q) i_d i_q) \tag{3.15}$$

Equation (3.15) reflects that $T_e$ is related to both the d and q axis currents. However, if $L_d = L_q$, or $i_d = 0$;

$$T_e = \frac{3}{2} n_p \Psi_f i_q \tag{3.16}$$

Therefore, to control the electrical torque of the PMSG, its q-axis current $i_q$ should be controlled. As for the approach to meet the prerequisites of (3.16), since the Interior Permanent Magnet Synchronous Generator (IPMSG) does not satisfy $L_d = L_q$, a current closed-loop control is usually used to make the current command $i_d = 0$ to control the electrical torque $T_e$.

### *3.2.3.4 Rotor-side converter control strategy*

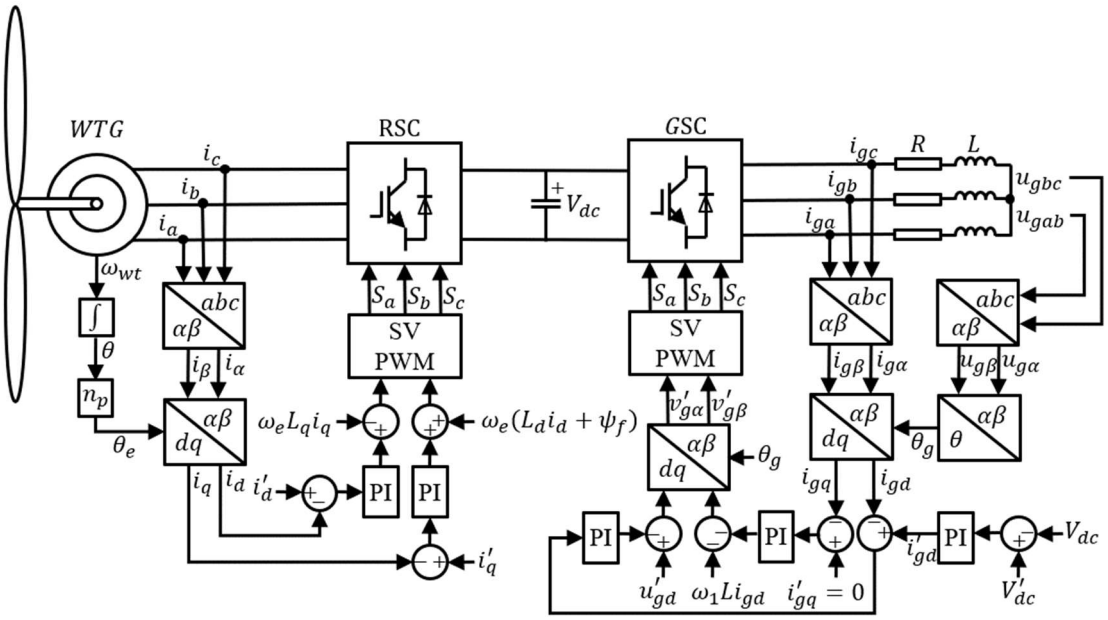


*Fig. 3.4 Type 4 WTG full scale PWM converter control diagram*

The control block diagram of the d-q axis current of the rotor-side converter is shown in Fig. 3.4. As aforementioned, after the d-axis is oriented to the rotor magnetic pole, if the d-axis current $i_d$ can be controlled to be 0, then the electrical torque $T_e$ of PMSG is proportional to the q-axis current $i_q$. By controlling $i_q$, $T_e$ can be effectively controlled [149].

$$i_q^* = -\frac{2T_e^*}{3p_p} \tag{3.17}$$

The reference value $i_q^*$ is calculated as (3.17), where $n_p$ is the number of pole pairs of PMSG rotor. $T_e^*$ is the reference value of electrical torque that is determined by the principle of maximum power point tracking (MPPT).

According to the MPPT with the optimal power characteristic, as long as the electrical torque of the generator $T_e$ is controlled in real time according to the speed of the rotor $\omega_{wt}$, the relationship between these two parameters can fit the optimal torque curve to achieve MPPT [155]. The MPPT control principle is explained by (3.18) and (3.19).

$$P_{mech\_opt} = \frac{3}{2}\rho C_{p\_max}\pi R^2 \left(\frac{R\omega_{wt}}{\lambda_{opt}}\right) \approx K_{opt}\omega_{wt}^3 = P_e^* \tag{3.18}$$

$$T_{mech\_opt} = \frac{P_{mech\_opt}}{\omega_{wt}} \approx K_{opt}\omega_{wt}^2 = T_e^* \tag{3.19}$$

where $\rho$ is the air density, $R$ is the rotor radius, $K_{opt}$ is a constant which can be calculated from (3.18) by keeping both tip speed ratio and wind turbine airfoils constant and equal to their optimal values $\lambda_{opt}$ and $C_{p\_max}$.

To sum up, the control strategy on the generator side is that the outer loop adopts active power closed-loop regulation, and the deviation between the actual power $P_e$ fed back by the grid and the reference power $P_e^*$ is adjusted by PI controller and used as the reference value $i_q^*$ of the generator's current. The q-axis current $i_q$ can in turn adjust the electromagnetic torque of the generator and then adjust the output power to achieve maximum power tracking [156].

#### *3.2.3.5 Grid-side converter control strategy*

The operating target of the grid-side converter is to transmit the power generated by the PMSG to the grid with high quality. This means that the waveform of the grid-connected current is sinusoidal, and in phase with the grid voltage, that is, the ideal power factor equals 1.

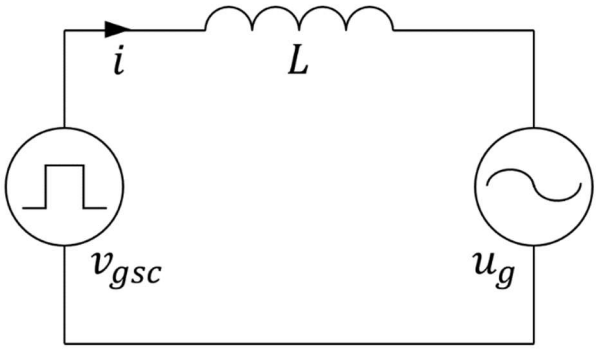


*Fig. 3.5 Simplified Model of Grid-side Converter*

The simplified model of the grid-side converter is shown in the Fig. 3.5, based on which the dynamic equation is:

$$v_{gsc} - u_g = L\frac{di}{dt} \tag{3.20}$$

where $u_g$ is the instantaneous value of the grid voltage; $v_{gsc}$ is the output voltage of the grid side converter, which is a pulse waveform of equal amplitude and unequal width, that is, a PWM (pulse width modulation) wave. It can be decomposed into the fundamental component and a series of harmonic voltage components, where the fundamental current is the main object of attention.

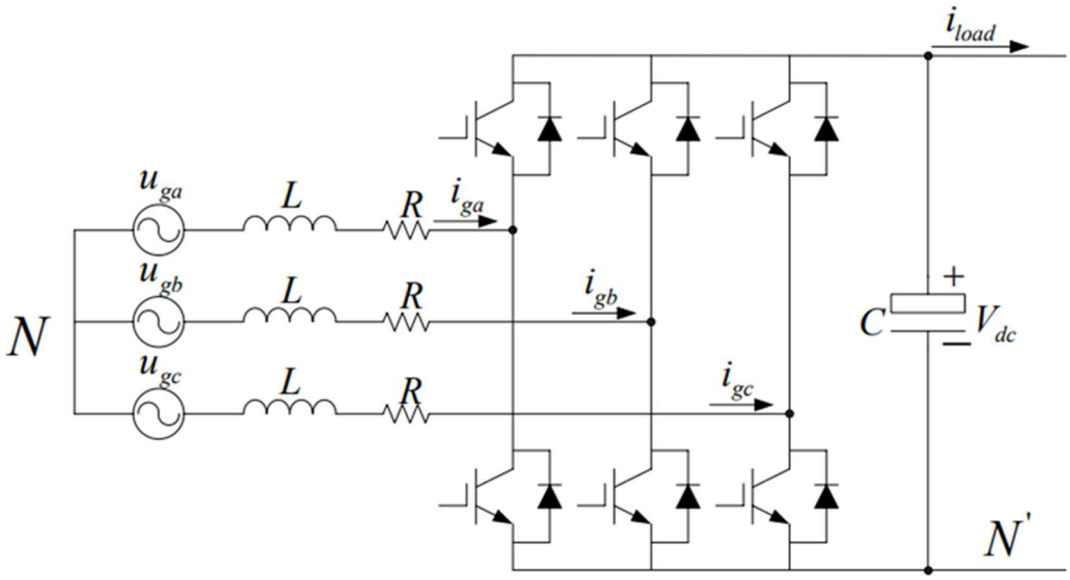


*Fig. 3.6 Equivalent Circuit of Voltage Source Converter*

The equivalent circuit of the PMSG grid-side voltage source converter is shown in the Fig. 3.6. In the calculation process, the triode in the figure can be equivalent to an ideal switch. Therefore, the following equations can be intuitively obtained.

$$\begin{cases} U_{NN'} = u_{ga} - i_{ga}R - L\dfrac{di_{ga}}{dt} - S_aV_{dc} \\ \qquad = u_{gb} - i_{gb}R - L\dfrac{di_{gb}}{dt} - S_bV_{dc} \\ \qquad = u_{gc} - i_{gc}R - L\dfrac{di_{gc}}{dt} - S_cV_{dc} \\ C\dfrac{dV_{dc}}{dt} = S_ai_{ga} + S_bi_{gb} + S_ci_{gc} - i_{load} \end{cases} \tag{3.21}$$

where $S_a$, $S_b$, $S_c$ represents the switching state of the triode of the branch, with a value of 0 or 1 depends on its condition. By further arranging (3.21), the expression for the voltage and current of each branch can be obtained as (3.22) and (3.23).

$$\begin{cases} u_{ga} + u_{gb} + u_{gc} = 0 \\ \dfrac{di_{ga}}{dt} = -\dfrac{R}{L}i_{ga} + \dfrac{1}{L}\left[u_{ga} - \left(S_{ga} - \dfrac{S_{ga}+S_{gb}+S_{gc}}{3}\right)V_{dc}\right] \\ \dfrac{di_{gb}}{dt} = -\dfrac{R}{L}i_{gb} + \dfrac{1}{L}\left[u_{gb} - \left(S_{gb} - \dfrac{S_{ga}+S_{gb}+S_{gc}}{3}\right)V_{dc}\right] \\ \dfrac{di_{gc}}{dt} = -\dfrac{R}{L}i_{gc} + \dfrac{1}{L}\left[u_{gc} - \left(S_{gc} - \dfrac{S_{ga}+S_{gb}+S_{gc}}{3}\right)V_{dc}\right] \\ C\dfrac{dV_{dc}}{dt} = S_ai_{ga} + S_bi_{gb} + S_ci_{gc} - i_{load} \end{cases} \tag{3.22}$$

$$\begin{cases} i_{ga}+i_{gb}+i_{gc}=0 \\ \frac{di_{ga}}{dt}=-\frac{R}{L}i_{ga}+\frac{1}{L}\left[\left(u_{ga}-\frac{u_{ga}+u_{gb}+u_{gc}}{3}\right)-\left(S_{ga}-\frac{S_{ga}+S_{gb}+S_{gc}}{3}\right)V_{dc}\right] \\ \frac{di_{gb}}{dt}=-\frac{R}{L}i_{gb}+\frac{1}{L}\left[\left(u_{gb}-\frac{u_{ga}+u_{gb}+u_{gc}}{3}\right)-\left(S_{gb}-\frac{S_{ga}+S_{gb}+S_{gc}}{3}\right)V_{dc}\right] \\ \frac{di_{gc}}{dt}=-\frac{R}{L}i_{gc}+\frac{1}{L}\left[\left(u_{gc}-\frac{u_{ga}+u_{gb}+u_{gc}}{3}\right)-\left(S_{gc}-\frac{S_{ga}+S_{gb}+S_{gc}}{3}\right)V_{dc}\right] \\ C\frac{dV_{dc}}{dt}=S_a i_{ga}+S_b i_{gb}+S_c i_{gc}-i_{load} \end{cases} \tag{3.23}$$

In order to make the expression more intuitive, let

$$\begin{cases} v_{ga}=f_a V_{dc} \\ v_{gb}=f_b V_{dc} \\ v_{gc}=f_c V_{dc} \end{cases} \tag{3.24}$$

$$\begin{cases} f_a=S_{ga}-\frac{S_{ga}+S_{gb}+S_{gc}}{3} \\ f_b=S_{gb}-\frac{S_{ga}+S_{gb}+S_{gc}}{3} \\ f_c=S_{gc}-\frac{S_{ga}+S_{gb}+S_{gc}}{3} \end{cases} \tag{3.25}$$

Therefore, by combining (3.24) and (3.25), the equation (3.22) could turn into

$$\begin{cases} u_{ga}=-Ri_{ga}+L\frac{di_{ga}}{dt}+v_{ga} \\ u_{gb}=-Ri_{gb}+L\frac{di_{gb}}{dt}+v_{gb} \\ u_{gc}=-Ri_{gc}+L\frac{di_{gc}}{dt}+v_{gc} \\ C\frac{dV_{dc}}{dt}=S_a i_{ga}+S_b i_{gb}+S_c i_{gc}-i_{load} \end{cases} \tag{3.26}$$

By applying space vector notation, electrical equations (3.26) in $abc$ coordinate system can be represented by $\alpha\beta$ components.

$$\begin{cases} u_{g\alpha}=-Ri_{g\alpha}+L\frac{di_{g\alpha}}{dt}+v_{g\alpha} \\ u_{g\beta}=-Ri_{g\beta}+L\frac{di_{g\beta}}{dt}+v_{g\beta} \\ C\frac{dV_{dc}}{dt}=S_\alpha i_{g\alpha}+S_\beta i_{g\beta}-i_{load} \end{cases} \tag{3.27}$$

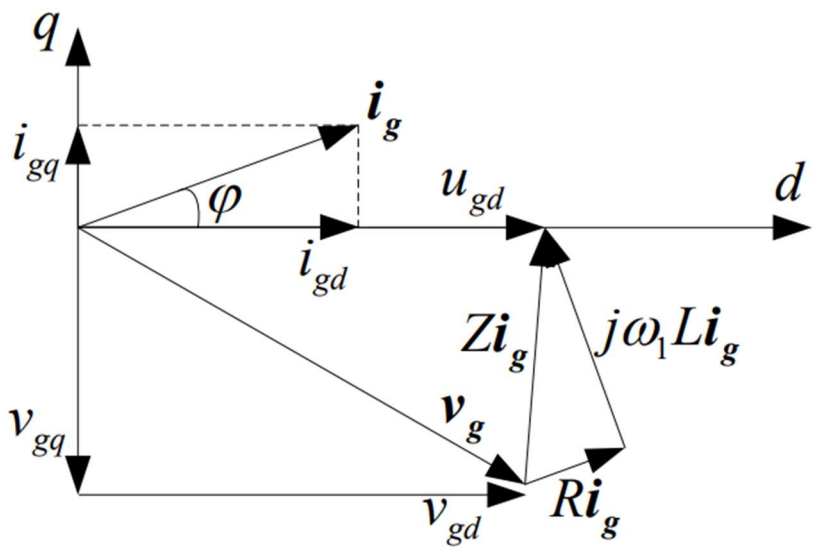


*Fig. 3.7 Space Vector of Grid-side Converter*

Thus, (3.27) was able to further be transformed to the expression in the $dq$ coordinate system. Since the set target power factor is 1, then $u_{gq} = 0$. As is shown in Fig. 3.7, orienting the d-axis in the synchronous rotating coordinate system of the grid voltage, here comes:

$$\begin{cases} u_{gd} = Ri_{gd} + L\frac{di_{gd}}{dt} - \omega_g Li_{gq} + v_{gd} \\ 0 = Ri_{gq} + L\frac{di_{gq}}{dt}\omega_g Li_{gd} + v_{gq} \\ C\frac{dV_{dc}}{dt} = S_d i_{gd} + S_q i_{gq} - i_{load} \end{cases} \tag{3.28}$$

where $\omega_g$ is the grid frequency in $rad/s$. Using parameters in the $dq$ coordinate system, the active power $P_g$ and reactive power $Q_g$ output by the grid-side converter can be obtained as below.

$$P_g = u_{gd}i_{gd} + u_{gq}i_{gq} = Ui_{gd} \tag{3.29}$$

$$Q_g = -u_{gd}i_{gq} = -Ui_{gq} \tag{3.30}$$

Therefore, concluding from (3.16) and (3.17), by controlling the dq axis current, the active and reactive power that the converter absorbs or supplies from the grid can be

controlled separately. Moreover, active power and reactive power do not affect each other, i.e. realizing decoupling control. The control block diagram of the grid-side converter is also shown in Fig. 3.4.

#### *3.2.3.6 Pitch control modelling*

Although a comprehensive pitch control file based on [66] is coded as a PLL link attached in the OC3-Hywind AHSE model, a simplified pitch control block is also reproduced to help the verification of the WECS model and lays the foundation for the deep optimization design of pitch angle control in the future research. As it shown in Fig. 3.8 , the PI gains are designed by linearizing the FAST model at rated wind speed of 11.4 $m/s$ and the optimization work is completed with the help of SISO tool in the MATLAB/Simulink [121].

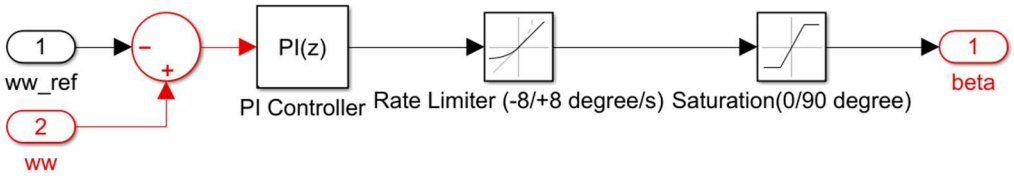


*Fig. 3.8 implified Pitch Control Scheme*

## 3.3 Model Test Set-up

The floating platform is referred as the OC3 Hywind spar buoy whereas the wind turbine model used is an NREL 5MW wind turbine [66]. Table 3.1 and Table 3.2 show the detailed parameters of the platform and mooring system, and the wind turbine, respectively.

*Table 3.1 Key Properties of the modified NREL 5-MW Spar Floating Platform*

| Property | Value |
|---|---|
| Blades & Hub (kg) | 109931 |

| | |
|---|---|
| Nacelle (kg) | 247291 |
| Tower (kg) | 287128 |
| Platform roll & pitch inertia（kg.m2） | $6.31 \times 10^9$ |

*Table 3.2 Key Properties for the modified NREL 5-MW Baseline Wind Turbine*

| Property | Value |
|---|---|
| Wind Turbine Parameters | |
| Rating capacity of power | $5MW$ |
| Rotor orientation, Configuration | $Upwind, 3\ Blades$ |
| Control type | Variable Speed, Collective pitch |
| Rated wind speed | $11.4\ m/s$ |
| Rated rotor speed | $12.1rpm\ (1.267rad/s)$ |
| Pitch angle initialization | $0^o$ |
| Gearbox ratio | 1(direct drive) |
| Drivetrain efficiency | 97% |
| Generator Parameters | |
| Nominal Power | $5.297MW$ |
| Nominal Torque | $4.18MN \cdot m$ |
| Number of pole pairs | 100 |
| Stator resistance | $0.08\Omega$ |
| D-axis Inductance | $8.38mH$ |
| Q-axis Inductance | $8.38mH$ |
| Flux linkage established by magnets | $17.8V \cdot S$ |
| Grid Side Parameters | |
| Grid Side Resistance | $0.08\Omega$ |
| Grid Side Inductance | $4mH$ |
| DC Reference Voltage | $6400V$ |
| DC capacitor | $4\mu F$ |
| Grid Parameters | |
| Grid Voltage | $4kV$ |

| | |
|---|---|
| Grid Frequency | $50Hz$ |

In this study, FAST v8[32] is used to predict the performance and stability of an FOWT under different operational scenarios, such as different wind and wave conditions, and to design the control system for the FOWT. The model can also be used to optimize the design of the FOWT, determining details such as its size, shape, and materials, to improve performance and reduce costs. FAST v8 uses a modular approach, allowing users to choose the appropriate level of details for each sub model based on specific needs of their analysis. The tool also includes a range of options for inputting environmental loads and turbine parameters, making it a versatile tool for simulating the performance of FOWTs under a wide range of operational conditions [121]. With dedicated communication port with Simulink, the mechanical dynamics model based on FAST can be coupled with the high-order WECS model used in this study to conduct more comprehensive and detailed experimental research on the electrical performance analysis of the complete system.

### 3.3.1 Case study settings

The coupled model simulates in a variable step solver with a total calculation time of $3600s$ in each case. In Simulink, the time step for the WECS model is set to $2 \times 10^{-6}s$, whereas in FAST, the time step for the AHSE model is reduced to $2 \times 10^{-3}s$ to minimize deviations from the electrical module. In addition, the time step of the meshing and numerical calculations performed by the Hydrodyn module also needs to be adjusted to $2 \times 10^{-3}s$ to match the AHSE model settings. Dynamic responses of the floating platform were analysed for translational (i.e. surge, sway, heave) and rotational (i.e. pitch, roll, yaw) motions along the x, y, and z axes. The motion of one of the floating platforms in six degrees of freedom is shown in Fig. 3.3. Specific environmental conditions are set as follows.

(a) Case 1: Bottom-fixed OWT at 12m/s wind speed

(b) Case 2: FOWT at 12m/s wind speed with no wave

(c) Case 3: FOWT at 12m/s wind speed with normal regular wave

(d) Case 4: FOWT at 12m/s wind speed with huge irregular wave

(e) Case 5: FOWT at wind-wave conditions within all operational range.

It is worth noting that Cases 1 to 4 are differentiated settings to explore the influence of hydrodynamics on FOWT power characteristics, but the requirements of the control variable method are still followed for comparison between every two adjacent cases. As for Case 5, FOWT undertakes testing on wind and wave conditions within its operational range in order to investigate the patterns and interrelationships between varying wind and wave conditions and the quality of power output. The tested input wind speed ranges from 8m/s to 14.8m/s with an interval of 0.2 m/s. The wave conditions considered are irregular and with ranges in height from 0m to 6.1m within 10-year return period sea state based on western Taiwan offshore location [157]. Table 3.3 shows listed case details. It is important to emphasize that wave conditions vary significantly in different maritime regions. To study more severe wave conditions than those in Taiwan Strait, reference can be made to the environments in areas represented by the Ireland offshore [158] and the North Sea [13].

*Table 3.3 Case setting details*

| Case | Turbine type | Input wind $(m/s)$ | Input wave | | | Scenario (western Taiwan offshore based) |
|---|---|---|---|---|---|---|
| | | | Model | $H_s(m)$ | $T_p(s)$ | |
| *1* | OC3-Tripod | 12.0 | - | 0 | 0 | Bottom-fixed OWT reference |
| *2* | OC3-Hywind | 12.0 | - | 0 | 0 | Still water conditions |
| *3* | OC3-Hywind | 12.0 | Regular | 1.67 | 5.17 | Normal sea conditions |
| *4* | OC3-Hywind | 12.0 | Irregular | 5.5 | 9.4 | Northeast monsoon sea conditions |
| *5* | OC3-Hywind | 8.0~14.8 | Irregular | 0~6.1 | 0~10.2 | Sub-10-year return period conditions |

*10-year return period wave reference at western Taiwan offshore:* $H_s = 6.1m$, $T_p = 10.4s$

*50-year return period wave reference at western Taiwan offshore:* $H_s = 9.1m$, $T_p = 13.0s$

### 3.3.2 Developed wind-wave scenarios

In this study, a turbulent wind field was created using TurbSim v1.5 [159] and inflow vertically into swept area of the wind turbine. The field has a height of 155m and a width of 145m, consisting of 225 grid points with 15 points along both the vertical and horizontal axes. The center of the field coincides with the hub point of the turbine. The turbulence intensity adheres to the specifications outlined in category-C of IEC 61400–1[151]. Moreover, the wind speed fluctuations, as depicted in the Velocity Spectra of various wind models based on the Turbsim-generated data, exhibit minimal high-frequency variations, with the peak in the spectra occurring near zero frequency. This indicates a general stability in wind speed, characterized by slower fluctuations compared to the higher and more concentrated distribution of hydrodynamic natural frequencies observed in the OC3-Hywind FOWT, reinforcing that the majority of detected WPREs with durations less than 15s primarily originate from hydrodynamic influences, such as waves or natural frequency responses.

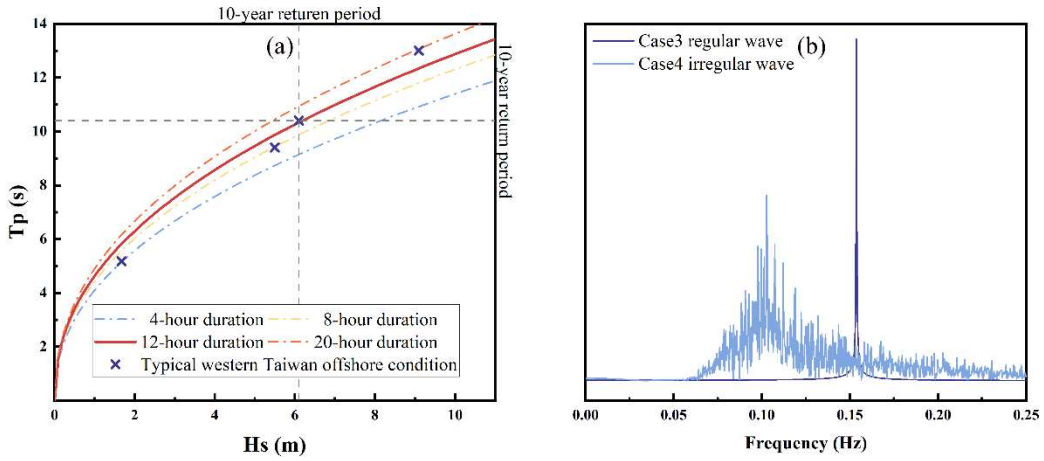


*Fig. 3.9 Input wave (a) characteristic determination, and (b) spectral analysis of Case 3 and Case 4*

The FAST input files specify the ocean wave setting for this study, which involves analysing and comparing regular and irregular waves, with spectral difference is presented

in Fig. 3.9(b). To simulate the actual irregular waves, JONSWAP spectral model [78] is selected in Hydrodyn with peak enhancement factor $\gamma = 2.08$ specialized for Taiwan Strait environment [157]. The relationship between significant wave height $H_s$ and average zero up-crossing period $T_z$ is determined by local wind generated wave equations (3.31) and (3.32) in duration limited offshore condition [160].

$$H_s = 0.0146 \times D^{5/7} U^{9/7} \tag{3.31}$$

$$T_z = 0.419 \times D^{3/7} U^{4/7} \tag{3.32}$$

$$T_p = 1.28\, T_z \tag{3.33}$$

where $T_p$ is peak wave period, $U$ is wind speed in $m/s$ at $10m$ above mean sea level, and $D$ is duration in hours. Relationship between $\mathrm{T_p}$ and $\mathrm{T_z}$ for waves based on the JONSWAP spectrum can be expressed as (3.33) [161]. Therefore, it is possible to consolidate (3.31) to (3.33) to derive the relationship between $H_s$ and $T_\mathrm{p}$.

$$T_p = (3.510 \times D^{1/9}) \times H_s^{4/9} \tag{3.34}$$

Based on (3.34), the wave characteristics for different durations is compared with the 4 representative conditions (illustrated in Table1) of the western Taiwan offshore [157] as shown in Fig. 3.9(a), with the curve for a 12-hour duration ($D = 12$) selected as wave setting reference for $H_s$ and $T_\mathrm{p}$ in Case 5.

### 3.3.3 WPRE definition and detection

Research focused on WPREs can be categorized into three primary domains: WPRE detection, WPRE prediction, and WPRE application. The initial phase, WPRE detection, involves extracting wind power slopes from real or forecasted wind power data through mathematical algorithms and definitions of wind power ramps. The accuracy of WPRE prediction is significantly reliant on the precision of WPRE detection.

An influential solution in this domain is the OpSDA, which was initially introduced in 2016 [162]. OpSDA has gained prominence within the WPRE detection field and has been adopted as a data preprocessing technique in various studies to enhance wind power prediction accuracy [138][144][145][163][164]. A key aspect highlighted in [162] underscores the significance of mitigating "fake ramp events" to enhance the effectiveness and precision of WPRE detection when utilizing OpSDA. However, in normal environmental conditions containing small wave loads, these "fake ramp events" characteristics could potentially disrupt WPRE detection. Consequently, the calibration of parameters such as the sampling interval and casement door width becomes pivotal. In the debugging process of this study, the pivotal calibration of parameters, including time resolution and threshold width, resulted in a substantial improvement in detection success as the model iteratively converged towards optimal settings. Differing from [138], OpSDA data processing was executed twice on time-domain power data: first with small time resolution (0.05s) and threshold width (0.1) for merging adjacent ramps, and then with larger settings (1s time resolution and 0.3 threshold width) to minimize errors stemming from abrupt slope changes.

*Table 3.4 WPRE definitions of grid connected wind power*

| Organization | Frequency Stability Focus | | | Unit Commitment (UC) Focus | |
|---|---|---|---|---|---|
| | Within 2s | Within 5s | Within 60s | Within 4h | ∞ |
| Eltra | $\Delta P/P_{nom} \leq 20\%$ | | | | |
| SvK | | $\Delta P/P_{nom} \leq 20\%$ | | | |
| E.ON | | | $\Delta P/P_{nom} \leq 10\%$ | | |
| Scotland | | | $\Delta P/P_{nom} \leq 20\%$ | | |
| Def 1 | | | | | $\Delta P/P_{nom} \leq 20\%$ |
| Def 2 | | | | $\Delta P/P_{nom} \leq 20\%$ | |
| Def 3 | | | | | $\frac{d(\Delta P/P_{nom})}{dt} \leq 3\%$ |

$\Delta P$ *: difference between the maximum and minimum power during the specified time period*

$P_{nom}$ *: rated output power of the WECS,*

*Unit of Def 3 is p.u./min, ramp duration without limitation is symbolled as* $\infty$

In the following Sections, the power curve of the simulation outcome will be analysed, revealing several significant WPRE cases beyond 20% of the total FOWT capacity. This observation was made despite the wind speed being set close to the rated value and the sea wave setting being normal. The possible observed fluctuation is of considerable concern as it approaches the limits set by major countries and regions that utilize large-scale offshore wind resource, for meeting operational requirements. Table 3.4 summarizes the WPRE boundary definitions of well-known reference [138], for wind farms comprising OWTs, with additional requirements from independent system operators (ISOs) available in [165].

## 3.4 Results and discussion

In this section, the verification of the PMSG and its converter model in MATLAB/Simulink is performed based on the power curve outlined in the existing literature for a 5 MW reference offshore wind turbine [66]. Subsequently, an assessment of the corresponding dynamic motion of the FOWT and the fluctuation in output power is conducted, taking into account the predetermined conditions of Cases 1-4. The power quality of the prevailing wind and wave circumstances is also analysed and compared. Finally, this section discusses the improved power curves and operating criteria for FOWTs. It is noteworthy that the simulation time resolution is 0.002 seconds, and the power output is recorded for a representative one-hour period of wind and wave conditions corresponding to the set cases.

### 3.4.1 Validation of coupled Models and WPRE detection methodology

To assess the accuracy of the WECS model, the AHSE dynamics were evaluated utilizing the OC3-Tripod bottom fixed OWT model [29]. Multiple sets of power and mechanical torque data were examined in the absence of ocean waves, and with a steady-state wind input. The findings of the experiments exhibited a remarkable level of agreement with the established 5MW baseline wind turbine model [66], indicating a high degree of consistency. This outcome is illustrated in Fig. 3.10(a), which further substantiates the validity and reliability of the generator and converter models. This alignment substantiates the efficacy and accuracy of the proposed model in simulating the behaviour and performance of the aforementioned reference wind turbine, and there is a consistent coherence between the generator power and output power. Moreover, during the WECS model's commissioning process, careful attention was given to monitor and authenticate the intermediate variables through diligent efforts. As a result, it was proved that these intermediate variables exhibit a high degree of reliability and accuracy, affirming their credibility in the overall system.

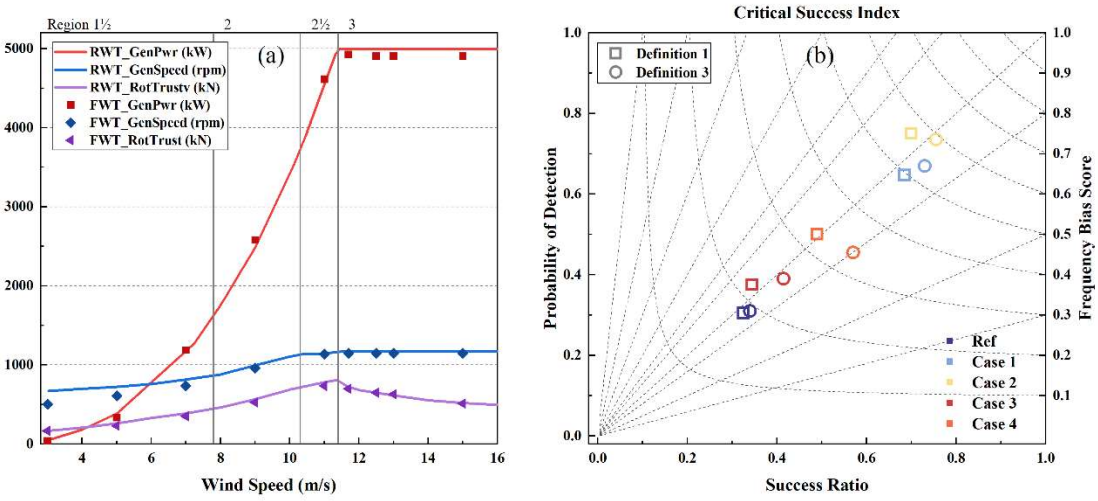


*Fig. 3.10 Validation outcome of (a) power and torque characteristic of the proposed fully coupled model and the reference model, and (b) revised OpSDA detection performance under definition 1,3 compared to reference* [138] *at 1-min time resolution*

The modified OpSDA's detection performance, as illustrated in Fig. 5(b), is evaluated against power output data at 0.05s time resolution. The performance diagram employed aligns with the design in [138], offering a visual comparison. The x-axis represents the ratio of "Start-YES" to "Start-YES-End-YES," while the y-axis reflects the proportion of "End-YES" within "Start-YES-End-YES." Results approaching the upper-right corner signify a superior Critical Success Index (CSI) and heightened WPRE detection accuracy. In contrast to the [138] result at 1-min time resolution (indicated as "Ref" in Fig. 3.10(b)), all cases in this study exhibit improved detection accuracy, affirming OpSDA's suitability for floating WPRE detection, especially evident in 1-minute time resolution cases due to the brief duration of a single WPRE cycle. Notably, FOWT based Case 2 outperforms OWT based Case 1, attributed to the platform's natural motion enhancing slope characteristics. Conversely, Cases 3 and 4, incorporating wave loads, exhibit reduced detection accuracy, with larger waves yielding better CSI. Case 3 presents a particularly formidable challenge due to subtle parameter deviations leading to the splitting of significant WPREs into smaller slopes, ultimately resulting in detection failures.

### 3.4.2 Impact of hydrodynamics on power characteristics

In Fig. 3.11, the temporal segments of simulation results showcase four distinct learning cases within the coupled models. This temporal domain exhibits a phase characterized by conspicuous wind speed stall, accompanied by a coherent power ramp evident in the conventional bottom-fixed OWT denoted as Case 1. In contrast, despite the absence of wave-induced forces, the FOWT in study Case 2 induces oscillations in the platform's natural frequency due to rapid wind speed variations, exacerbating the amplitude of the power ramp. Cases 3 and 4, which incorporate wave loading, moderately amplify the overall slope's magnitude relative to Case 2. Notably, under the influence of substantial wave loading as depicted in Case 4, a significant high-frequency WPRE is detected. Conversely, the wave scenario reflecting the rated operational state in Case 3 effectively

fragments the complete WPRE into multiple segments, thereby impacting the accuracy of WPRE detection.

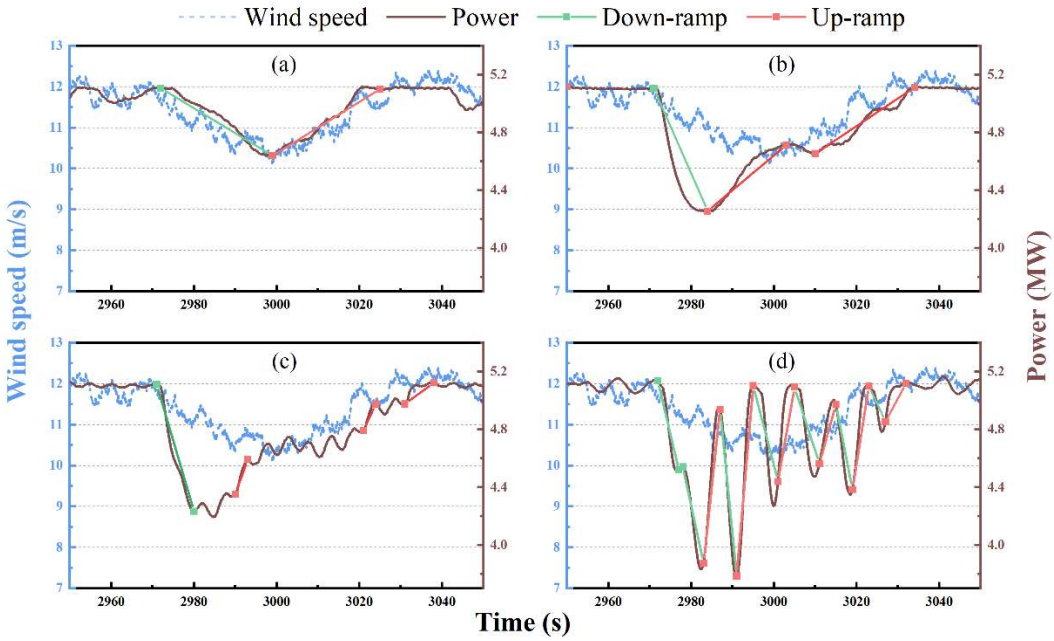


*Fig. 3.11 Segments of simulation results for (a) Case1, (b) Case2, (c) Case3, (d) Case4, including wind speed, WECS output power, major WPRE components*

In order to further correlate the relationship between the power characteristics and the hydrodynamic characteristics, it is necessary to do a qualitative analysis of the DoFs motion of the floating platform. Fig. 3.12 depicts the mean value and range of translational and rotational dynamics during simulation period for the Cases 1-4 scenarios. Relatively speaking, in Case 1, the bottom-fixed OWT exhibits negligible motion across 6 DoFs. Conversely, the FOWT in Cases 2 through 4 demonstrates a discernible range of motion across all DoFs. By comparing Cases 2 and 3, it becomes evident that the resulting motions in each DoF are highly similar. This finding suggests that the aerodynamics of the FOWT largely govern its overall dynamics, with hydrodynamics playing a minimal role, under common wind-wave conditions. When comparing the common waves in Case 3 with the 10-year sea state waves set in Case 4, it is observed that the latter case emerges a lower average angle and better stability within the surge motion, which is often attributed to the presence of irregular waves. Despite there being no notable differences in the mean value

when comparing the remaining 5 DoFs, there is an increase in the fluctuation range of 0.5m or 0.2 degree.

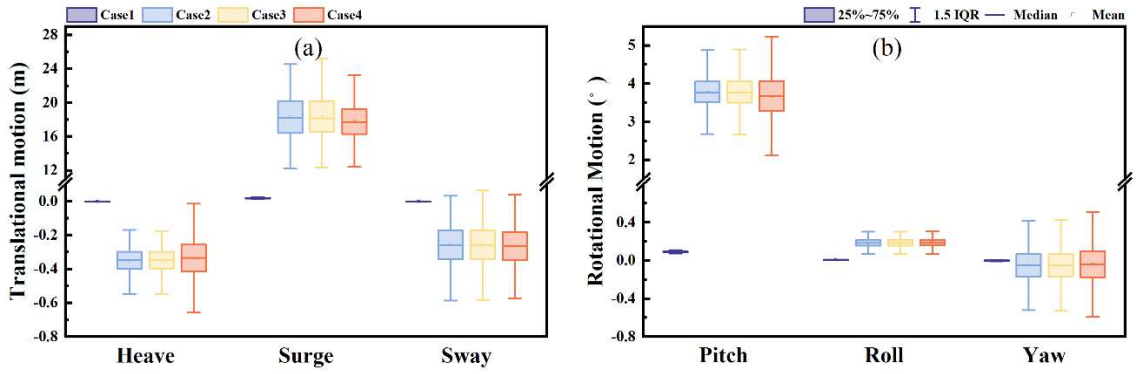


*Fig. 3.12 Statistics of wind turbine (a) translational, (b) rotational motions under Case 1 to 4*

The spectrum of the active power in the low frequency range for Cases 1 to 4 is depicted in Fig. 3.13. The most intuitive conclusion is that FOWT has a significant difference in pitch and surge motion compared with fixed OWT. Analysis of the frequency spectrum for Case 1 indicates that, with the exception of the DC component located around the origin, the low-frequency components of the power output can be attributed solely to the dynamic characteristics of the FOWT introduced by the floating platform. The comparison between Case 1 and Case 2 provides insight into the impact of ocean waves on the dynamics of floating platforms. In the absence of waves, the pitch and surge motion of FOWT had a decisive impact on the output power fluctuation, causing the spectrum's peak frequency to coincide with the FOWT natural frequency below 0.05 Hz. Comparing Case 2 to Case 3-4, it further demonstrates that wave activity on the platform induces additional power fluctuations, with the resulting harmonic frequency corresponding to the oscillation period of the waves. These findings suggest that ocean waves play a significant role in influencing the power output of floating platforms, emphasizing the additional requirement for structural vibration mitigation approaches, such as the integration of wave energy conversion systems[166] and turned mass dampers[167]. A comparison between Case 3 and

Case 4 reveals that larger waves lead to a decrease in the peak frequency of the platform's motion component, resulting in a larger platform motion period. Moreover, it can be observed that the periodic waves introduced in Case 3 possess a relatively concentrated and robust weight, while the irregular P-M wave body introduced in Case 4 exhibits a low but decentralized weight within a specific frequency bandwidth.

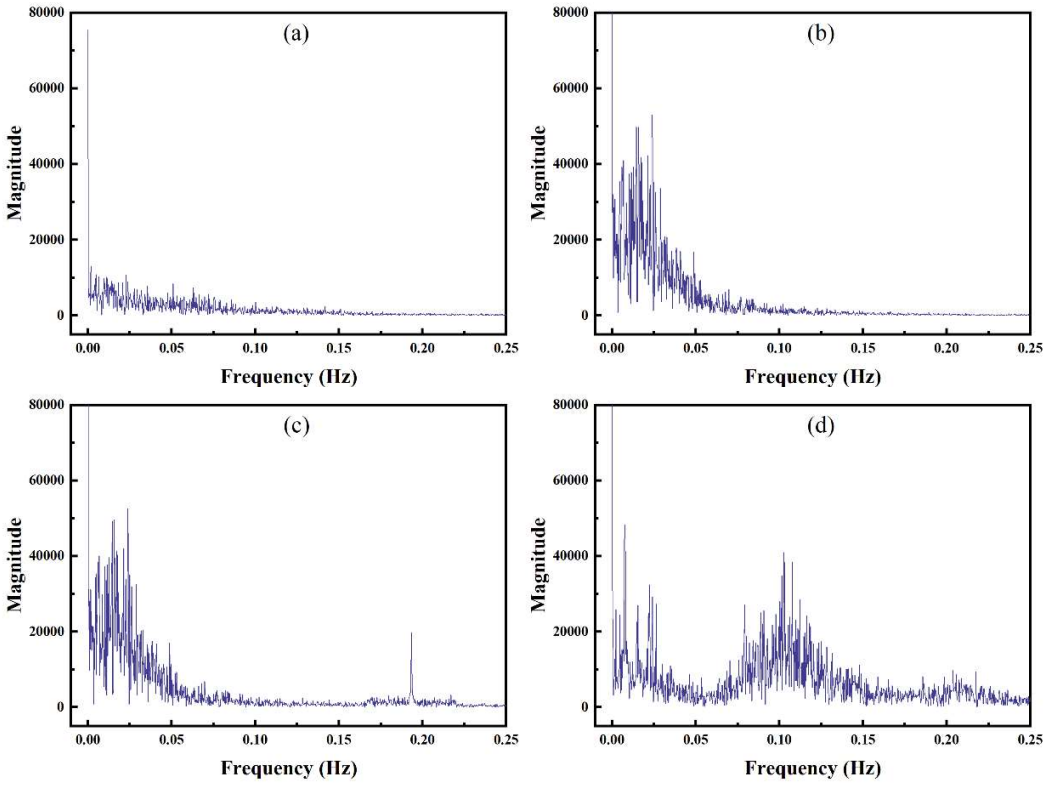


*Fig. 3.13 Spectral analysis of FOWT output power in (a) Case1, (b) Case2, (c) Case3 and (d) Case4*

This study also focuses on the power characteristics of FOWT on account of its inherent structural vibration. Curve fitting for the power characteristic is based on the wind speed and output power data, excluding the initial 600 seconds of the startup phase, and encompassing the remaining 3000 seconds of simulation duration. The fitted curve in Fig. 3.14 illustrates the overall relationship between wind speed and power. However, the presence of data points significantly deviating from the fitted curve highlights the impact of

hydrodynamics on the correlation between wind speed and power, which the curve cannot fully capture. The analysis indicates that, as the wave conditions intensify in the examined scenario, the relationship between wind speed and power deviates from the expected ideal power characteristic. Instead, it becomes more focused and confined within a considerably lower power range. Despite the wind speed being set at 12m/s for all four cases, turbulent wind conditions resulted in wind speed fluctuations ranging from 10 to 14m/s. The trend observed in the 4 cases at low wind speed is consistent with the operational behaviour of conventional wind turbines, demonstrating a positive correlation between wind speed and power output below the rated wind speed. Notably, the power characteristic curve of the fixed foundation Case 1 did not match previous validation test results, particularly with respect to high power output at low wind speeds. This phenomenon is likely attributable to the rotor's limited responsiveness, characterized by its significant inertia, which impedes swift adjustments to abrupt variations in wind speed. The large inertia associated with the PMSG employed in this experiment may result in the rotor not promptly reaching its target speed during episodes of rapid wind speed reduction, contributing to the observed deviations in the power curve, particularly in the lower wind speed range. This underscores the influence of the rotor's inertia on the dynamic response of the wind turbine system. Cases 2-4 showed significant dynamic impacts, resulting in power fluctuations of up to 20% of the rated power in extreme situations. Furthermore, these impacts became more severe with increasing wave intensities.

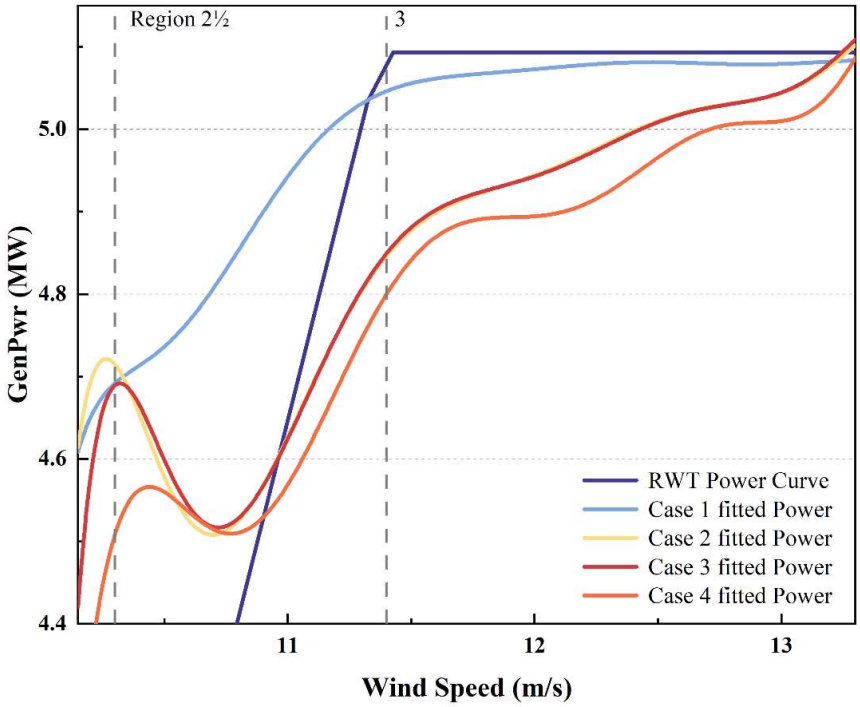


*Fig. 3.14 Fitted power characteristics of FOWT in Cases 1-4 wind & wave conditions*

Fig. 3.15 and Fig. 3.16 is the density estimation of wind speed and FOWT output power. As the hydrodynamic influence gradually increases, a comparison of the 4 cases reveals that the centre of FOWT output power distribution thus drops, and the occurrence of extreme scenario samples below 90% of the rated power increases. Cases 2 and 3 exhibit a similar trend within the power drop range, suggesting that the primary determinant of the significant power drop is the movement of the floating platform influenced by the wind. In contrast, the impact of regular sea waves appears to be minimal.

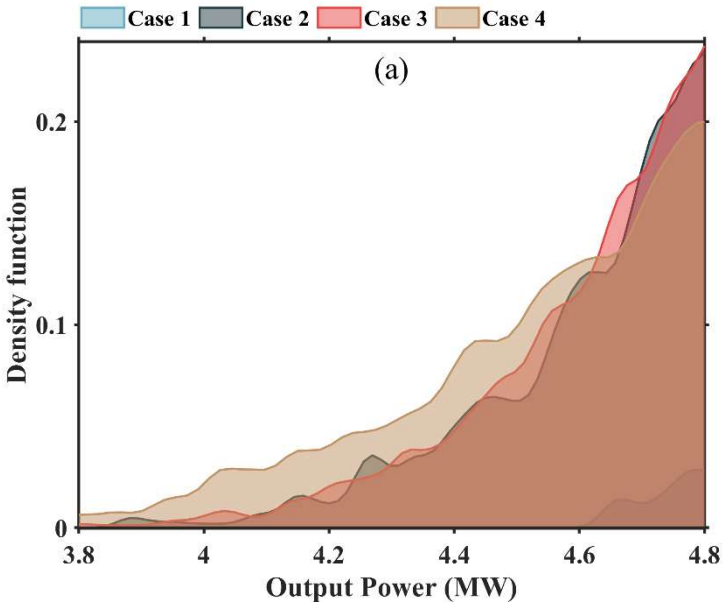


*Fig. 3.15 Kernel density estimate (bandwidth = 0.02) of FOWT output power at WPRE range*

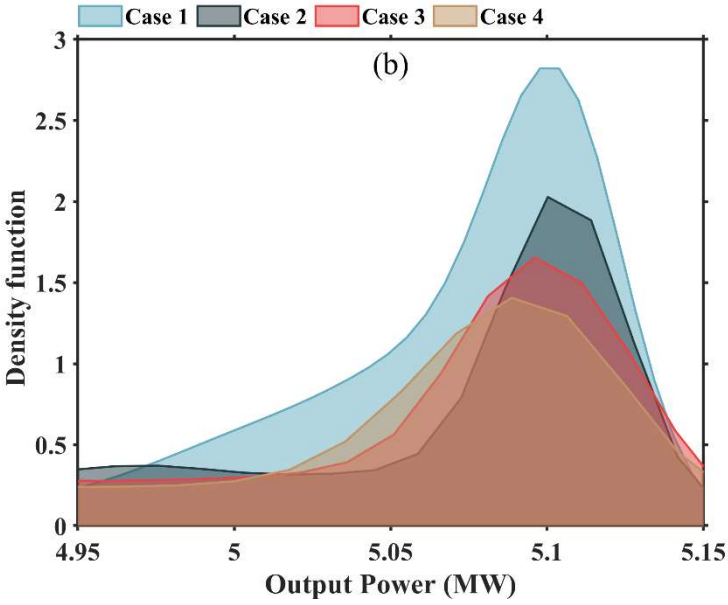


*Fig. 3.16 Kernel density estimate (bandwidth = 0.02) of FOWT output power at rated range*

### 3.4.3 WPRE analysis of FOWT

The processed results of time-domain power output from the four different learning cases are analysed using the OpSDA, leading to the presentation of the statistical distribution of power ramps in Fig. 3.17. This representation effectively reveals several significant observations. Firstly, the alteration rate of WPREs for the FOWT, operating without the influence of sea wave load, mirrors that of the bottom-fixed OWT upon

comparison between Case 1 and Case 2. Secondly, with increasing wave load, a steeper incline becomes apparent and accelerates progressively. Lastly, the analysis of power fluctuations demonstrates a consistent tendency, wherein the rate of increase in power during upward transitions exceeds that during downward transitions in Case 3 and Case 4.

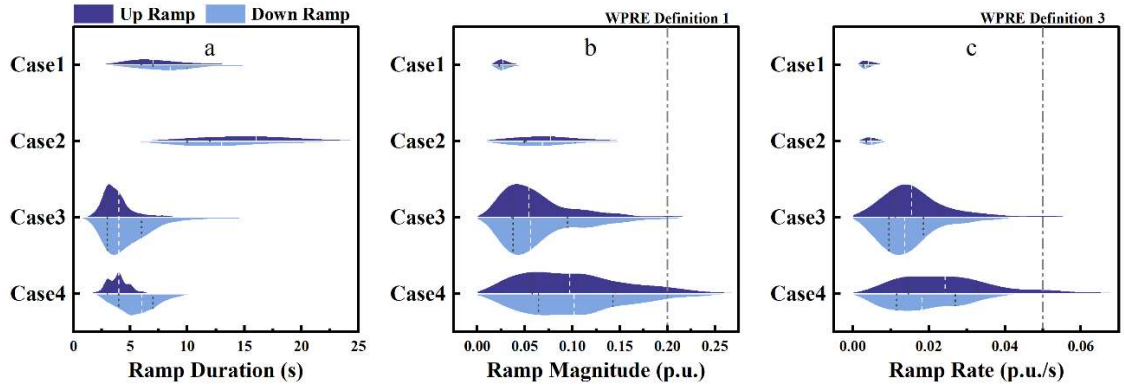


*Fig. 3.17 Probability distribution for the study cases of (a) the WPRE duration, (b) the WPRE Magnitude, (c) the WPRE rate.*

Fig. 3.18 presents a comparative analysis of the significant WPREs observed in bottom fixed OWT (OC3-Tripod) and FOWT (OC3-Hywind) during a simulation period of $3600s$ characterized by intense wave activity. To facilitate a clear comparison, $H_s$ and $T_p$ were aligned with 10-year condition of western Taiwan offshore. The power fluctuation observed in fixed foundation OWTs is generally restricted, with peak values being recorded around the rated wind speed. Nevertheless, the power fluctuation per minute for a single OWT occasionally surpasses the standard during wind speeds ranging from 9.4m/s to 11.4m/s. On the other hand, FOWTs display a substantially higher power fluctuation in the complete wind speed spectrum when compared to the reference OWTs. The active power fluctuation of FOWTs, subject to severe waves, is challenging to be constrained within the required range, with the peak value occurring when the wind speed is 9.8m/s.

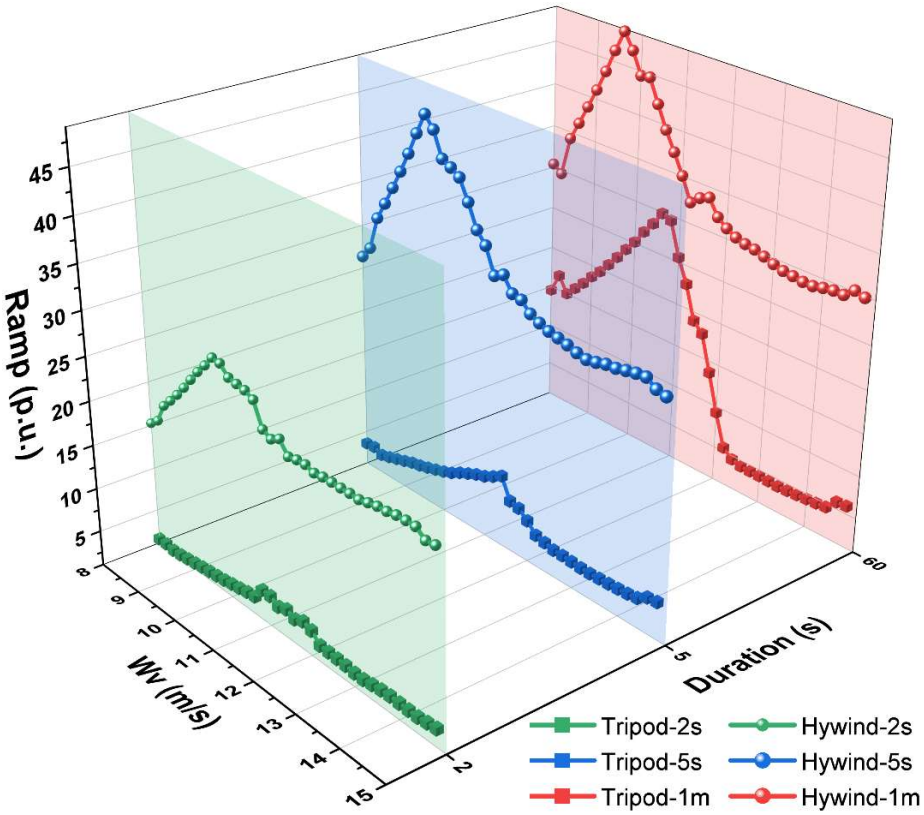


*Fig. 3.18 Significant WPRE magnitude comparison between bottom-fixed OWT and FOWT under 10-year return period wave conditions at western Taiwan offshore*

As shown in Fig. 3.19, the present study examines the maximum power fluctuation within time period of 2s, 5s, and 60s under varying wind-wave conditions. The findings demonstrate that the most severe power fluctuations occur at high wind speeds and large waves of 9.6 m/s. With decreasing wave heights, the wind speed corresponding to the maximum power fluctuation gradually increases and approaches the rated value of 11.4 m/s. The outcomes of the analysis reveal that the difference in power fluctuations for the same wave at different wind speeds is limited over a short time period, indicating that the second-level instantaneous power fluctuation primarily reflects the impact of ocean waves. Additionally, it is observed that the second-level power fluctuation remains below the threshold of 20% as long as the $H_s$ does not exceed 3.27m, across all wind speeds. However, in contrast to (a) and (b), the power fluctuation in (c) is generally unsatisfactory under most wind-wave conditions, with a "dead zone" observed at wind speeds between 10.4m/s-

11.8m/s as shown in Fig. 15, where all sea wave conditions cannot limit the fluctuation within 20% of the rated power. Nonetheless, based on the overall test results, the wind-wave boundary for FOWTs to operate compliantly has been identified. This finding can be utilized as a reference for future research aimed at quantifying the level of power quality enhancement in combination with existing research on dynamic optimization and power compensation using power conditioning equipment.

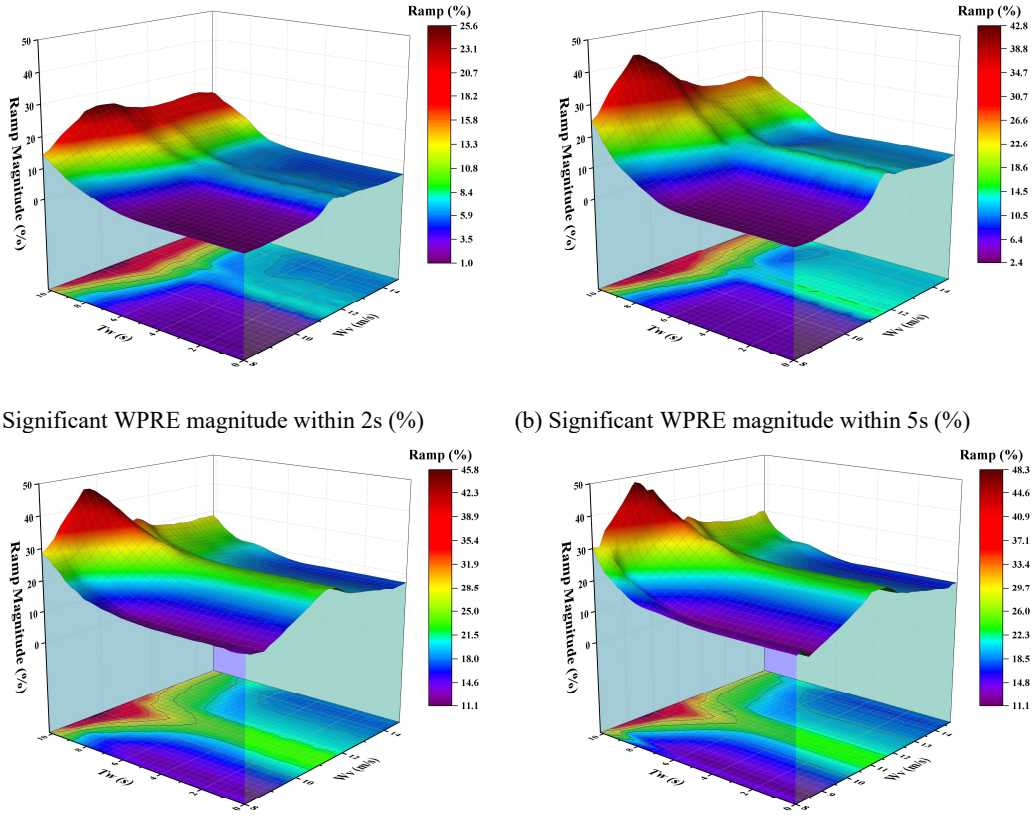


(a) Significant WPRE magnitude within 2s (%)

(b) Significant WPRE magnitude within 5s (%)

(c) Significant WPRE magnitude within 60s (%)

(d) Significant WPRE magnitude without time resolution (%)

*Fig. 3.19 Fig. 13 Maximum WPRE under operational wind and wave range at different time spans in Case 5*

By analysing the most significant WPRE cases within different time spans (2s, 5s, 60s and ∞) from Fig. 3.20, it can be observed that there is an intersection between the analysed data and the fully-developed wind-wave scenario (blue straight line) [168]. The analysis reveals that the wind speed corresponding to the maximum fluctuation point is

approximately 11m/s, and $T_p$ is around 6.6s. It is noteworthy that the wind speed associated with the maximum fluctuation point is in close proximity to the rated wind speed of 5MW wind turbine (11.4 m/s), indicating that such wind-wave conditions are likely to occur frequently during the designed operational range of FOWT.

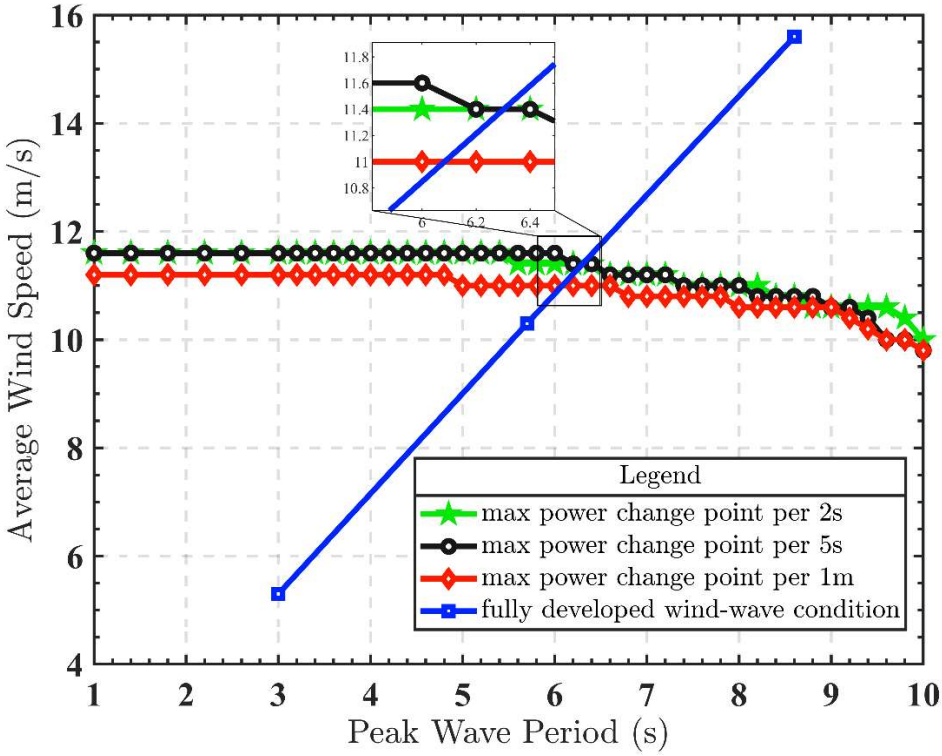


*Fig. 3.20 The coordinates of the most significant wind power ramp events and fully developed wind-wave relationship*

## 3.5 Determine "Pitch Angle-Power" Characteristics on FOWT

Based on the comprehensive results of the tests in Section 3.4, in the study cases where wind and waves are set in the same direction, the wind power of the FOWT exhibits significant cyclic variations, with high-frequency components concentrated at the natural pitch motion frequency of the FOWT and the wave frequency. It is observed that changes in the pitch angle of the floating platform seem to directly influence the wind power. Although many studies emphasize the impact of pitch angle on FOWT power [2][5][33], there is limited qualitative research providing a comprehensive description of the correlation. To obtain generalizable conclusions, this section conducts tests and comparisons of the

relationship between the pitch angle of the FOWT and active power, further demonstrating their correlation.

This study rigorously establishes 12 essential learning cases, with the wind and wave parameters summarized and named in Table 3.5. Cases (a) to (i) in the FAST inflow wind model are set as steady, while the inflow wave models are set as regular. In these nine cases, instances with the same wind speed under different wave conditions and vice versa can be found. The purpose is to observe the "pitch angle-power" characteristics of the OC3-Hywind FOWT when it reaches static stability. The influence of changes in wind or wave conditions on this characteristic is analysed through mutual comparisons between cases. Cases 2 to 4 inherit from Table 3.3, employing the Tidal wind model and irregular wave model based on real-world operational conditions. This is designed to test the "pitch angle-power" characteristics of the FOWT in non-static and complex environments, analysing the similarities and differences with characteristics in static environments.

*Table 3.5 Case settings for FOWT "pitch angle-power" characterization*

| Case | Input wind | | Input wave | | | Scenario |
|---|---|---|---|---|---|---|
| | Model | $v_w(m/s)$ | Model | $H_s(m)$ | $T_p(s)$ | (western Taiwan offshore) |
| a | Steady | 9.6 | Regular | 1.67 | 5.17 | Normal sea conditions |
| b | | 11.4 | | | | |
| c | | 13.2 | | | | |
| d | | 9.6 | | 5.5 | 9.4 | Northeast monsoon sea conditions |
| e | | 11.4 | | | | |
| f | | 13.2 | | | | |
| g | | 9.6 | | 6.1 | 10.4 | 10-year return period sea conditions |
| h | | 11.4 | | | | |
| i | | 13.2 | | | | |
| 2 | Tidal | 12.0 | - | 0 | 0 | Still water |
| 3 | | 12.0 | Irregular | 1.67 | 5.17 | Normal |
| 4 | | 12.0 | Irregular | 5.5 | 9.4 | Northeast monsoon |

### 3.5.1 Case analysis based on steady wind-wave conditions

Excluding the initial 600s startup phase, the summarized "pitch angle-power" relationships for cases (a) to (i) containing 1200s of simulation output data in FAST are presented in Fig. 3.21. Cases in the same row share identical input wave conditions, while cases in the same column share the same wind speed conditions. It is observed that the data distribution in all subplots is highly concentrated. This implies that, under steady wind and wave conditions, changes in pitch angle directly influence the power of the FOWT.

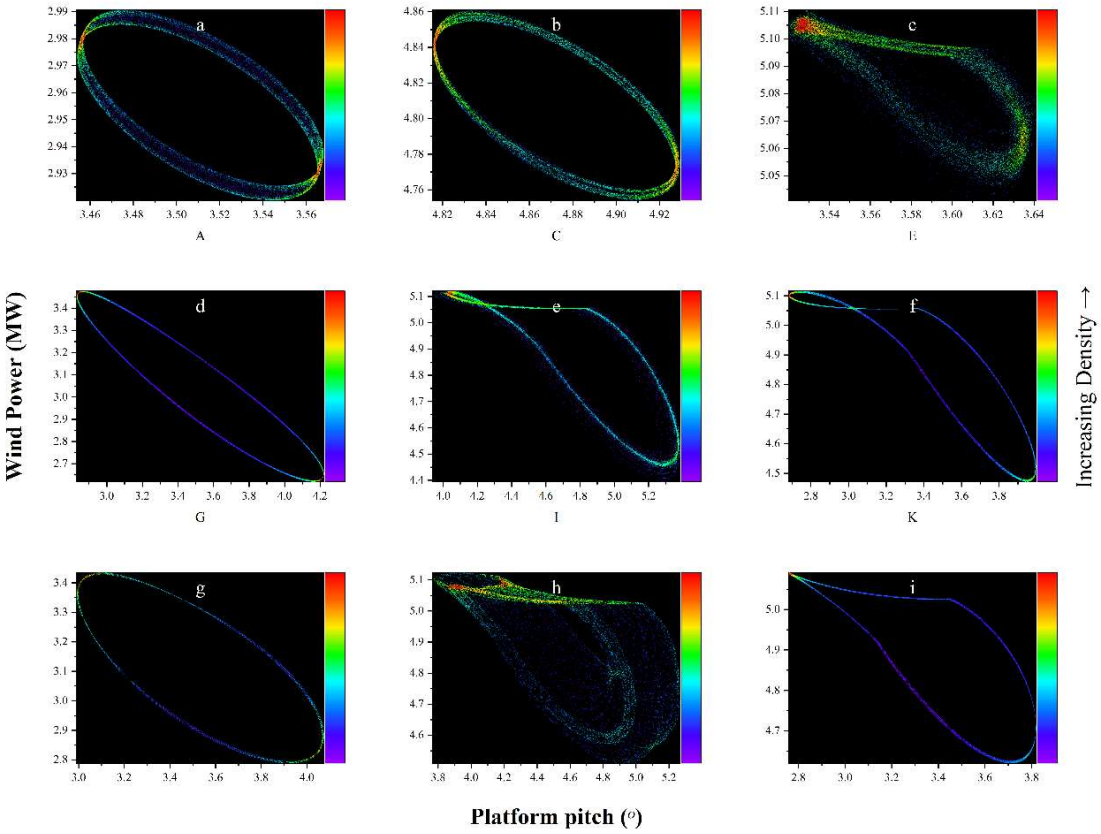


*Fig. 3.21 "Pitch angle-Power" relationship of FOWT under different load cases*

In cases where the maximum wind power does not exceed the rated power of the turbine (as in Fig. 3.21(a), (b), (d), (g)), the FOWT in a steady state completes an elliptical trajectory in the "pitch angle-power" coordinate system during one complete pitch motion

cycle. During this motion, as the pitch angle increases, the horizontal component of the linear velocity of the FOWT pitch motion is in the same direction as the wind, resulting in a lower effective wind speed received by the FOWT. The trajectory corresponds to the lower half of the "elliptical" movement. Conversely, when the pitch angle decreases, the horizontal component of the linear velocity of the FOWT pitch motion is opposite to the wind direction, leading to an increased effective wind speed received by the FOWT. The trajectory corresponds to the upper half of the "elliptical" movement. When the wind power exceeds the rated power of 5MW, the system enters the WECS Operating Region 3 control mode. As a result, data points in the low pitch angle range are restricted, leading to an overall smoother trend in this region. This phenomenon is observed in Fig. 3.21(c), (e), (f), (h), and (i). Furthermore, under the same wave conditions, cases at the rated wind speed in Fig. 3.21(b), (e), (h) exhibit the largest range of pitch motion, resulting in the maximum power fluctuations, aligning with the discussions conducted in Fig. 3.20.

In summary, under steady wind and wave conditions, FOWT power fluctuations are closely related to pitch angle motion and exhibit a negative correlation, indicating that an increase in pitch angle leads to a decrease in wind power.

### 3.5.2 Case analysis based on dynamic wind-wave conditions

In the simulation environment of this subsection, both wind speed and wave conditions are unsteady and conform to reality. In Cases 2 and 3, the wave-induced loads are significantly lower than the aerodynamic loads. Therefore, in Fig. 3.22(a) and Fig. 3.22(b), power fluctuations primarily stem from changes in wind speed, and the correlation between power and platform pitch angle is not observable. However, under extreme wave condition ($H_s = 6.4m, T_p = 10s$) in Case 4, the power ramp becomes notably inversely proportional to the pitch angle. In this scenario, the motion state of the floating platform becomes the predominant factor determining floating wind power.

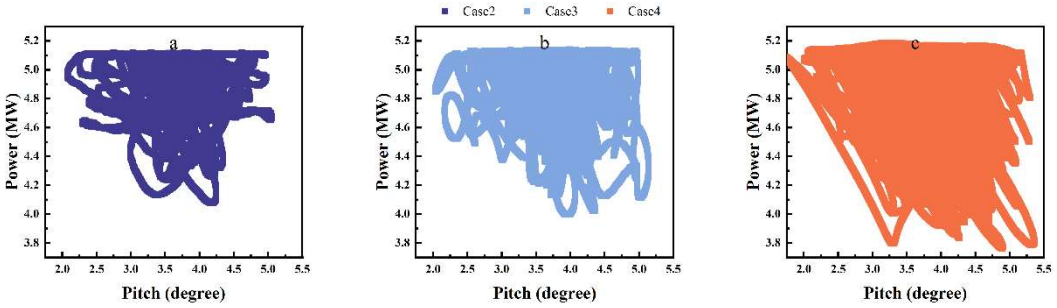


*Fig. 3.22 FOWT dynamic "Pitch Angle-Power" relationship under (a)Case 2, (b)Case 3 and (c)Case 4 conditions*

## 3.6 Conclusion to this chapter

In summary, this study developed an integrated, fully coupled mathematical model for FOWTs, delving extensively into the interactions between wind-induced and wave-induced loads and their resultant influence on WPREs. By synergizing mechanical and electrical constituents within a complete framework encompassing a spar buoy FOWT equipped with generator, converter, and AHSE dynamics, the following conclusions are drawn:

- **Manifestation of Periodic WPREs through Floating Dynamics:** The distinctive buoyant configuration of FOWTs engenders a cyclic recurrence of WPREs characterized by their periodic and pronounced dynamics. This phenomenon arises from the interplay between wave-induced loads and platform oscillations, giving rise to low (0.1-0.5 Hz) and ultra-low frequency (less than 0.05 Hz) responses. In contrast to conventional bottom-fixed offshore counterparts, FOWTs exhibit amplified power fluctuations during WPREs, thus highlighting the unique dynamical traits inherent to these floating structures.
- **Ramp Peaks and Load Dynamics Relationship:** Result in 3.4.3 reflects the zenith of ramping phenomena primarily hinges on aerodynamic loading dynamics, albeit exhibiting heightened sensitivity to wave-induced loading effects, particularly discernible when significant wave heights surpass the threshold of

2.52 meters. This underscores the pertinence of accounting for wave-induced loading intricacies in the design, operation, and risk management of FOWTs.

- **Operational Impact of Peak WPREs under Rated Wind and Wave Conditions:** Notably, the pinnacle of WPREs surfaces conspicuously within the ambit of rated wind and wave conditions. This convergence heralds a distinctive operational scenario wherein the turbine perpetually operates within the ambit of the most exacerbated WPRE manifestations. This operational facet underscores the turbine's perpetual exposure to the most adverse ramping dynamics, accentuating the intricacies of power instability inherent within this specific operational regime.
- **Significance of Pitch Motion and Wave-Induced Loading:** The significance of pitch motion and the profound ramifications of wave-induced loads in shaping the landscape of WPREs for FOWTs are unequivocally underscored. These dynamics constitute pivotal parameters for explicating the transient response of FOWTs across diverse operational scenarios.

In summary, this study not only addresses a significant research gap pertaining to WPRE studies in the domain of FOWTs, but also engenders profound insights into the underpinning dynamical intricacies shaping the operational integrity and reliability of wind energy systems. Pioneering the integration of hydrodynamic complexities and mechanical motion dynamics within a holistic model framework, this investigation advances the strategic design, deployment, and grid integration of FOWTs.

# Chapter 4: Real-Time Coordination Control of Hybrid Energy Storage Systems for Floating Offshore Wind Power

## 4.1 Introduction

In comparison to the rigid body structure of bottom-fixed OWTs, FOWTs exhibit distinct hydrodynamic effects due to their unique floating structures. These effects manifest through 6 DoFs of motion, exerting a notable influence on the rotational speed of the generator. Among these DoFs, the pitch motion emerges as the predominant factor negatively impacting the operational characteristics of the generator [20]. Larsen and Hanson conducted studies elucidating that pitch motion experiences a substantial increase as wind speeds surpass the rated wind speed conditions [169]. This exacerbates concerns regarding the ramp event represented power quality of FOWT output, consequently posing a significant challenge. Comprehensive testing of FOWT power quality in Chapter 3: confirms this concern.

Based on the research findings of Yang et al. and evidenced in Chapter 3: , the power spectrum density of each DoF motion exhibits prominent density peaks that concentrate within two frequency intervals: the natural frequency range and the wave frequency range [13]. Specifically, the platform motion exhibits a low natural frequency, which is rigorously designed in the very-soft frequency domain below 0.1Hz to avoid resonance at the rotor frequency associated with cyclic loading caused by ocean waves and OWT blade mass imbalance [170]. The density distribution in this range demonstrates complex and challenging changes to quantify and analyse, owing to the influence of various wind-wave conditions. On the other hand, the frequency associated with waves is relatively high, with power density distributed independently around 0.2 Hz. Notably, the power spectrum density of the pitching motion aligns remarkably well with the power spectral density distribution of wave height dynamics. This correlation facilitates the development of

straightforward and uncomplicated optimization strategies for mitigating power fluctuations specifically occurring at ocean wave frequencies in WECS.

Significant endeavours have been dedicated to enhancing FOWT power quality, primarily emphasizing external compensation of dynamics through means such as WECs[171] and TMDs[14] to mitigate the structure vibration. Additionally, the optimal design of control strategies, including more intricate feasible control mechanisms [5], has garnered considerable attention. However, the scope of actively optimizing power waveforms through power electronic components remains considerably limited.

From the perspective of stable operation of the power system and to further enhance the grid integration of wind power, efforts must be directed towards the continuous development of robust smart grids. Simultaneously, the friendliness and autonomy of wind power systems need continuous improvement. Research has already explored the addition of supplementary electrical modules, such as PSS[172] and LCL filter[11][173], to the design of WECS. This is done to ensure the elimination of harmonics and enhance power quality. Additionally, feasible solutions within wind farms involve the integration of other energy sources with wind energy, resulting in systems like wind-solar[174], wind-ESS[175], and wind-hydrogen[176]. These systems are complemented by efficient control strategies. While these integrated solutions have undergone comprehensive research and have matured in their application and deployment in today's power systems, there remains a gap in practical applied research for floating wind farms with floating wind power characteristics.

In response to the completed testing and analysis of floating WPRE characteristics, a comprehensive Wind-HESS coupling system can be constructed. This system incorporates four types of WECS, LC low-pass filters, lithium-ion batteries, and supercapacitors. To address the power quality deficiencies, a real-time coordinated control strategy is designed for this system, taking into account multiple boundary conditions. By effectively utilizing the power-type supercapacitors to compensate for the energy-type hydrogen storage's

startup delay power, the strategy aims to track and compensate for the power harmonics related to both the FOWT's natural frequency and wave frequency. This approach significantly improves the output power quality.

The organizational structure of this chapter is as follows: Firstly, the design and testing of a low-pass filter, connected in series on the DC bus of four types of WECS, are introduced. The effectiveness of suppressing wave frequency harmonic power is evaluated. In the third section, the modelling, control scheme, and coupling methodology of the HESS are presented. The fourth section involves experimental analysis and discussion of the optimal parameter settings. Finally, a summary is provided for the designed approach.

## 4.2 DC Bus Wave Frequency Filter Design and Testing

The primary objective of this section is to investigate and enhance power quality and mitigate power fluctuations in the context of FOWT. To achieve this goal, a comprehensive electromechanical coupling FOWT model is constructed, along with a new dedicated wave filter designed for the DC link. The FAST-Simulink co-simulation platform is employed for the hydrodynamic wave frequency analysis. The proposed approach aims to improve the power quality of FOWT output by effectively eliminating harmonics associated with ocean wave frequencies. This is accomplished through the implementation of a band-stop filter within the full-scale converter, strategically positioned on the DC bus. The parameter settings for the band-stop filter are determined through independent analysis, considering the filtering effectiveness, filterable frequency range, and the response speed of the WECS.

### 4.2.1 LC Oscillator Included DC bus Design

In the conventional back-to-back converter utilized in the IEC wind turbine Type 4 configuration, the sole mechanism employed for maintaining stable terminal voltage on the DC-link entails the utilization of energy storage capacitors. However, in this experimental

model, a LC series resonant circuit as a targeted band-stop filter has been introduced onto the DC bus to address power fluctuations occurring at the wave frequency. This arrangement is depicted in Fig. 4.1.

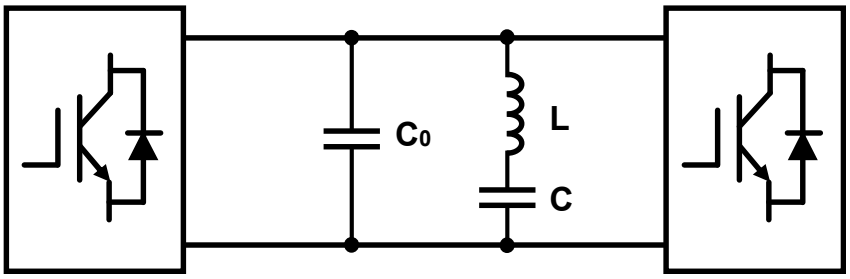


*Fig. 4.1 Composition of DC bus electrical components*

For a series resonant circuit, the formula to calculate the resonant frequency is:

$$f_0 = \frac{1}{2\pi\sqrt{LC}} \tag{4.1}$$

where $f_0$ is the resonant frequency of the LC resonant circuit, $L$ is the resonant circuit inductance, and $C$ is the resonant circuit capacitance.

Quality factor is able to measure the degree of underdamping and filter bandwidth of the LC resonant circuit, the formula is:

$$Q_f = \frac{\omega_0 L}{R} = \frac{1}{R}\sqrt{\frac{L}{C}} \tag{4.2}$$

where $Q_f$ represents the quality factor and $\omega_0$ refers to the input signal angular frequency. The larger the quality factor, the better the filtering effect at the central oscillation frequency. It is noted that the equivalent resistance R of the LC resonant circuit is not discussed in detail in this study, it was set to $0.1\ \Omega$ through all the simulation tests except Fig. 4.4 & Fig. 4.5 while not showing in Fig. 4.1.

### 4.2.2 Load case settings

The methodology of the hydrodynamic analysis for FOWT output power is divided into two aspects, hydrodynamics at wave frequency and power output analysis.

In this part of the study, it is focused on investigating and distinguishing the impact of hydrodynamics on output power at wave frequency. Different cases are considered where mainly identical turbulent wind conditions at the IEC standard rated wind speed are used [159]. Each case incorporates distinct hydrodynamic characteristics. By comparing these cases, the power characteristics of the various dynamic components can be clearly observed and analysed.

Specific load cases are inherited and modified from Table 3.3, summarized as follows:

Case1: conventional bottom-fixed OWT at rated wind speed

Case2: FOWT at rated wind speed with no waves

Case3: FOWT at rated wind speed with regular waves (6s, 2.5m)

Case4: FOWT at rated wind speed with irregular PM waves (10s, 6m)

Data analysis is required for the output power, in conjunction with the quantified impacts in the Chapter 3: . The analysis aims to validate the potential improvement effect on power quality resulting from the power signal processing conducted at the wave frequency. Additionally, data analysis results are used to optimize design parameters of PQ solutions. Here the wind and wave conditions considered are those exceeding the rated operating conditions of the FOWT, as hydrodynamics will have the greatest negative impact on FOWT power quality under these occasions.

Data required include a significant amount of ocean states. In the next section, one 1-year sea state data with a resolution of 10 seconds is used [158], correspondingly the resonant frequency of the LC circuit is set to 0.1 Hz.

By adopting this approach, the differentiation of hydrodynamics on output power at wave frequency can be addressed, with confidence in enhancing power quality through signal processing and optimizing filter design parameters via data analysis.

### 4.2.3 Simulation results and discussion

#### *4.2.3.1 FOWT Output Power Characteristics*

Fig. 4.2 display the simulation results of active power output time series for FOWTs under four different case settings based on the same model in Chapter 3. A comparative analysis of the cases depicted in Fig. 4.2(a) reveals that Cases 2 and 3, which utilize the floating platform structure, exhibit substantial power fluctuations when subjected to rated wind or wind-wave inputs, in contrast to Case 1 representing the bottom-fixed OWT. Particularly, when compared to Case 2 without ocean wave input, Case 3 displays additional power fluctuations in the time domain. These fluctuations exhibit a stable period of 6 seconds and possess a discernible amplitude. Moreover, Fig. 4.2(b) demonstrates that, under identical wind speed conditions, the presence of greater wave input leads to more pronounced power fluctuations at wave frequencies. These irregular fluctuation characteristics align with the PM wave features attributed to ocean wave inputs.

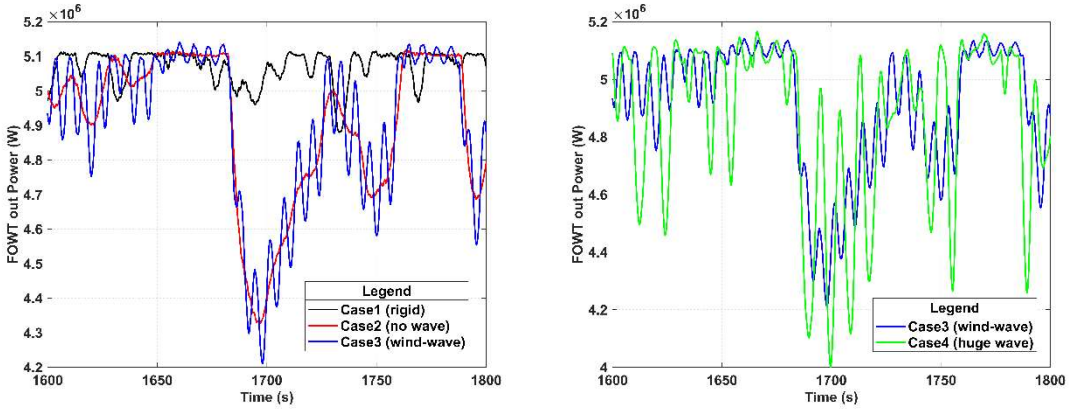


(a) Case 1, 2, 3 (b) Case 3 and Case 4

*Fig. 4.2 FOWT output power under Case 1-4 in time domain*

#### *4.2.3.2 Filtering Effect Testing and Analysis*

The hydrodynamic impact of waves is significantly influenced by the quality factor of the second-order LC resonance circuit. This section aims to compare and analyse the selection of the quality factor in relation to this effect.

*Table 4.1 Wave period to frequency conversion*

| Wave frequency (Hz) | 0.067 | 0.083 | 0.1 | 0.125 | 0.167 | 0.5 |
|---|---|---|---|---|---|---|
| Wave period (s) | 15 | 12 | 10 | 8 | 6 | 2 |

To conduct the study, the frequency of the LC oscillating circuit is specifically set at 0.1 Hz, which corresponds to the occurrence of one year state giant waves. In order to assess the filtering effect, a test was conducted within the wave frequency range that represents the 10-year return period of Taiwan offshore, as depicted in Fig. 4.3. To provide a clearer understanding of the relationship between frequency and wave conditions in Fig. 4.3, Table 4.1 has been included.

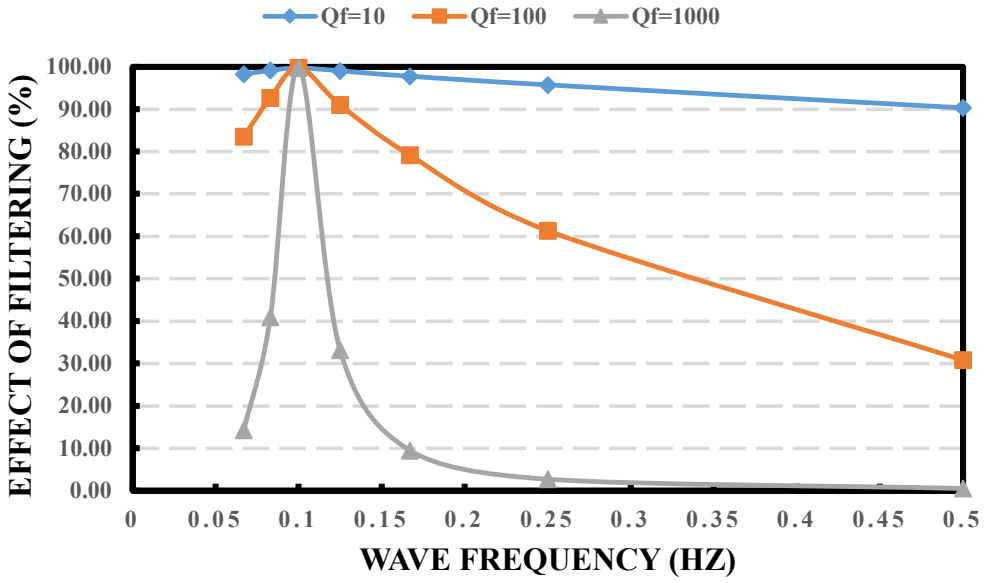


*Fig. 4.3 Filter effect under different quality factors*

By focusing on the quality factor of the system, it is possible to examine its impact on the hydrodynamic treatment of waves. Through a thorough analysis of this parameter, valuable insights can be gained regarding the selection process.

Upon examining the comparative analysis of signal processing effects at various quality factor $Q_f$ settings presented in Fig. 4.3, it becomes apparent that different $Q_f$ settings applied to the resonance frequency yield favourable filtering outcomes. Notably, an increase in the quality factor results in enhanced accuracy of frequency selectivity. Furthermore, it is important to establish a reasonable upper limit for the value of $Q_f$ to better focus the filtering effects on the certain wave frequency. Doing so serves two purposes: firstly, it prevents the filterable interval from becoming excessively wide, thereby avoiding any adverse impact on the DC component. Secondly, it ensures that there is a significant effect in processing conventional small wave signals, which are more prevalent and higher in frequency compared to relatively larger wave conditions.

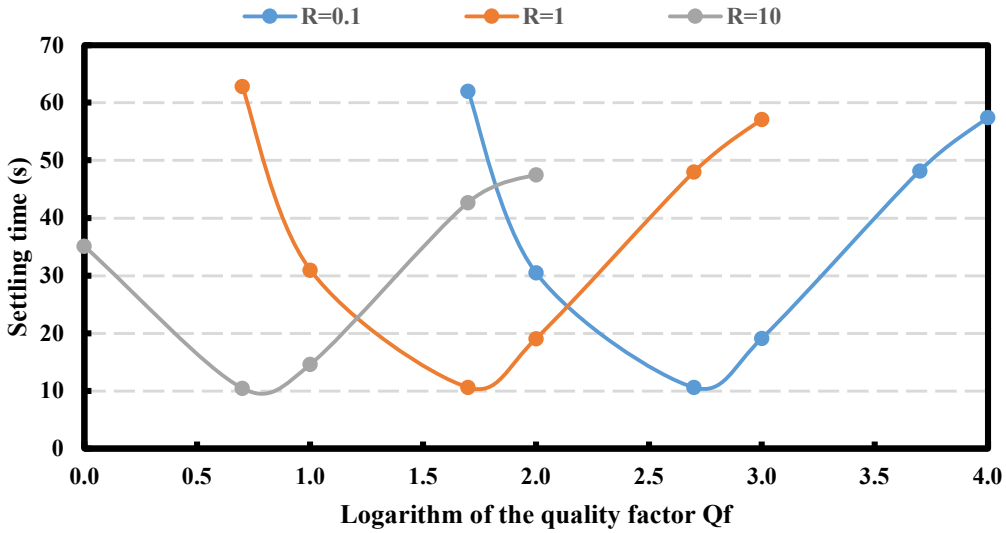


*Fig. 4.4 The relationship between control system settling time and quality factor*

By analysing Fig. 4.4, it becomes evident that an optimal quality factor value exists for the settling time. Moreover, it can be observed that the optimal $Q_f$ is inversely correlated with the equivalent resistance $R$ of the circuit, while being independent of the values of inductance $L$ and capacitance $C$. On the other hand, Fig. 4.5 illustrates a substantial reduction in the overshoot of the system response as the $Q_f$ increases. This relationship is particularly pronounced when the resistor values are decreased.

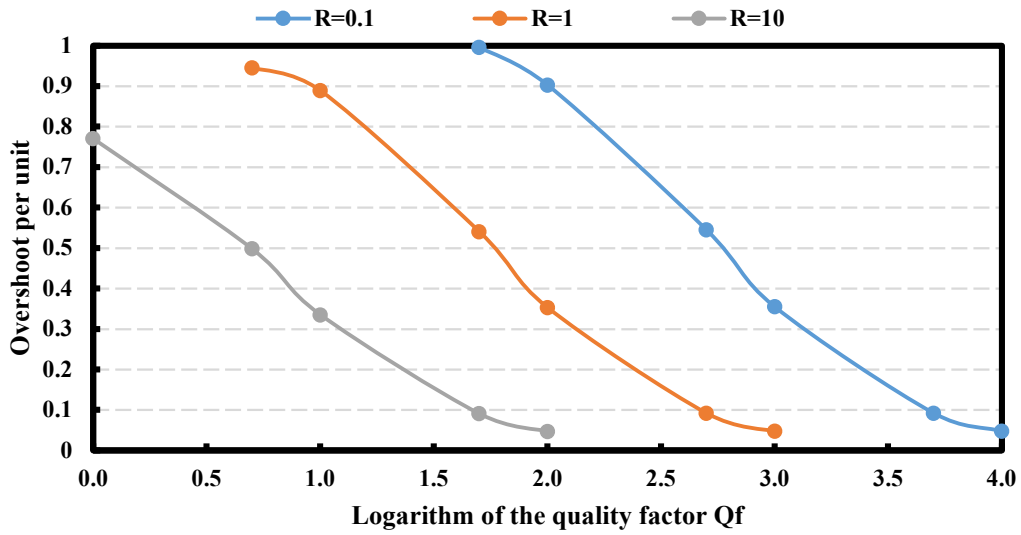


*Fig. 4.5 The relationship between the overshoot and the quality factor of the control system*

Synthesizing the findings from the system characteristics analysis depicted in Fig. 4.3 and Fig. 4.4, it can be deduced that by configuring the resistance $R$ as 1 and selecting a quality factor $Q_f$ of 100, the LC circuit exhibits several desirable attributes. These include the fastest settling time, minimal overshoot, and a relatively wide range of wave frequency signal processing capabilities. Building upon these conclusions, the final experiment focuses on the parameter settings of this LC oscillator circuit and evaluates the filtering effectiveness in Case 3 and Case 4, as outlined in 4.2.2.

Fig. 4.6 depict the simulation results of power output from a FOWT operating at its rated wind speed of $11.4m/s$. In these simulations, different scenarios were examined. In case 3, the system was subjected to common far-offshore wave conditions with a period of $6s$ and a significant wave height of $2.5m$. However, there was a noticeable discrepancy between the frequency set by the filter circuit and the desired frequency. As illustrated in Fig. 4.6(a), despite the LC resonant circuit being designed to accommodate a wide range of filtering frequencies, the power optimization effect in Case 3 was relatively modest.

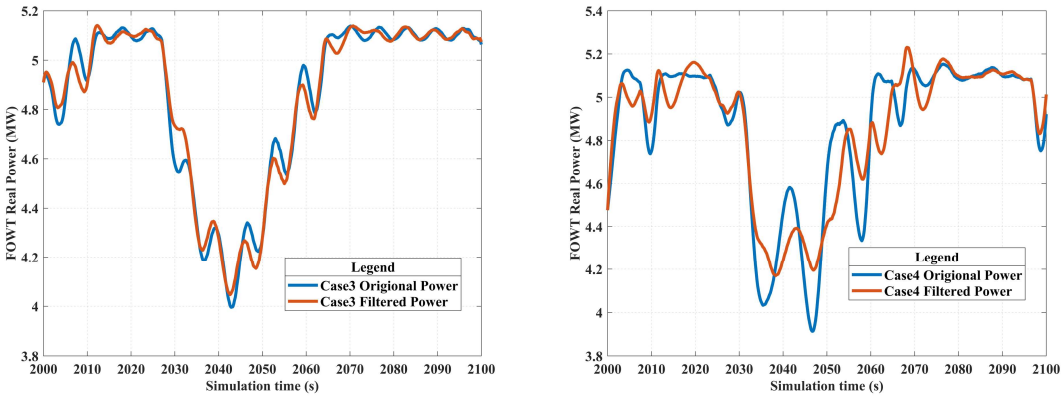


(a) Power filtering effect under Case 3 (b) Power filtering effect under Case 3

*Fig. 4.6 Power filtering effect for the low pass filter*

To assess the filtering effectiveness of the control system's centre frequency, a 10-year wave state was considered in Case 4, characterized by a wave centre period of $10s$ and a significant wave height of $6m$. The simulation results, as depicted in Fig. 4.6(b), indicate that the power drop in the FOWT was effectively controlled within a short time period, and the quality of active power was significantly enhanced throughout the simulation duration.

These findings highlight the importance of accurately setting the filtering frequency to optimize power output in FOWTs. The simulations demonstrate that the system's performance was suboptimal when the filtering frequency deviated from the desired value, but it significantly improved when the centre frequency matched the wave conditions. These findings contribute to a better understanding of FOWT dynamics and inform the development of strategies to enhance power generation and system stability.

### 4.2.4 Conclusion to this section

This section presents an added LC resonant circuit design at the DC-link of a WECS converter in FOWT, aiming to compensate the hydrodynamic effects caused by offshore

wave frequencies and improve the quality of power output. Prior to proposing a new design, the study conducted an analysis involving four different cases to demonstrate the existence and influence of hydrodynamics at wave frequencies on power output. Experimental results validate that the filter design effectively mitigates power fluctuations induced by wave frequency hydrodynamics, resulting in a power quality improvement level of 5% of the rated capacity within a 60-second time resolution.

However, it should be noted that the suppression of fluctuations is constrained to a certain range around the resonant frequency. In practical operations, the design of the filter's centre frequency yields the greatest benefits when set slightly higher than the rated wave frequency, making it an optimal choice for passive control. If the power quality of the wave trap, particularly the L/C property, can be manipulated and controlled, upgrading to an active feedback control, it can significantly improve the potential for enhancing the power quality of FOWTs under full wind and wave conditions. Future research endeavours will therefore be required on suppressing ultra-low-frequency hydrodynamics associated with the natural frequency response of FOWT, thus further improving the power quality of individual Floating WECS.

## 4.3 Customized HESS design for FOWT

Energy storage, as a crucial technological support for the high-proportion integration of new energy into the power grid, plays a key role in smoothing fluctuating power [177]. It can effectively enhance the penetration rate of wind power and the reliability of grid connection. Most research on energy storage assisting wind power grid integration has been focused on improving control methods to enhance the smoothness of the grid-connected wind power [178]. Considering the significant gap between power quality and grid standards, in the application scenarios of integrating energy storage with floating offshore wind farm, improving power quality should be considered as a primary factor.

Building upon the insights derived from the summary of the characteristics of the floating WPREs in Chapter 3: , this section endeavours to enhance the power quality of floating wind power to its maximum extent. The focus here lies in mitigating wind power fluctuations and concurrently considering the operational costs of HESS. This is achieved through the optimization of parameters in the Kalman filter, aiming to attain the optimal power distribution within the HESS. The ultimate goal is to achieve an optimal allocation of power that maximizes the quality of floating wind power while ensuring the stability of voltage and frequency in the WECS, particularly during critical moments.

### 4.3.1 HESS modelling

The optimal design of the HESS should effectively address the power and energy requirements inherent in floating offshore wind power applications. Given the intermittent nature of power generation in floating WECS and the rapid fluctuations between output power and load demand, a desirable HESS should exhibit characteristics such as high energy capacity, reliability, swift dynamic response, minimal maintenance, cost-effectiveness, and safe operation [175].

The variability and unpredictability of output power in floating WECS necessitate an ESS with high specific energy (ESS-E), defined as the maximum available energy per unit mass. This ensures the ability to consistently meet long-term energy demands. Concurrently, the HESS in floating WECS faces highly fluctuating and irregular charging/discharging cycles influenced by FOWT hydrodynamics. To effectively address these challenges, the ESS should possess high specific power (ESS-P), denoting the maximum power per unit mass, coupled with fast response times to accommodate the fluctuations in floating wind power. This comprehensive approach aims to optimize the HESS for floating offshore wind power, ensuring a balance between energy and power requirements while accounting for the unique operational conditions posed by the floating WECS environment [33].

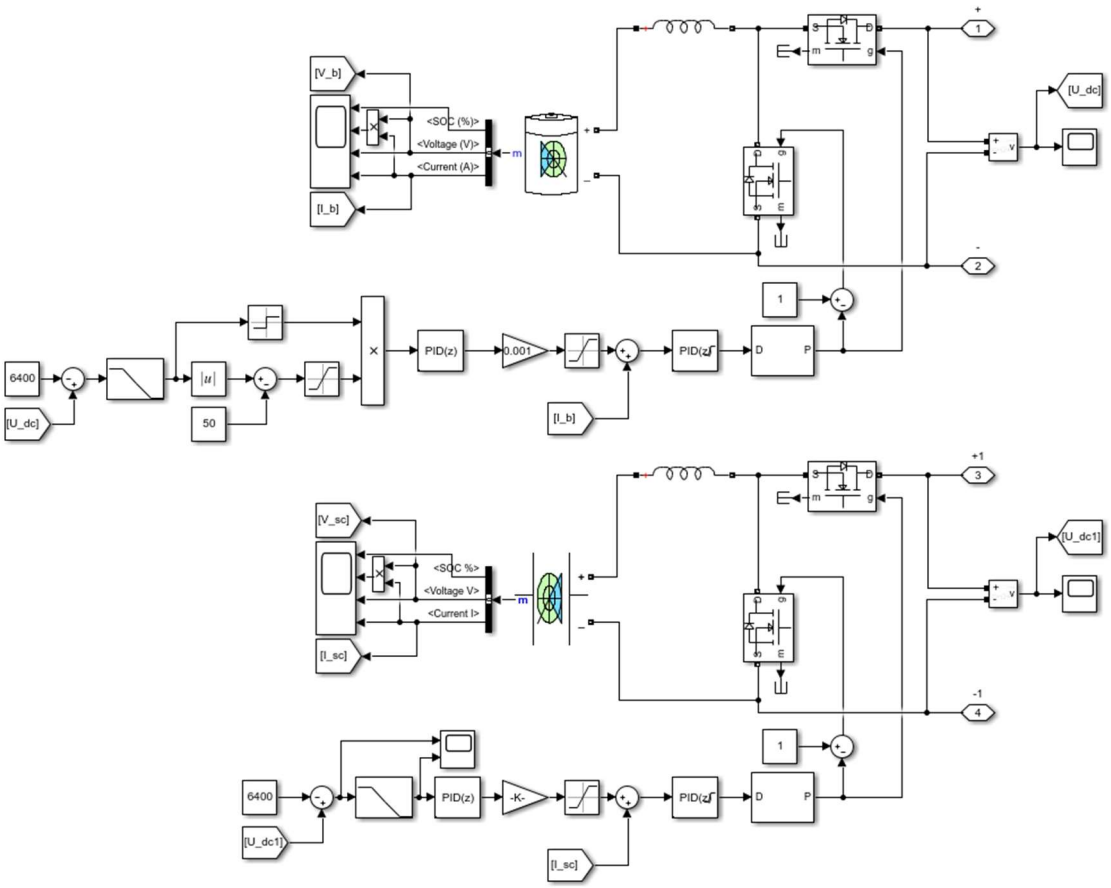


*Fig. 4.7 Block diagram of HESS module in Simulink*

The HESS model, depicted in Fig. 4.7, is implemented in Simulink to meet the specified requirements. Lithium-ion batteries are chosen as the ESS-E due to their high energy density, round-trip efficiency, power density, and fast discharge operation. Equation (4.3) is used to estimate the battery storage capacity capable of supplying a fraction of the rated current demand.

$$Ah_{rating} = \frac{t_{LiB} \times \gamma_{LiB} \times I_{rated}}{60 \times k_{LiB}} \tag{4.3}$$

(4.3) involves parameters where $\gamma_{\mathrm{LiB}}$ represents the fraction of the rated current of the load demand, and $\mathrm{I_{rated}}$ signifies the rated current of the load demand. Additionally, $\mathrm{t_{LiB}}$ stands for the time duration during which the battery supplies power to the system, while $\mathrm{k_{LiB}}$ is a fraction defining the average discharge/charge current of the battery.

A supercapacitor is responsible for the role of ESS-P module. In practical applications, the supercapacitor must adhere to three key constraints below. (4.4) ensures that the supercapacitor operates within safe voltage limits, as specified by the manufacturer. (4.5) facilitates the determination of the maximum peak current the supercapacitor can handle. Additionally, (4.6) defines the maximum allowable power of the supercapacitor during operation.

$$V_{Sc\_min} < V_{Sc} < V_{Sc\_max} \tag{4.4}$$

$$i_{Sc\_pk} = \frac{0.5 \times C_{Sc} \times V_{Sc}}{C_{Sc} \times ESR_{dc} + 1} \tag{4.5}$$

$$P_{Sc\_max} = \pm C_{Sc} \times V_{Sc} \times \left|\frac{dV_{Sc}}{dt}\right|_{max} \tag{4.6}$$

In the equations: $V_{Sc\_min}$ and $V_{Sc\_max}$ denote the minimum and maximum operating voltages of the supercapacitor; $ESR_{dc}$ represents the equivalent series resistor of the supercapacitor; $C_{Sc}$ is the capacitance value of the supercapacitor; $P_{Sc\_max}$ is the maximum power rating of the supercapacitor; $\left|\frac{dV_{Sc}}{dt}\right|_{max}$ signifies the maximum rate of change of voltage across the supercapacitor.

(4.7), (4.8) and (4.9) play a role in estimating the size of the supercapacitor.

$$E_{Sc} = \frac{1}{2} C_{Sc} V_{Sc}^2 \tag{4.7}$$

$$E_{Sc} = \frac{1}{2} C_{Sc} (V_{Sc\_max}^2 - V_{Sc\_min}^2) \tag{4.8}$$

$$C_{Sc} = \frac{2E_{Sc}}{(V_{Sc\_max}^2 - V_{Sc\_min}^2)'} \tag{4.9}$$

Here, $E_{Sc}$ represents the energy rating of the supercapacitor. These equations provide valuable insights into determining the appropriate specifications for the supercapacitor, ensuring it meets the required energy storage and performance criteria.

### 4.3.2 Floating WECS-HESS coupling

In the realm of type 4 WECS, there exist three viable configurations of HESS through DC bus coupling: passive, semi-active, and active HESS. This study adopts the parallel active HESS topology, as illustrated in Fig. 4.8. In contrast to passive or semi-active HESS, the active configuration stands out for its superior performance, leveraging the use of two power electronic units. This design choice leads to improved overall system efficiency and an extended lifespan [179], highlighting the advantages of the active HESS configuration for type 4 WECS applications.

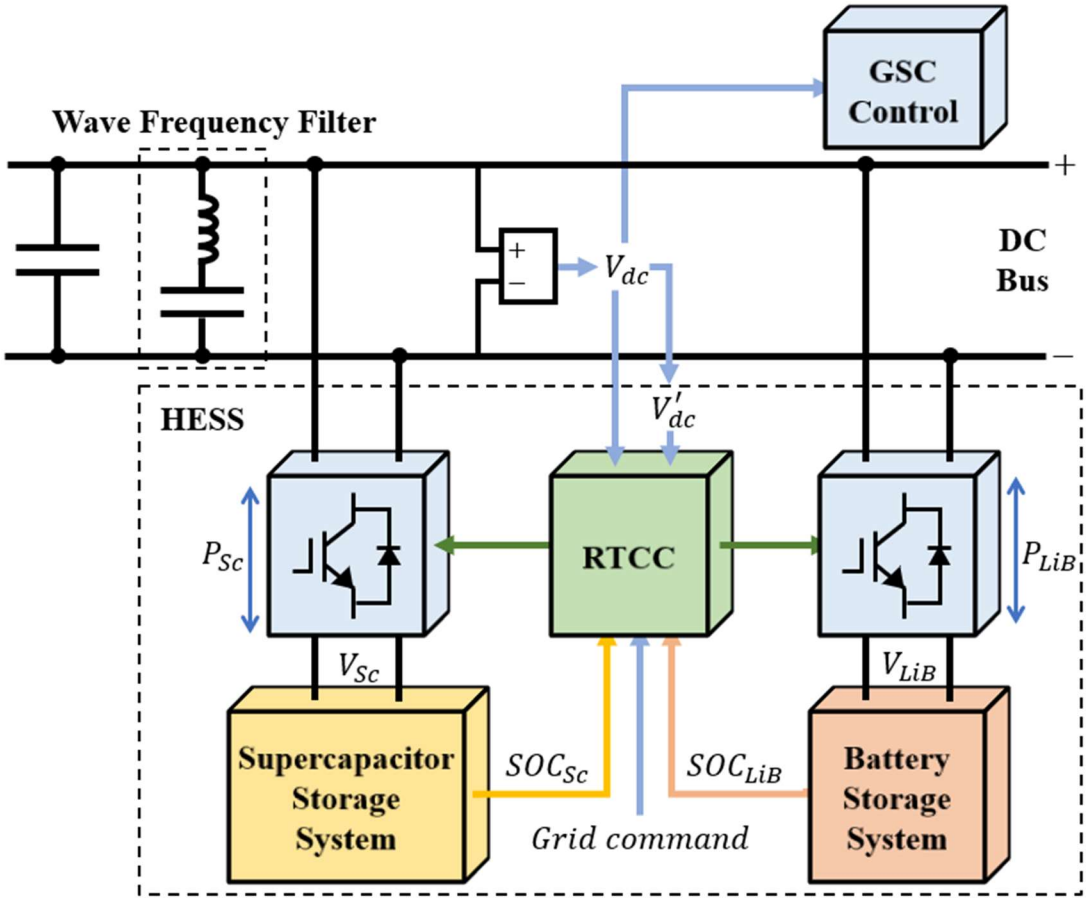


*Fig. 4.8 Parallel active HESS topology on Floating WECS*

### 4.3.3 Real-time coordinated control of HESS coupled on FOWT

In consideration of the short time intervals of the RTCC (set to 60 seconds in this study), energy flows with slower response rates, such as heating and cooling, are excluded

from this phase. Only short-term power fluctuations resulting from random variations in renewable energy and load demands are considered for adjustment through the HESS during the RTCC process. To facilitate a better understanding of the RTCC process and the dynamic behaviour of various sub-models and variables, Fig. 4.9 presents a flowchart depicting the dynamic processes within the model. Detailed explanation of RTCC sub-models is organized as follows.

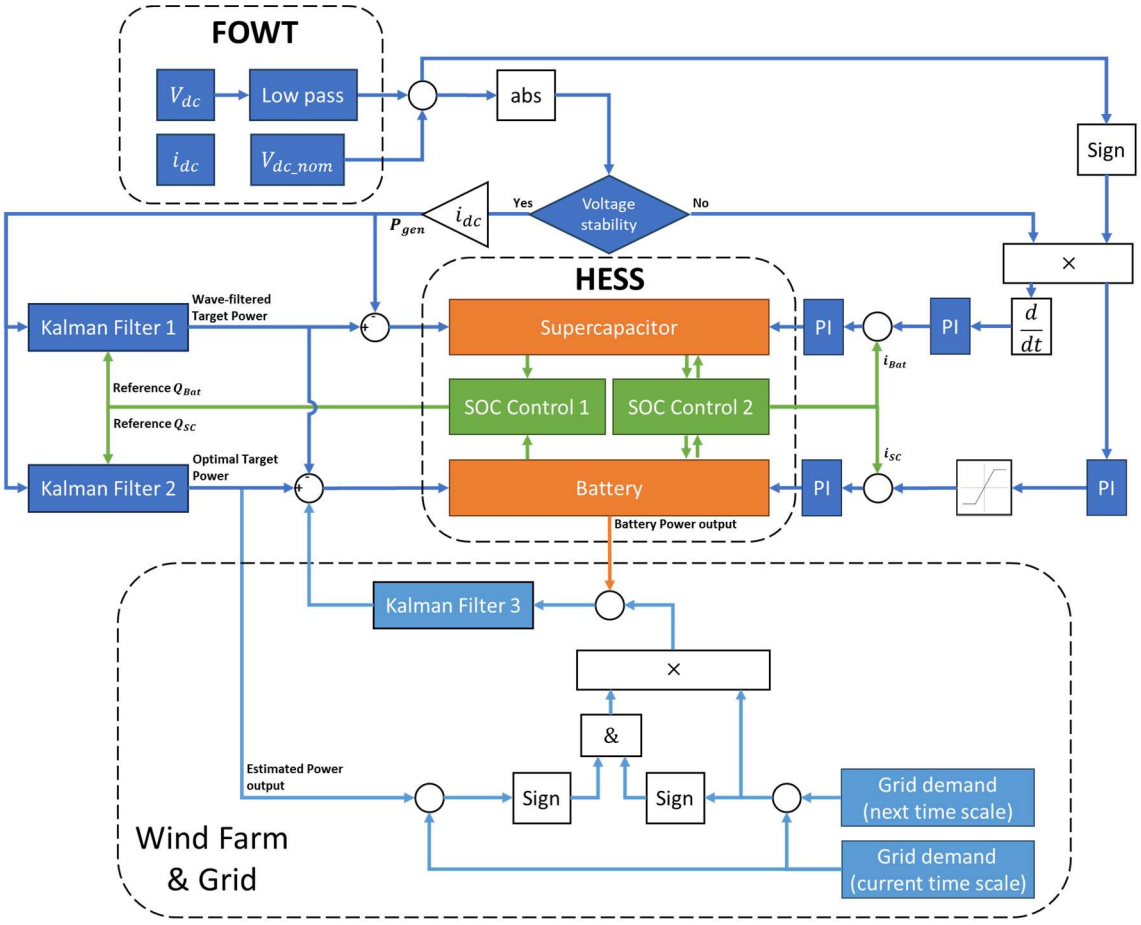


*Fig. 4.9 Real-time coordinated control strategy framework of the HESS*

### *4.3.3.1 Voltage & current control scheme*

For the HESS in the Type 4 WECS with a DC bus, a dual-loop control strategy is designed and implemented in the charging/discharging DC/DC converter. This converter meets voltage and current reference values. The inner loop is a current control loop,

regulating the current of the battery or supercapacitor, while the outer loop controls the DC bus voltage. The outer loop controller provides the reference current for the inner loop. The reference value of the DC bus voltage is compared with the actual value in the outer loop. Subsequently, the error between these values is fed into a voltage PI controller, responsible for generating the reference current signal for the inner loop based on Equation (4.10).

$$I_{ESS\_ref} = (k_p + \frac{k_i}{s})(V_{dc\_ref} - V_{dc}) \tag{4.10}$$

Here, $I_{ESS\_ref}$ represents the current reference value of the inner PI controller, while $V_{dc\_ref}$ and $V_{dc}$ are the reference and actual values of the DC bus voltage, respectively. Subsequently, the error between this reference current and the actual inductor current is provided to the current PI controller to adjust the duty cycle of the charging/discharging switch.

#### *4.3.3.2 Kalman filter based power smoothing target allocation of HESS*

In the pursuit of smoothing the power output from wind farms using energy storage systems, the accurate determination of the target grid-connected power becomes pivotal, directly influencing the overall quality of integrated wind energy. Existing methodologies for extracting the target grid-connected power encompass a diverse array of data processing techniques, such as Fourier transformation, wavelet analysis[180], first-order low-pass filtering[181], and associated algorithms, sliding average filtering, Kalman filtering[182], as well as alternative approaches like modal decomposition and model predictive control [178].

The prevalent use of the first-order low-pass filtering algorithm, acknowledged for its simplicity in design and operational efficiency, encounters a persistent challenge in addressing the inherent phase delay issues during runtime, thereby impacting the final power smoothing outcomes within a HESS.

Advanced algorithms are playing a catalytic role in ascertaining the target power for wind energy grid integration, providing valuable insights into enhancing the SOC of energy

storage systems and prolonging the lifespan of batteries [183]. Nevertheless, a majority of these studies heavily rely on algorithmic adjustments tailored for regulating the SOC of energy storage systems, resulting in sluggish computational speeds and constricting the power smoothing capabilities of energy storage [184].

Kalman filters, acclaimed for their exemplary performance, find extensive application in fields like communication and control. When confronted with abrupt changes in wind farm power, the optimization of filter gain through Kalman filtering emerges as an effective strategy for achieving superior target grid-connected power. Leveraging both observed and estimated values, the Kalman filter adeptly collaborates to determine the target value, demonstrating prowess in predicting the subsequent state using estimated values while concurrently refining the previous estimation based on the current observation. Noteworthy for its robust real-time capabilities and rapid convergence speeds, the application of Kalman filtering to mitigate wind power fluctuations necessitates the establishment of corresponding time update equations (4.11), (4.12), and state update equations (4.13), (4.14), (4.15) [184].

$$P_w(t|t-1) = P_1(t-1|t-1) \tag{4.11}$$

$$P(t|t-1) = P(t-1|t-1) + Q \tag{4.12}$$

$$P_1(t|t) = P_w(t|t-1) + G(t)[P_w(t) - P_w(t-1)] \tag{4.13}$$

$$P(t|t) = [1 - G(t)]P(t|t-1) \tag{4.14}$$

$$G_1(t) = P(t|t-1)/[P(t|t-1) + \delta_1 R] \tag{4.15}$$

In the given equations: $P_w(t|t-1)$ is the prior estimate of wind power at time $t$ based on the previous estimate at time $t-1$; $P_1(t-1|t-1)$ is the wind farm's grid-connected power at time $t-1$; $P(t|t-1)$ is the prior estimate covariance; $\mathrm{P}(t-1|t-1)$ is the covariance of the state estimate at time $t-1$; $P_1(t|t)$ is the grid-connected wind power at

time $t$; $P_w(t)$ is the wind power output at time $t$; $G_1(t)$ is the Kalman filter gain; $Q$ is the process noise covariance. $R$ is the measurement noise covariance. $\delta_1$ represents the correction term for adjusting the Kalman filter gain when obtaining the target power controlled by the supercapacitor in grid-connected applications. In the 1st Kalman filter, the power smoothing focused target of the supercapacitor is determined by:

$$P_{Sc}^0 = P_w(t) - P_1(t|t) \tag{4.16}$$

The $R$ value in the Kalman filter directly influences the target grid-connected power. To achieve the desired effect, a correction term δ is introduced for obtaining the smoothest target curve. Based on the SOC of the energy storage system, timely adjustment commands are made to prevent energy storage overload. When obtaining the smoothest target curve, (4.15) could be modified to:

$$G_2(t) = P(t|t-1)/[P(t|t-1) + \delta_2 R] \tag{4.17}$$

Here, $\delta_2$ represents the correction term for adjusting the 2nd Kalman filter gain when obtaining the smoothest grid-connected target power. The modified equation yields the smoothest grid-connected wind power value as:

$$P_2(t|t) = P_w(t|t-1)G_2(t)[P_w(t) - P_w(t|t-1)] \tag{4.18}$$

Value of δ should be determined while satisfying constraints on active power fluctuations in the power system, considering both the electrical system grid connection and filter limitations. The modified lithium-ion batteries smoothing power target is:

$$P'_{LiB\_S} = P_1(t|t) - P_2(t|t) \tag{4.19}$$

#### *4.3.3.3 Supercapacitor SoC control scheme*

The wind power smoothing strategy based on multiple Kalman filter energy management refers to adjusting the energy storage system's action power at the next time step based on the SOC of the supercapacitor. The multi-objective grid-connected power

aims to smooth wind power fluctuations while improving the SOC of the ESS_P. During system operation, as the SOC of the lithium-ion battery changes, the command for smoothing energy fluctuation adjusts accordingly. This study divides the SOC value of the supercapacitor into three levels, namely $SOC_{high}$, $SOC_{low}$, and $SOC_{LiB}$, representing the upper and lower limits of normal operation.

$$P'_{Sc}(t)=\begin{cases}+\left|P'_{LiB\_s}\right| & SOC_{low}\geq SOC_{Sc}(t)\\ P^{0}_{Sc} & SOC_{low}<SOC_{Sc}(t)<SOC_{high}\\ -\left|P'_{LiB\_s}\right| & SOC_{Sc}(t)\geq SOC_{high}\end{cases} \tag{4.20}$$

During the operation of the *ESS_P*, efforts should be made to control the SOC towards 50% as much as possible to meet the requirements of smoothing fluctuations in future time steps. The power of the ESS_P varies with SOC, and the curve of smoothing wind power fluctuations is depicted in Fig. 4.10. From Fig. 4.10, it can be observed that when the SOC deviates over prolonged periods, real-time adjustments to the target smoothing power can be made to mitigate issues of overcharging or over-discharging in the ESS_P.

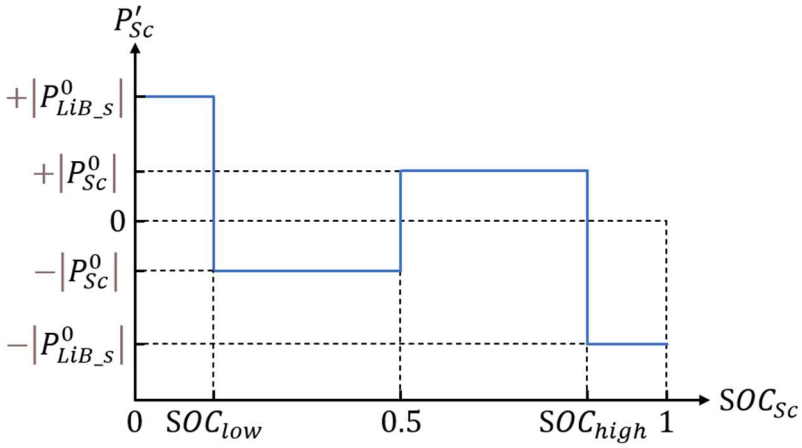


*Fig. 4.10 Kalman filter based supercapacitor energy management strategy*

#### *4.3.3.4 Extension strategy of battery control for enhanced dispatch response*

According to the application objectives of energy storage, the control strategy of the energy storage system can be divided into autonomous mode and scheduling mode. The autonomous mode, as described above, aims to achieve applications that require rapid response, such as short-term power smoothing, frequency and voltage regulation, and power quality compensation. The scheduling mode mainly refers to accepting demands from the upper-level grid system.

Through the analysis in Chapter 3: , it is evident that due to power losses caused by floating structure vibrations, the average wind power of FOWTs is always lower than their theoretical characteristics. Therefore, without additional control design in the HESS, the output power of the floating wind farm after smoothing fluctuations may not match the scheduling commands, and there is no universally effective predictive algorithm quantifying the specific volume of this loss. Hence, an additional control sub-scheme is designed and integrated into the SOC control module to achieve a reduction in the gap between actual wind power and theoretical wind power, or even the scheduled commands, through more efficient utilization of battery SOC.

Therefore, for the power control objective of lithium-ion batteries, in addition to the power smoothing target $P'_{LiB\_s}$ determined by the second Kalman filter as described in (4.19), it is necessary to supplement an additional power control target to bridge the gap between wind power and dispatch targets. The target power $P'_{LiB\_d}$ is determined with the assistance of the third Kalman filter, and the derivation of the equations is provided from (4.21) to (4.24).

$$G_3(t) = P(t|t-1)/[P(t|t-1) + \delta_3 R] \tag{4.21}$$

$$P_3(t|t) = P_w(t|t-1)G_3(t)[P_w(t) - P_w(t|t-1)] \tag{4.22}$$

$$P^0_{LiB\_d} = P_2(t|t) - P_c(t|t) \tag{4.23}$$

$$P'_{LiB\_d} = \eta_d \times P^0_{LiB\_d} \tag{4.24}$$

In this context, $P_c(t|t)$ represents the power dispatch requirement for the current time period; $\eta_d$ is the dispatch coefficient; and $\delta_3$ is the correction term used to adjust the gain of the 3rd Kalman filter when determining the dispatch target power. Clearly, $\delta_3$ will be larger than the values of the previous two filters because the objective of this control is to approach the dispatch command over a longer time interval, while minimizing additional changes in battery power to enhance its lifespan. $\eta_d$ is controlled by the battery SOC to ensure that the SOC remains within the range of 0.2 to 0.8 during battery operation, as shown in Fig. 4.11.

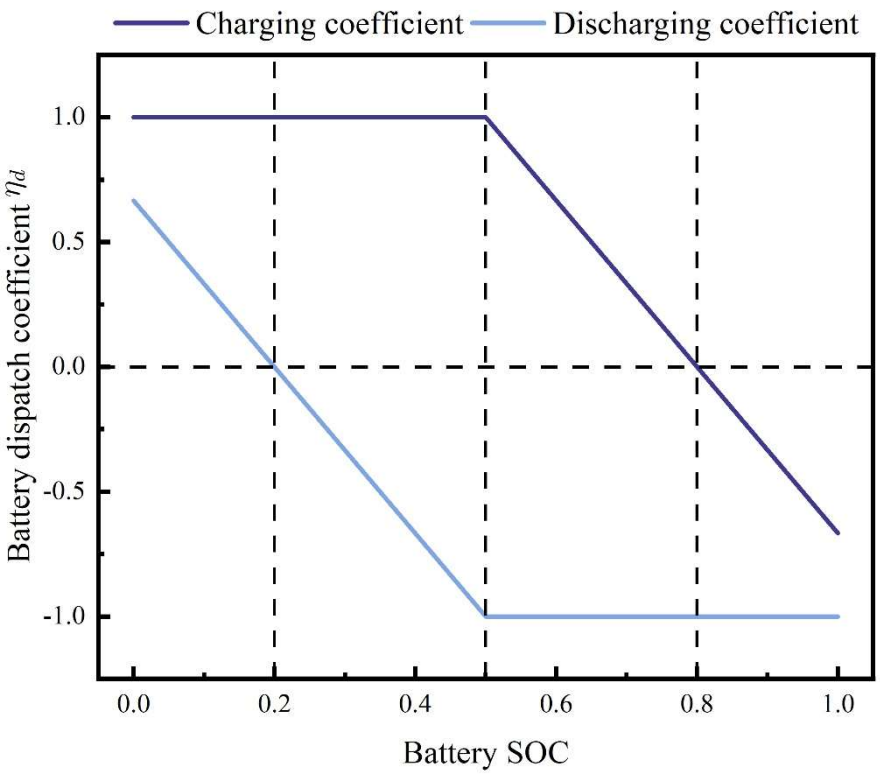


*Fig. 4.11 Battery SOC based dispatch coefficient control*

The actual ESS_E power is determined through the combined influence of power smoothing control summarized in equations (4.19) and response dispatch control as outlined in equations (4.24). It ensures that the battery power does not exceed its rated capacity. This integration is summarized as equation (4.25), and the comprehensive battery control logic is encapsulated in Fig. 4.12.

$$P_{LiB} = \begin{cases} P'_{LiB\_s} + P'_{LiB\_d} \\ |P_{LiB}| \leq P_{LiB\_rated} \end{cases} \tag{4.25}$$

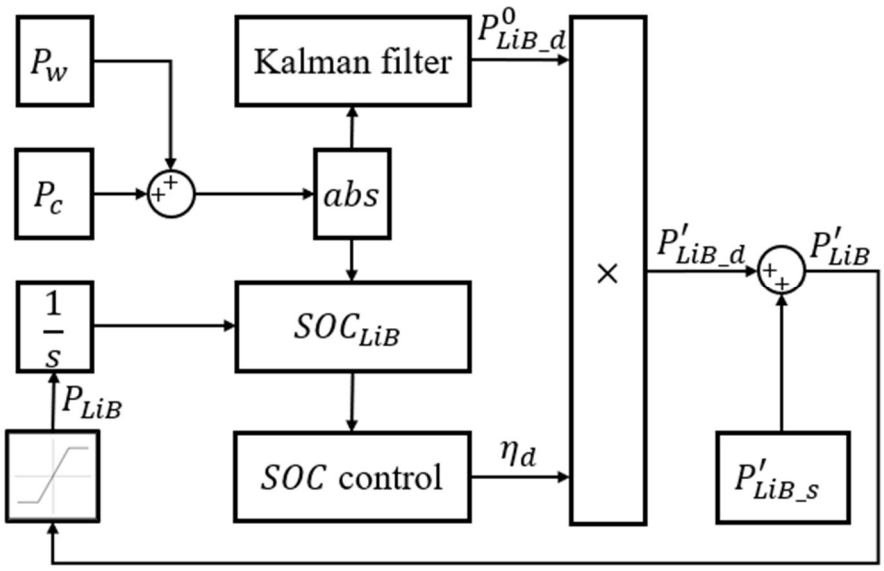


*Fig. 4.12 Complete battery SOC control structure*

## 4.4 Case Study-Based Analysis of HESS Performance

### 4.4.1 HESS property description & Environment preset

To ensure the analysis and discussion of the case study are meaningful and insightful for the actual operation of FOWTs, it's crucial to set up the HESS and simulation environment to closely resemble real-world conditions.

As shown in Table 4.2, the default settings of HESS are derived based on the wind-to-storage capacity ratio established in [175] and calculated using (4.3) to (4.9). It's

worth noting that the rated capacity of the lithium-ion battery is intentionally set to be small. This intentional setting induces more significant variations in battery SOC, allowing for more comprehensive SOC control performance data to be collected within the finite simulation duration. The default parameters of the Kalman filters are determined based on testing experience, with different objectives satisfying the constraint $\delta_3 \ll \delta_1 < \delta_2$.

*Table 4.2 HESS properties for simulation*

| Property | Value |
|---|---|
| Capacity of the type 4 WECS coupled to the HESS (MW) | 5.1 |
| DC link voltage of type 4 WECS (V) | 6,400 |
| Rated voltage of ESS_E (V) | 1,600 |
| Rated voltage of ESS_P (V) | 1,600 |
| $P_{LiB\_rated}$ (MW) | 0.9 |
| $P_{Sc\_rated}$ (MW) | 1.0 |
| Rated capacity of ESS_E (MWh) | 0.225 |
| Rated capacity of ESS_P (MWh) | 0.1 |
| $Q$ of all Kalman filters | 0.05 |
| Default $\delta_1 R$ of the 1st Kalman filter | $2 \times 10^6$ |
| Default $\delta_2 R$ of the 2nd Kalman filter | $11 \times 10^6$ |
| Default $\delta_3 R$ of the 3rd Kalman filter | 10 |

Regarding the operating environment of the WECS and the entire simulation system, it can be described as follows: it simulates the 25-minute performance of the WECS under the rated wind speed and the corresponding severe waves associated with the northeast monsoon in the Taiwan Strait. The initial 500 seconds of the simulation are discarded as they include the step response generated by WECS start-up and the entire system has not yet entered a stable operating state during this time

period. Starting from 500 seconds, the dispatch command is updated every 5 minutes (300 seconds) to simulate a real-time dispatch environment. The relevant parameters are summarized in Table 4.3.

*Table 4.3 Environmental properties of the study case*

| Property | Value |
|---|---|
| Wind model | Tidal |
| Average wind speed (m/s) | 11.4 |
| Wave model | JONSWAP |
| Peak-shape parameter of incident wave spectrum | 2.08 |
| $H_s$ (m) | 5.5 |
| $T_p$ (s) | 9.4 |
| Simulation time (s) | 2000 |
| Effective simulation period (s) | [500: 2000] |
| Power dispatch command update time (s) | [0, 800, 1100, 1400, 1700] |
| Power dispatch command value (MW) | [4.7, 5.0, 4.9, 4.5, 5.1] |

### 4.4.2 Analysis of RTCC Performance

To verify the effectiveness of the designed RTCC scheme for the HESS, this study conducts an analysis and discussion based on the simulation results obtained under the default parameter settings of HESS and the environment provided in 4.4.1. This section focuses more on the overall trends, emphasizing temporal data presentation.

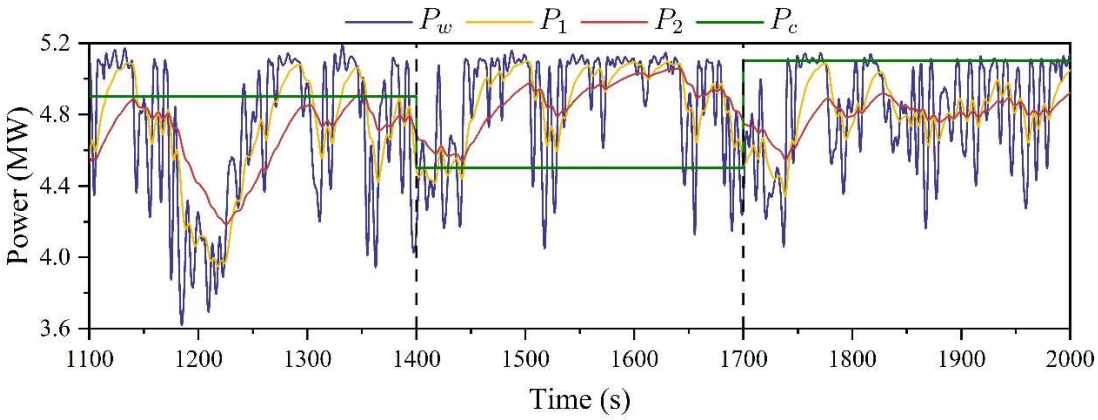


*Fig. 4.13 FOWT power smoothing target determined by RTCC*

Fig. 4.13 illustrates the power targets determined by the RTCC system of HESS. $P_1$ represents the power smoothing target derived after signal processing by the 1st Kalman filter, with the difference between $P_1$ and $P_w$ allocated as control signals to the supercapacitor. $P_2$, on the other hand, represents the optimal power smoothing target derived after signal processing by the 2nd Kalman filter, with the difference between $P_2$ and $P_1$ allocated as control signals to the lithium-ion battery. It is evident that $P_2$ exhibits superior power quality compared to $P_1$, while $P_1$ outperforms $P_w$. Moreover, for the FOWT operating under the rated wind speed model, the smoothest power target $P_2$ determined by the RTCC is lower than the rated power by several hundred kilowatts, demonstrating the significant power loss attributed to the motion of the floating platform.

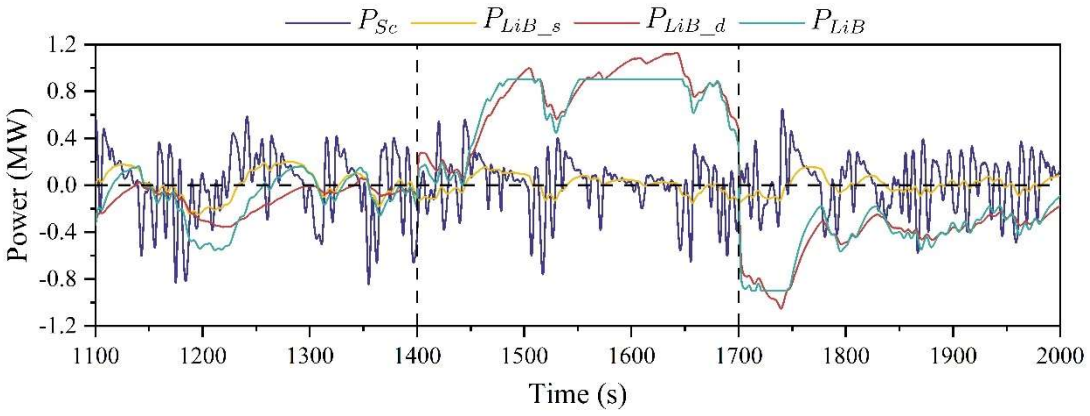


*Fig. 4.14 Power command for HESS by RTCC*

The power commands allocated to the supercapacitor and lithium-ion battery by the RTCC are illustrated in Fig. 4.14, which also includes the sub-targets $P_{LiB\_s}$ and $P_{LiB\_d}$ for the lithium-ion battery. It can be observed that the power smoothing command $P_{Sc}$ and its variation $P_{LiB\_s}$ exhibit rapid changes, with a relatively balanced charge and discharge energy. In contrast, the power dispatch command $P_{LiB\_d}$ for the lithium-ion battery remains relatively stable and consumes more power and energy from the battery compared to $P_{LiB\_s}$. This aligns with the original design intent of the battery operation, which prioritizes compensating for the dispatch gap and, when there is surplus capacity, further enhancing the FOWT power quality already improved by the supercapacitor. For the battery with a rated power of 0.9 MW, it is feasible to achieve the optimal power smoothing dispatch commands for all time periods. Additionally, in the majority of instances, the battery can simultaneously respond to dispatch commands while ensuring the optimal power quality control.

The balanced charge and discharge operation observed in Fig. 4.14 reflects the ease with which power smoothing control can maintain the HESS within a healthy SOC range. However, further analysis of the data is necessary to confirm whether the introduction of dispatch control can effectively restrict the battery SOC within the target range under full RTCC.

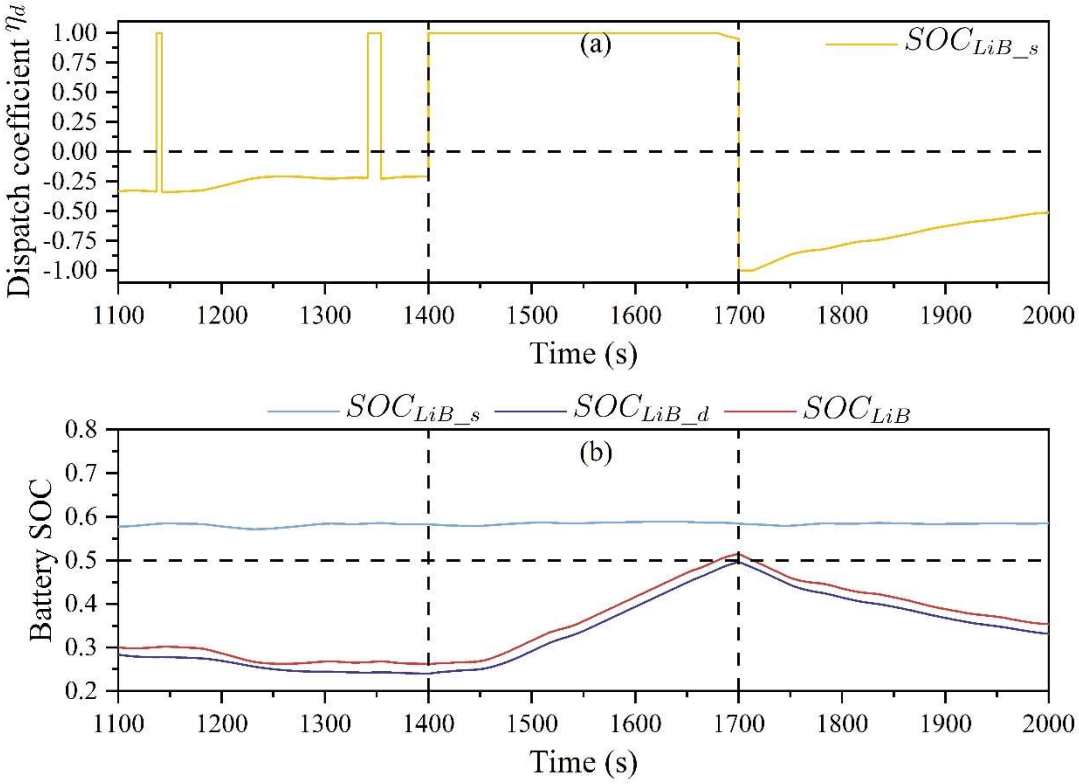


*Fig. 4.15 Battery (a) dispatch coefficient and (b) SOC under default conditions*

As depicted in Fig. 4.15(a), during the initial 1100 seconds of simulation, the wind power output of the FOWT remains persistently below the dispatch command. Consequently, the battery undergoes an extended period of discharge, leading to the battery SOC dropping below 0.3 between 1100 and 1400 seconds. Following the dispatch coefficient control strategy illustrated in Fig. 4.15(b), the absolute value of $\eta_d$ similarly decreases to lower levels, aiming to mitigate the battery's discharge command and ensure that the SOC does not fall below the healthy threshold of 0.2.

In Fig. 4.15(b), $SOC_{LiB\_s}$ solely under the power smoothing commands exhibit remarkable stability. Conversely, the $SOC_{LiB\_d}$, representing the lithium-ion battery's response to dispatch commands, is significantly influenced by grid dispatch instructions. However, when operating under the complete mechanism, the resulting $SOC_{LiB}$ slightly outperforms $SOC_{LiB\_d}$, with a trend highly similar to $SOC_{LiB\_d}$. Upon reaching 1400 seconds,

the FOWT receives a new dispatch from the grid, with the overall wind power exceeding the dispatch command. At this point, the lithium-ion battery can fully respond to the dispatch command by charging itself. Despite the abrupt changes in $\eta_d$ due to the transition between charging and discharging environments, the final control commands are smoothed out through signal processing by the 3rd Kalman filter.

### 4.4.3 Optimal parameter discussion of RTCC

In Section 4.4.2, the analysis of RTCC performance demonstrates its effectiveness and tailored optimization for handling floating wind power. However, in the preceding experiments, RTCC parameters were determined based on empirically derived default settings, leaving potential room for optimization. Clearly, the core variables determining the optimization of RTCC are $\delta_1$, $\delta_2$, and $\delta_3$. These parameters dictate the degree of power smoothing for the three Kalman filters and determine the power commands for HESS. For HESS systems with different properties, the optimization outcomes are likely to vary significantly. Therefore, the experiments and analysis in this section are conducted based on the default properties of HESS.

Through the analysis of the RTCC logic, we can describe the characteristics of these three parameters. A larger $\delta_1$ corresponds to a higher power command for the supercapacitor in RTCC. Under the assumption of a fixed $\delta_1$, a larger $\delta_2$ results in a greater power smoothing command for the lithium-ion battery in RTCC. The parameter $\delta_3$ is associated with the degree of smoothing between $P_2$ and $P_c$. Therefore, adjusting $\delta_1$ is solely aimed at fully utilizing the supercapacitor's capabilities for power smoothing tasks and can be analyzed independently. The relationship between $\delta_2$ and $\delta_3$ determines the multi-objective optimization of the lithium-ion battery for improving power quality and compensating for dispatch gaps. It is essential to find the corresponding optimal range for $\delta_2$ and $\delta_3$.

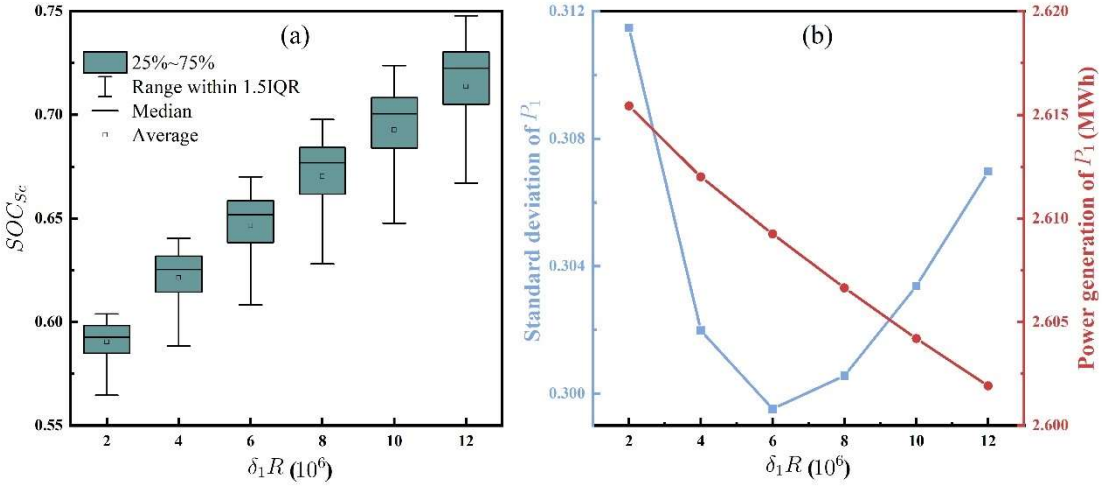


*Fig. 4.16 The impact of changes in $\delta_1$ on (a) supercapacitor SOC,and (b) $P_1$ for RTCC*

As shown in Fig. 4.16, six different values of $\delta_1$ for RTCC are tested and compared. It can be observed that as the value of δ_1 increases gradually, the deviation of the supercapacitor's SOC from 50% and the range of fluctuations also slightly increase. This indicates that a higher $\delta_1$ setting results in larger SOC variations, especially when handling significant power changes associated with wind turbine startup.

Regarding the analysis of the wind power $P_1$ after smoothing with the supercapacitor, it is observed that an increase in $\delta_1$ leads to a decrease in power generation. However, the standard deviation of $P_1$ reaches its minimum value when $\delta_1 R = 6 \times 10^6$, indicating the most reliable and stable performance of $P_1$. Therefore, it can be confirmed that $6 \times 10^6$ is the optimal value, which effectively utilizes the supercapacitor's capacity and achieves the best quality of $P_1$.

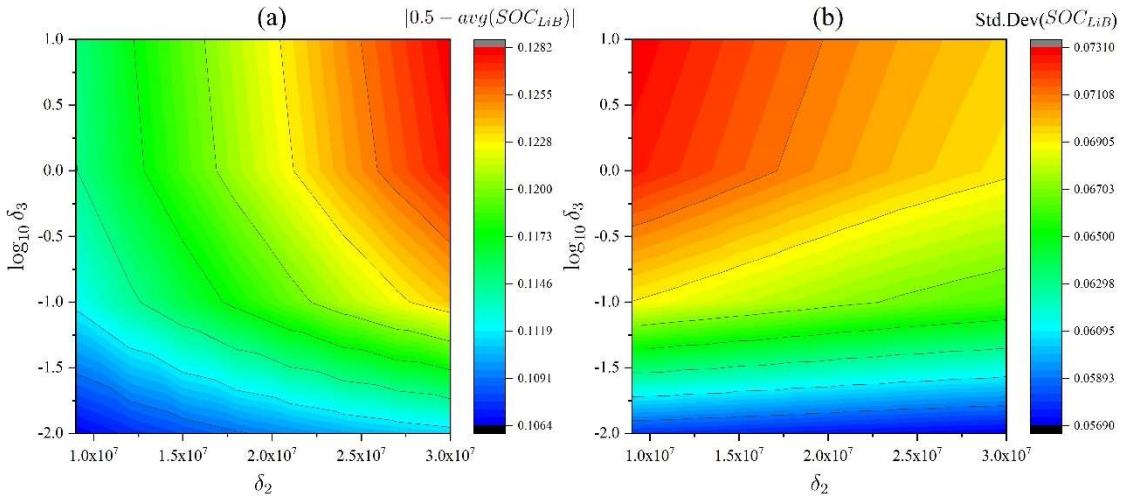


*Fig. 4.17 RTCC performance in battery SOC management, reflected by (a) the average offset of SOC from the midpoint, and (b) the standard deviation of battery SOC*

After simulating data from RTCC based on multiple different delta values, statistical analysis is conducted and presented in Fig. 4.17-Fig. 4.19. Apart from the SOC average value set at a moderate level being optimal in Fig. 4.17(a), all other parameters show that lower numerical values are preferable. Fig. 4.17 focuses on RTCC's management of the battery SOC. It is evident that the SOC offset should both fully exploit its own capacity potential and be reasonably controlled to avoid frequent approaches to the health boundary of SOC. The magnitude of the SOC indicator parameters in Fig. 4.17 is positively correlated with $\delta_3$, implying that a smaller $\delta_3$ value is needed to achieve optimization. A larger $\delta_2$ allows for better utilization of SOC capacity but leads to more drastic changes in the charging and discharging instructions of RTCC, thus reducing the potential battery lifespan.

The performance indicators of output power are statistically analysed in Fig. 4.18, which intuitively reflects the similar trends of $\delta_2$ and $\delta_3$ in affecting the stability of output power and responsiveness to scheduling instructions. Therefore, to obtain more excellent output power, appropriate adjustments to larger $\delta_2$ and smaller $\delta_3$ settings can be made.

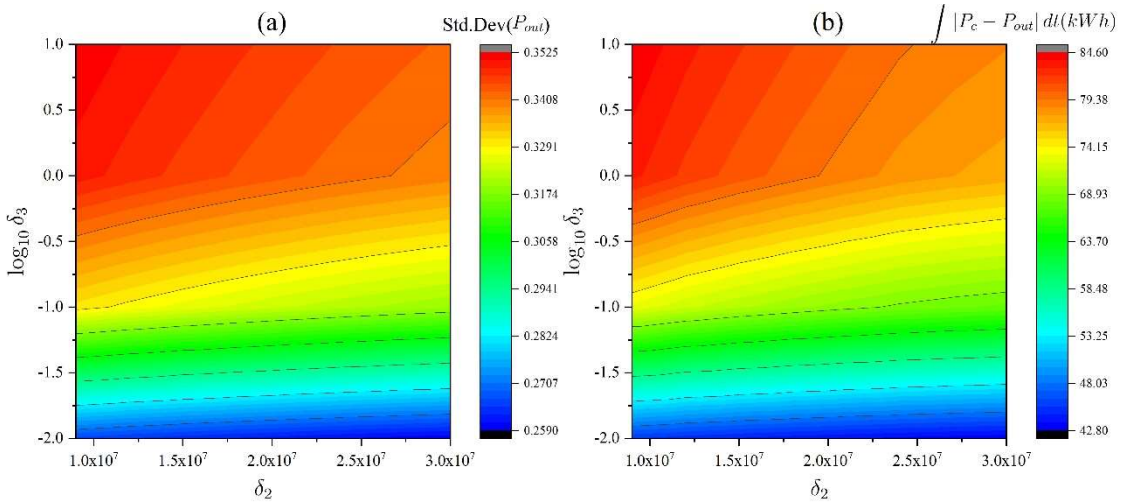


*Fig. 4.18 RTCC performance of output power optimization, reflected by (a) the standard deviation, and (b) the energy difference from the dispatch commands*

Although previous conclusions pointed towards the optimality of smaller $\delta_3$, setting the measurement noise covariance too small can reduce the smoothing level of the instructions output by 3rd Kalman filter to the minimum. Consequently, RTCC fails to effectively manage the step signals generated by the instant updates of scheduling instructions, significantly affecting battery lifespan, as shown in Fig. 4.19(a). At simulation times of 1400s and 1700s, real-time scheduling instruction updates occur. Under the same $\delta_2$ settings, the control signals generated by smaller $\delta_3$ values (black line) exhibit much larger abrupt changes compared to those generated by larger $\delta_3$ values (red line) at these moments. Under the same $\delta_3$ settings, smaller $\delta_2$ values (blue line) further enhance RTCC's ability to respond to step responses. Fig. 4.19(b) reflects the highly correlated relationship between $\delta_3$ and RTCC's step response handling capability, while $\delta_2$ shows a relatively limited influence.

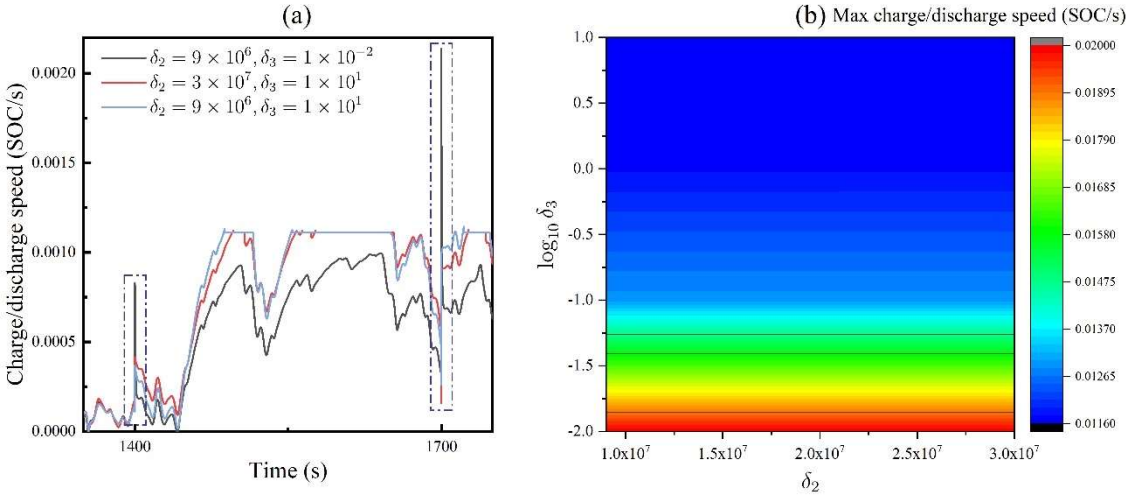


*Fig. 4.19 RTCC performance of responding to dispatch command updates*

It is evident that, considering the comprehensive concerns discussed above, the selection of $\delta_2$ and $\delta_3$ constitutes a multi-objective optimization problem, entailing a range of optimal solutions. Therefore, their specific values should be determined based on the requirements of practical operation.

## 4.5 Conclusion to this chapter

The research is inspired from two significant distinctions between the output power of FOWTs and fixed-bottom counterparts: the notable low-frequency power fluctuations induced by structural oscillations, and the decrease in power generation efficiency compared to traditional wind turbines, leading to greater disparities from dispatch commands.

To tackle these challenges, a tailored bus extension scheme has been devised in this chapter, incorporating a sea wave band stop filter and a HESS under Real-Time Coordinated Control to unleash the maximum potential of energy storage systems and achieve optimal power output. By flexibly adjusting the measurement noise covariance of the Kalman filter, distinct command signals have been successfully separated and allocated

to supercapacitors and lithium batteries, a feat unattainable by conventional low-pass filters due to the extremely low harmonic frequencies of floating wind power. The control of battery charging and discharging not only enhances power quality but also compensates for discrepancies in dispatch commands, with the weights of both aspects adjusted through the measurement noise covariance. RTCC further ensures that the battery SOC stabilizes within a healthy range.

This work fills a gap in the control strategies of HESS coupled with FOWTs and represents a bold exploration of power ramp mitigation strategies for FOWTs. WPREs can be regulated up to 30% of the rated power. A comprehensive analysis and discussion on the settings of Kalman filter parameters have been provided, revealing an optimal solution set for the measurement noise covariance parameters, which is planned for extensive testing and validation in future work.

# Chapter 5: Optimal Control for Enhancing Power Quality in Floating Wind Turbines Integrated with Photovoltaic Solar Farms

## 5.1 Introduction

The mitigation of wind turbine wake effects within a wind power station is achieved through a prescribed inter-turbine spacing criterion, requiring the separation between turbines as 7 times the rotor diameter in the prevailing wind direction [185]. This stipulation not only minimizes the wake interference but also unlocks substantial potential for energy exploitation at wind farm sites. Research [186] indicates that the aggregated power generation potential from diverse sources within the offshore wind farm area can reach sixfold the wind farm's intrinsic capacity. Promising avenues for further development encompass Wave Energy [187], Solar Energy [188], Tidal Energy & Marine Current Energy [189], Ocean Thermal Energy [190], Salinity Gradient Energy [191], etc. As a result, by pursuing enhanced energy utilization within wind farms, a notable reduction in the Levelized Cost of Electricity (LCOE) is achievable [176]. This approach, centred around offshore hybrid power plants primarily harnessing wind energy, effectively mitigates concerns arising from the variability of wind resources, thereby bolstering overall system reliability [19].

While established solutions have emerged for onshore and nearshore wind farms, the comprehensive exploration of this energy potential confronts formidable challenges in the context of offshore floating wind farms, particularly in distant oceanic regions. The commercialization of such ventures is still in its nascent stages. Crucially, the establishment of a dependable and cost-effective platform for floating wind farms, along with seamless integration with external energy sources, stands as a paramount inquiry necessitating comprehensive elucidation.

Two pivotal queries demand rigorous examination: firstly, how can floating wind farms furnish a reliable and economical infrastructure? Secondly, how can external energy

sources be adeptly harnessed to achieve seamless synergy with floating wind energy? These questions underscore the pressing need for additional offshore resource investigation and resolution.

### 5.1.1 Hybrid Potential of Floating Solar Farm

Floating solar farms (FSFs) offer several advantages due to their minimal land footprint, resulting in cost-effectiveness. Their geographical location on the surface of water bodies not only provides a more favourable ambient temperature for photovoltaic panels but also significantly reduces solar light reflection and scattering losses, thereby enhancing energy conversion efficiency. Consequently, the installation scale of floating solar farms has exhibited exponential growth in recent years, with deployment sites expanding from inland lakes to coastal areas. However, especially in offshore deployments, FSFs face challenges related to poor equipment stability and high maintenance costs, requiring further research and technological innovation to overcome these issues [192]. Research outlined in [193] indicates that under conditions of strong winds and waves, power fluctuations in FSFs typically remain within 5% of the rated power, ensuring that FSFs can reliably provide power output under normal environmental conditions. Literature [194] introduces a novel adaptive mooring system that enhances FSF stability by 40% in wave action, while also offering cost advantages. Research presented in literature [195] emphasizes the potential risks of photovoltaic panel submersion or tilting at the perimeter under high wind loads. Meanwhile, central solar panels experience significantly reduced wind load, allowing for modifications to the system materials to manage cost-effectiveness. It is noteworthy that these studies collectively underscore the importance of platform stability, implying that an economically and reliably designed support platform could contribute significantly to the dependable operation of FSFs.

### 5.1.2 Wind-Solar Hybrid Floating Platform Scheme

The integration of onshore wind energy and solar energy is already a highly mature solution. However, recent research suggests that hybrid offshore wind energy and solar energy also exhibit advantages. Literature [196] has found strong complementarity in wind and solar resources in the Belgian North Sea at weekly and monthly timescales. This characteristic is projected to remain stable until the year 2100. In literature [197], a case study in the North Sea region demonstrates the hybrid of offshore floating photovoltaic solar technology into offshore wind farms, resulting in excellent economic viability by maximizing the utilization of grid cable capacity in the wind farm. Despite the emphasized value of offshore wind-solar integration [198], it is noteworthy that the design and operational strategies for this integration remain in a preliminary stage. While [199] offers a planning framework utilizing Particle Swarm Optimization (PSO) for optimizing hybrid offshore wind-solar power plant layouts, it is evident that the hydrodynamic aspects of these power plants have not received comprehensive attention.

As a complement, economically integrating PV panels into existing FOWT is another reasonable proposition, with one of the viable solutions being the utilization of FOWT's floating platforms for installation. The advantages of this approach are manifold: the FSF seamlessly integrates onto the floating platform, incurring minimal integration costs; it enhances power generation capacity while improving overall stability of power output. Among various FOWT floating platform designs, the barge is considered an excellent multi-purpose platform (MPP). It offers cost-effective manufacturing and convenient installation procedures. Furthermore, in comparison to other floating platforms, the ITI Energy Barge demonstrates significant advantages in platform motion-induced ultimate and fatigue loading parameters [69].

Based on this, barge-based floating platforms have undergone extensive testing for various expansion applications. For example, [200] developed a multi-source barge

demonstration platform capable of accommodating three wind turbines and ten Wave Energy Converters (WECs). [201] achieved power fluctuation control by coupling modelling and controlling four Oscillating Water Columns (OWCs) installed on the barge-based FOWT platform. [202] Designed fish cages within the float's moon pool, confirming the superior economic benefits and excellent hydrodynamic characteristics of this MPP. What is particularly intriguing is the design proposed in literature [203] for a new barge structure tailored for 5MW FOWT. The research results ensure that this design, offering a spacious 60m by 45m platform, maintains low cost and reliable dynamic stability comparable to the classic ITI Energy Barge design. Importantly, this additional large platform space holds significant potential for accommodating renewable energy installations, providing ample room for the installation and maintenance of photovoltaic (PV) arrays.

This study draws inspiration from the foundational design principles of an FOWT based on [203]. Leveraging the novel catamaran FOWT model within F2A & MATLAB/Simulink, it further explores the operational states of both the FOWT and the FPV system, seeking potential strategies for their coupled optimal operation. Finally, by integrating a three-dimensional solar azimuth model and a fully detailed electrical–mechanical coupled model, and referencing in-situ data from the Taiwan Strait, including solar radiation, temperature, and wind-wave conditions, a comprehensive real-world operational performance test is conducted. The major innovations of this study can be highlighted and summarized as follows:

The remaining structure of this chapter is as follows: Section 5.2 presents the mathematical modelling principles for FOWT and the theoretical derivation of the three-dimensional FSF model. Section 5.3 provides a brief overview of the model's overall framework and parameter settings, including the acquisition and rationalization of environmental parameters. Section 5.4 discusses the simulation results, with a focus on the

power complementarity effects of the FSF, the general relationship between wind-solar angles and power compensation, and the simulated operational results in the water areas off Penghu. Section 5.5 summarizes the key findings of the entire experiment.

## 5.2 Floating wind-solar platform modelling method

### 5.2.1 Framework description

The wind-solar co-platform design in this study shows a high degree of integration in terms of both dynamics and electrical aspects. As shown in Fig. 5.1, the barge-type floating platform used to support the FOWT was reused as a support for the solar farm. Therefore, the two power sources from wind-solar share a completely consistent dynamic state, as shown in Fig. 5.2.

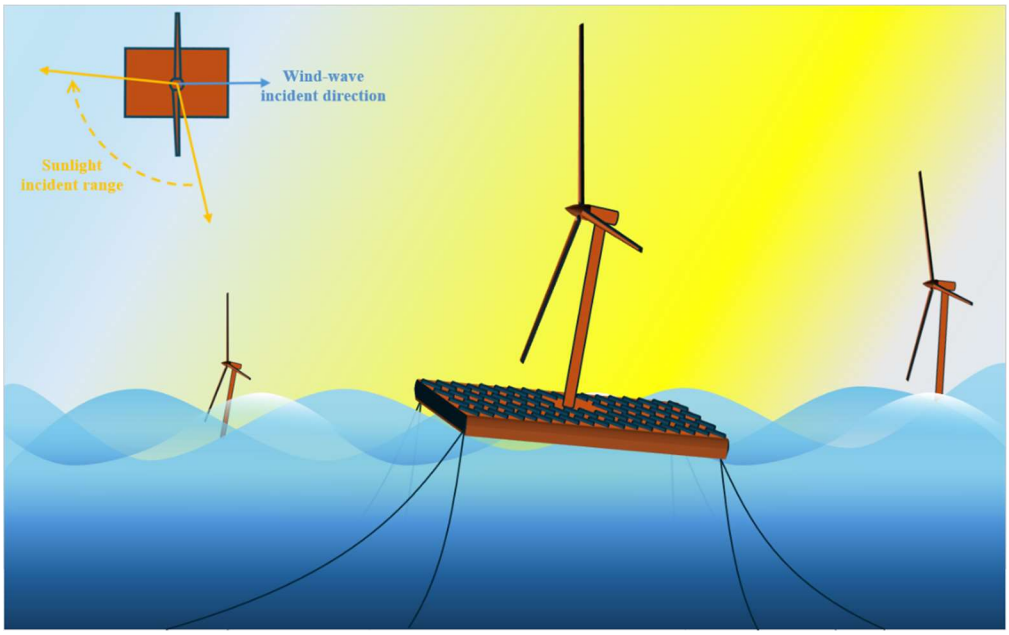


*Fig. 5.1 Schematic diagram of wind-solar co-platform installation*

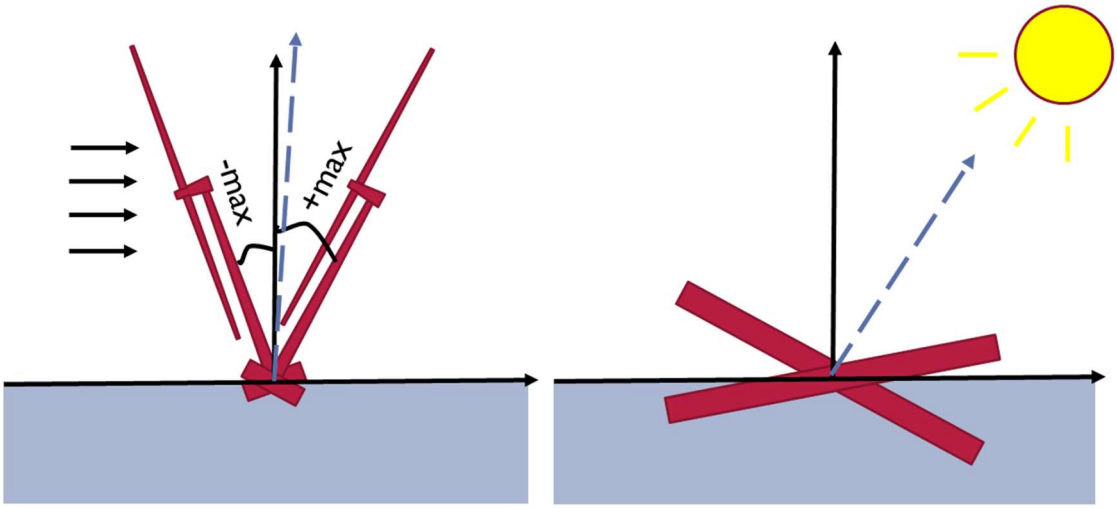


*Fig. 5.2 Schematic diagram of the wind farm and solar farm hydrodynamics*

In addition, the design of the generator for wind turbines uses a permanent magnet synchronous motor with a full-power PWM converter, so that the output of the photoelectric field is directly integrated into the DC side of the FOWT converter after boosting, as shown in Fig. 5.3.

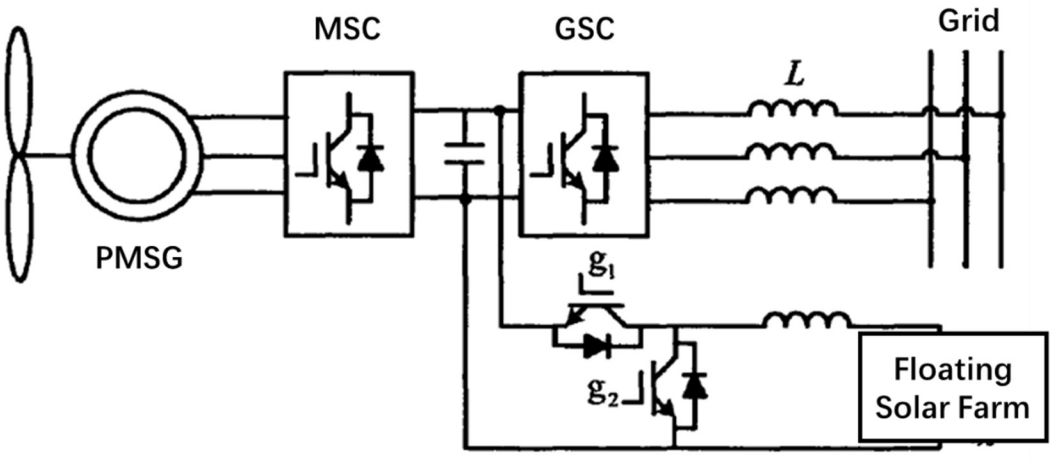


*Fig. 5.3 Schematic diagram of wind-solar electrical coupling*

### 5.2.2 AHSE modelling of FOWT

While FAST stands out as one of the leading computational platforms for AHSE modelling in wind turbines, persuasive simulation experiments often draw upon model cases from the OC projects organized by IEA Wind [67][68][79]. These cases often undergo extensive simulation and actual model testing, confirming and optimizing parameters for hydrodynamic calculations through numerous international collaborative projects. The challenge persists in rationalizing the setup and modification of parameters for innovative designs of floating structures. Hence, for researchers intending to test custom novel floating structures, specialized hydrodynamic computational software such as AQWA remains the optimal choice. AQWA primarily addresses technical challenges faced in the design analysis of floating systems in North Sea oil and gas development, and even broader aspects of global offshore oil and gas development, including navigation, installation, operations, positioning, and more. AQWA enables the modelling of various connecting components such as mooring cables, hinges, fenders, winches, pulleys, tension tendons, facilitating intricate analyses of mooring and installation [204].

Dr. Yang Yang implemented the coupling of aerodynamic, servo-elastic behaviour with platform motion for floating wind turbines in AQWA through the user_force64.dll in March 2020, thus achieving the coupling of FAST with AQWA in the time domain, termed FAST2AQWA or simply F2A [86].

### 5.2.3 WECS modelling of FOWT

The WECS model established in this chapter adopts the design of a Type-4 wind turbine generator from Chapter 3. Due to the utilization of the FAST and AQWA models occupying the DLL ports, coupling between the mechanical and electrical components of the catamaran FOWT in this study was not achieved. However, for steady-state operational environments, this decoupling does not result in the loss of simulation data accuracy. The

generator angular speed, platform pitch angle, and platform roll angle obtained from the F2A platform's AHSE model computations are stored and utilized as temporal inputs in running the WECS simulation model established in FAST/Simulink.

### 5.2.4 Solar azimuth modelling

Based on the modelling in reference [205], originally used for computing the orientation of spacecraft in near-Earth space relative to the Sun, this theoretical calculation maintains perfect precision from 1950 to 2050. It guarantees angular errors within 1/60 degree and time errors less than 3.5 seconds. Therefore, the study here applies this theory to precisely calculate the solar azimuth angle on the Earth's ocean surface in FSFs. Hence, the observer's coordinate system located in the FSF could be established:

$$n = -1.5 + 365 \cdot (Y_{in} - 2000) + N_{leap} + Day + Day_{frac\_UT} \tag{5.1}$$

$$L = 280.466 + 0.9856474n \ (°) \tag{5.2}$$

$$g = 357.528 + 0.9856003n \ (°) \tag{5.3}$$

$$\lambda = L + 1.915\, sin\, g + 0.020\, sin(2g) \ (°) \tag{5.4}$$

$$\varepsilon = 23.440 + 0.0000004n \ (°) \tag{5.5}$$

$$\alpha = tan^{-1}(cos\, \varepsilon\, tan\, \lambda) \cdot 180/\pi \ (°) \tag{5.6}$$

$$\delta = sin^{-1}(sin\, \varepsilon\, sin\, \lambda) \cdot 180/\pi \ (°) \tag{5.7}$$

$$E_{min} = 4 \cdot (L - \alpha) \ (min) \tag{5.8}$$

where $Y_{in}$ represents the input year, $N_{leap}$ is the number of leap years in the time period from 1950 to the input year, $\alpha$ is the right ascension, $\delta$ is the declination of the Sun, and $E_{min}$ is the equation of time. It must be emphasized that only $L$, $g$, and $\lambda$ need to be adjusted within the $[0°, 360°]$ range during the calculation process to obtain accurate results.

Next, based on the observer's coordinate system, the components of the solar azimuth angle in the spatial coordinate axes can be derived as follows:

$$\varphi_s = \delta \tag{5.9}$$

$$\lambda_s = -15 \cdot (T_{GMT} - 12 + E_{min}/60) \tag{5.10}$$

$$S_x = cos\,\varphi_s\, sin(\lambda_s - \lambda_0) \tag{5.11}$$

$$S_y = cos\,\varphi_0\, sin\,\varphi_s - sin\,\varphi_0\, cos\,\varphi_s\, cos(\lambda_s - \lambda_0) \tag{5.12}$$

$$S_z = sin\,\varphi_0\, sin\,\varphi_s + cos\,\varphi_0\, cos\,\varphi_s\, cos(\lambda_s - \lambda_0) \tag{5.13}$$

In this context, $(\varphi_0, \lambda_0)$ represents the observer's longitude and latitude on Earth, while $(\varphi_s, \lambda_s)$ represents the longitude and latitude of the subpoint. Since $S$ is the unit vector for the solar azimuth angle, it is evident that $S_x^2 + S_y^2 + S_z^2 = 1$. Consequently, the South-Clockwise converted azimuth angle $\gamma_s$ and zenith angle Z can be derived as follows:

$$\gamma_s = atan2(-S_x, -S_y) \tag{5.14}$$

$$Z = cos^{-1} S_z \tag{5.15}$$

The $atan2$ function is also available in Simulink and outputs values within the range of $[-\pi, \pi]$. For the North-Clockwise calculation, it needs to be adjusted as $\gamma_s = atan2(S_x, S_y)$, whereas for the East-Clockwise calculation, it needs to be adjusted as $\gamma_s = atan2(S_y, S_x)$.

### 5.2.5 Solar farm modelling

The influence of the floating platform movement on the light-receiving area of the PV panel is very complicated. In order to quantify this change, the PV panel is projected on the three planes composed of the coordinate axes, and the effect is shown in Fig. 5.5.

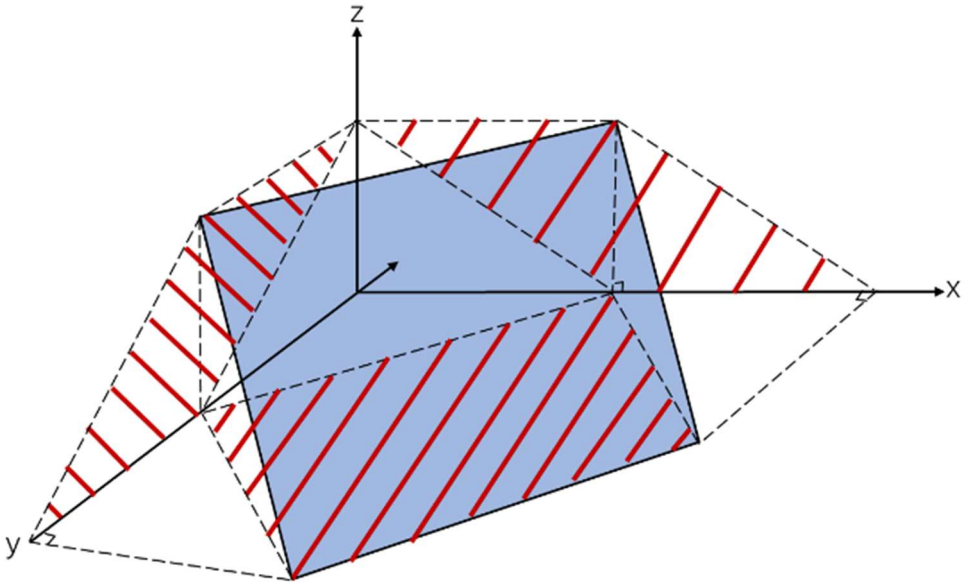


*Fig. 5.4 Projection of PV panels on three coordinate axis planes*

At the same time, the incident direct irradiation vector is also decomposed into components $B_x$, $B_y$ and $B_z$ parallel to the three coordinate axes in the same coordinate system according to requirements. Based on Fig. 5.5, dimensionality reduction of sunlight direct irradiation can be completed:

$$B_x = G(b) \cdot cos\,\theta_h\, sin\,\theta_{ay} \tag{5.16}$$

$$B_y = G(b) \cdot cos\,\theta_h\, cos\,\theta_{ay} \tag{5.17}$$

$$B_z = G(b) \cdot sin\,\theta_h = G(b) \cdot cos\,\theta_z \tag{5.18}$$

$\theta_{ay}$ is azimuth angle to y axis, $\theta_h$ is altitude angle and G(b) represents direct solar irradiation.

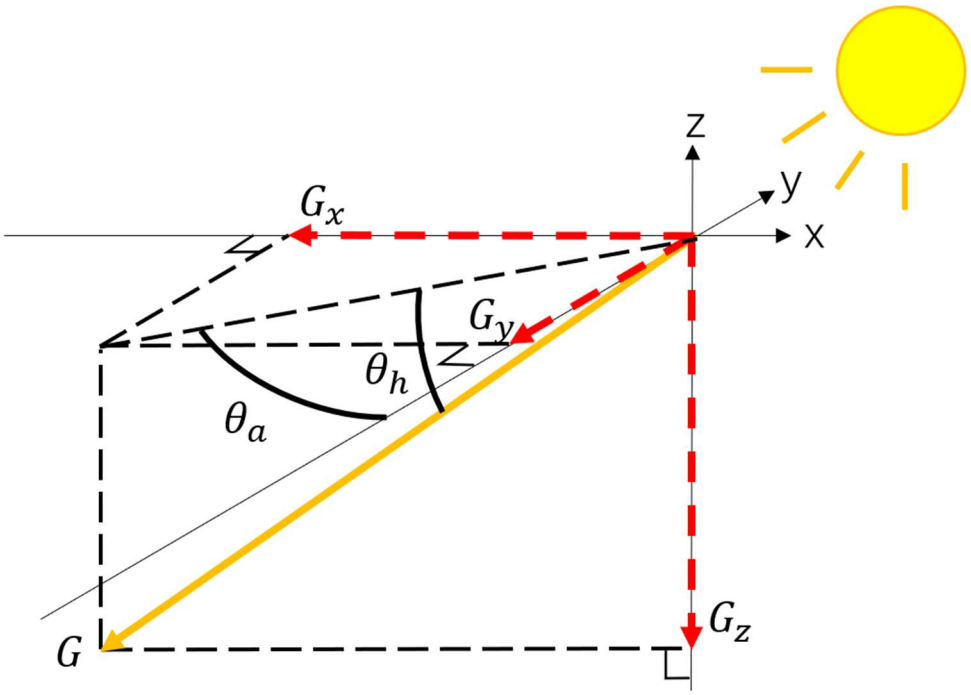


*Fig. 5.5 Projection of sunlight direct irradiation on the coordinate axes*

For a photovoltaic panel fixed on a floating platform, a three-dimensional coordinate system ($xyz$) is established with the floating platform as the reference. The light-receiving surface of the photovoltaic panel is equivalently represented as its projected areas on the various coordinate planes: $S_{xy}$, $S_{yz}$ and $S_{xz}$, as it shown in Fig. 5.4. This approach facilitates the intuitive derivation and calculation of the solar irradiance received by the photovoltaic panel on the floating platform during pitch and roll movements.

Next, as shown in Fig. 5.6, statistics are performed on the three projections. It can be found that the projected areas of the x-z and y-z planes are only affected by the motion of one degree of freedom, and the changes in the projected areas of the x-y plane are directly related to the cosine values of the pitch and roll angles.

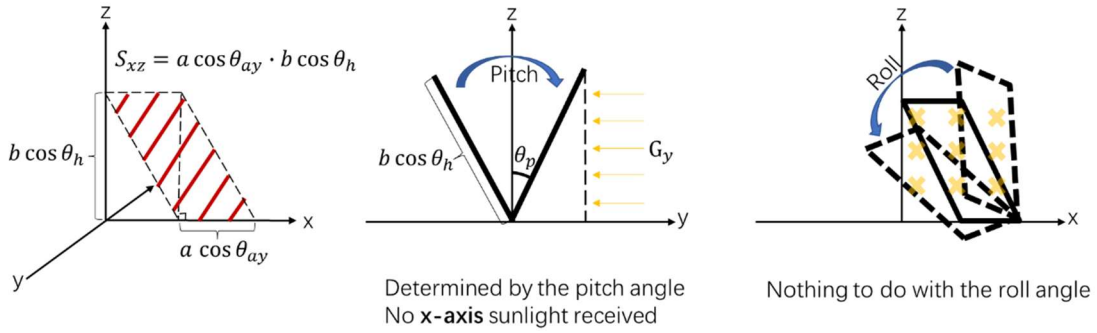


(a) PV equivalent model in x-z plane

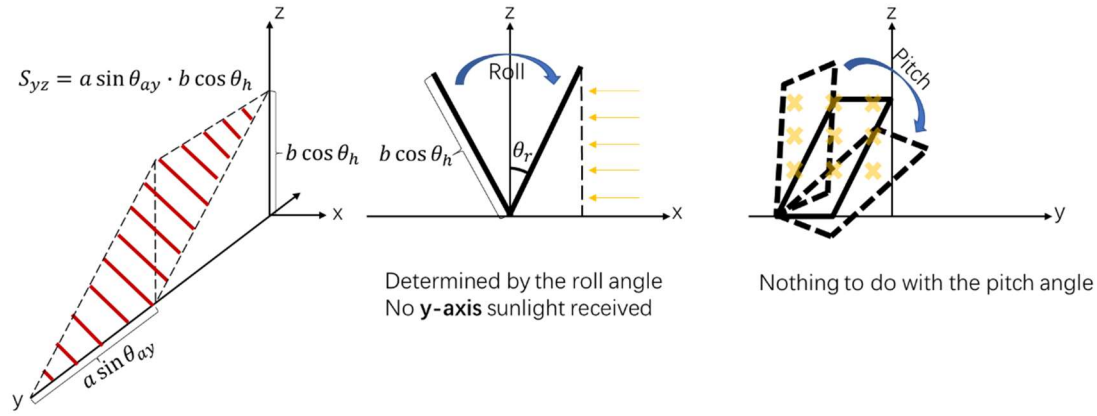


(b) PV equivalent model in y-z plane

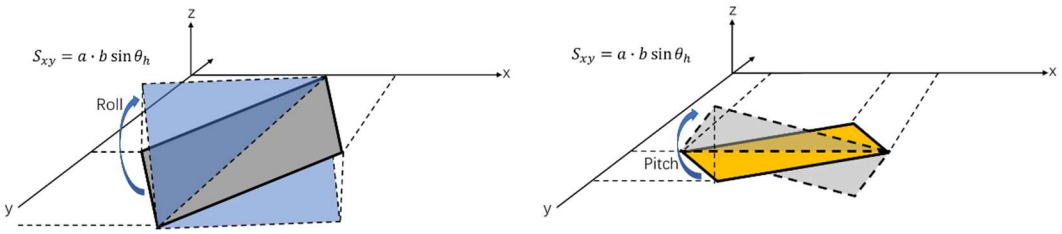


*Fig. 5.6 Direct solar energy absorbed by the equivalent projected area of the photovoltaic panel during the movement of the floating platform*

Ultimately, the PV equivalent area is the sum of the projected areas on the three coordinate system planes. The calculation formula of x-z, y-z, x-y plane projected areas are as follows:

$$S_{xz} = a\cos\theta_{ay} \cdot b\cos\theta_h \tag{5.19}$$

$$S_{yz} = a\sin\theta_{ay} \cdot b\cos\theta_h \tag{5.20}$$

$$S_{xy} = a \cdot b\sin\theta_h \tag{5.21}$$

Direct solar power of these 3 projected areas of the PV panel thus can be calculated:

$$P_{bxz} = S_{xz} \cdot \cos\theta_p \cdot B_y \tag{5.22}$$

$$P_{byz} = S_{yz} \cdot \cos\theta_r \cdot B_x \tag{5.23}$$

$$P_{bxy} = S_{xy} \cdot \cos\theta_r \cos\theta_p \cdot B_z \tag{5.24}$$

Substitute (5.16)-(5.21) into (5.22)-(5.24), then direct solar energy of the PV panel during the movement of the floating platform $P_{pv\_b}$ is derived:

$$P_{xz} = a\cos\theta_{ay} \cdot b\cos\theta_h \cos\theta_p \cdot B_y \tag{5.25}$$

$$P_{yz} = a\sin\theta_{ay} \cdot b\cos\theta_h \cos\theta_r \cdot B_x \tag{5.26}$$

$$P_{xy} = a \cdot b\sin\theta_h \cdot \cos\theta_r \cos\theta_p \cdot B_z \tag{5.27}$$

$$P_{pv\_b} = P_{bxz} + P_{byz} + P_{bxy} \tag{5.28}$$

The computation of diffuse irradiation $D_{pv}$ and reflectance irradiation $R_{pv}$ references the Isotropic sky model, which provides an accurate overall description of illumination levels [206]. It is noted that the Isotropic sky model tends to underestimate the irradiance in cases of clear skies and partially overcast conditions, particularly where there is heightened intensity near the horizon and within the circumsolar region of the sky.

$$Z_s' = \frac{\pi}{2} - (H_s - \theta_p \sin\theta_{ay} - \theta_r \cos\theta_{ay}) \tag{5.29}$$

$$D_{pv} = \frac{1+\cos Z_s'}{2} G(d) \tag{5.30}$$

$$R_{pv} = \frac{1-cos\ \ {}'_s}{2}\rho_a G(r) \tag{5.31}$$

where $\rho_a$ is the reflection coefficient, which is recommended to be set to 0.06 within the offshore ocean surface [207]. Thus, the diffuse power and reflectance power received by a single PV panel are:

$$P_{pv\_d} = a \cdot b \cdot D_{pv} \tag{5.32}$$

$$P_{pv\_r} = a \cdot b \cdot R_{pv} \tag{5.33}$$

Finally, total irradiance power received by a PV panel on the FOWT is:

$$P_{pv} = P_{pv\_b} + P_{pv\_d} + P_{pv\_r} \tag{5.34}$$

### 5.2.6 Tilt angle control Mode 1: Optimizing solar energy harvesting

To optimize the photovoltaic system's power production on the floating platform, it is imperative to statistically assess the average orientation of the platform's rotational movement and align the photovoltaic panels accordingly to maximize direct sunlight irradiance. To achieve this, a proposed methodology involves utilizing the Kalman Filter module within Simulink to compute the dynamic average values of platform pitch and roll measurements derived from AQWA-FAST outputs. Subsequently, aligning the photovoltaic panels to the sun is intended under this averaged platform state. However, a significant challenge arises in determining the actual setting of the photovoltaic tilt angle in the floating platform's $x''y''z''$ coordinate system as shown in Fig. 5.7, given the known fixed space $xyz$ coordinate system where the photovoltaic system's tilt angle corresponds to the solar elevation angle. This challenge constitutes the primary focus of this section.

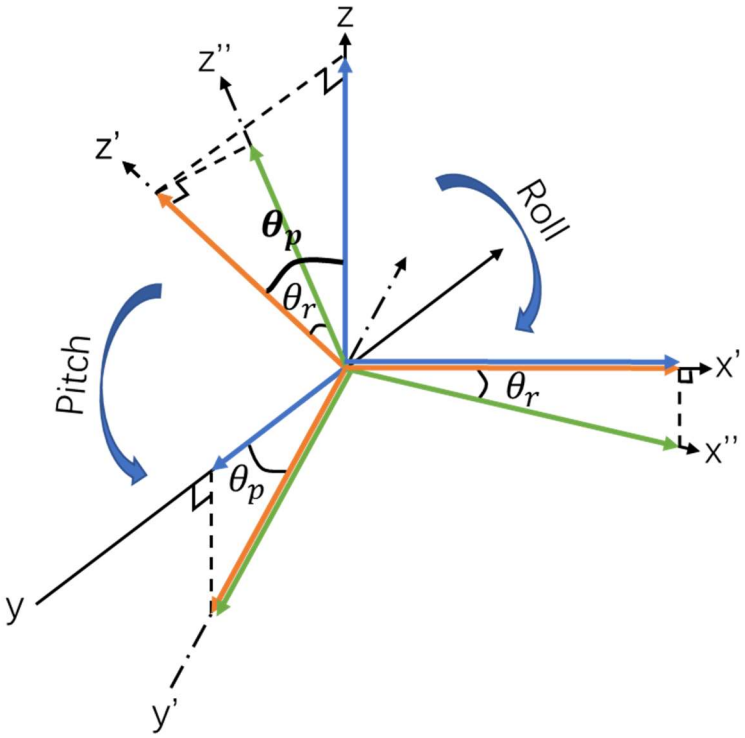


*Fig. 5.7 The relationship between the space coordinate system of the floating platform coordinate system*

Fig. 5.7 demonstrates the relationship between the floating platform coordinate system in motion and the fixed space coordinate system. Obviously the two coordinate systems coincide exactly when there is no pitch and roll motion. Therefore, the corresponding solar intensity received by each axis of the PV panel on the $xyz$ plane and the $x''y''z''$ plane is:

$$PV_x = 1 \cdot cos\,\theta_h\, sin\,\theta_{ay} \tag{5.35}$$

$$PV_y = 1 \cdot cos\,\theta_h\, cos\,\theta_{ay} \tag{5.36}$$

$$PV_z = 1 \cdot sin\,\theta_h \tag{5.37}$$

$$PV_x'' = 1 \cdot cos\,\theta_h''\, sin\,\theta_{ay}'' \tag{5.38}$$

$$PV_y'' = 1 \cdot cos\,\theta_h''\, cos\,\theta_{ay}'' \tag{5.39}$$

$$PV_z'' = 1 \cdot sin\,\theta_h'' \tag{5.40}$$

$\theta_h''$ and $\theta_{ay}''$ are equivalent height and azimuth angle on x-y-z axis. Then the PV elevation angle conversion in the two coordinate systems is as follows:

$$PV_x'' = PV_x \cdot cos\,\theta_p \tag{5.41}$$

$$PV_y'' = PV_y \cdot cos\,\theta_r \tag{5.42}$$

$$PV_z'' = PV_z \cdot cos\,\theta_r\, cos\,\theta_p \tag{5.43}$$

Substituting (5.35)-(5.40) into (5.41)-(5.43), they can be further deduced:

$$cos\,\theta_r\, sin(\overrightarrow{\theta_{ay}''} + \overrightarrow{\theta_r} + \overrightarrow{\theta_p}) = sin\,\theta_{ay} \tag{5.44}$$

$$cos\,\theta_p\, cos(\overrightarrow{\theta_{ay}''} + \overrightarrow{\theta_r} + \overrightarrow{\theta_p}) = cos\,\theta_{ay} \tag{5.45}$$

$$sin(\overrightarrow{\theta_h''} + \overrightarrow{\theta_r} + \overrightarrow{\theta_p}) = sin\,\theta_h \cdot cos\,\theta_r\, cos\,\theta_p \tag{5.46}$$

Divide (5.44) and (5.45), then target azimuth and height angle are:

$$\begin{cases} tan(\overrightarrow{\theta_{ay}''} + \overrightarrow{\theta_r} + \overrightarrow{\theta_p}) = (\frac{cos\,\theta_p}{cos\,\theta_r}) \cdot\ tan\,\theta_{ay} \\ sin(\overrightarrow{\theta_h''} + \overrightarrow{\theta_r} + \overrightarrow{\theta_p}) = (cos\,\theta_r\, cos\,\theta_p) \cdot sin\,\theta_h \end{cases} \tag{5.47}$$

The actual tilt angle to be set for the photovoltaic panels to directly face the sun at specific inclined states of the platform is computed through the coordinate system transformation, defined as *Mode 1* scheme. The pivotal formula (5.47) stands as the crux of the 'Coordinate system transformation' submodule. Fig. 5.8 illustrates the comprehensive flowchart depicting the computation process for determining the optimal tilt angle for maximizing power production (*Mode 1*) of the photovoltaic panels with dual-axis tracking system. Additionally, it should be noted that the speed of change for dual-axis tracking systems should be limited to no more than $0.5°/s$.

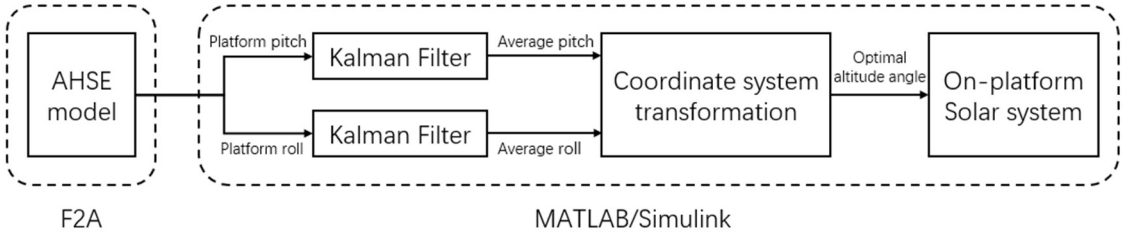


*Fig. 5.8 Optimal photovoltaic panel altitude angle calculation process*

### 5.2.7 Tilt angle control Mode 2: Enhancing hybrid power quality

Based on a comprehensive examination of the active power characteristics of FOWT in reference [33], it is evident that the motion of the floating platform, particularly pitch motion, induces significant wind power ramp events (WPREs), with the amplitude increasing with the height of the waves. Considering the 'Pitch Angle-Power' characteristics of WECS and the solar energy system, a design strategy controlling the photovoltaic tilt angle is proposed to achieve the complementarity between wind power and solar power during the pitch motion of the floating platform, thereby enhancing the overall power quality of the Wind-Solar system. This approach is herein referred to as the *Mode 2* scheme.

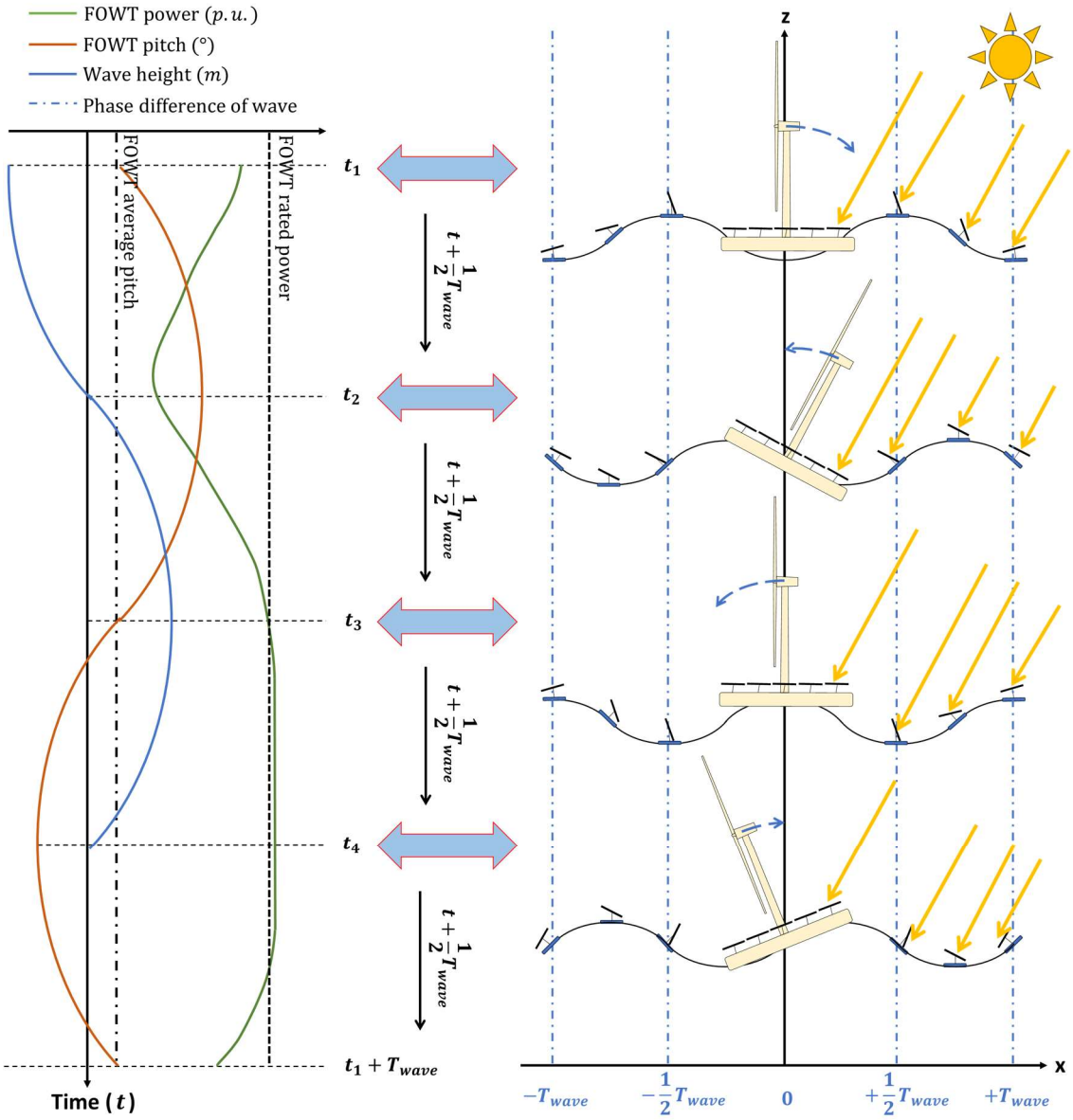


*Fig. 5.9 Illustration of optimal hybrid power quality scheme*

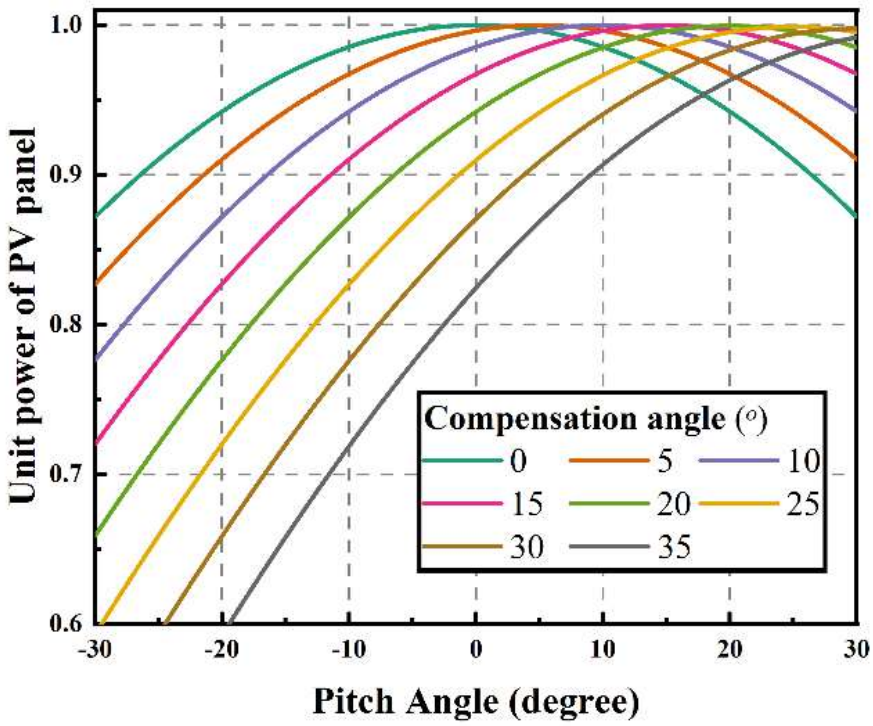


*Fig. 5.10 Pitch angle-PV power characteristics under different tilt angle offset settings*

The visual representation of this approach is illustrated in Fig. 5.9, providing an intuitive depiction of the power characteristics influenced by the dynamics (pitch motion) of both the wind and solar systems. On one hand, as demonstrated in Section 3.5, within the pitch motion range of the FOWT, there is a negative correlation between pitch angle and wind power. On the other hand, as depicted in Fig. 5.10, the shape of the photovoltaic system's pitch angle-power characteristic curve, derived from the formula in 5.2.5, closely resembles the upper half of a cosine function within a single period. By adjusting the photovoltaic panel tilt angle, the power curve can be 'horizontally shifted' along the x-axis. The "optimal hybrid power quality" scheme is achieved by moving the pitch angle-power characteristic curve of the solar energy system to the right in Fig. 5.10, establishing an overall positive correlation between pitch angle and solar power within the pitch motion

range of the FOWT. This can be achieved by adding a optimal offset angle to the optimal PV tilt angle. The electricity generation performance under this mode is depicted in Fig. 5.9, where the wind and solar power exhibit an inverse relationship during pitch motion, reflecting a decrease in wind power and an increase in solar power as the pitch angle increases, and vice versa when the pitch angle decreases on the novel catamaran floating platform.

Due to the dynamic variations in the pitch and roll motion ranges of the floating platform during actual operations, the proposal of a real-time coordinated control scheme faces challenges. Therefore, the setting of offset angles will be fixed and selected prior to simulation. The offset angles are all greater than 15 degrees, ensuring an overall positive correlation between the pitch angle and power of the solar energy system. Additionally, the configuration of this scheme, actively deviating the photovoltaic panels from their optimal angles, evidently leads to a certain loss in their power generation efficiency. Under this scheme, the optimal offset angle, considering both efficiency and performance, will be comprehensively analysed and discussed through comparative testing with a series of angle values.

## 5.3 Model Test Set-up

### 5.3.1 The Novel Catamaran FOWT testing through FAST-AQWA (F2A)

The novel catamaran model developed based on F2A serves as the foundation for this research. Detailed dynamic characteristics have been validated in [203]. Compared to the ITI Energy barge FOWT, the novel catamaran FOWT exhibits reduced pitch angle oscillations in mild sea states while showcasing similar pitch angle fluctuations in high sea states. Specific parameters of this floating structure and ITI Energy barge are summarized in Table 5.1.

*Table 5.1 Comparison of floating platform properties*

| Properties | Catamaran | ITI Energy Barge |
|---|---|---|
| **Platform** | | |
| Diameter ($m \times m$) | $45 \times 60$ | $40 \times 40$ |
| Space between demi-hulls ($m$) | 25 | – |
| Draught ($m$) | 4 | 4 |
| Total volume ($m^3$) | 15,684 | 16,000 |
| Water displacement ($m^3$) | 5,480 | 6,400 |
| Mass ($kg$) | 4,901,080 | 5,452,000 |
| CM Location ($m$) | (0,0,1.51) | $(0,0,-0.2818)$ |
| Roll inertia about CM ($kg \cdot m^2$) | 4,672,683,194 | 726,900,000 |
| Pitch inertia about CM ($kg \cdot m^2$) | 6,800,310,371 | 726,900,000 |
| Yaw inertia about CM ($kg \cdot m^2$) | 11,190,569,096 | 1,454,000,000 |
| **Mooring System** | | |
| Number of mooring lines | 8 | 8 |
| Depth to fairleads and anchors ($m$) | 4 & 150 | 4 & 150 |
| Radius to fairleads and anchors ($m$) | 42.436, 429.095 & 439.566 | 28.28 & 423.4 |
| Section length ($m$) | 474.1 | 473.4 |
| Mooring line diameter ($m$) | 0.0809 | 0.0809 |
| Line Mass Density ($kg/m$) | 130.4 | 130.4 |
| Line extensional stiffness, EA ($N$) | 589,000,000 | 589,000,000 |

### 5.3.2 Solar farm modelling and coupling with FOWT through FAST-Simulink

The overall framework of the FSF sub-model, as depicted in Fig. 5.11, encompasses a comprehensive solar angle model, a coordinate system conversion module, an equivalent solar area calculation module, an electrical model, and a PV angle control module. FSF, coupled with the Type-4 WECS, operates in parallel via a common DC bus, effectively integrating wind and solar energy sources to provide a unified output. The integrated model simulation is executed through the joint operation of MATLAB/SIMULINK and FAST

software and shown in Fig. 5.11. This simulation process requires five types of input data: (i) weather conditions associated with the FOWT, including wind speeds and wave characteristics, (ii) weather conditions relevant to the FSF, such as irradiance and temperature, (iii) the tilt angles of photovoltaic panels set for power complementarity mode, (iv) PV panel data, and (v) FSF attributes based on the barge floating platform. These data types are discussed in detail below.

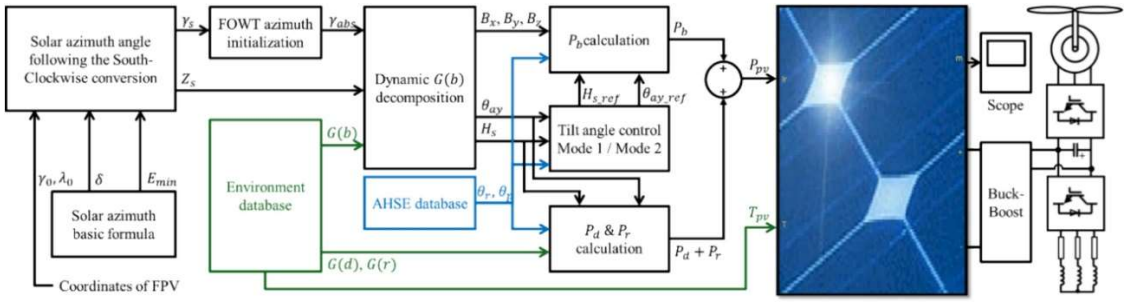


*Fig. 5.11 Model Framework in Simulink*

### 5.3.3 Targeted experimental environment conditions

To begin with, the overall simulation environment is established in the Taiwan Strait, a region renowned for its abundant wind and light resources, along with stable wind patterns, aligning closely with the requirement of having wind and wave directions coinciding. The selected simulation location represents the deepwater area of the Taiwan Strait, situated offshore of Penghu Island, and all specific environmental configuration parameters are sourced from literature and empirical case studies conducted in this maritime region. Furthermore, the high-quality caisson manufacturing expertise available on both sides of the Taiwan Strait has significantly lowered the production costs of domestic floating barge bodies, presenting a substantial competitive advantage [208]. In the following, five important aspects (i to v) of assumptions, data input sources and cases are considered:

(i) The wind-wave load case for this study, as referenced in [33], is based on the environmental conditions of normal, northeast monsoon, and 10-year return period western

Taiwan offshore scenarios. In FAST, it is configured as input data, specifically turbulent wind and Pierson-Moskowitz waves. This setup typically considered a once-in-a-year wind-wave condition in experimental settings, effectively tests the offset angle effects of the floating solar farm under various DoF states of the floating platform, with a particular focus on pitch motion.

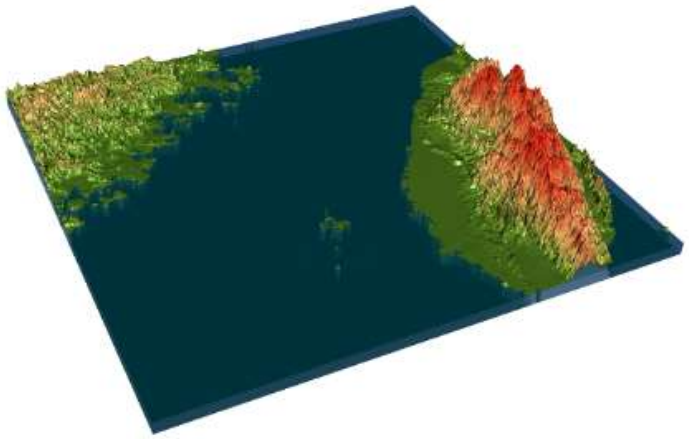

(a) Taiwan Strait topography

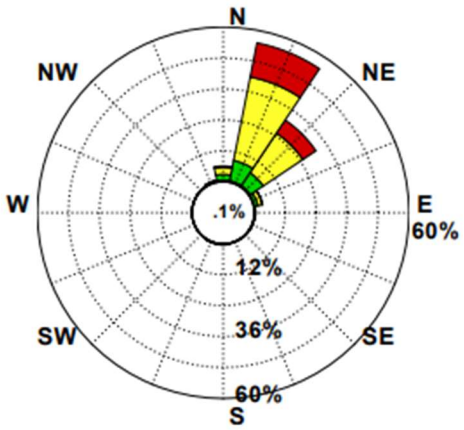


(b) wind rose diagram of Penghu

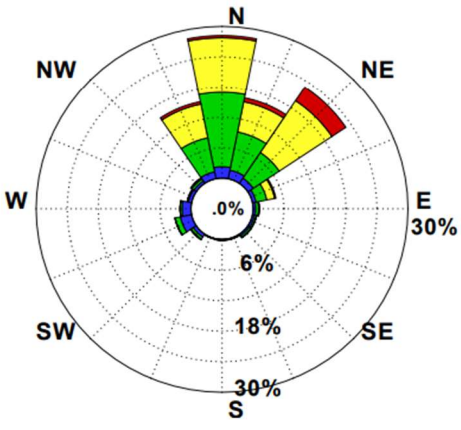


(c) wave rose diagram of Penghu

*Fig. 5.12 Taiwan Strait environmental characteristics, including (a) topography, rose diagram of (b) wind and (c) wave in summer*

The wind and wave directions are determined using data from the local department's annual statistics for the summer of 2019 [209]. As illustrated in Fig. 5.12(a), due to the geographic location of the water body in the strait, the statistical data in Fig. 5.12(b) and Fig. 5.12(c) indicate that the wind and wave directions are closely aligned during that period, creating an ideal scenario of co-incident wind and waves. Hence, in the subsequent research, the wind-wave direction is simplified and consistently set as co-incident. In the South-Clockwise-based three-dimensional coordinate system, the wind-wave inflow direction is established as North-East by 30 degrees.

(ii) The photovoltaic intensity and temperature data utilized in this study were sourced from the Photovoltaic Geographical Information System (PVGIS) in Europe [210]. The geographical coordinates input for data collection in this database were set at (23.630, 119.507), located on the northern coast of Penghu Island, and the input time was specified as June 17, 2020, aligning with the wind-wave conditions defined in (i). The temperature and photovoltaic intensity data for the given latitude and longitude within a 24-hour period on that day are illustrated in Fig. 5.13(a). Following the modelling approach described in reference [205], a 24-hour solar azimuth model is generated using the geographical coordinates of Penghu Island. As depicted in Fig. 5.13(b), the solar azimuth angle and zenith angle are reasonably computed in the South-Clockwise configuration within the module, where the azimuth angle falls within the range of [-90°, 90°] during daylight hours, while the data for the remaining night-time hours are considered invalid, with zero photovoltaic intensity.

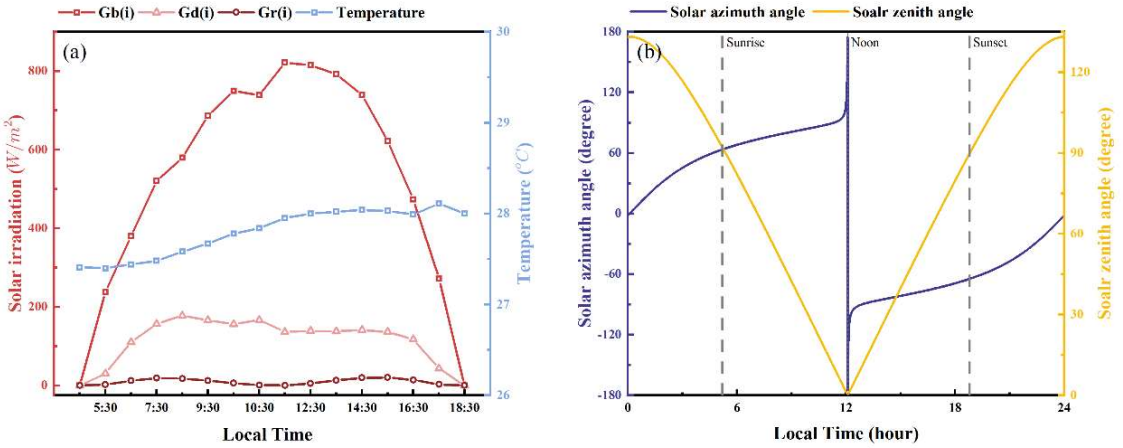


*Fig. 5.13 (a) Temperature and irradiation daily hour data, (b) solar azimuth angle and zenith angle at Penghu (Taiwan Strait) on June 17, 2020*

(iii) In theory, setting the maximum pitch angle of an operating FOWT as the PV tilt offset angle can achieve minimal energy losses and the optimal overall power output with minimized power ramp. However, in practical operation, determining the maximum pitch angle is not always stable and may require complex algorithms for detection and prediction. As a preliminary step in this research, PV tilt offset angles were simulated at 0, 15, 30, and 45 degrees to derive general conclusions that apply across various operational environments.

In actual operational testing, as an initial approach, the PV tilt offset angle was set slightly larger than the distribution range of the maximum pitch angle observed in experiments, ensuring that it remains below the peak of the photovoltaic panel's pitch angle-power curve. Since this study primarily focuses on the power compensation effects brought about by this control strategy, the impact of seawater on the photovoltaic panels at larger pitch angles is not considered, even though such extreme motion states are rarely encountered in the actual operation of FOWTs. Fig. 5.10 illustrates the pitch angle-power characteristic curves under different PV tilt offset angle settings.

(iv) From a forward-looking perspective on the capacity and potential of floating solar farms, this study explores three representative photovoltaic panel parameter settings. Firstly,

the AIKO-A465-MAH54Mw [211] stands as research baseline for PV panels, epitomizing the current pinnacle of commercial products available for practical application. It aptly mirrors the actual capacity permitted by the current FSF design. The Six-junction III–V [212] panel signifies the peak of PV panel photovoltaic conversion efficiency achieved in laboratory settings, demonstrating the practical potential for power expansion over the next decade. Meanwhile, GaAs-Based photovoltaic cells [213] represent the theoretical limit of photovoltaic conversion efficiency and serve as a bold conjecture for the long-term future of photovoltaic power development. The summarized designs of these three representative PV panels are presented in Table 5.2. While efficiency values strictly adhere to referenced literature, sizes, rated voltage and associated power align with AIKO-A465-MAH54Mw to eliminate insignificant variations, providing an intuitive representation of FSF's power generation potential.

*Table 5.2 PV panel types with key properties*

| Datasheet Parameters | A465-MAH54Mw | Six-junction III–V | GaAs-Based PV cells |
|---|---|---|---|
| Institute | AIKO Energy, China | NREL, USA | ISE, Germany |
| Efficiency (%) | 23.8 | 47.1 | 68.9 |
| Status | Commercially available | Fabrication available | Confirmed material specifications |
| Dimension (mm) | $1722 \times 1134 \times 30$ | $1722 \times 1134 \times 30^{\downarrow}$ | $1722 \times 1134 \times 30^{\downarrow}$ |
| Weight (kg) | $20.5 \pm 3\%$ | $20.5 \pm 3\%^{\downarrow}$ | $20.5 \pm 3\%^{\downarrow}$ |
| $V_{pv\_oc}$ (V) | 40.29 | $40.29^{\downarrow}$ | $40.29^{\downarrow}$ |
| $I_{pv\_sc}$ (A) | 14.14 | $27.98^{\downarrow}$ | $40.93^{\downarrow}$ |
| $V_{pv\_max}$ (V) | 34.11 | $34.11^{\downarrow}$ | $34.11^{\downarrow}$ |
| $I_{pv\_max}$ (A) | 13.64 | $26.99^{\downarrow}$ | $39.49^{\downarrow}$ |
| $P_{pv\_max}$ (W) | 465.26 | 920.71 | 1346.85 |

*Tested condition:* $AM1.5\ 1000W/m^2 25℃$

$V_{pv\_max}$*: voltage at maximum power point;* $I_{pv\_max}$*: current at maximum power point;* $P_{pv\_max}$*: maximum power point.*

*NREL: National Renewable Energy Laboratory; ISE: Fraunhofer Institute for Solar Energy Systems*

↓*The mechanical & electrical characteristics of Six-junction III–V and GaAs-Based photovoltaic cells are modified to facilitate the simulation experiment, and do not represent the manufacturer's final design.*

(v) Inspired by the design and experimental outcomes presented in [208], the dimensions of the novel catamaran floating platform in this experiment have been extended to $45m \times 60m$, as depicted in Fig. 5.14. Relevant mass adjustments have been incorporated into the FAST setup. Consequently, with photovoltaic panels measuring $1.722m \times 1.134m$ meters and a spacing diameter of $2.062m$, a maximum of 734 such panels can be accommodated on this floating platform. An area of $10m \times 10m$ on one side has been left empty to facilitate engineer access during wind turbine maintenance and to preserve space for additional equipment. Additionally, leaving space on the backlit side helps reduce the shading effects of the wind turbine tower on the solar panels, minimizing solar energy losses. As shown in Table 5.3, a total of 3 solar system cases were ultimately tested. These three cases were based on the practical considerations of the photovoltaic panels in (iv). If the overall power output stability in the simulation results for Case 4 is demonstrated, it would make larger barge floating platform designs more appealing.

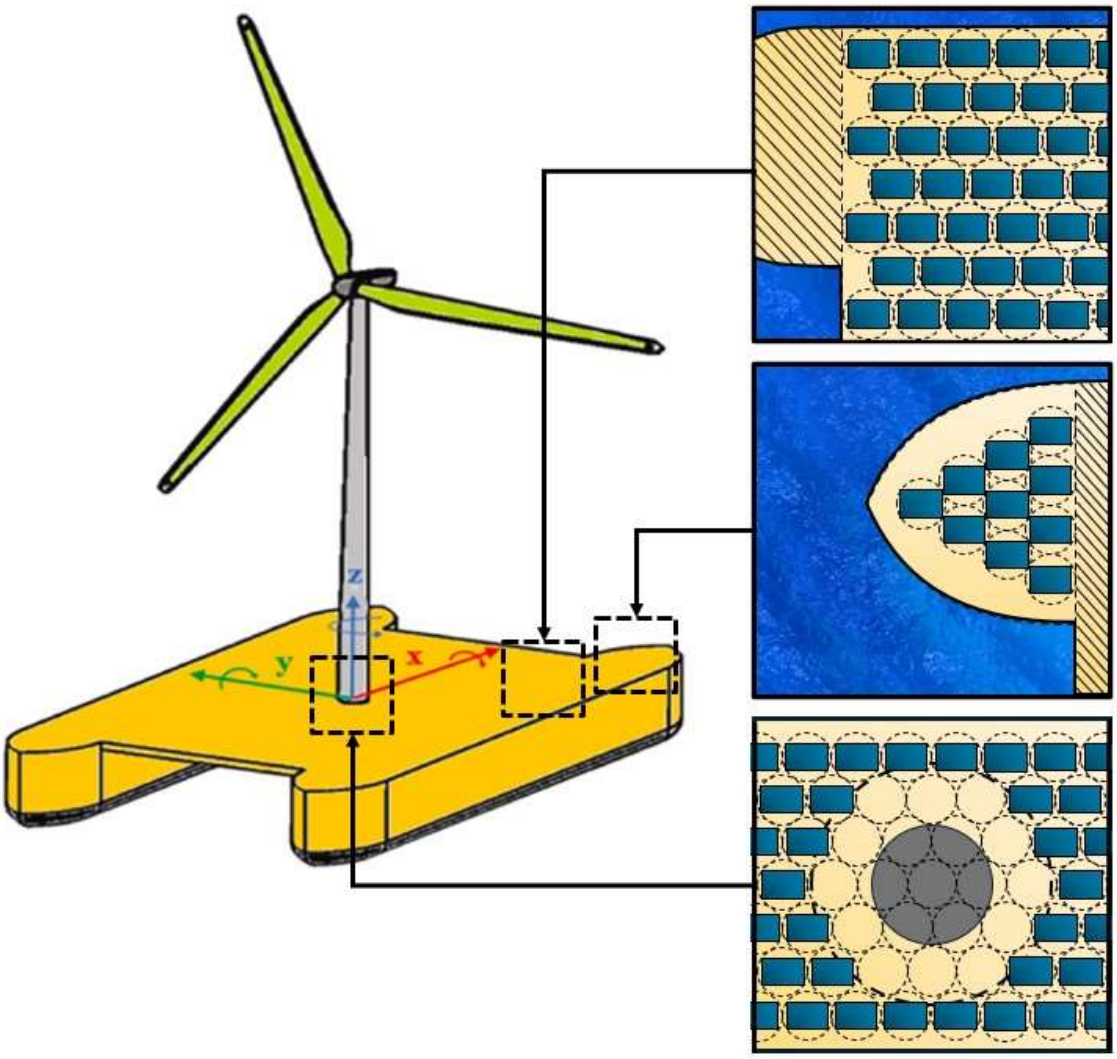


*Fig. 5.14 PV panel distribution on the Novel Catamaran FOWT floating platform*

*Table 5.3 Floating solar farm properties*

| Datasheet Parameters | Case Number | | |
|---|---|---|---|
| | A | B | C |
| PV panel Type | A465-MAH54MB | Six-junction III–V | GaAs-Based |
| PV efficiency (%) | 23.8 | 47.1 | 68.9 |
| $P_{pv\_max}$ (W) | 465.26 | 920.71 | 1346.85 |
| Designed PV panel quantity | 734 | 734 | 734 |

| | | | |
|---|---|---|---|
| FSF Total Weight (kg) | 15047 | 15047 | 15047 |
| FSF Rated Power (kW) | 341.50 | 675.80 | 988.59 |
| $\frac{Solar\ power}{Wind\ power}$ (%) | 6.70 | 13.25 | 19.38 |

*Environmental condition:* $AM1.5\ 1000W/m^2 25℃$

(vi) In summary, the classification and nomenclature of the various experimental data have been organized into three main sections, encompassing the load cases, proposed photovoltaic angle control schemes, and the sub-parts of the wind-solar platform, respectively. These have been summarized in Table 5.4.

*Table 5.4 Load cases description*

| Prefixes | Load case Scheme | Suffixes | Description | $U_w(m/s)$ | $T_p(s)$ | $H_s(m)$ | $\theta_{h_{ref}}(°)$ |
|---|---|---|---|---|---|---|---|
| LC1 | | | Normal | 12.0 | 5.17 | 1.67 | |
| LC2 | | | Monsoon | 12.0 | 9.4 | 5.5 | |
| LC3 | | | 10-year return period | 12.0 | 6.1 | 10.4 | |
| | 000 | | PV panel fixed at on platform | | | | 0 |
| | opt | | Height angle for max solar power | | | | $H_s$ |
| | c15 | | 15° additional offset of from optimal | | | | $\theta_h'(+15^\circ)$ |
| | c30 | | 30° additional offset of from optimal | | | | $\theta_h'(+30^\circ)$ |
| | c45 | | 45° additional offset of from optimal | | | | $\theta_h'(+45^\circ)$ |
| | | WT | The novel catamaran FOWT | | | | |
| | | PV | Solar_A/B/C system | | | | |
| | | WA | Wind-Solar_A system | | | | |
| | | WB | Wind-Solar_B system | | | | |
| | | WC | Wind-Solar_C system | | | | |

## 5.4 Results and Discussions

In this section, results are presented based on the above modelling and data selections. The study begins by evaluating the impact of varying PV array capacities under strong wind and wave conditions on the overall power performance of the wind-solar coupled platform. Subsequently, employing a controlled variables approach, the influence of solar azimuth angle, elevation angle, and the selected tilt offset angle on the PV panel pitch angle-power characteristic curve is examined. Following this, the proposed floating solar array design is compared with other external energy sources that can be integrated, using a 5MW-scale FOWT as a reference. Finally, the practical operational outcomes of the floating wind-solar platform in the summer season within the Taiwan Strait region are discussed. Notably, due to the highly detailed temporal resolution of the electrical module ( $20\,\mu s$ ), for computational efficiency, the FOWT simulation records power data from 10:45 AM to 11:45 AM, representing a typical one-hour duration for analysis. The remaining time's FOWT dynamics and electrical transient data are concatenated to form an identical copy of the simulation results for this one-hour interval. The time resolution of the photovoltaic module is set at $2\,s$.

### 5.4.1 Realization and quantification of power complementarity

As depicted in Fig. 5.15(a), under conditions of high winds and waves, the pitch angle plays a decisive role in the power generation of the FOWT. Simulation results indicate that when the FOWT is in a forward pitch, the impact on power output is not substantial. However, as the pitch angle increases in the backward direction, the FOWT's output power exhibits a linear decline, which is a determining factor leading to the emergence of high-frequency WPREs. Meanwhile, Fig. 5.15(b) illustrates that, in the time domain, the application of the "Maximum Power Complementarity" PV angle control strategy leads to the PV panels generating greater power in a sunward orientation during the declining phase

of FOWT output power. This effectively compensates for the high-frequency periodicity of WPREs. This control strategy limits efficiency losses for the FSF to be within 10% of peak power, thereby ensuring that solar energy complements floating wind energy almost perfectly across various platform pitch angles.

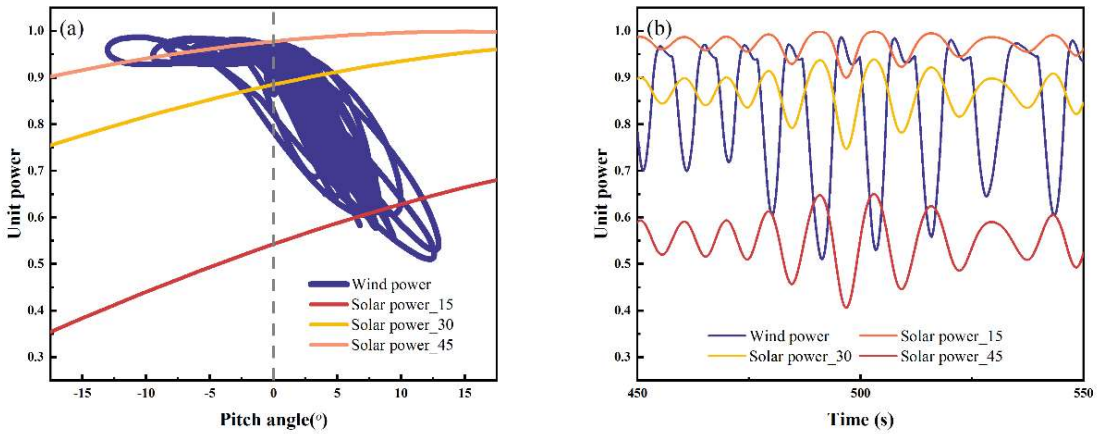


*Fig. 5.15 Floating offshore wind-solar hybrid platform (a) pitch angle-power characteristics and (b) time domain power simulation results under LC3 at 15:00 local time environment*

Fig. 5.15(a) illustrates the enhancement in power quality for the wind power plant with a capacity ratio ranging from Case 1 to Case 4 compared to the standalone FOWT. It becomes evident that the larger the photovoltaic array capacity, the more pronounced the power compensation effect on wind power fluctuations caused by dynamic state changes. Regarding the improvement in power quality, as demonstrated in Fig. 5.15(b), under the operation of the compensation control strategy in conjunction with the FSF, pitch induced WPRE peak is optimized from a decline up to 0.45 of rated power to 0.41, 0.38, 0.35 and 0.17 when wind and solar energy operate at capacity ratio set in Case 1, 2, 3 and 1:1.

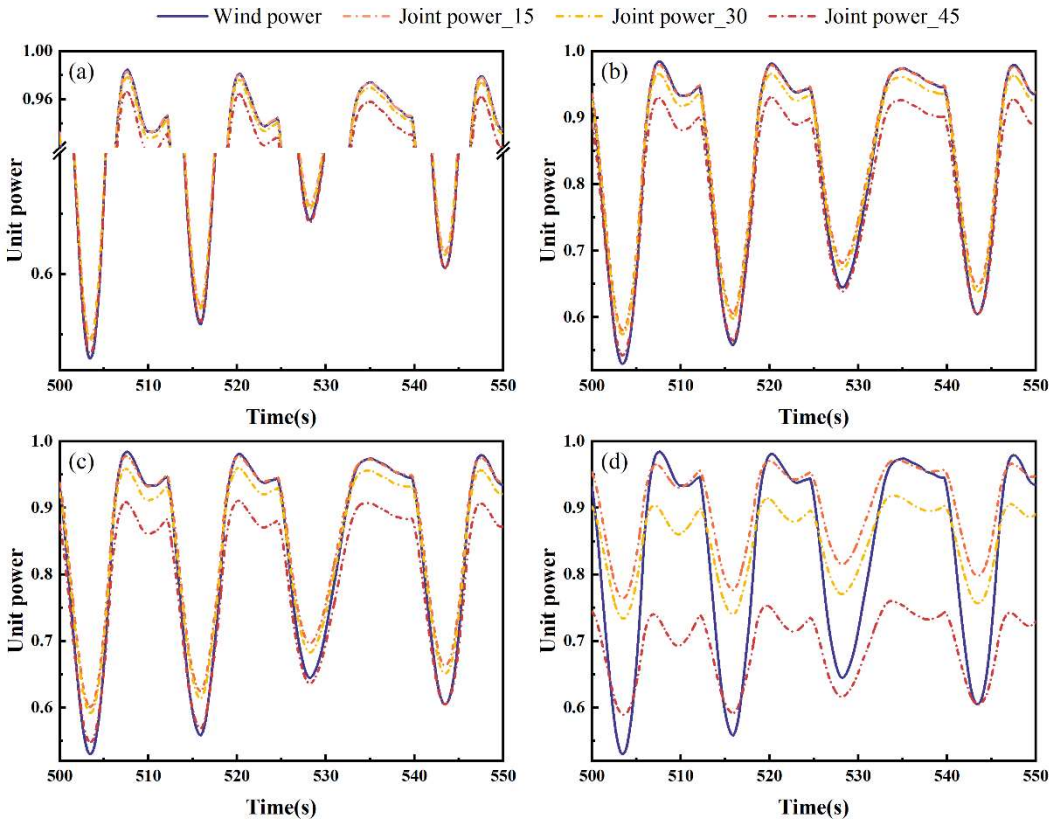


(a) Time domain power generation on Wind-Solar platform

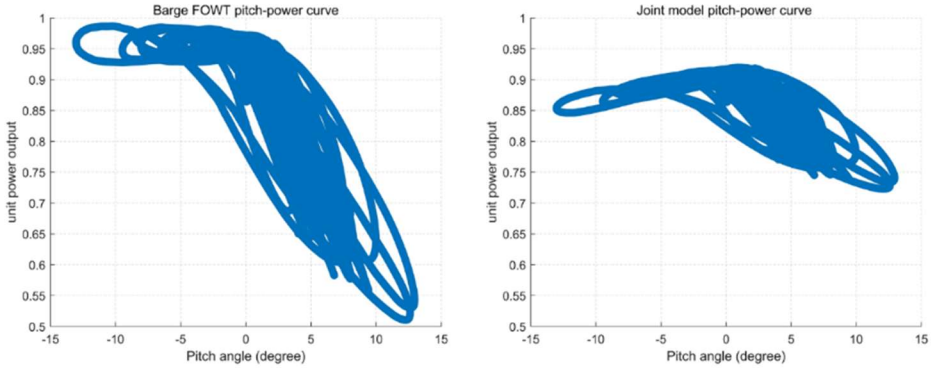


(b) Pitch-power characteristic optimization on Wind-Solar platform

*Fig. 5.16 Effect of maximum wind power fluctuation compensation mode*

Fig. 5.17 consolidates a comparison between the designed capacity of WECs from various literature sources and the capacity of the integrated photovoltaic array in this design.

In the context of existing solution Solar_A, the PV system on the $45m \times 60m$ barge platform is capable of generating up to 341.50 kW of active power during daylight hours, effectively reaching the power levels achieved by WECs designed for FOWTs in mainstream research [18]. Furthermore, the integration of the photovoltaic plant does not conflict with the installation of WECs on or near the FOWT, highlighting the design's commendable compatibility.

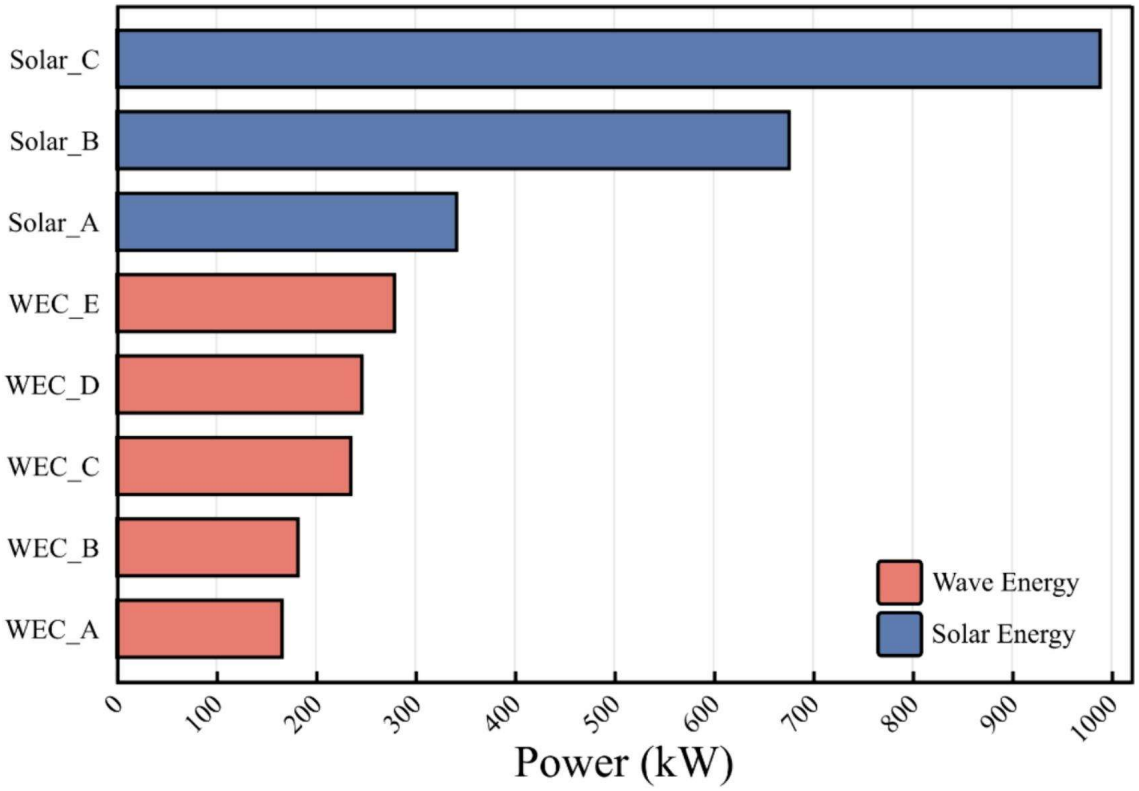


*Fig. 5.17 Maximum capacity comparison between proposed soalr farms (Solar_A, Solar_B & Solar_C) on the 5MW novel catamaran FOWT and WEC integration designs (WEC_A*[18]*, WEC_B*[214]*, WEC_C*[215]*, WEC_D*[216] *& WEC_E*[171]*) on 5MW FOWT*

### 5.4.2 Effect of solar angles and PV tilt angle settings

Solar azimuth angle, solar elevation angle, and the tilt offset angle set by the control strategy, collectively influence the photovoltaic panel's dynamic power characteristics. Employing a controlled variables approach, it is possible to examine the impact of one angle while keeping the other two fixed, providing a qualitative assessment of how changes

in the chosen angle affect the pitch angle-power relationship. To enhance the comprehensibility of the relationship between the solar azimuth angle and the FOWT, the solar azimuth angle is transformed into a wave-solar angle.

Firstly, Fig. 5.18 presents the pitch angle-power characteristics for various solar height angles, with the wave-solar angle fixed at 90 degrees and tilt offset angles set at 20°, 25°, 30°, and 35°. The range is set the same of each axis to allow observational comparison between subfigures. It is evident that the power characteristics split into two categories at a critical angle, which is the complementary angle of the set PV tilt offset angle. At lower elevation angles, the overall photovoltaic efficiency is high, but the power compensation effect is less pronounced. As the elevation angle approaches the critical angle, overall efficiency decreases, while the power compensation effect improves. At higher solar height angles, the power compensation effect remains consistently significant, with a slight reduction in overall efficiency as the solar height angle approaches the critical angle.

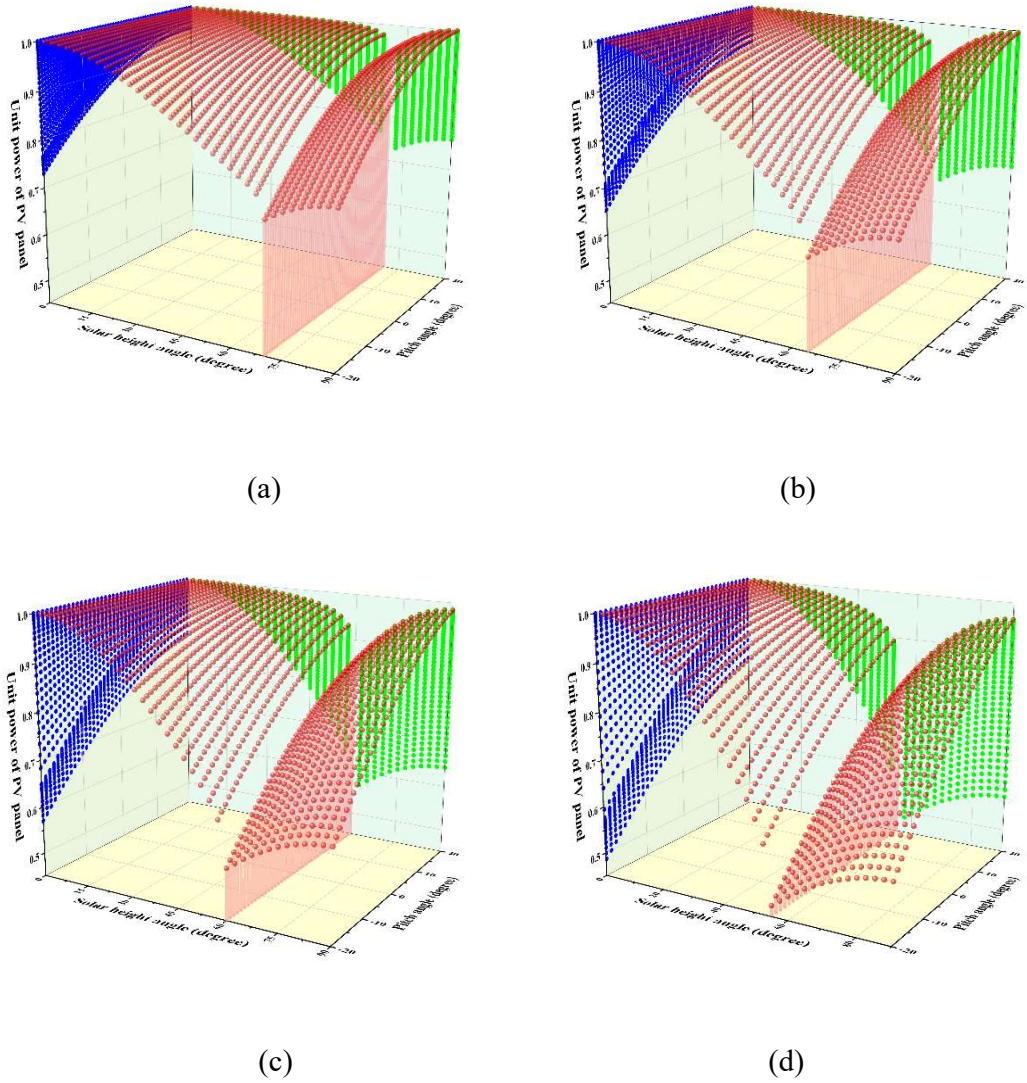


(a) (b)

(c) (d)

*Fig. 5.18 PV panel pitch-power characteristics with solar azimuth angle at 90 degrees and tilt offset angle at (a)20, (b)25 (c)30 and (d)35 degrees*

Subsequently, Fig. 5.19 illustrates the comparison of power characteristics at different wave-solar angles for four fixed solar height angle conditions, with the tilt offset angle set at 30 degrees. At lower elevation angles, larger wave-solar angles lead to more distinct variations in power characteristics. As the elevation angle increases, the differences in photovoltaic panel power characteristics diminish. When the elevation angle is sufficiently large, varying solar azimuth angles do not result in differences in power characteristics. This critical point is also the complementary angle of tilt offset angle, which is 60 degrees. Furthermore, the power characteristics in Fig. 5.18 also share the same viewpoint,

indicating that solar azimuth angles do not significantly impact the overall PV panel efficiency.

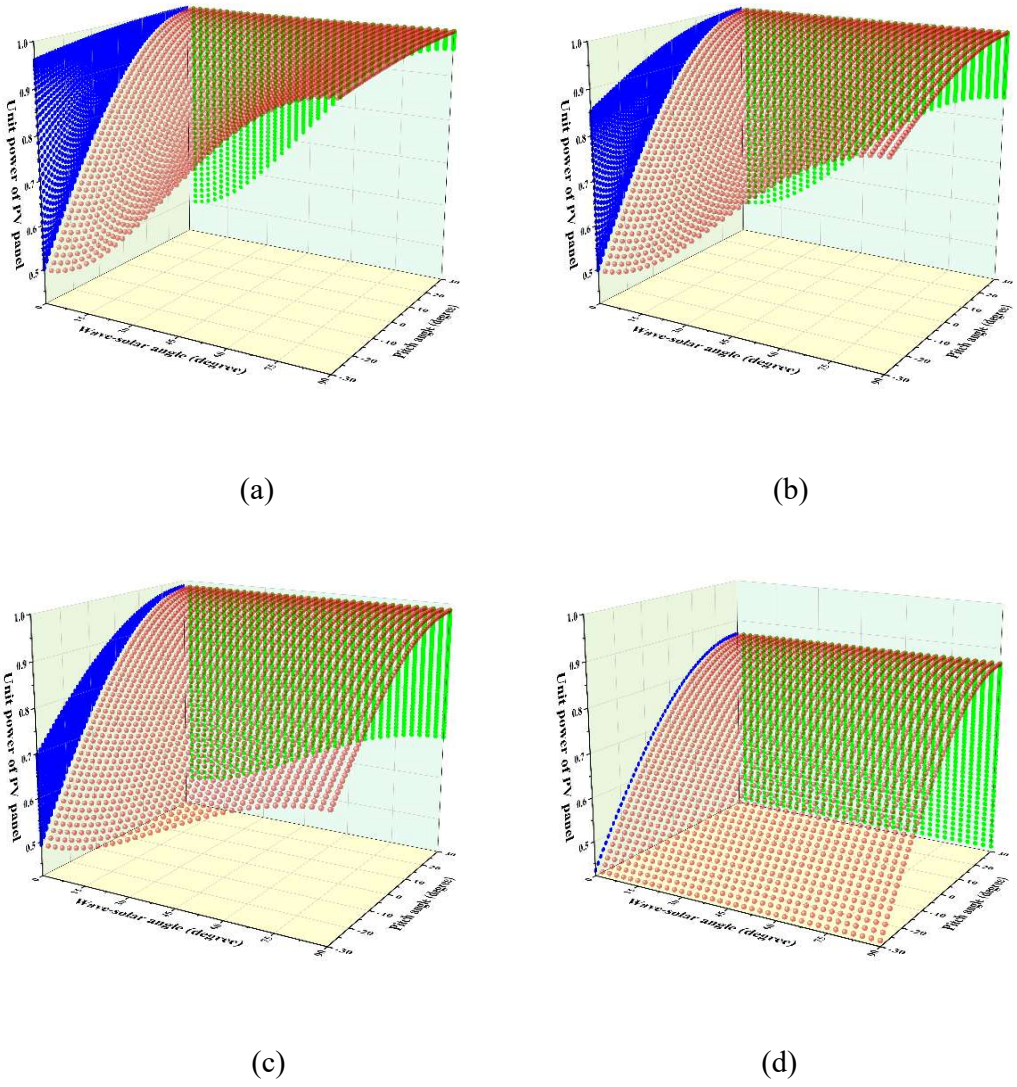


*Fig. 5.19 PV panel pitch-power characteristics with tilt offset angle at 30 degrees and solar height angle at (a)15, (b)30, (c)45 and (d)60 degrees*

### 5.4.3 Simulation in the offshore environment of Penghu in summer

#### *5.4.3.1 Power characteristic comparisons among the tilt angle control strategies*

The simulation results for the Taiwan Strait, based on data from Penghu, are discussed in this section. A complex and accurate model is established using AQWA-FAST-Simulink

to confirm the power performance of the Wind-Solar_A system on the FOWT and the actual operational effectiveness of the proposed control schemes. Regarding the tested schemes: 000 serves as the experimental reference sample; the opt scheme aims to maximize the efficiency of the solar energy system; and the c15, c30, and c45 schemes aim to effectively compensate for the WPRE induced by the pitch and roll movements of the FOWT.

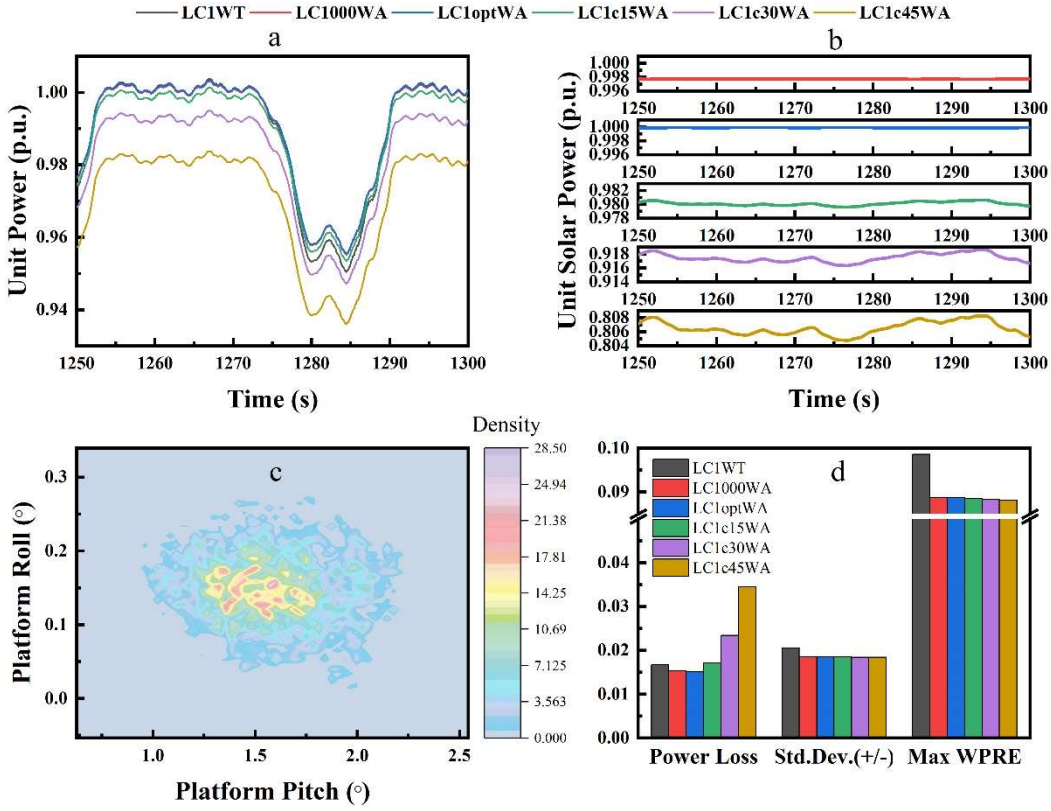


*Fig. 5.20 Power Performance of Floating Wind-Solar Hybrid Platform under normal sea state (LC1) at Taiwan Strait in June (11:45 AM local time)*

First of all, the Wind-Solar_A platform operates smoothly under the LC1 conditions with wind and waves in the same direction. As shown in Fig. 5.20(b), all schemes exhibit solar power fluctuations within the displayed range, not exceeding 0.4% of the rated power. Fig. 5.20(c) illustrates the range of pitch angle movement for the floating platform, which is 1.5 degrees, and the range of roll angle is 0.3 degrees. Additionally, as indicated in Fig.

5.20(a) and Fig. 5.20(b), the relationship between pitch angle and power is not significant under mild sea conditions. In the time domain, there is no apparent complementary relationship between solar power and wind power under the c15, c30, and c45 schemes. According to the statistics in Fig. 5.20(d), the power of the photovoltaic system is much more stable than the wind power, resulting in an overall power fluctuation reduction of over 10% compared to the FOWT, with the potential for higher power generation efficiency. The variations among the photovoltaic control schemes are mainly reflected in generation efficiency, while their differences in power fluctuations are minimal. It can be concluded that under mild sea conditions, the opt scheme performs optimally, and the 000 scheme exhibits similar performance at around 11:45 AM.

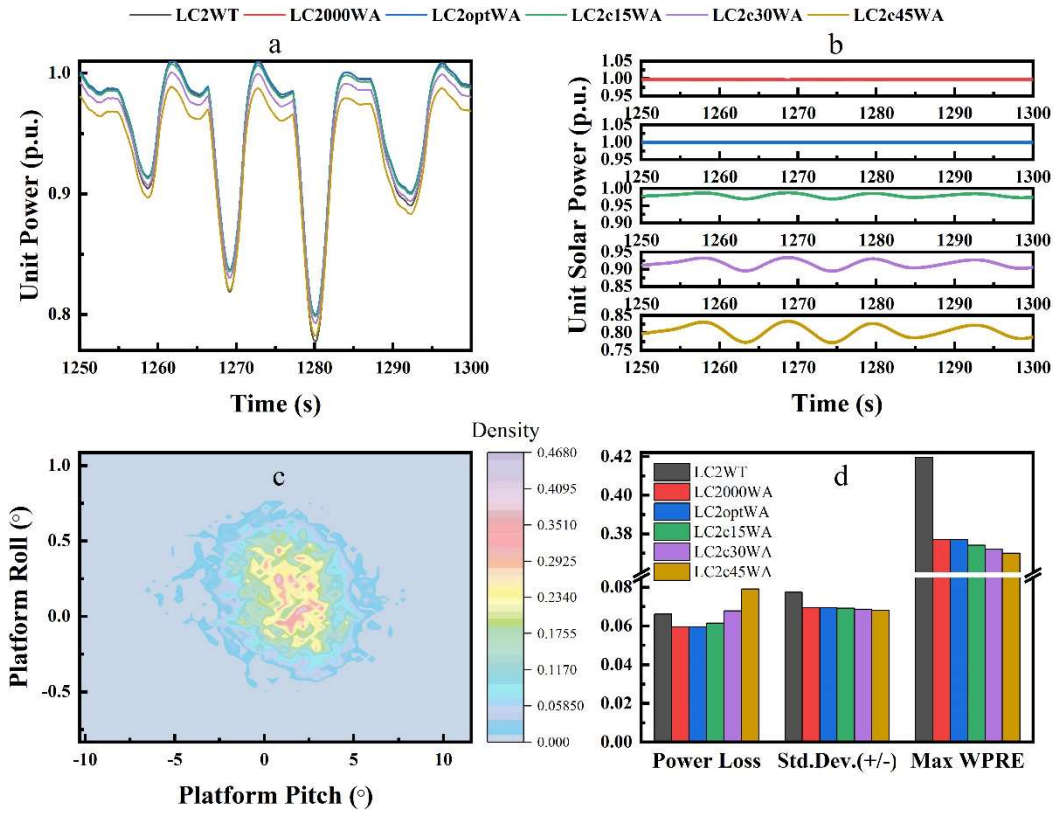


*Fig. 5.21 Power Performance of Floating Wind-Solar Hybrid Platform under Northeast moonson sea state (LC2) at Taiwan Strait in June (11:45 AM local time)*

As shown in Fig. 5.21, under the influence of the Taiwan Strait northeast monsoon conditions (LC2), the FOWT with the novel catamaran platform has a maximum pitch angle limit of 6 degrees and a range exceeding 12 degrees. Wind power is height-dependent on the pitch angle of the floating platform, with the maximum WPRE amplitude reaching 0.42 of the rated power. After integration with the solar energy system, this can be constrained to within 0.38. Fig. 5.21(b) indicates that the opt scheme still ensures power production close to the rated value. Meanwhile, under the c15, c30, and c45 schemes, the solar energy system exhibits periodicity and complementarity with wind power in the time domain. The strength of complementarity reaches power fluctuation levels of 3%, 5%, and 8% of the rated power for c15, c30, and c45 schemes, respectively.

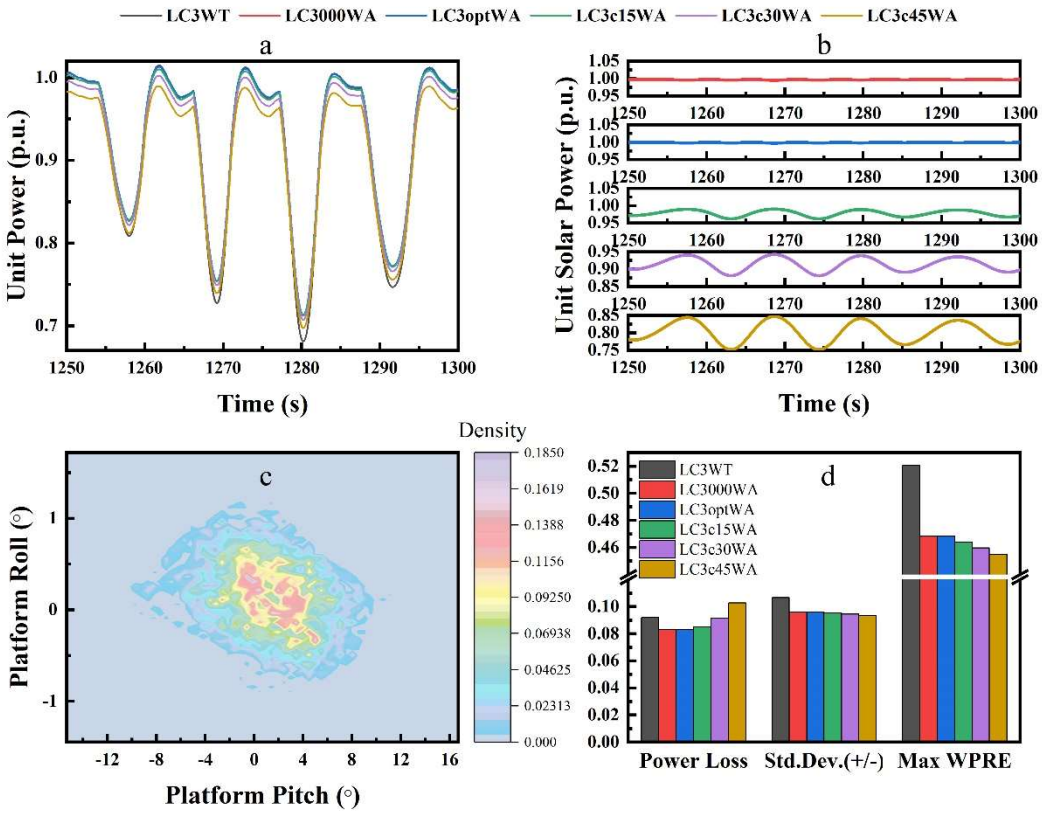


*Fig. 5.22 Power Performance of Floating Wind-Solar Hybrid Platform under 10-year sea state (LC3) at Taiwan Strait in June (11:45 AM local time)*

As illustrated in Fig. 5.22, under the Taiwan Strait 10-year return period offshore conditions (LC3), the dual-hulled FOWT's floating platform has a maximum pitch angle limit of positive and negative 10 degrees, with the roll angle restricted to within 2 degrees. The maximum WPRE amplitude reaches 0.52 of the rated power. Under the control of the opt scheme, the solar energy system's active power can still be maintained at an average level of 99.9%, ensuring high power quality. The power complementarity performance of the solar energy system under the c15, c30, and c45 schemes is more pronounced in LC3 conditions compared to LC2, reaching power fluctuation levels of 5%, 8%, and 10% of the rated power, respectively. Additionally, it is evident that wind energy losses are more significant under LC3 conditions, and, comparatively, the power losses under the c30 and c45 schemes are less significant. This further underscores the value of the Mode 2 in adverse sea conditions.

#### *5.4.3.2 Daytime extreme sea state testing considering solar capacity potential*

The performance testing of solar photovoltaic systems across various daytime periods holds significant value due to the nuanced variations in power characteristics, as indicated by the theoretical analyses in 5.4.2. Different solar positions and elevations introduce distinctive power output variations. For this study, testing occurred between 6:45 AM to 5:45 PM local time, with hourly intervals, excluding tests conducted during sunrise and sunset. This exclusion was necessary due to the potential mechanical angle requirements exceeding the equipment's limitations at low solar elevations, introducing substantial simulation errors. Additionally, low solar elevations can cause front-to-back shading on photovoltaic panels, a factor not considered in this model, further augmenting potential inaccuracies. The wave load was set to the most severe condition, LC3, despite not representing the majority of scenarios. However, this choice was deliberate, aiming to

ascertain the platform's ability to maintain optimal solar energy production or enhance overall power quality even under the most adverse conditions.

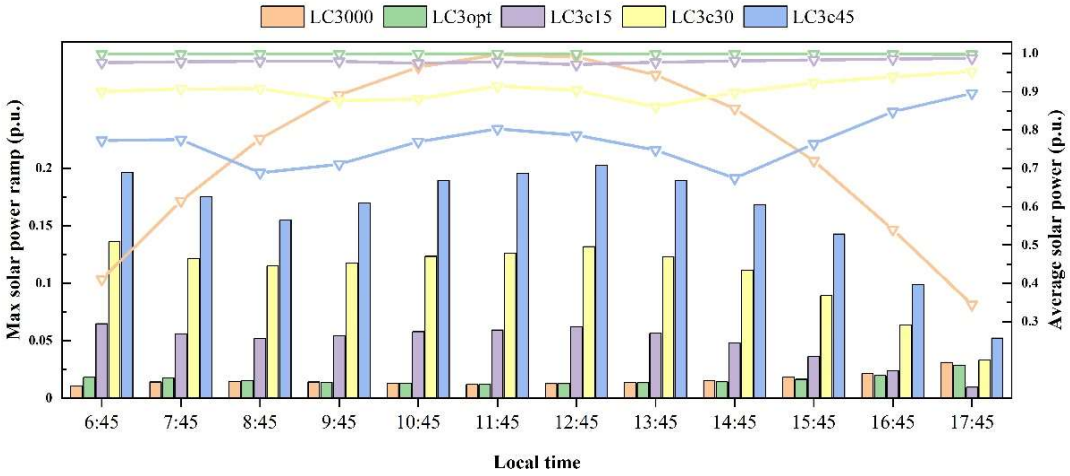


*Fig. 5.23 Daytime power performance of the floating solar farm at Taiwan Strait, June*

Firstly, the statistics of the photovoltaic system's self-generation efficiency and maximum power ramp event under LC3 conditions during daytime are depicted in Fig. 5.23. As a benchmark, the efficiency under LC3000 is minimal during sunrise and sunset, reaching below 0.3, progressively increasing with rising solar elevation, and sharply peaking close to 100% at 11:45 AM. On the contrary, LC3opt, designed for extreme sea conditions occurring once every ten years, consistently maintains an average generation efficiency of over 99% throughout the entire daytime period. Engineered to enhance wind power quality, LC3c15, LC3c30, and LC3c45 exhibit overall generation efficiencies falling between LC3000 and LC3opt, with the lowest efficiency periods occurring at 9:45 AM and 2:45 PM. As analysed in 5.4.2, these time intervals correspond to the highest wave-solar angles.

Secondly, concerning the inherent power fluctuations of the photovoltaic system, under the reference of LC3000, these fluctuations proportionally increase, converging, however, to the same pattern as LC3opt – minimal fluctuations – precisely at 11:45 AM, the

moment the sun reaches its maximum elevation. Throughout the entire daytime, LC3opt constrains its fluctuations within 4% of the rated value. Designed to complement wind power, LC3c15, LC3c30, and LC3c45 exhibit larger power ramps, aligning better with the design expectations. Overall, the differences in ramps due to increased tilt angles of the photovoltaic panels are notably distinct throughout daytime intervals except at 4:45 PM and 5:45 PM.

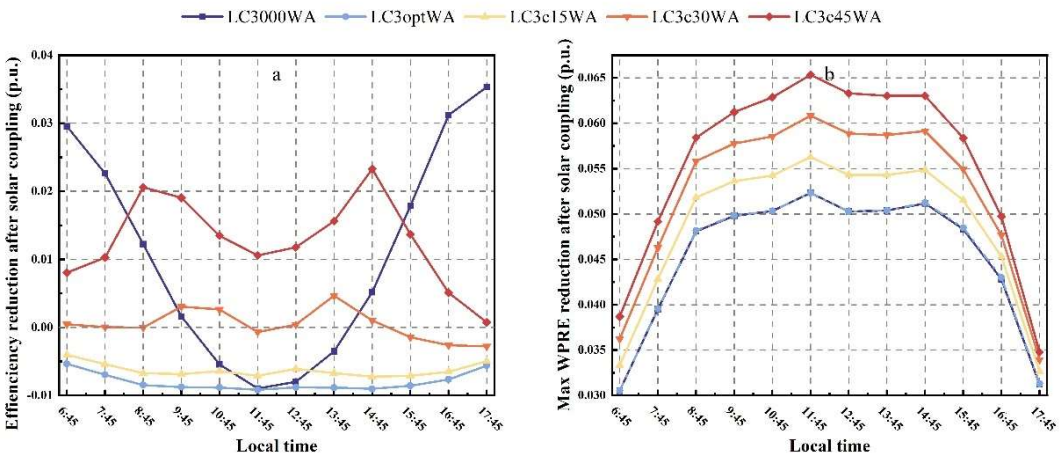


*Fig. 5.24 Daytime (a) unit power efficiency deduction and (b) unit max power ramp deduction of Wind-Solar_A platform under LC3*

The comparative analysis of the photovoltaic system integrated with the FOWT regarding its own power quality during daytime is illustrated in Fig. 5.24. The rated solar power here is a dynamically calculated variable based on the power received by the photovoltaic panels when directly facing the sun. Consequently, it's evident that the midday solar photovoltaic system with a higher rated power also exhibits a more pronounced impact.

For the Wind-Solar_A platform with a solar energy conversion efficiency of 23.8%, both the opt and c15 schemes demonstrate a nearly 1% enhancement in generation efficiency compared to the FOWT alone. The wind-solar system under the 000 scheme exhibits an increasing trend in average generation efficiency with the elevation of the solar altitude angle. Maximum efficiency losses exceeding 3% occur during sunrise and sunset,

while at 11:45 AM, it passively attains the same peak efficiency as observed in the opt scheme. The c30 scheme incurs negligible efficiency losses, while c45 and 000 schemes result in relatively higher losses, albeit not exceeding 4%. In terms of power quality enhancement, due to the lower sensitivity of solar power to platform movement compared to wind power, the opt scheme yields an overall 5% suppression in rated power ramp between 8:45 AM to 3:45 PM. Complementary schemes c15, c30, and c45 offer additional 0.5%, 1%, and 1.5% power ramp suppressions beyond the opt scheme.

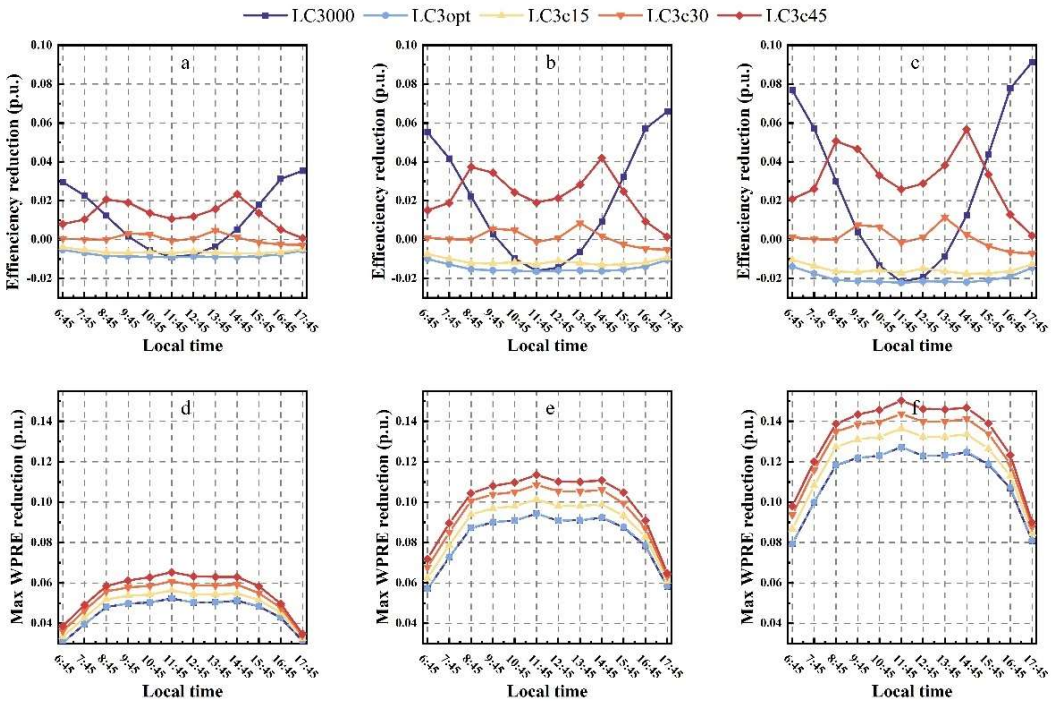


*Fig. 5.25 Daytime unit power efficiency deduction of (a) Wind-Solar_A, (b) Wind-Solar_B, (c) Wind-Solar_C platforms; and unit max power ramp deduction of (a) Wind-Solar_A, (b) Wind-Solar_B, (c) Wind-Solar_C platforms under LC3*

Considering the ongoing breakthroughs in photovoltaic conversion efficiency and the inherent potential in solar energy system capacity, the power performance improvements of the Wind-Solar_B (solar energy conversion efficiency of 47.1%) and Wind-Solar_C systems (solar energy conversion efficiency of 68.9%) are comprehensively tested

compared to the intrinsic performance of the FOWT. The results are presented comprehensively in Fig. 5.25. It is evident that as the rated power of the solar energy system increases, the impact of different photovoltaic system control schemes in the Wind-Solar system becomes more significant, exhibiting noticeable differences in the electricity production process. During most daylight hours, the opt scheme enhances the average generation efficiency by 1.9% and 2.1% in the Wind-Solar_B and Wind-Solar_C systems, respectively, while limiting the amplitude of the entire system power ramp events to 9% and 12% of the rated power. The c15 scheme performs similarly in the Wind-Solar_B and Wind-Solar_C systems, reducing the average generation efficiency by approximately 0.2% compared to the opt scheme, and additionally constraining the maximum power ramp amplitude by 1%. Similarly, the c15 scheme exhibits comparable performance in the Wind-Solar_B and Wind-Solar_C systems, maintaining overall generation efficiency at par with wind power, while limiting the maximum power ramp by over 2% compared to the opt scheme. The capacity enhancement has limited impact on the power quality improvement of the c45 scheme compared to c30. Under the c45 scheme, the loss in system generation efficiency is noticeably higher compared to c30, averaging at 3% and 4% in the Wind-Solar_B and Wind-Solar_C systems, respectively. The trade-off between generation efficiency loss and power quality improvement means this conflicting correlation would require the selection of control schemes, involving an analysis of optimal control, a decision that recommend being made by the wind farm operators.

## 5.5 Conclusion to this chapter

In this chapter, a comprehensive exploration of the challenges associated with the fluctuating output of floating wind turbines is conducted, considering the structural limitations of floating solar farms, and high manufacturing costs, ultimately proposing a power complementarity control strategy for a wind-solar coupled system based on the novel

catamaran FOWT. To substantiate this, a dynamic model for FOWT is constructed, including a Permanent Magnet Synchronous Generator (PMSG) power generation system, and the mathematical model of the PV system, creating a hybrid wind-solar system through a common DC bus. The simulations have yielded the following key findings:

1. As the solar elevation angle increases, the power characteristics at different wind-solar angles exhibit reduced variation, and this variation ceases when the elevation angle surpasses the complementary angle of PV tilt offset angle. Photovoltaic power efficiency decreases as the elevation angle approaches the effect of the complementary angle, and a distinctive shift in photovoltaic power characteristics is observed, with the complementary angle of PV tilt offset angle serving as the boundary.

2. The power generation of the photovoltaic system is much less sensitive to the pitch and roll movements of the platform compared to the wind turbine. Under the OPT scheme, even with a sea state of 6.1m wave height on the catamaran FOWT, the PV system ensures an efficiency of over 97% throughout the entire period.

3. Greater pitch motion leads to superior power complementarity effects for both wind and solar energy, with power fluctuations rising in tandem with the capacity of the photovoltaic array. In Wind-Solar_C system with a solar-to-wind capacity ratio of 0.1938, the impact of pitch motion on the max power ramp magnitude is reduced from 8% to 15% of the normalized power under different control schemes.

4. The efficacy of the wind-solar power compensation by tilt offset control can be summarized as follows: the smaller the wave-solar angle, the more effective the compensation, and a higher solar elevation angle enhances the compensation effect. Real-world operation in the Taiwan Strait results in two instances of the lowest efficiency, occurring in the morning and afternoon.

These findings highlight the considerable potential of the wind-solar coupled platform and offer insights into optimizing its performance. Furthermore, the proposed control strategy promises enhanced power generation and energy complementarity, making this approach a promising solution for future renewable energy systems in coastal regions with similar environmental conditions.

# Chapter 6: Conclusions and Future Work

## 6.1 Conclusions

The integration of mechanical and electrical models for FOWTs signifies a pivotal advancement, allowing for a more nuanced understanding of turbine operation. Historically, research in these two domains proceeded independently, but recent endeavours have converged towards joint modelling, enhancing the accuracy, depth and applications of wind turbine power system analysis. The adoption of co-simulation platforms like FAST+Simulink has facilitated comprehensive research, although more advanced platforms like RTDS and RT-LAB are emerging as preferable alternatives for detailed power system studies. However, the application of co-simulation remains in its infancy, with a notable lack of integrated models for floating wind turbines. Future research aims to establish comprehensive co-simulation platforms for FOWTs to enable thorough testing and optimization.

Motivated from the above, firstly, the development of a fully coupled mathematical model for FOWTs is accomplished, to provide valuable insights into the dynamic interactions between wind and wave-induced loads, particularly regarding WPREs. These events exhibit distinctive periodic dynamics, primarily influenced by wave-induced loads and platform oscillations. Understanding these dynamics is crucial for designing, operating, and managing FOWTs, especially under rated wind and wave conditions. Furthermore, the significance of pitch motion and wave-induced loading underscores the need for comprehensive modelling approaches to elucidate transient responses across diverse operational scenarios. This study fills a significant research gap and advances the understanding of FOWT operational dynamics.

Then using the fully coupled model, key distinctions between the output power of floating wind turbines and fixed-bottom counterparts are addressed, highlighting the challenges posed by low-frequency power fluctuations and efficiency disparities. A tailored

control scheme incorporating RTCC and HESS is proposed to optimize power output and enhance power quality. The study provides valuable insights into parameter optimization for RTCC and underscores the importance of addressing power fluctuations and dispatch command disparities in FOWT operation. This work represents a significant advancement in mitigating power quality issues and optimizing power output for floating wind turbines.

To further applications of FOWTs, wind-solar coupled systems are investigated, specifically on catamaran FOWTs, reveals promising potential for enhancing power generation and energy complementarity. By integrating dynamic models for FOWTs and floating solar farms, the study demonstrates the efficacy of power complementarity control strategies. Notably, the study identifies the impact of solar elevation angle on power characteristics and the influence of platform motion on power generation. These findings offer valuable insights into optimizing wind-solar coupled systems and present a promising solution for future renewable energy systems in coastal regions.

Overall, this thesis presents a comprehensive exploration of FOWTs in modelling, performance for grid connection, and their integration with solar energy systems. Through detailed modelling, analysis, and experimentation, the study addresses critical research gaps and advances understanding in several key areas. Notably, the development of integrated mechanical-electrical models, the investigation into dynamic responses and power quality issues, and the proposal of novel control strategies signify significant contributions to the field of renewable energy. The findings highlight the potential for enhancing power generation, improving energy complementarity, and optimizing the operation of wind-solar coupled systems in offshore environments. As renewable energy continues to play a crucial role in the transition to a sustainable future, the insights gained from this thesis are instrumental in shaping the development and deployment of offshore renewable energy technologies.

## 6.2 Future Work

Although research work in Chapter 3 demonstrated the significant impact of sustained structural vibrations on the output power quality of FOWTs and provided a quantitative description of WPREs under different wind and wave conditions, quantifying the overall wind power loss for floating wind turbines remains unresolved. Using generic power characteristics (wind speed-power) from Fixed-Bottom OWTs for predicting FOWT output would lead to significant deviations. Hence, one of the future tasks is to quantify the actual effective output power of FOWTs under various wind and wave conditions through testing.

In Chapter 4, the discussion on the optimization of parameters in RTCC revealed that parameters $\delta_2$ and $\delta_3$ in the Kalman filter involve multi-objective optimization issues. The conclusion of the chapter comprehensively describes the optimal range for these two parameters under comprehensive considerations and provides recommendations for their values based on practical circumstances. Future work entails employing more multi-objective optimization assessment methods for deeper analysis.

Additionally, in extreme wave conditions, the amplitude of WPREs for floating wind power is substantial, and FOWTs resonate closely with each other and with the low-frequency resonance centre frequency of the grid. A potential future task can be investigating whether wave frequency resonance characteristics could potentially lead to resonance accidents and system collapse during power system operation.

# References

[1] IEA, "Key electricity trends 2019," IEA(2020). [Online]. Available: https://www.iea.org/articles/key-electricity-trends-2019

[2] P. Chen, C. Jia, C. Ng, and Z. Hu, "Application of SADA method on full-scale measurement data for dynamic responses prediction of Hywind floating wind turbines," *Ocean Eng.*, vol. 239, p. 109814, Nov. 2021, doi: 10.1016/J.OCEANENG.2021.109814.

[3] T. R. Lucas, A. F. Ferreira, R. B. Santos Pereira, and M. Alves, "Hydrogen production from the WindFloat Atlantic offshore wind farm: A techno-economic analysis," *Appl. Energy*, vol. 310, p. 118481, Mar. 2022, doi: 10.1016/J.APENERGY.2021.118481.

[4] S. Bashetty and S. Ozcelik, "Review on dynamics of offshore floating wind turbine platforms," *Energies*, vol. 14, no. 19, 2021, doi: 10.3390/en14196026.

[5] K. A. Shah *et al.*, "A synthesis of feasible control methods for floating offshore wind turbine system dynamics," *Renew. Sustain. Energy Rev.*, vol. 151, no. July, 2021, doi: 10.1016/j.rser.2021.111525.

[6] J. López-Queija, E. Robles, J. Jugo, and S. Alonso-Quesada, "Review of control technologies for floating offshore wind turbines," *Renew. Sustain. Energy Rev.*, vol. 167, p. 112787, Oct. 2022, doi: 10.1016/J.RSER.2022.112787.

[7] Y. Tumewu, P. Crescenzo, and M. Sivaselvan, "Numerical Simulation of the Influence of Platform Pitch Motion on Power Generation Steadiness in Floating Offshore Wind Turbines," *Int. J. Environ. Sci. Sustain. Dev.*, vol. 2, no. 1, p. 92, 2017, doi: 10.21625/essd.v2i1.39.

[8] M. Tsili and S. Papathanassiou, "A review of grid code technical requirements for wind farms," *IET Renew. Power Gener.*, vol. 3, no. 3, pp. 308–332, 2009.

[9] O. N. Nobela, R. C. Bansal, and J. J. Justo, "A review of power quality compatibility of wind energy conversion systems with the South African utility grid," *Renew. Energy Focus*, vol. 31, pp. 63–72, Dec. 2019, doi: 10.1016/J.REF.2019.10.001.

[10] A. Pratap, N. Urasaki, and T. Senjyu, "Instantaneous frequency and voltage control of PMSG-based WECS using controllable load," *Proc. Int. Conf. Power Electron. Drive Syst.*, no. 6, pp. 468–473, 2013, doi: 10.1109/PEDS.2013.6527064.

[11] D. Zhang and K. J. Tseng, "Design and modelling of grid-connected PMSG-based wind energy conversion through diode rectifier, DC/DC and DC/AC converters," *2014 Australas. Univ. Power Eng. Conf. AUPEC 2014 - Proc.*, no. October, pp. 1–5, 2014, doi: 10.1109/AUPEC.2014.6966520.

[12] H. Emanuel, M. Schellschmidt, S. Wachtel, and S. Adloff, "Power quality measurements of wind energy converters with full-scale converter according to IEC 61400-21," *2009 10th Int. Conf. Electr. Power Qual. Util. EPQU'09*, 2009, doi: 10.1109/EPQU.2009.5318814.

[13] J. Yang, Y. P. He, Y. S. Zhao, Y. L. Shao, and Z. L. Han, "Experimental and numerical studies on the low-frequency responses of a spar-type floating offshore wind turbine," *Ocean Eng.*, vol. 222, no. January, p. 108571, 2021, doi: 10.1016/j.oceaneng.2021.108571.

[14] Y. Si, H. R. Karimi, and H. Gao, "Modelling and optimization of a passive structural control design for a spar-type floating wind turbine," *Eng. Struct.*, vol. 69, pp. 168–182, 2014, doi: 10.1016/j.engstruct.2014.03.011.

[15] Z. Liu, Q. Zhou, Y. Tu, W. Wang, and X. Hua, "Proposal of a novel semi-submersible floating wind turbine platform composed of inclined columns and multi-segmented mooring lines," *Energies*, vol. 12, no. 9, pp. 1–32, 2019, doi: 10.3390/en12091809.

[16] Q. Ding, C. Li, S. Cheng, W. Hao, Z. Huang, and W. Yu, "Study on TMD Control on Stability Improvement of Barge-Supported Floating Offshore Wind Turbine Based on the Multi-Island Genetic Algorithm," *China Ocean Eng.*, vol. 33, no. 3, pp. 309–321, 2019, doi: 10.1007/s13344-019-0030-8.

[17] X. Tong, X. Zhao, and A. Karcanias, "Passive vibration control of an offshore floating hydrostatic wind turbine model," *Wind Energy*, vol. 21, no. 9, pp. 697–714, 2018, doi: 10.1002/we.2188.

[18] J. Hu *et al.*, "Optimal design and performance analysis of a hybrid system combing a floating wind platform and wave energy converters," *Appl. Energy*, vol. 269, no. April, p. 114998, 2020, doi: 10.1016/j.apenergy.2020.114998.

[19] J. M. Kluger, M. N. Haji, and A. H. Slocum, "The power balancing benefits of wave energy converters in offshore wind-wave farms with energy storage," *Appl. Energy*, vol. 331, no. April 2022, p. 120389, 2023, doi: 10.1016/j.apenergy.2022.120389.

[20] T. Wakui, M. Yoshimura, and R. Yokoyama, "Multiple-feedback control of power output and platform pitching motion for a floating offshore wind turbine-generator system," *Energy*, vol. 141, pp. 563–578, 2017, doi: 10.1016/j.energy.2017.09.100.

[21] M. F. Akorede, "Design and performance analysis of off-grid hybrid renewable energy systems," *Hybrid Technol. Power Gener.*, pp. 35–68, Jan. 2022, doi: 10.1016/B978-0-12-823793-9.00001-2.

[22] A. Honrubia-Escribano, E. Gómez-Lázaro, J. Fortmann, P. Sørensen, and S. Martin-Martinez, "Generic dynamic wind turbine models for power system stability analysis: A comprehensive review," *Renew. Sustain. Energy Rev.*, vol. 81, no. January 2017, pp. 1939–1952, 2018, doi: 10.1016/j.rser.2017.06.005.

[23] IRENA, *Renewable Power Generation Costs in 2019*. 2020. [Online]. Available: https://www.irena.org/-/media/Files/IRENA/Agency/Publication/2018/Jan/IRENA_2017_Power_Costs_2018.pdf

[24] H. Li and Z. Chen, "Overview of different wind generator systems and their comparisons," *IET Renew. Power Gener.*, vol. 2, no. 2, pp. 123–138, 2008, doi: 10.1049/iet-rpg:20070044.

[25] Y. Nam, P. T. Kien, and Y. H. La, "Alleviating the tower mechanical load of Multi-MW wind turbines with LQR control," *J. Power Electron.*, vol. 13, no. 6, pp. 1024–1031, 2013, doi: 10.6113/JPE.2013.13.6.1024.

[26] W. Musial, S. Butterfield, and A. Boone, "Feasibility of floating platform systems for wind turbines," *Collect. ASME Wind Energy Symp. Tech. Pap. AIAA Aerosp. Sci. Meet. Exhib.*, no. November 2003, pp. 476–486, 2004, doi: 10.2514/6.2004-1007.

[27] U. S. D. of Energy, *20% Wind Energy by 2030 Increasing Wind Energy's Contribution to U.S. Electricity Supply*. U.S. Department of Energy, 2008.

[28] A. Cordle and J. Jonkman, "State of the art in floating wind turbine design tools," *Proc. Int. Offshore Polar Eng. Conf.*, no. October, pp. 367–374, 2011.

[29] J. Jonkman and W. Musial, "Offshore Code Comparison Collaboration ( OC3 ) for IEA Task 23 Offshore Wind Technology and Deployment Offshore Code Comparison Collaboration ( OC3 ) for IEA Task 23 Offshore Wind Technology and Deployment," no. December, pp. 1–74, 2010, [Online]. Available: https://www.nrel.gov/docs/fy11osti/48191.pdf

[30] J. Chen, Z. Hu, G. Liu, and D. Wan, "Coupled aero-hydro-servo-elastic methods for floating wind turbines," *Renew. Energy*, vol. 130, pp. 139–153, 2019, doi: 10.1016/j.renene.2018.06.060.

[31] P. Breeze, "Offshore Wind," *Wind Power Gener.*, pp. 75–84, 2016, doi: 10.1016/b978-0-12-804038-6.00009-8.

[32] M. L. B. Jr, "FAST User Guide 2005," *Contract*, no. October, 2005.

[33] L. Chen, J. Yang, and C. Lou, "Characterizing ramp events in floating offshore wind power through a fully coupled electrical-mechanical mathematical model," *Renew. Energy*, vol. 221, p. 119803, Feb. 2024, doi: 10.1016/J.RENENE.2023.119803.

[34] W. Warmbrod and P. Friedmann, "Coupled rotor/tower aeroelastic analysis of large horizontal axis wind turbines," *AIAA J.*, vol. 18, no. 9, pp. 1118–1124, 1980, doi: 10.2514/3.50861.

[35] P. P. Friedmann, "Aeroelastic Modeling of Large Wind Turbines," *J. Am. Helicopter Soc.*, vol. 21, no. Number 4, pp. 17-27(11), 1976.

[36] P. P. Friedmann, "Aeroelastic stability and response analysis of large horizontal-axis wind turbines," *J. Wind Eng. Ind. Aerodyn.*, vol. 5, no. 3–4, pp. 373–401, 1980, doi: 10.1016/0167-6105(80)90043-4.

[37] T. J. Larsen, a M. Hansen, and T. Buhl, "Aeroelastic effects of large blade deflections for wind turbines," *Sci. Mak. torque from Wind*, no. January 2004, pp. 238–246, 2004.

[38] M. H. Hansen and T. Buhl, *Design guidelines for passive instability suppression – Task-11 Report*. 2006.

[39] M. H. Hansen, "Aeroelastic stability analysis of wind turbines using an eigenvalue approach," *Wind Energy*, vol. 7, no. 2, pp. 133–143, 2004, doi: 10.1002/we.116.

[40] J. J. Chattot, "Helicoidal vortex model for wind turbine aeroelastic simulation," *Comput. Struct.*, vol. 85, no. 11–14, pp. 1072–1079, 2007, doi: 10.1016/j.compstruc.2006.11.013.

[41] D. Matha, S. Hauptmann, T. Hecquet, and M. Kühn, "Methodology and Results of Loads Analysis of Wind Turbines with Advanced Aeroelastic Multi-Body Simulation," *AES-ATEMA' 2011*, vol. 17, no. 6, pp. 553–561, 2011.

[42] M. F. Jørgensen, *Aerodynamic and Mechanical System Modelling*. 2013.

[43] M. M. Pedersen, T. J. Larsen, H. A. Madsen, and G. C. Larsen, "More accurate aeroelastic wind-turbine load simulations using detailed inflow information," *Wind Energy Sci.*, vol. 4, no. 2, pp. 303–323, 2019, doi: 10.5194/wes-4-303-2019.

[44] P. Moriarty, "Database for validation of design load extrapolation techniques," *Wind Energy*, vol. 11, no. 6, pp. 559–576, 2008, doi: 10.1002/we.305.

[45] J. P. Murcia *et al.*, "Uncertainty propagation through an aeroelastic wind turbine model using polynomial surrogates," *Renew. Energy*, vol. 119, pp. 910–922, 2018, doi: 10.1016/j.renene.2017.07.070.

[46] T. T. Tran and D. H. Kim, "A CFD study of coupled aerodynamic-hydrodynamic loads on a semisubmersible floating offshore wind turbine," *Wind Energy*, vol. 21, no. 1, pp. 70–85, 2018, doi: 10.1002/we.2145.

[47] T. Tran, D. Kim, and J. Song, "Computational fluid dynamic analysis of a floating offshore wind turbine experiencing platform pitching motion," *Energies*, vol. 7, no. 8, pp. 5011–5026, 2014, doi: 10.3390/en7085011.

[48] C. Lienard, R. Boisard, and C. Daudin, "Aerodynamic behavior of a floating offshore wind turbine," *AIAA J.*, vol. 58, no. 9, pp. 3835–3847, 2020, doi: 10.2514/1.J059255.

[49] L. Cambier, S. Heib, and S. Plot, "The Onera elsA CFD software: Input from research and feedback from industry," *Mech. Ind.*, vol. 14, no. 3, pp. 159–174, 2013, doi: 10.1051/meca/2013056.

[50] R. Kyle, Y. C. Lee, and W. G. Früh, "Propeller and vortex ring state for floating offshore wind turbines during surge," *Renew. Energy*, vol. 155, pp. 645–657, 2020, doi: 10.1016/j.renene.2020.03.105.

[51] V. Leroy, J. C. Gilloteaux, M. Lynch, A. Babarit, and P. Ferrant, "Impact of aerodynamic modeling on seakeeping performance of a floating horizontal axis wind turbine," *Wind Energy*, vol. 22, no. 8. pp. 1019–1033, 2019. doi: 10.1002/we.2337.

[52] A. Combourieu, M. Philippe, F. Rongère, and A. Babarit, "InWave: A new flexible design tool dedicated to wave energy converters," *Proceedings of the International Conference on Offshore Mechanics and Arctic Engineering - OMAE*, vol. 9B. 2014. doi: 10.1115/OMAE2014-24564.

[53] J. Murray and M. Barone, "The Development of CACTUS, a Wind and Marine Turbine Performance Simulation Code," no. January, pp. 1–21, 2011, doi: 10.2514/6.2011-147.

[54] M. Sayed, T. Lutz, E. Krämer, S. Shayegan, and R. Wüchner, "Aeroelastic analysis of 10 MW wind turbine using CFD–CSD explicit FSI-coupling approach," *J. Fluids Struct.*, vol. 87, pp. 354–377, 2019, doi: 10.1016/j.jfluidstructs.2019.03.023.

[55] R. F. Mikkelsen, *Actuator Disc Methods Applied to Wind Turbines*. 2004. [Online]. Available: http://orbit.dtu.dk/en/publications/actuator-disc-methods-applied-to-wind-turbines(baf52b7c-f8a4-4073-9925-ee985b59bb00).html

[56] J. B. de Vaal, M.O.L.Hansen, and T. Moan, "Effect of wind turbine surge motion on rotor thrust and induced velocity," *Wind Energy*, no. October 2012, pp. 1–20, 2013, doi: 10.1002/we.

[57] D. Micallef and T. Sant, "Loading effects on floating offshore horizontal axis wind turbines insurge motion," *Renew. Energy*, vol. 83, pp. 737–748, 2015, doi: 10.1016/j.renene.2015.05.016.

[58] T. Sant, *Improving BEM-based Aerodynamic Models in Wind Turbine Design Codes1*. 2007.

[59] U. Fernandez-Gamiz, E. Zulueta, A. Boyano, I. Ansoategui, and I. Uriarte, "Five megawatt wind turbine power output improvements by passive flow control devices," *Energies*, vol. 10, no. 6, 2017, doi: 10.3390/en10060742.

[60] G. R. Pirrung, H. A. Madsen, and S. Schreck, "Trailed vorticity modeling for aeroelastic wind turbine simulations in standstill," *Wind Energy Sci.*, vol. 2, no. 2, pp. 521–532, 2017, doi: 10.5194/wes-2-521-2017.

[61] V. A. Riziotis and S. G. Voutsinas, "Fatigue loads on wind turbines of different control strategies operating in complex terrain," *J. Wind Eng. Ind. Aerodyn.*, vol. 85, no. 3, pp. 211–240, 2000, doi: 10.1016/S0167-6105(99)00127-0.

[62] V. A. Riziotis, E. S. Politis, S. G. Voutsinas, and P. K. Chaviaropoulos, "Stability analysis of pitch-regulated, variable-speed wind turbines in closed loop operation using a linear eigenvalue approach," *Wind Energy*, vol. 11, no. 5, pp. 517–535, 2008, doi: 10.1002/we.276.

[63] J. M. Mauricio, A. E. León, A. Gómez-Expósito, and J. A. Solsona, "An electrical approach to mechanical effort reduction in wind energy conversion systems," *IEEE Trans. Energy Convers.*, vol. 23, no. 4, pp. 1108–1110, 2008, doi: 10.1109/TEC.2008.2001463.

[64] A. Ahlström, "Aeroelastic Simulation of Wind Turbine Dynamics," 2005.

[65] X. Jin, Y. He, L. Hua, and J. He, "Coupled Vibration Analysis of Wind Tturbine," *J. Vib. Shock*, vol. 26, no. 08, pp. 144-147,153, 2007.

[66] J. Jonkman, S. Butterfield, W. Musial, and G. Scott, "Definition of a 5-MW Reference Wind Turbine for Offshore System Development," 2009. doi: 10.1115/1.4038580.

[67] J. Jonkman, "Definition of the Floating System for Phase IV of OC3," *NREL*, vol. 1, no. May, p. 31, 2010, [Online]. Available: http://scholar.google.com/scholar?hl=en&btnG=Search&q=intitle:Definition+of+the+Floating+System+for+Phase+IV+of+OC3#0

[68] A. Robertson, J. Jonkman, F. Wendt, A. Goupee, and H. Dagher, *Definition of the OC5 DeepCwind Semisubmersible Floating System*, vol. 3, no. 4. 2016. [Online]. Available: http://www.osti.gov/servlets/purl/1155123/

[69] J. Jonkman and D. Matha, "A Quantitative Comparison of the Responses of Three Floating Platforms," *Eur. Offshore Wind 2009 Conf. Exhib.*, vol. 1, no. March, p. 21, 2010, [Online]. Available: http://www.nrel.gov/wind/pdfs/46726.pdf

[70] M. Karimirad and C. Michailides, "V-shaped semisubmersible offshore wind turbine: An alternative concept for offshore wind technology," *Renew. Energy*, vol. 83, pp. 126–143, 2015, doi: 10.1016/j.renene.2015.04.033.

[71] W. Shi, L. Zhang, J. You, M. Karimirad, and C. Michailides, "Hydrodynamic characteristics of the modified V-shaped Semi-floating offshore wind turbine with heave plates," *J. Phys. Conf. Ser.*, vol. 1356, no. 1, pp. 0–12, 2019, doi: 10.1088/1742-6596/1356/1/012017.

[72] M. Karimirad, Q. Meissonnier, Z. Gao, and T. Moan, "Hydroelastic code-to-code comparison for a tension leg spar-type floating wind turbine," *Mar. Struct.*, vol. 24, no. 4, pp. 412–435, 2011, doi: 10.1016/j.marstruc.2011.05.006.

[73] I. Fylling, K. Mo, K. Merz, and N. Luxcey, "Floating wind turbine-response analysis with rigid-body model," *Proc. Eur. Offshore Wind Conf. Exhib. Stock. Sweden.*, 2009.

[74] J. E. Withee, “Fully coupled dynamic analysis of a floating wind turbine system,” 2004.

[75] D. Matha, M. Schlipf, A. Cordle, R. Pereira, and J. Jonkman, “Challenges in simulation of aerodynamics, hydrodynamics, and mooring-line dynamics of floating offshore wind turbines,” *Proc. Int. Offshore Polar Eng. Conf.*, no. October, pp. 421–428, 2011.

[76] P. Cheng, Y. Huang, and D. Wan, “A numerical model for fully coupled aero-hydrodynamic analysis of floating offshore wind turbine,” *Ocean Eng.*, vol. 173, no. July 2018, pp. 183–196, 2019, doi: 10.1016/j.oceaneng.2018.12.021.

[77] J. M. Jonkman, “Dynamics of offshore floating wind turbines-model development and verification,” *Wind Energy*, vol. 12, no. 5, pp. 459–492, 2009, doi: 10.1002/we.347.

[78] J. M. Jonkman, *Dynamics Modeling and Loads Analysis of an Offshore Floating Wind Turbine*, vol. 8, no. 11. 2007. doi: 10.4161/hv.21225.

[79] A. Robertson *et al.*, “Definition of the Semisubmersible Floating System for Phase II of OC4,” 2014.

[80] A. N. Robertson *et al.*, “OC5 Project Phase II: Validation of Global Loads of the DeepCwind Floating Semisubmersible Wind Turbine,” *14th Deep Sea Offshore Wind R&D Conf.*, vol. 137, pp. 38–57, 2017, doi: 10.1016/j.egypro.2017.10.333.

[81] D. Matha and J. Jonkman, “Model Development and Loads Analysis of a Wind Turbine on a Floating Offshore Tension Leg Platform,” *Eur. Offshore Wind Conf.*, no. February, p. 129, 2010, [Online]. Available: http://www.nrel.gov/docs/fy10osti/46725.pdf

[82] K. Ramachandran and G. K. Vasanta, “A Numerical Model for a Floating TLP Wind Turbine A numerical model for a floating TLP wind turbine Department of Wind Energy Technical University of Denmark,” 2013.

[83] M. Karimirad and C. Michailides, “V-shaped semisubmersible offshore wind turbine subjected to misaligned wave and wind,” *J. Renew. Sustain. Energy*, vol. 8, no. 2, 2016, doi: 10.1063/1.4944964.

[84] F. Sandner, D. Schlipf, D. Matha, R. Seifried, and P. W. Cheng, “Reduced nonlinear model of a spar-mounted floating wind turbine,” in *Proceedings of the 11th German Wind Energy Conference DEWEK 2012, 7th-8th November 2012 in Bremen, Germany*, 2012, pp. 1–4.

[85] F. Lemmer, W. Yu, B. Luhmann, D. Schlipf, and P. W. Cheng, “Multibody modeling for concept-level floating offshore wind turbine design,” *Multibody Syst. Dyn.*, vol. 49, no. 2, pp. 203–236, 2020, doi: 10.1007/s11044-020-09729-x.

[86] Y. Yang, M. Bashir, C. Michailides, C. Li, and J. Wang, “Development and application of an aero-hydro-servo-elastic coupling framework for analysis of floating offshore wind turbines,” *Renew. Energy*, vol. 161, pp. 606–625, 2020, doi: 10.1016/j.renene.2020.07.134.

[87] M. Leimeister, A. Kolios, and M. Collu, “Development and verification of an aero-hydro-servo-elastic coupled model of dynamics for fowt, based on the MoWIT library,” *Energies*, vol. 13, no. 8, pp. 1–33, 2020, doi: 10.3390/en13081974.

[88] J. Chen, Z. Hu, D. Wan, and Q. Xiao, “Comparisons of the dynamical characteristics of a semi-submersible floating offshore wind turbine based on two different blade concepts,” *Ocean Eng.*, vol. 153, no. April 2017, pp. 305–318, 2018, doi: 10.1016/j.oceaneng.2018.01.104.

[89] N. Ramos-García, M. Sessarego, and S. G. Horcas, “Aero-hydro-servo-elastic coupling of a multi-body finite-element solver and a multi-fidelity vortex method,” *Wind Energy*, no. February 2020, pp. 1–21, 2020, doi: 10.1002/we.2584.

[90] Z. Lin, D. Cevasco, and M. Collu, “A methodology to develop reduced-order models to support the operation and maintenance of offshore wind turbines,” *Appl. Energy*, vol. 259, no. December 2019, p. 114228, 2020, doi: 10.1016/j.apenergy.2019.114228.

[91] M. Karimirad and T. Moan, “A simplified method for coupled analysis of floating offshore wind turbines,” *Mar. Struct.*, vol. 27, no. 1, pp. 45–63, 2012, doi: 10.1016/j.marstruc.2012.03.003.

[92] A. Beardsell, A. Alexandre, B. Child, R. Harries, and D. McCowen, "Beyond OC5 - Further advances in floating wind turbine modelling using Bladed," *J. Phys. Conf. Ser.*, vol. 1102, no. 1, 2018, doi: 10.1088/1742-6596/1102/1/012023.

[93] L. Sethuraman, Y. Xing, Z. Gao, V. Venugopal, M. Mueller, and T. Moan, "A 5MW direct-drive generator for floating spar-buoy wind turbine: Development and analysis of a fully coupled Mechanical model," *Proc. Inst. Mech. Eng. Part A J. Power Energy*, vol. 228, no. 7, pp. 718–741, 2014, doi: 10.1177/0957650914537262.

[94] S. Okpokparoro and S. Sriramula, "Uncertainty modeling in reliability analysis of floating wind turbine support structures," *Renew. Energy*, vol. 165, pp. 88–108, 2021, doi: 10.1016/j.renene.2020.10.068.

[95] NREL, *OpenFAST Documentation Release v2.5.0*. 2021. [Online]. Available: http://openfast.readthedocs.io/en/master/source/user/beamdyn/introduction.html

[96] T. Larsen and A. Hansen, *How 2 HAWC2, the user's manual*, vol. 2, no. May. 2019.

[97] E. Bossanyi, *GH Bladed Version 3.51 User Manual*. 2003. [Online]. Available: http://scholar.google.com/scholar?hl=en&btnG=Search&q=intitle:GH+Bladed+user+manual#0%5Cnhttp://scholar.google.com/scholar?hl=en&btnG=Search&q=intitle:GH+Bladed+User+Manual%230

[98] Z. Mingming, L. Xin, and X. Jianzhong, "Smart control of fatigue loads on a floating wind turbine with a tension-leg-platform," *Renew. Energy*, vol. 134, pp. 745–756, 2019, doi: 10.1016/j.renene.2018.11.079.

[99] Matthew Hannon, Eva Topham, James Dixon, David Mcmillan, and Maurizio Collu, "Offshore wind, ready to float? Global and UK trends in the floating offshore wind market", doi: 10.17868/69501.

[100] J. Liu and Z. Liu, "Harmonic analyzing of the double PWM converter in DFIG based on mathematical model," *Energies*, vol. 10, no. 12, pp. 1–19, 2017, doi: 10.3390/en10122087.

[101] X. Lie, Y. Liangzhong, and S. Christian, "Grid integration of large DFIG-based wind farms using VSC transmission," *IEEE Trans. Power Syst.*, vol. 22, no. 3, pp. 976–984, 2007, doi: 10.1109/TPWRS.2007.901306.

[102] B. Yang, L. Jiang, L. Wang, W. Yao, and Q. H. Wu, "Nonlinear maximum power point tracking control and modal analysis of DFIG based wind turbine," *Int. J. Electr. Power Energy Syst.*, vol. 74, pp. 429–436, 2016, doi: 10.1016/j.ijepes.2015.07.036.

[103] B. Yang, T. Yu, H. Shu, J. Dong, and L. Jiang, "Robust sliding-mode control of wind energy conversion systems for optimal power extraction via nonlinear perturbation observers," *Appl. Energy*, vol. 210, no. July 2017, pp. 711–723, 2018, doi: 10.1016/j.apenergy.2017.08.027.

[104] J. López, E. Gubía, P. Sanchis, X. Roboam, and L. Marroyo, "Wind turbines based on doubly fed induction generator under asymmetrical voltage dips," *IEEE Trans. Energy Convers.*, vol. 23, no. 1, pp. 321–330, 2008, doi: 10.1109/TEC.2007.914317.

[105] J. Ma, Z. Song, Y. Zhang, Y. Shen, and J. S. Thorp, "Model order reduction analysis of DFIG integration on the power system small-signal stability considering the virtual inertia control," *IET Gener. Transm. Distrib.*, vol. 11, no. 16, pp. 4087–4095, 2017, doi: 10.1049/iet-gtd.2017.0518.

[106] L. N. W. Arachchige, A. D. Rajapakse, and D. Muthumuni, "Implementation, comparison and application of an average simulation model of a wind turbine driven doubly fed induction generator," *Energies*, vol. 10, no. 11, 2017, doi: 10.3390/en10111726.

[107] S. Tammaruckwattana and K. Ohyama, "Modeling and simulation of permanent magnet synchronous generator wind power generation system using boost converter circuit," *2013 15th Eur. Conf. Power Electron. Appl. EPE 2013*, no. September, 2013, doi: 10.1109/EPE.2013.6634358.

[108] M. Singh, E. Muljadi, J. Jonkman, and V. Gevorgian, "Simulation for Wind Turbine Generators — With FAST and MATLAB-Simulink Modules," *Natl. Renew. Energy Labotory*, no. April, pp. 1–125, 2014.

[109] A. Akinrinde, A. Swanson, and R. Tiako, "Dynamic behavior of wind turbine generator configurations during ferroresonant conditions," *Energies*, vol. 12, no. 4, pp. 1–16, 2019, doi: 10.3390/en12040639.

[110] R. Fadaeinedjad, M. Moallem, and G. Moschopoulos, "Simulation of a wind turbine with doubly fed induction generator by FAST and Simulink," *IEEE Trans. Energy Convers.*, vol. 23, no. 2, pp. 690–700, 2008, doi: 10.1109/TEC.2007.914307.

[111] T. Utsunomiya, T. Sato, H. Matsukuma, and K. Yago, "Experimental Validation For Motion of a Spar-type Floating Offshore Wind Turbine Using 1/22.5 Scale Model," *OMAE2009*, pp. 1–9, 2009.

[112] G. Stewart and M. Muskulus, "A Review and Comparison of Floating Offshore Wind Turbine Model Experiments," *Energy Procedia*, vol. 94, no. 1876, pp. 227–231, 2016, doi: 10.1016/j.egypro.2016.09.228.

[113] A. J. Goupee, B. Koo, R. W. Kimball, K. F. Lambrakos, and H. J. Dagher, "Experimental comparison of three floating wind turbine concepts," *Proc. Int. Conf. Offshore Mech. Arct. Eng. - OMAE*, vol. 7, pp. 467–476, 2012, doi: 10.1115/OMAE2012-83645.

[114] M. Fowler, R. Kimball, D. A. T. Iii, and A. Goupee, "Wave basin model tests of floating offshore wind turbines," *Proc. ASME 32nd Int. Conf. Ocean. Offshore Arct. Eng.*, pp. 1–11, 2013.

[115] F. Duan, Z. Hu, G. Liu, and J. Wang, "Experimental comparisons of dynamic properties of floating wind turbine systems based on two different rotor concepts," *Appl. Ocean Res.*, vol. 58, pp. 266–280, 2016, doi: 10.1016/j.apor.2016.04.012.

[116] Fons Huijs, E.-J. de Ridder, and Feike Savenije, "Comparison of model tests and coupled simulations for a semi-submersible floating wind turbine.," *Proc. ASME 2014 33rd Int. Conf. Ocean. Offshore Arct. Eng.*, pp. 1–10, 2014.

[117] A. Jain, A. N. Robertson, J. M. Jonkman, A. J. Goupee, R. W. Kimball, and A. H. P. Swift, "Fast code verification of scaling laws for deepcwind floating wind system tests," *Proc. Int. Offshore Polar Eng. Conf.*, no. April, pp. 355–365, 2012.

[118] H. R. Martin, "Development of a scale model wind turbine for testing of offshore floating wind turbine systems," *Univ. Maine*, pp. 1–181, 2009, [Online]. Available: http://medcontent.metapress.com/index/A65RM03P4874243N.pdf%5Cnhttp://library.umaine.edu/theses/pdf/MartinH2011.pdf

[119] A. J. Coulling, A. J. Goupee, A. N. Robertson, J. M. Jonkman, and H. J. Dagher, "Validation of a FAST semi-submersible floating wind turbine numerical model with DeepCwind test data," *Journal of Renewable and Sustainable Energy*, vol. 5, no. 2. 2013. doi: 10.1063/1.4796197.

[120] Thomas Sauder, V. Chabaud, M. Thys, E. E. Bachynski, and Lars Ove Sæther, "Real-time hybrid model testing of a braceless semi-submersible wind turbine. Part I: The hybrid approach," *OMAE2016*, no. 3, pp. 1–12, 2016.

[121] A. M. Hemeida, W. a Farag, and O. a Mahgoub, "Modeling and Control of Direct Driven PMSG for Ultra Large Wind Turbines," *Eng. Technol.*, vol. 59, no. August 2015, pp. 918–924, 2011.

[122] H. Shariatpanah, R. Fadaeinedjad, and M. Rashidinejad, "A new model for PMSG-based wind turbine with yaw control," *IEEE Trans. Energy Convers.*, vol. 28, no. 4, pp. 929–937, 2013, doi: 10.1109/TEC.2013.2281814.

[123] D. S. Ochs, R. D. Miller, and W. N. White, "Simulation of electromechanical interactions of permanent-magnet direct-drive wind turbines using the fast aeroelastic simulator," *IEEE Trans. Sustain. Energy*, vol. 5, no. 1, pp. 2–9, 2014, doi: 10.1109/TSTE.2013.2269681.

[124] H. Malik and S. Mishra, "Application of Probabilistic Neural Network in Fault Diagnosis of Wind Turbine Using FAST, TurbSim and Simulink," *Procedia Comput. Sci.*, vol. 58, no. December 2014, pp. 186–193, 2015, doi: 10.1016/j.procs.2015.08.052.

[125] H. Malik and S. Mishra, "Artificial neural network and empirical mode decomposition based imbalance fault diagnosis of wind turbine using TurbSim, FAST and Simulink," *IET Renew. Power Gener.*, vol. 11, no. 6, pp. 889–902, 2017, doi: 10.1049/iet-rpg.2015.0382.

[126] A. Chen, *Parameter identification of Doubly-fed Wind Power Simulation Experiment Platform*. Harbin, 2012.

[127] C. Yang, *Active Control Strategies and Characteristics of Dyniamic Loads of Wind Turbine*. Chongqing: Chongqing University, 2015.

[128] M. Mata-Dumenjó, J. Sánchez-Navarro, M. Rossetti, A. Junyent-Ferré, and O. Gomis-Bellmunt, "Integrated simulation of a doubly fed induction generator wind turbine," in *2009 13th European Conference on Power Electronics and Applications, EPE '09*, 2009.

[129] S. Wang, *Research on Influence of Key Components on LVRT Characteristics of DFIG Wind Turbine*. China Electric Power Research Institute, 2015.

[130] F. Jia, X. Cai, Y. Lou, and Z. Li, "Interfacing technique and hardware-in-loop simulation of real-time co-simulation platform for wind energy conversion system," pp. 3030–3038, 2017, doi: 10.1049/iet-gtd.2016.1371.

[131] F. Miao, H. Shi, and X. Zhang, "Modelling ofWind Turbines Coupled in Multi-domain and Dynamic Response Analysis," *Proc. CSEE*, vol. 35, pp. 1704–1712, 2015.

[132] B. Li, H. Zhao, S. Gao, and S. Hu, "Digital real-time co-simulation platform of refined wind energy conversion system," *Int. J. Electr. Power Energy Syst.*, vol. 117, no. July 2019, p. 105676, 2020, doi: 10.1016/j.ijepes.2019.105676.

[133] J. Diao, *Refind Modeling and Real-time Simulation of Wind Farm Based on FAST and RT-LAB*. Jinan: Shandong University, 2020.

[134] L. Chen, J. Yang, and C. Lou, "Hydrodynamic Frequency Analysis based Floating OWT Power Quality Mitigation," in *2023 IEEE Sustainable Power and Energy Conference (iSPEC)*, 2023, pp. 1–6. doi: 10.1109/iSPEC58282.2023.10403087.

[135] IEA, *Renewables 2019 – Market analysis and forecast from 2019 to 2024*. 2019. [Online]. Available: https://www.iea.org/reports/renewables-2019

[136] W. Musial, D. Heimiller, P. Beiter, G. Scott, and C. Draxl, *2016 Offshore Wind Energy Resource Assessment for the United States*, no. September. 2016.

[137] M. Lochmann, H. Kalesse-Los, M. Schäfer, I. Heinrich, and R. Leinweber, "Analysing wind power ramp events and improving very short-term wind power predictions by including wind speed observations," *Wind Energy*, vol. 26, no. 6, pp. 573–588, 2023, doi: https://doi.org/10.1002/we.2816.

[138] M. Cui, J. Zhang, C. Feng, A. R. Florita, Y. Sun, and B. M. Hodge, "Characterizing and analyzing ramping events in wind power, solar power, load, and netload," *Renew. Energy*, vol. 111, pp. 227–244, Oct. 2017, doi: 10.1016/J.RENENE.2017.04.005.

[139] J. Hu, L. Zhang, J. Tang, and Z. Liu, "A novel transformer ordinal regression network with label diversity for wind power ramp events forecasting," *Energy*, vol. 280, p. 128075, Oct. 2023, doi: 10.1016/J.ENERGY.2023.128075.

[140] S. Das and B. Singh, "Mitigating Impact of High Power Ramp Rates in Utility Grid Integrated Wind-Solar System Using an RLMAT Adaptive Control Strategy," *IEEE Trans. Energy Convers.*, vol. 38, no. 1, pp. 343–354, 2023, doi: 10.1109/TEC.2022.3192994.

[141] X. Jin *et al.*, "Wasserstein metric-based two-stage distributionally robust optimization model for optimal daily peak shaving dispatch of cascade hydroplants under renewable energy uncertainties," *Energy*, vol. 260, p. 125107, Dec. 2022, doi: 10.1016/J.ENERGY.2022.125107.

[142] X. Fang, Q. Hu, R. Bo, and F. Li, "Redesigning capacity market to include flexibility via ramp constraints in high-renewable penetrated system," *Int. J. Electr. Power Energy Syst.*, vol. 128, p. 106677, Jun. 2021, doi: 10.1016/J.IJEPES.2020.106677.

[143] Y. Fujimoto, Y. Takahashi, and Y. Hayashi, "Alerting to Rare Large-Scale Ramp Events in Wind Power Generation," *IEEE Trans. Sustain. Energy*, vol. 10, no. 1, pp. 55–65, 2019, doi: 10.1109/TSTE.2018.2822807.

[144] H. Fan *et al.*, "Fluctuation pattern recognition based ultra-short-term wind power probabilistic forecasting method," *Energy*, vol. 266, p. 126420, Mar. 2023, doi: 10.1016/J.ENERGY.2022.126420.

[145] F. Wang *et al.*, "Wind process pattern forecasting based ultra-short-term wind speed hybrid prediction," *Energy*, vol. 255, p. 124509, Sep. 2022, doi: 10.1016/J.ENERGY.2022.124509.

[146] M. T. Qaiser, J. Ejaz, O. Osen, and A. Hasan, "Digital twin-driven energy modeling of Hywind Tampen floating wind farm," *Energy Reports*, vol. 9, pp. 284–289, Oct. 2023, doi: 10.1016/J.EGYR.2023.09.023.

[147] Y. Guo, X. Wang, Y. Mei, Z. Ye, and X. Guo, "Effect of coupled platform pitch-surge motions on the aerodynamic characters of a horizontal floating offshore wind turbine," *Renew. Energy*, vol. 196, pp. 278–297, Aug. 2022, doi: 10.1016/J.RENENE.2022.06.108.

[148] B. Golparvar, P. Papadopoulos, A. A. Ezzat, and R. Q. Wang, "A surrogate-model-based approach for estimating the first and second-order moments of offshore wind power," *Appl. Energy*, vol. 299, p. 117286, Oct. 2021, doi: 10.1016/J.APENERGY.2021.117286.

[149] J. Carmona-Sanchez, Z. Lin, M. Collu, M. Barnes, O. Marjanovic, and D. Cevasco, "An analysis of the impact of an advanced aero-hydro-servo-elastic model of dynamics on the generator-converter dynamics, for an offshore fixed 5MW PMSG wind turbine," *IET Conf. Publ.*, vol. 2019, no. CP751, pp. 1–6, 2019, doi: 10.1049/cp.2019.0080.

[150] F. Meng *et al.*, "Co-located offshore wind–wave energy systems: Can motion suppression and reliable power generation be achieved simultaneously?," *Appl. Energy*, vol. 331, p. 120373, Feb. 2023, doi: 10.1016/J.APENERGY.2022.120373.

[151] A. C. P. A. S. Committee, *ACP 61400-1-202x: Wind Energy Generation Systems – Part 1: Design requirements – Modified Adoption of IEC 61400-1*, 4th ed. Washington DC, 2019.

[152] P. Rosas, *Dynamic influences of wind power on the power system*. 2004. [Online]. Available: http://www.risoe.dk/rispubl/vea/veapdf/ris-r-1408.pdf

[153] T. Pan and Z. Ma, "Wind turbine individual pitch control for load reduction based on fuzzy controller design," *Proc. Inst. Mech. Eng. Part I J. Syst. Control Eng.*, vol. 227, no. 3, pp. 320–328, 2013, doi: 10.1177/0959651812466526.

[154] S. Das, N. Karnik, and S. Santoso, "Time-Domain Modeling of Tower Shadow and Wind Shear in Wind Turbines," *ISRN Renew. Energy*, vol. 2011, pp. 1–11, 2011, doi: 10.5402/2011/890582.

[155] Y. Xia, K. H. Ahmed, and B. W. Williams, "Wind turbine power coefficient analysis of a new maximum power point tracking technique," *IEEE Trans. Ind. Electron.*, vol. 60, no. 3, pp. 1122–1132, 2013, doi: 10.1109/TIE.2012.2206332.

[156] Q. Xing-hong, L. Yong, Y. Jun, and L. Ren, "Design of Grid-connected Converter for a Permanent Magnet Synchronous Direct-drive Wind Power Generation System.pdf," *Power Electron.*, vol. 42, no. 3, pp. 22–34, 2008.

[157] R. Y. Yang, C. W. Wang, C. C. Huang, C. H. Chung, C. P. Chen, and C. J. Huang, "The 1:20 scaled hydraulic model test and field experiment of barge-type floating offshore wind turbine system," *Ocean Eng.*, vol. 247, p. 110486, Mar. 2022, doi: 10.1016/J.OCEANENG.2021.110486.

[158] L. Chen and B. Basu, "Wave-current interaction effects on structural responses of floating offshore wind turbines," *Wind Energy*, vol. 22, no. 2, pp. 327–339, 2019, doi: 10.1002/we.2288.

[159] B.J. Jonkman, *TurbSim User's Guide : Version 1.50*, no. September. 2009.

[160] D. J. T. Carter, "Prediction of wave height and period for a constant wind velocity using the JONSWAP results," *Ocean Eng.*, vol. 9, no. 1, pp. 17–33, Jan. 1982, doi: 10.1016/0029-8018(82)90042-7.

[161] R. L. Soulsby, "Simplified calculation of wave orbital velocities," *HR Wallingford Rep. TR 155*, no. Report TR 155, p. 12, 2006, [Online]. Available: http://eprints.hrwallingford.co.uk/692/1/TR155.pdf

[162] M. Cui, J. Zhang, A. R. Florita, B. M. Hodge, D. Ke, and Y. Sun, "An optimized swinging door algorithm for identifying wind ramping events," *IEEE Trans. Sustain. Energy*, vol. 7, no. 1, pp. 150–162, 2016, doi: 10.1109/TSTE.2015.2477244.

[163] R. Hemmati, H. Mehrjerdi, M. Shafie-Khah, P. Siano, and J. P. S. Catalao, "Managing multitype capacity resources for frequency regulation in unit commitment integrated with large wind ramping," *IEEE Trans. Sustain. Energy*, vol. 12, no. 1, pp. 705–714, 2021, doi: 10.1109/TSTE.2020.3017231.

[164] D. Lyners, H. Vermeulen, and M. Groch, "Wind power ramp event detection using a multi-parameter segmentation algorithm," *Energy Reports*, vol. 7, pp. 5536–5548, Nov. 2021, doi: 10.1016/J.EGYR.2021.08.137.

[165] T. Ackermann, *Wind Power in Power Systems*. 2005. doi: 10.1002/0470012684.

[166] M. J. Muliawan, M. Karimirad, Z. Gao, and T. Moan, "Extreme responses of a combined spar-type floating wind turbine and floating wave energy converter (STC) system with survival modes," *Ocean Eng.*, vol. 65, pp. 71–82, 2013, doi: 10.1016/j.oceaneng.2013.03.002.

[167] J. J. Yang and E. M. He, "Coupled modeling and structural vibration control for floating offshore wind turbine," *Renew. Energy*, vol. 157, pp. 678–694, 2020, doi: 10.1016/j.renene.2020.05.075.

[168] S. Earle, *Physical Geology- 2nd Edition*. 2019. [Online]. Available: http://www.springer.com/978-0-387-35416-3

[169] T. J. Larsen and T. D. Hanson, "A method to avoid negative damped low frequent tower vibrations for a floating, pitch controlled wind turbine," *J. Phys. Conf. Ser.*, vol. 75, p. 012073, Jul. 2007, doi: 10.1088/1742-6596/75/1/012073.

[170] L. V. Andersen, M. J. Vahdatirad, M. T. Sichani, and J. D. Sørensen, "Natural frequencies of wind turbines on monopile foundations in clayey soils—A probabilistic approach," *Comput. Geotech.*, vol. 43, pp. 1–11, Jun. 2012, doi: 10.1016/J.COMPGEO.2012.01.010.

[171] Y. Wang, W. Shi, C. Michailides, L. Wan, H. Kim, and X. Li, "WEC shape effect on the motion response and power performance of a combined wind-wave energy converter," *Ocean Eng.*, vol. 250, p. 111038, Apr. 2022, doi: 10.1016/j.oceaneng.2022.111038.

[172] R. Yang, J. Jin, Q. Zhou, M. Zhang, S. Jiang, and X. Chen, "Superconducting Magnetic Energy Storage Integrated Current-source DC/DC Converter for Voltage Stabilization and Power Regulation in DFIG-based DC Power Systems," *J. Mod. Power Syst. Clean Energy*, vol. 11, no. 4, pp. 1356–1369, 2023, doi: 10.35833/MPCE.2022.000051.

[173] R. Chen, J. Zeng, X. Huang, and J. Liu, "An H∞ filter based active damping control strategy for grid-connected inverters with LCL filter applied to wind power system," *Int. J. Electr. Power Energy Syst.*, vol. 144, p. 108590, Jan. 2023, doi: 10.1016/J.IJEPES.2022.108590.

[174] Q. Hassan, S. Algburi, A. Z. Sameen, H. M. Salman, and M. Jaszczur, "A review of hybrid renewable energy systems: Solar and wind-powered solutions: Challenges, opportunities, and policy implications," *Results Eng.*, vol. 20, p. 101621, Dec. 2023, doi: 10.1016/J.RINENG.2023.101621.

[175] H. Kord, A. A. Zamani, and S. M. Barakati, "Active hybrid energy storage management in a wind-dominated standalone system with robust fractional-order controller optimized by Gases Brownian Motion Optimization Algorithm," *J. Energy Storage*, vol. 66, p. 107492, Aug. 2023, doi: 10.1016/J.EST.2023.107492.

[176] A. M. Al-Orabi, M. G. Osman, and B. E. Sedhom, "Evaluation of green hydrogen production using solar, wind, and hybrid technologies under various technical and financial scenarios for multi-sites in Egypt," *Int. J. Hydrogen Energy*, Jul. 2023, doi: 10.1016/J.IJHYDENE.2023.06.218.

[177] X. Sun, H. He, and L. Ma, "Harmony search meta-heuristic algorithm based on the optimal sizing of wind-battery hybrid micro-grid power system with different battery technologies," *J. Energy Storage*, vol. 75, p. 109582, Jan. 2024, doi: 10.1016/J.EST.2023.109582.

[178] L. Lin, Y. Cao, X. Kong, Y. Lin, Y. Jia, and Z. Zhang, "Hybrid energy storage system control and capacity allocation considering battery state of charge self-recovery and capacity attenuation in wind farm," *J. Energy Storage*, vol. 75, p. 109693, Jan. 2024, doi: 10.1016/J.EST.2023.109693.

[179] L. W. Chong, Y. W. Wong, R. K. Rajkumar, R. K. Rajkumar, and D. Isa, "Hybrid energy storage systems and control strategies for stand-alone renewable energy power systems," *Renew. Sustain. Energy Rev.*, vol. 66, pp. 174–189, Dec. 2016, doi: 10.1016/J.RSER.2016.07.059.

[180] J. Shi, L. Wang, W. J. Lee, X. Cheng, and X. Zong, "Hybrid Energy Storage System (HESS) optimization enabling very short-term wind power generation scheduling based on output feature extraction," *Appl. Energy*, vol. 256, p. 113915, Dec. 2019, doi: 10.1016/J.APENERGY.2019.113915.

[181] C. Pan, H. Fan, R. Zhang, J. Sun, Y. Wang, and Y. Sun, "An improved multi-timescale coordinated control strategy for an integrated energy system with a hybrid energy storage system," *Appl. Energy*, vol. 343, p. 121137, Aug. 2023, doi: 10.1016/J.APENERGY.2023.121137.

[182] A. Biswas, P. G. Anselma, A. Rathore, and A. Emadi, "Effect of coordinated control on real-time optimal mode selection for multi-mode hybrid electric powertrain," *Appl. Energy*, vol. 289, p. 116695, May 2021, doi: 10.1016/J.APENERGY.2021.116695.

[183] N. Belbachir, S. Kamel, M. H. Hassan, and M. Zellagui, "Optimizing energy management of hybrid wind generation-battery energy storage units with long-term memory artificial hummingbird algorithm under daily load-source uncertainties in electrical networks," *J. Energy Storage*, vol. 78, p. 110288, Feb. 2024, doi: 10.1016/J.EST.2023.110288.

[184] S. Song, H. Wei, Y. Lin, C. Wang, and A. Gómez-Expósito, "A Holistic State Estimation Framework for Active Distribution Network with Battery Energy Storage System," *J. Mod. Power Syst. Clean Energy*, vol. 10, no. 3, pp. 627–636, 2022, doi: 10.35833/MPCE.2020.000613.

[185] T. Wizelius, "Design and Implementation of a Wind Power Project," *Compr. Renew. Energy, Second Ed. Vol. 1-9*, vol. 1–2, pp. 390–429, Jan. 2022, doi: 10.1016/B978-0-12-819727-1.00155-2.

[186] M. López, N. Rodríguez, and G. Iglesias, "Combined floating offshore wind and solar PV," *J. Mar. Sci. Eng.*, vol. 8, no. 8, 2020, doi: 10.3390/JMSE8080576.

[187] Y. Zhang, Y. Zhao, W. Sun, and J. Li, "Ocean wave energy converters: Technical principle, device realization, and performance evaluation," *Renew. Sustain. Energy Rev.*, vol. 141, p. 110764, May 2021, doi: 10.1016/J.RSER.2021.110764.

[188] E. C. Edwards, A. Holcombe, S. Brown, E. Ransley, M. Hann, and D. Greaves, "Evolution of floating offshore wind platforms: A review of at-sea devices," *Renew. Sustain. Energy Rev.*, vol. 183, p. 113416, Sep. 2023, doi: 10.1016/J.RSER.2023.113416.

[189] G. Li and W. Zhu, "Tidal current energy harvesting technologies: A review of current status and life cycle assessment," *Renew. Sustain. Energy Rev.*, vol. 179, p. 113269, Jun. 2023, doi: 10.1016/J.RSER.2023.113269.

[190] J. Langer, J. Quist, and K. Blok, "Recent progress in the economics of ocean thermal energy conversion: Critical review and research agenda," *Renew. Sustain. Energy Rev.*, vol. 130, p. 109960, Sep. 2020, doi: 10.1016/J.RSER.2020.109960.

[191] X. Zhou *et al.*, "An electrochemical system for salinity gradient energy harvesting," *Energy Convers. Manag.*, vol. 255, p. 115315, Mar. 2022, doi: 10.1016/J.ENCONMAN.2022.115315.

[192] H. M. Pouran, M. Padilha Campos Lopes, T. Nogueira, D. Alves Castelo Branco, and Y. Sheng, "Environmental and technical impacts of floating photovoltaic plants as an emerging clean energy technology," *iScience*, vol. 25, no. 11, p. 105253, Nov. 2022, doi: 10.1016/J.ISCI.2022.105253.

[193] C. Bi and A. W. K. Law, "Co-locating offshore wind and floating solar farms – Effect of high wind and wave conditions on solar power performance," *Energy*, vol. 266, p. 126437, Mar. 2023, doi: 10.1016/J.ENERGY.2022.126437.

[194] F. Zeng, C. Bi, D. Sree, G. Huang, N. Zhang, and A. W.-K. Law, "An Adaptive Barrier-Mooring System for Coastal Floating Solar Farms," *Appl. Energy*, vol. 348, p. 121618, Oct. 2023, doi: 10.1016/J.APENERGY.2023.121618.

[195] S. M. Choi, C. D. Park, S. H. Cho, and B. J. Lim, "Effects of wind loads on the solar panel array of a floating photovoltaic system – Experimental study and economic analysis," *Energy*, vol. 256, p. 124649, Oct. 2022, doi: 10.1016/J.ENERGY.2022.124649.

[196] O. Delbeke, J. D. Moschner, and J. Driesen, "The complementarity of offshore wind and floating photovoltaics in the Belgian North Sea, an analysis up to 2100," *Renew. Energy*, vol. 218, p. 119253, Dec. 2023, doi: 10.1016/J.RENENE.2023.119253.

[197] S. Z. M. Golroodbari *et al.*, "Pooling the cable: A techno-economic feasibility study of integrating offshore floating photovoltaic solar technology within an offshore wind park," *Sol. Energy*, vol. 219, pp. 65–74, May 2021, doi: 10.1016/J.SOLENER.2020.12.062.

[198] A. Ghosh, "A comprehensive review of water based PV: Flotavoltaics, under water, offshore & canal top," *Ocean Eng.*, vol. 281, p. 115044, Aug. 2023, doi: 10.1016/J.OCEANENG.2023.115044.

[199] S. R. Ara, S. Paul, and Z. H. Rather, "Two-level planning approach to analyze techno-economic feasibility of hybrid offshore wind-solar pv power plants," *Sustain. Energy Technol. Assessments*, vol. 47, p. 101509, Oct. 2021, doi: 10.1016/J.SETA.2021.101509.

[200] A. Yde, T. J. Larsen, A. M. Hansen, M. Fernandez, and S. Bellew, "Comparison of simulations and offshore measurement data of a combined floating wind and wave energy demonstration platform," *J. Ocean Wind Energy*, vol. 2, no. 3, pp. 129–137, 2015, doi: 10.17736/jowe.2015.jcr34.

[201] P. Aboutalebi, F. M'zoughi, I. Garrido, and A. J. Garrido, "A control technique for hybrid floating offshore wind turbines using oscillating water columns for generated power fluctuation reduction," *J. Comput. Des. Eng.*, vol. 10, no. 1, pp. 250–265, 2023, doi: 10.1093/jcde/qwac137.

[202] Y. Zhai, H. Zhao, X. Li, and W. Shi, "Design and Dynamic Analysis of a Novel Large-Scale Barge-Type Floating Offshore Wind Turbine with Aquaculture Cage," *J. Mar. Sci. Eng.*, vol. 10, no. 12, 2022, doi: 10.3390/jmse10121926.

[203] J. Cutler, M. Bashir, Y. Yang, J. Wang, and S. Loughney, "Preliminary development of a novel catamaran floating offshore wind turbine platform and assessment of dynamic behaviours for intermediate water depth application," *Ocean Eng.*, vol. 258, p. 111769, Aug. 2022, doi: 10.1016/J.OCEANENG.2022.111769.

[204] D. Zhang *et al.*, "A coupled numerical framework for hybrid floating offshore wind turbine and oscillating water column wave energy converters," *Energy Convers. Manag.*, vol. 267, p. 115933, Sep. 2022, doi: 10.1016/J.ENCONMAN.2022.115933.

[205] T. Zhang, P. W. Stackhouse, B. Macpherson, and J. C. Mikovitz, "A solar azimuth formula that renders circumstantial treatment unnecessary without compromising mathematical rigor: Mathematical setup, application and extension of a formula based on the subsolar point and atan2 function," *Renew. Energy*, vol. 172, pp. 1333–1340, Jul. 2021, doi: 10.1016/J.RENENE.2021.03.047.

[206] P. G. Loutzenhiser, H. Manz, C. Felsmann, P. A. Strachan, T. Frank, and G. M. Maxwell, "Empirical validation of models to compute solar irradiance on inclined surfaces for building energy simulation," *Sol. Energy*, vol. 81, no. 2, pp. 254–267, Feb. 2007, doi: 10.1016/J.SOLENER.2006.03.009.

[207] A. Alcañiz, N. Monaco, O. Isabella, and H. Ziar, "Offshore floating PV–DC and AC yield analysis considering wave effects," *Energy Convers. Manag.*, vol. 300, p. 117897, Jan. 2024, doi: 10.1016/J.ENCONMAN.2023.117897.

[208] T. C. Chuang, W. H. Yang, and R. Y. Yang, "Experimental and numerical study of a barge-type FOWT platform under wind and wave load," *Ocean Eng.*, vol. 230, p. 109015, Jun. 2021, doi: 10.1016/J.OCEANENG.2021.109015.

[209] "Annual Statistic Report of Oceanographical Observation Data in Peng-Hu Offshoe Region at 2019," 2019. [Online]. Available: https://www.ihmt.gov.tw/periodical/pdf/B1100390.pdf

[210] J. R. C.- Inst. and E. Transp, "JRC. Photovoltaic geographical information system (PVGIS)." [Online]. Available: https://re.jrc.ec.europa.eu/pvg_tools/en/

[211] "AIKO-A-MAH54Mw Datasheet," 2023. [Online]. Available: https://aikosolar.com/static/pdfjs/web/viewer.html?file=/wp-content/uploads/2023/10/N-Type_ABC_module_Aiko-A-MAH54Mw_450-465W_en.pdf

[212] J. F. Geisz *et al.*, "Six-junction III–V solar cells with 47.1% conversion efficiency under 143 Suns concentration," *Nat. Energy*, vol. 5, no. 4, pp. 326–335, 2020, doi: 10.1038/s41560-020-0598-5.

[213] H. Helmers *et al.*, "68.9% Efficient GaAs-Based Photonic Power Conversion Enabled by Photon Recycling and Optical Resonance," *Phys. Status Solidi - Rapid Res. Lett.*, vol. 15, no. 7, pp. 1–7, 2021, doi: 10.1002/pssr.202100113.

[214] Y. Si *et al.*, "The influence of power-take-off control on the dynamic response and power output of combined semi-submersible floating wind turbine and point-absorber wave energy converters," *Ocean Eng.*, vol. 227, p. 108835, May 2021, doi: 10.1016/J.OCEANENG.2021.108835.

[215] H. Yazdi, H. R. Ghafari, H. Ghassemi, G. He, and M. Karimirad, "Wave power extraction by Multi-Salter's duck WECs arrayed on the floating offshore wind turbine platform," *Energy*, vol. 278, p. 127930, Sep. 2023, doi: 10.1016/J.ENERGY.2023.127930.

[216] M. Neshat *et al.*, "Enhancing the performance of hybrid wave-wind energy systems through a fast and adaptive chaotic multi-objective swarm optimisation method," *Appl. Energy*, vol. 362, p. 122955, May 2024, doi: 10.1016/J.APENERGY.2024.122955.

# Appendix A: OpSDA code for WPRE characterization

```
% Generate and input data array
data = [t0, pr3];  % Sample data, the first column is time, and the
second column is power
% Backup original data
backup_data = data;

% Set step size
time_step = 0.002;
% Custom data processing interval
data_processing_interval = 200;
% Select threshold width
threshold_width = 1;
% Select the function in step 5
function_type = 0; % (0: do nothing)/(1: delete slopes with absolute
values less than 1.05)/(2: delete slopes with absolute values less
than 3)

% Step 1: Generate trends of upward and downward slopes
upward_trends = [];  % Store upward trends
downward_trends = [];  % Store downward trends

for i = 2:data_processing_interval:size(data, 1)
    delta_time = data(i, 1) - data(i - 1, 1);
    delta_power = data(i, 2) - data(i - 1, 2);
    slope = delta_power / delta_time;

    if slope > 0
        upward_trends = [upward_trends; data(i - 1, 1), data(i - 1, 2),
data(i, 1), data(i, 2), delta_time, delta_power];
    elseif slope < 0
        downward_trends = [downward_trends; data(i - 1, 1), data(i - 1,
2), data(i, 1), data(i, 2), delta_time, delta_power];
    end
end

% Step 2+3: Merge adjacent trends
combined_trends = sortrows([upward_trends; downward_trends]);
merged_trends = merge_trends(combined_trends, threshold_width,
data_processing_interval);

% Step 4: Remove spikes
filtered_trends = merged_trends;

i = 1;
while i <= size(filtered_trends, 1)
    if abs(filtered_trends(i, 6)) < 0.00
        filtered_trends(i, :) = [];  % Delete flat trends
    else
        i = i + 1;
    end
end

% Step 2+3: Merge adjacent trends
combined_trends = sortrows([upward_trends; downward_trends]);
merged_trends = merge_trends(combined_trends, threshold_width,
data_processing_interval);

% Step 5: Process according to the selected function
```

```
if function_type == 1
    % Function 1: Delete slopes with absolute values less than 1.05
    filtered_trends(abs(filtered_trends(:, 6)) < 1.05, :) = [];
elseif function_type == 2
    % Function 2: Delete slopes with absolute values less than 3
    slope_rate = filtered_trends(:, 6) ./ (filtered_trends(:, 5) *
time_step);
    filtered_trends(abs(slope_rate) < 3, :) = [];
else
    % Function 0: Do nothing
end

smoothed_output = filtered_trends;

% Plot the comparison between data processing results and raw data
figure;
subplot(2, 1, 1);
plot(backup_data(:, 1), backup_data(:, 2), '-b', 'LineWidth', 1.5);
hold on;
plot(filtered_trends(:, 1), filtered_trends(:, 2), '-r', 'LineWidth',
1.5);
title('Raw Data and Processed Data');
legend('Raw Data', 'Processed Data');

subplot(2, 1, 2);
plot(backup_data(:, 1), backup_data(:, 2), '-b', 'LineWidth', 1.5);
hold on;

% Plot merged trend segments
for i = 1:size(filtered_trends, 1)-1
    if filtered_trends(i+1, 2) > filtered_trends(i, 2)
        if abs(filtered_trends(i+1, 2) - filtered_trends(i, 2)) > 0.05
            plot([filtered_trends(i, 1), filtered_trends(i+1, 1)],
[filtered_trends(i, 2), filtered_trends(i+1, 2)], 'r', 'LineWidth', 2);
        end
    elseif filtered_trends(i+1, 2) < filtered_trends(i, 2)
        if abs(filtered_trends(i+1, 2) - filtered_trends(i, 2)) > 0.05
            plot([filtered_trends(i, 1), filtered_trends(i+1, 1)],
[filtered_trends(i, 2), filtered_trends(i+1, 2)], 'g', 'LineWidth', 2);
        end
    end
end

title('Raw Data and Merged Trend Segments');
legend('Raw Data', 'Merged Trend Segments');

% Merge trend function
function merged_trends = merge_trends(trends, threshold_width,
data_processing_interval)
    merged_trends = trends;

    i = 1;
    while i < size(merged_trends, 1)
        current_trend = merged_trends(i, :);
        j = i + 1;

        while j <= size(merged_trends, 1) && ...
              sign(merged_trends(j, 6)) == sign(current_trend(6))
&& ...
              abs(merged_trends(j, 1) - current_trend(3)) <=
data_processing_interval
```

```
            % Calculate line parameters (k*x + b) and determine
successful ranges
            k = (current_trend(4) - current_trend(2)) /
(current_trend(3) - current_trend(1));
            b0 = current_trend(2) - k * current_trend(1);
            b1 = merged_trends(j, 2) - k * merged_trends(j, 1);
            b2 = current_trend(4) - k * current_trend(3);

            % Check if intercepts meet the condition
            if (b1 >= b0 - threshold_width && b1 <= b0 +
threshold_width) && ...
               (b2 >= b0 - threshold_width && b2 <= b0 +
threshold_width)

                current_trend(3) = merged_trends(j, 3);
                current_trend(4) = merged_trends(j, 4);
                current_trend(5) = current_trend(3) - current_trend(1);
                current_trend(6) = current_trend(4) - current_trend(2);

                merged_trends(i, :) = current_trend;
                merged_trends(j, :) = [];  % Delete merged trends

            else
                j = j + 1;  % Continue to check the next trend
            end
        end

        i = i + 1;
    end
end
```

**The code should run a second time with adjusted parameters, taking input from the outcome of the first run.**

# Appendix B: Raw data of Max WPREs

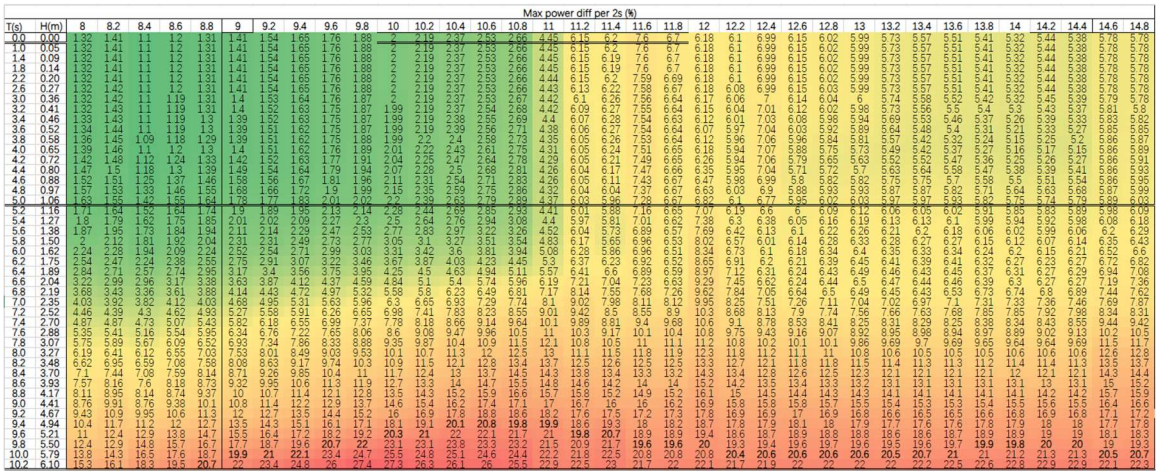

Max power diff per 2s (%)

| T(s) | H(m) | 8 | 8.2 | 8.4 | 8.6 | 8.8 | 9 | 9.2 | 9.4 | 9.6 | 9.8 | 10 | 10.2 | 10.4 | 10.6 | 10.8 | 11 | 11.2 | 11.4 | 11.6 | 11.8 | 12 | 12.2 | 12.4 | 12.6 | 12.8 | 13 | 13.2 | 13.4 | 13.6 | 13.8 | 14 | 14.2 | 14.4 | 14.6 | 14.8 |
|---|---|---|---|---|---|---|---|---|---|---|---|---|---|---|---|---|---|---|---|---|---|---|---|---|---|---|---|---|---|---|---|---|---|---|---|---|
| 0.0 | 0.00 | 1.32 | 1.41 | 1.1 | 1.2 | 1.31 | 1.41 | 1.54 | 1.65 | 1.76 | 1.88 | 2 | 2.19 | 2.37 | 2.53 | 2.66 | 2.45 | 6.15 | 6.2 | 7.6 | 6.7 | 6.18 | 6.1 | 6.99 | 6.15 | 6.02 | 5.99 | 5.73 | 5.57 | 5.51 | 5.41 | 5.32 | 5.44 | 5.38 | 5.78 | 5.78 |
| 1.0 | 0.05 | 1.32 | 1.41 | 1.1 | 1.2 | 1.31 | 1.41 | 1.54 | 1.65 | 1.76 | 1.88 | 2 | 2.19 | 2.37 | 2.53 | 2.66 | 4.45 | 6.15 | 6.2 | 7.6 | 6.7 | 6.18 | 6.1 | 6.99 | 6.15 | 6.02 | 5.99 | 5.73 | 5.57 | 5.51 | 5.41 | 5.32 | 5.44 | 5.38 | 5.78 | 5.78 |
| 1.4 | 0.09 | 1.32 | 1.41 | 1.1 | 1.2 | 1.31 | 1.41 | 1.54 | 1.65 | 1.76 | 1.88 | 2 | 2.19 | 2.37 | 2.53 | 2.66 | 4.45 | 6.15 | 6.19 | 7.6 | 6.7 | 6.18 | 6.1 | 6.99 | 6.15 | 6.02 | 5.99 | 5.73 | 5.57 | 5.51 | 5.41 | 5.32 | 5.44 | 5.38 | 5.78 | 5.78 |
| 1.8 | 0.14 | 1.32 | 1.41 | 1.1 | 1.2 | 1.31 | 1.41 | 1.54 | 1.65 | 1.76 | 1.88 | 2 | 2.19 | 2.37 | 2.53 | 2.66 | 4.45 | 6.15 | 6.19 | 7.6 | 6.7 | 6.18 | 6.1 | 6.99 | 6.15 | 6.02 | 5.99 | 5.73 | 5.57 | 5.51 | 5.41 | 5.32 | 5.44 | 5.38 | 5.78 | 5.78 |
| 2.2 | 0.20 | 1.32 | 1.41 | 1.1 | 1.2 | 1.31 | 1.41 | 1.54 | 1.65 | 1.76 | 1.88 | 2 | 2.19 | 2.37 | 2.53 | 2.66 | 4.44 | 6.15 | 6.2 | 7.59 | 6.69 | 6.18 | 6.1 | 6.99 | 6.15 | 6.03 | 5.99 | 5.73 | 5.57 | 5.51 | 5.41 | 5.32 | 5.44 | 5.38 | 5.78 | 5.78 |
| 2.6 | 0.27 | 1.32 | 1.42 | 1.1 | 1.2 | 1.31 | 1.41 | 1.54 | 1.65 | 1.76 | 1.88 | 2 | 2.19 | 2.37 | 2.53 | 2.66 | 4.43 | 6.13 | 6.22 | 7.58 | 6.67 | 6.18 | 6.08 | 6.99 | 6.15 | 6.03 | 5.99 | 5.73 | 5.57 | 5.51 | 5.41 | 5.32 | 5.44 | 5.38 | 5.78 | 5.78 |
| 3.0 | 0.36 | 1.32 | 1.42 | 1.1 | 1.19 | 1.31 | 1.4 | 1.53 | 1.64 | 1.76 | 1.87 | 2 | 2.19 | 2.37 | 2.53 | 2.67 | 4.42 | 6.1 | 6.26 | 7.56 | 6.64 | 6.17 | 6.06 | 7 | 6.14 | 6.04 | 6 | 5.74 | 5.58 | 5.52 | 5.42 | 5.32 | 5.45 | 5.39 | 5.79 | 5.78 |
| 3.2 | 0.41 | 1.32 | 1.43 | 1.1 | 1.19 | 1.31 | 1.4 | 1.52 | 1.63 | 1.75 | 1.87 | 1.99 | 2.19 | 2.37 | 2.54 | 2.68 | 4.42 | 6.09 | 6.27 | 7.55 | 6.64 | 6.15 | 6.04 | 7.01 | 6.12 | 6.02 | 5.98 | 5.73 | 5.56 | 5.5 | 5.4 | 5.3 | 5.43 | 5.37 | 5.81 | 5.8 |
| 3.4 | 0.46 | 1.33 | 1.43 | 1.1 | 1.19 | 1.32 | 1.4 | 1.52 | 1.63 | 1.75 | 1.87 | 1.99 | 2.19 | 2.38 | 2.55 | 2.69 | 4.4 | 6.07 | 6.28 | 7.54 | 6.63 | 6.12 | 6.02 | 7.03 | 6.08 | 5.98 | 5.94 | 5.69 | 5.53 | 5.46 | 5.37 | 5.26 | 5.39 | 5.33 | 5.83 | 5.82 |
| 3.6 | 0.52 | 1.34 | 1.44 | 1.1 | 1.19 | 1.3 | 1.39 | 1.51 | 1.62 | 1.75 | 1.87 | 1.99 | 2.19 | 2.39 | 2.56 | 2.71 | 4.38 | 6.06 | 6.27 | 7.54 | 6.64 | 6.07 | 5.97 | 7.04 | 6.03 | 5.92 | 5.89 | 5.64 | 5.48 | 5.4 | 5.31 | 5.21 | 5.33 | 5.27 | 5.85 | 5.85 |
| 3.8 | 0.58 | 1.36 | 1.45 | 1.09 | 1.18 | 1.29 | 1.39 | 1.51 | 1.62 | 1.75 | 1.88 | 1.99 | 2.2 | 2.4 | 2.58 | 2.73 | 4.35 | 6.05 | 6.26 | 7.53 | 6.64 | 6.12 | 5.96 | 7.06 | 5.96 | 5.84 | 5.81 | 5.57 | 5.42 | 5.32 | 5.24 | 5.15 | 5.25 | 5.2 | 5.86 | 5.87 |
| 4.0 | 0.65 | 1.39 | 1.46 | 1.1 | 1.2 | 1.3 | 1.4 | 1.51 | 1.62 | 1.75 | 1.88 | 2.01 | 2.22 | 2.41 | 2.61 | 2.75 | 4.31 | 6.05 | 6.24 | 7.51 | 6.65 | 6.18 | 5.94 | 7.07 | 5.88 | 5.75 | 5.73 | 5.49 | 5.42 | 5.37 | 5.27 | 5.16 | 5.27 | 5.15 | 5.86 | 5.89 |
| 4.2 | 0.72 | 1.42 | 1.48 | 1.12 | 1.24 | 1.33 | 1.42 | 1.52 | 1.63 | 1.77 | 1.91 | 2.04 | 2.25 | 2.47 | 2.64 | 2.78 | 4.29 | 6.05 | 6.21 | 7.49 | 6.65 | 6.26 | 5.94 | 7.06 | 5.79 | 5.65 | 5.63 | 5.52 | 5.52 | 5.47 | 5.36 | 5.25 | 5.26 | 5.27 | 5.86 | 5.91 |
| 4.4 | 0.80 | 1.47 | 1.5 | 1.18 | 1.3 | 1.39 | 1.49 | 1.54 | 1.64 | 1.79 | 1.94 | 2.07 | 2.28 | 2.5 | 2.68 | 2.81 | 4.26 | 6.04 | 6.17 | 7.47 | 6.66 | 6.35 | 5.95 | 7.04 | 5.71 | 5.72 | 5.7 | 5.63 | 5.64 | 5.58 | 5.47 | 5.38 | 5.39 | 5.41 | 5.86 | 5.93 |
| 4.6 | 0.88 | 1.52 | 1.51 | 1.25 | 1.37 | 1.46 | 1.58 | 1.56 | 1.67 | 1.81 | 1.96 | 2.11 | 2.31 | 2.54 | 2.71 | 2.83 | 4.26 | 6.05 | 6.11 | 7.43 | 6.67 | 6.47 | 5.98 | 6.99 | 5.8 | 5.82 | 5.82 | 5.75 | 5.75 | 5.7 | 5.58 | 5.5 | 5.51 | 5.54 | 5.86 | 5.95 |
| 4.8 | 0.97 | 1.57 | 1.53 | 1.33 | 1.46 | 1.55 | 1.68 | 1.63 | 1.72 | 1.9 | 1.99 | 2.15 | 2.35 | 2.59 | 2.76 | 2.86 | 4.32 | 6.04 | 6.04 | 7.37 | 6.67 | 6.63 | 6.03 | 6.9 | 5.88 | 5.93 | 5.93 | 5.87 | 5.87 | 5.82 | 5.71 | 5.64 | 5.63 | 5.66 | 5.87 | 5.99 |
| 5.0 | 1.06 | 1.63 | 1.55 | 1.42 | 1.55 | 1.64 | 1.78 | 1.77 | 1.83 | 2.01 | 2.02 | 2.2 | 2.39 | 2.63 | 2.79 | 2.89 | 4.37 | 6.03 | 5.96 | 7.28 | 6.67 | 6.82 | 6.1 | 6.77 | 5.95 | 6.02 | 6.03 | 5.97 | 5.97 | 5.93 | 5.82 | 5.75 | 5.74 | 5.79 | 5.89 | 6.03 |
| 5.2 | 1.16 | 1.71 | 1.64 | 1.52 | 1.64 | 1.74 | 1.9 | 1.89 | 1.95 | 2.13 | 2.14 | 2.28 | 2.44 | 2.69 | 2.85 | 2.93 | 4.41 | 6.01 | 5.88 | 7.16 | 6.65 | 7.07 | 6.19 | 6.6 | 6 | 6.09 | 6.12 | 6.06 | 6.05 | 6.02 | 5.91 | 5.85 | 5.83 | 5.89 | 5.98 | 6.09 |
| 5.4 | 1.27 | 1.8 | 1.79 | 1.62 | 1.75 | 1.85 | 2.01 | 2.02 | 2.09 | 2.27 | 2.3 | 2.5 | 2.64 | 2.76 | 2.94 | 3.08 | 4.4 | 5.97 | 5.81 | 7.01 | 6.62 | 7.39 | 6.3 | 6.38 | 6.05 | 6.16 | 6.19 | 6.13 | 6.13 | 6.1 | 5.99 | 5.84 | 5.92 | 5.98 | 6.08 | 6.18 |
| 5.6 | 1.38 | 1.87 | 1.95 | 1.73 | 1.84 | 1.94 | 2.12 | 2.13 | 2.27 | 2.53 | 2.57 | 2.77 | 2.93 | 3.07 | 3.22 | 3.26 | 4.52 | 6.04 | 5.78 | 6.93 | 6.69 | 6.57 | 7.69 | 6.45 | 6.13 | 6.1 | 6.26 | 6.21 | 6.23 | 6.18 | 6.06 | 5.96 | 6.02 | 6.08 | 6.2 | 6.29 |
| 5.8 | 1.50 | 2 | 2.12 | 1.81 | 1.92 | 2.04 | 2.31 | 2.31 | 2.49 | 2.73 | 2.77 | 3.05 | 3.1 | 3.27 | 3.51 | 3.54 | 4.83 | 6.17 | 5.65 | 6.96 | 6.53 | 8.02 | 6.57 | 6.01 | 6.14 | 6.28 | 6.33 | 6.28 | 6.27 | 6.27 | 6.15 | 6.12 | 6.07 | 6.14 | 6.35 | 6.43 |
| 6.0 | 1.62 | 2.24 | 2.28 | 1.94 | 2.09 | 2.24 | 2.52 | 2.54 | 2.71 | 2.99 | 3.03 | 3.31 | 3.42 | 3.6 | 3.81 | 3.94 | 5.08 | 6.28 | 5.86 | 6.96 | 6.51 | 8.34 | 6.73 | 6.1 | 6.18 | 6.34 | 6.4 | 6.35 | 6.33 | 6.34 | 6.24 | 6.2 | 6.15 | 6.21 | 6.52 | 6.6 |
| 6.2 | 1.75 | 2.54 | 2.57 | 2.24 | 2.38 | 2.55 | 2.93 | 2.91 | 3.07 | 3.36 | 3.46 | 3.67 | 3.87 | 4.03 | 4.23 | 4.45 | 5.3 | 6.37 | 6.23 | 6.92 | 6.65 | 8.65 | 6.91 | 6.2 | 6.21 | 6.39 | 6.45 | 6.41 | 6.39 | 6.41 | 6.27 | 6.23 | 6.27 | 6.32 | 6.77 | 6.92 |
| 6.4 | 1.89 | 2.84 | 2.71 | 2.57 | 2.74 | 2.95 | 3.17 | 3.4 | 3.56 | 3.75 | 3.95 | 4.25 | 4.5 | 4.63 | 4.94 | 5.11 | 5.57 | 6.41 | 6.6 | 6.89 | 6.59 | 8.97 | 7.12 | 6.31 | 6.24 | 6.43 | 6.49 | 6.46 | 6.43 | 6.45 | 6.37 | 6.31 | 6.27 | 6.29 | 6.94 | 7.08 |
| 6.6 | 2.04 | 3.22 | 2.99 | 2.96 | 3.17 | 3.38 | 3.63 | 3.87 | 4.12 | 4.37 | 4.59 | 4.84 | 5.1 | 5.4 | 5.74 | 5.96 | 6.19 | 7.21 | 7.04 | 7.23 | 6.63 | 9.29 | 7.45 | 6.62 | 6.24 | 6.44 | 6.5 | 6.47 | 6.44 | 6.46 | 6.39 | 6.3 | 6.27 | 6.27 | 7.19 | 7.36 |
| 6.8 | 2.19 | 3.68 | 3.43 | 3.36 | 3.61 | 3.88 | 4.14 | 4.43 | 4.72 | 4.97 | 5.32 | 5.58 | 5.8 | 6.23 | 6.49 | 6.81 | 7.17 | 8.14 | 7.55 | 7.68 | 7.26 | 9.62 | 7.84 | 7.05 | 6.64 | 6.5 | 6.49 | 6.45 | 6.43 | 6.53 | 6.73 | 6.74 | 6.8 | 6.89 | 7.44 | 7.62 |
| 7.0 | 2.35 | 4.01 | 3.92 | 3.82 | 4.12 | 4.03 | 4.68 | 4.95 | 5.21 | 5.63 | 5.93 | 6.3 | 6.65 | 6.93 | 7.29 | 7.74 | 8.1 | 9.02 | 7.98 | 8.11 | 8.12 | 9.95 | 8.25 | 7.51 | 7.35 | 7.11 | 7.04 | 7.02 | 6.97 | 7.1 | 7.31 | 7.36 | 7.46 | 7.69 | 7.87 | |
| 7.2 | 2.52 | 4.46 | 4.39 | 4.3 | 4.62 | 4.93 | 5.27 | 5.58 | 5.91 | 6.26 | 6.65 | 6.98 | 7.41 | 7.83 | 8.23 | 8.55 | 9.01 | 9.42 | 8.5 | 8.55 | 8.9 | 10.3 | 8.68 | 8.13 | 7.9 | 7.74 | 7.56 | 7.66 | 7.63 | 7.68 | 7.85 | 7.85 | 7.92 | 7.98 | 8.34 | 8.31 |
| 7.4 | 2.70 | 4.87 | 4.87 | 4.73 | 5.07 | 5.43 | 5.82 | 6.18 | 6.55 | 6.99 | 7.37 | 7.78 | 8.18 | 8.66 | 9.14 | 9.64 | 10.1 | 9.89 | 8.81 | 9.4 | 9.68 | 10.6 | 9.1 | 8.78 | 8.53 | 8.41 | 8.25 | 8.31 | 8.29 | 8.25 | 8.38 | 8.34 | 8.43 | 8.55 | 9.44 | 9.42 |
| 7.6 | 2.88 | 5.35 | 5.41 | 5.16 | 5.54 | 5.95 | 6.34 | 6.76 | 7.22 | 7.65 | 8.06 | 8.6 | 9.06 | 9.47 | 9.96 | 10.5 | 11 | 10.3 | 9.17 | 10.1 | 10.4 | 10.6 | 9.75 | 9.43 | 9.16 | 9.07 | 8.92 | 8.95 | 8.98 | 8.94 | 8.97 | 8.89 | 9.02 | 9.13 | 10.2 | 10.5 |
| 7.8 | 3.07 | 5.75 | 5.89 | 5.67 | 6.09 | 6.52 | 6.93 | 7.34 | 7.86 | 8.35 | 8.88 | 9.38 | 9.87 | 10.4 | 10.9 | 11.5 | 12.1 | 10.8 | 10.1 | 11.1 | 11.2 | 10.8 | 10.2 | 10.1 | 10.1 | 9.86 | 9.86 | 9.7 | 9.69 | 9.65 | 9.64 | 9.64 | 9.69 | 9.72 | 11.1 | 11.7 |
| 8.0 | 3.27 | 6.19 | 6.41 | 6.12 | 6.55 | 7.03 | 7.53 | 8.01 | 8.49 | 9.03 | 9.53 | 10.1 | 10.7 | 11.3 | 12 | 12.5 | 13 | 11.1 | 11.5 | 11.8 | 11.9 | 12.3 | 11.8 | 11.2 | 11.1 | 11 | 10.8 | 10.6 | 10.5 | 10.5 | 10.5 | 10.6 | 10.6 | 10.6 | 12.6 | 12.8 |
| 8.2 | 3.48 | 6.62 | 6.95 | 6.59 | 7.08 | 7.58 | 8.08 | 8.63 | 9.17 | 9.74 | 10.3 | 10.9 | 11.5 | 12.1 | 12.8 | 13.4 | 13.7 | 12.5 | 12.6 | 12.5 | 12.5 | 13.3 | 12.7 | 12.1 | 11.8 | 11.8 | 11.5 | 11.4 | 11.3 | 11.3 | 11.2 | 11.4 | 11.3 | 11.3 | 13.5 | 13.7 |
| 8.4 | 3.70 | 7.1 | 7.44 | 7.08 | 7.59 | 8.14 | 8.71 | 9.26 | 9.85 | 10.4 | 11 | 11.7 | 12.4 | 13 | 13.7 | 14.5 | 14.3 | 13.8 | 13.4 | 13.3 | 13.2 | 14.3 | 13.4 | 12.8 | 12.6 | 12.5 | 12.3 | 12.1 | 12.1 | 12.1 | 12.1 | 12.1 | 12.1 | 12.1 | 14.3 | 14.4 |
| 8.6 | 3.93 | 7.57 | 8.16 | 7.6 | 8.18 | 8.73 | 9.32 | 9.95 | 10.6 | 11.3 | 11.9 | 12.7 | 13.3 | 14 | 14.7 | 15.5 | 14.8 | 14.6 | 14.2 | 14 | 14 | 15.2 | 14.2 | 13.5 | 13.4 | 13.3 | 13.2 | 13.1 | 13.1 | 13.1 | 13.1 | 13.1 | 13 | 13.1 | 15 | 15.2 |
| 8.8 | 4.17 | 8.11 | 8.95 | 8.14 | 8.74 | 9.37 | 10 | 10.7 | 11.4 | 12.1 | 12.8 | 13.5 | 14.3 | 15.2 | 15.9 | 16.6 | 15.7 | 15.8 | 15.2 | 14.9 | 15.2 | 16.1 | 15 | 14.5 | 14.4 | 14.3 | 14.3 | 14.1 | 14.1 | 14.1 | 14.1 | 14.2 | 14.2 | 14.2 | 15.7 | 15.9 |
| 9.0 | 4.41 | 8.76 | 9.91 | 8.76 | 9.38 | 10.1 | 10.8 | 11.4 | 12.2 | 12.9 | 13.7 | 14.6 | 15.4 | 16.2 | 17.4 | 17.1 | 17 | 16.7 | 16 | 16 | 16.2 | 16.9 | 15.8 | 15.8 | 15.8 | 15.7 | 15.5 | 15.4 | 15.3 | 15.3 | 15.4 | 15.5 | 15.6 | 15.5 | 16.4 | 16.6 |
| 9.2 | 4.67 | 9.43 | 10.9 | 9.95 | 10.6 | 11.3 | 12 | 12.7 | 13.5 | 14.4 | 15.2 | 16 | 16.9 | 17.8 | 18.8 | 18.6 | 18.2 | 17.6 | 17.5 | 17.2 | 17.3 | 17.8 | 16.9 | 16.9 | 17 | 16.9 | 16.8 | 16.6 | 16.5 | 16.6 | 16.8 | 16.9 | 16.8 | 16.9 | 17.2 | |
| 9.4 | 4.94 | 10.4 | 11.7 | 11.2 | 12 | 12.7 | 13.5 | 14.3 | 15.1 | 16.1 | 17.1 | 18.1 | 19.1 | 20.1 | 20.8 | 19.8 | 19.9 | 18.6 | 19.3 | 18 | 18.2 | 18.7 | 17.8 | 17.9 | 18.1 | 18 | 17.9 | 17.7 | 17.6 | 17.6 | 17.8 | 17.9 | 18 | 18 | 17.7 | 17.8 |
| 9.6 | 5.21 | 11 | 12.4 | 12.9 | 13.8 | 14.7 | 15.5 | 16.4 | 17.2 | 18.2 | 19.2 | 20.3 | 21 | 22 | 22.1 | 21.7 | 21 | 19.8 | 20.7 | 18.9 | 18.9 | 19.4 | 18.6 | 18.7 | 18.9 | 18.8 | 18.8 | 18.6 | 18.6 | 18.6 | 18.7 | 18.9 | 18.9 | 19 | 19 | 18.1 | 18.3 |
| 9.8 | 5.50 | 11.4 | 12.9 | 13.6 | 14.6 | 15.7 | 16.7 | 17.7 | 18.7 | 19.6 | 20.7 | 22 | 23.1 | 23.1 | 23.8 | 23.6 | 23.2 | 21.5 | 20.9 | 21.7 | 19.6 | 20 | 19.3 | 19.4 | 19.6 | 19.7 | 19.6 | 19.5 | 19.6 | 19.7 | 19.9 | 19.8 | 20 | 20 | 19 | 19.3 |
| 10.0 | 5.79 | 12.8 | 14.3 | 14.9 | 16.5 | 17.6 | 18.7 | 19.9 | 21 | 22.1 | 23.4 | 24.7 | 25.5 | 24.8 | 25.1 | 24.6 | 24.4 | 22.2 | 21.8 | 22.5 | 20.9 | 20.8 | 20.4 | 20.6 | 20.6 | 20.6 | 20.5 | 20.7 | 21 | 20.8 | 21.2 | 21.3 | 21.2 | 20.5 | 20.7 | |
| 10.2 | 6.10 | 15.3 | 16.1 | 18.3 | 19.5 | 20.7 | 22 | 23.4 | 24.8 | 26 | 27.4 | 27.3 | 26.3 | 26.1 | 26 | 25.5 | 22.9 | 22.5 | 23 | 21.7 | 22 | 22.1 | 21.7 | 21.9 | 22 | 22 | 22 | 22 | 22.2 | 22.5 | 22.6 | 22.8 | 22.9 | 22.9 | 22.1 | 22.3 |

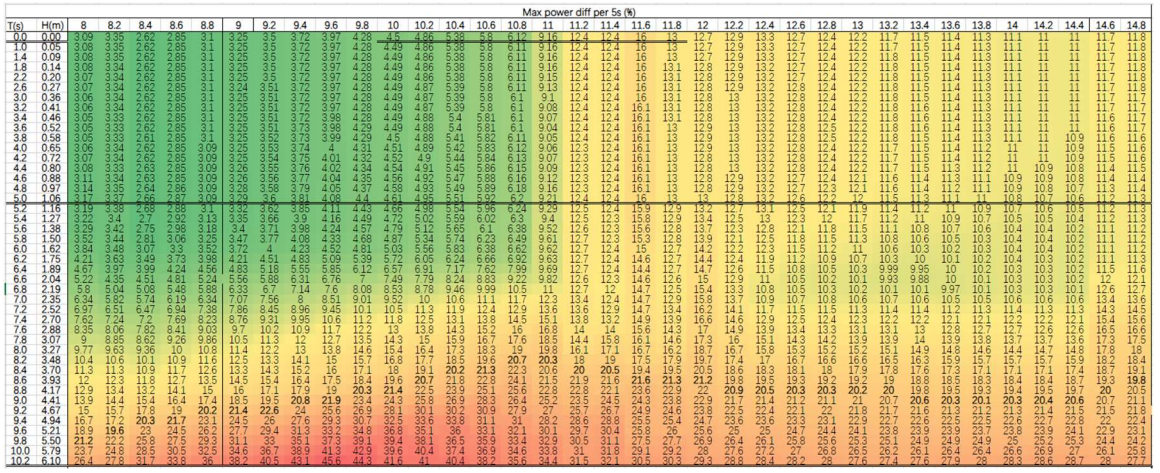

Max power diff per 5s (%)

| T(s) | H(m) | 8 | 8.2 | 8.4 | 8.6 | 8.8 | 9 | 9.2 | 9.4 | 9.6 | 9.8 | 10 | 10.2 | 10.4 | 10.6 | 10.8 | 11 | 11.2 | 11.4 | 11.6 | 11.8 | 12 | 12.2 | 12.4 | 12.6 | 12.8 | 13 | 13.2 | 13.4 | 13.6 | 13.8 | 14 | 14.2 | 14.4 | 14.6 | 14.8 |
|---|---|---|---|---|---|---|---|---|---|---|---|---|---|---|---|---|---|---|---|---|---|---|---|---|---|---|---|---|---|---|---|---|---|---|---|---|
| 0.0 | 0.00 | 3.09 | 3.35 | 2.62 | 2.85 | 3.1 | 3.25 | 3.5 | 3.72 | 3.97 | 4.28 | 4.6 | 4.86 | 5.38 | 5.8 | 6.12 | 9.16 | 12.4 | 12.4 | 16 | 13 | 12.7 | 12.9 | 13.3 | 12.7 | 12.4 | 12.2 | 11.7 | 11.5 | 11.4 | 11.3 | 11.1 | 11 | 11 | 11.7 | 11.8 |
| 1.0 | 0.05 | 3.08 | 3.35 | 2.62 | 2.85 | 3.1 | 3.25 | 3.5 | 3.72 | 3.97 | 4.28 | 4.49 | 4.86 | 5.38 | 5.8 | 6.11 | 9.16 | 12.4 | 12.4 | 16 | 13 | 12.7 | 12.9 | 13.3 | 12.7 | 12.4 | 12.2 | 11.7 | 11.5 | 11.4 | 11.3 | 11.1 | 11 | 11 | 11.7 | 11.8 |
| 1.4 | 0.09 | 3.08 | 3.34 | 2.62 | 2.85 | 3.1 | 3.25 | 3.5 | 3.72 | 3.97 | 4.28 | 4.49 | 4.86 | 5.38 | 5.8 | 6.11 | 9.16 | 12.4 | 12.4 | 16 | 13 | 12.7 | 12.9 | 13.3 | 12.7 | 12.4 | 12.2 | 11.8 | 11.5 | 11.4 | 11.3 | 11.1 | 11 | 11 | 11.7 | 11.8 |
| 1.8 | 0.14 | 3.08 | 3.34 | 2.62 | 2.85 | 3.1 | 3.25 | 3.5 | 3.72 | 3.97 | 4.28 | 4.49 | 4.86 | 5.38 | 5.8 | 6.11 | 9.15 | 12.4 | 12.4 | 16 | 13.1 | 12.8 | 12.9 | 13.2 | 12.7 | 12.4 | 12.2 | 11.8 | 11.5 | 11.4 | 11.3 | 11.1 | 11 | 11 | 11.7 | 11.8 |
| 2.2 | 0.20 | 3.07 | 3.34 | 2.62 | 2.85 | 3.1 | 3.25 | 3.5 | 3.72 | 3.97 | 4.28 | 4.49 | 4.86 | 5.38 | 5.8 | 6.11 | 9.15 | 12.4 | 12.4 | 16 | 13.1 | 12.8 | 12.9 | 13.2 | 12.7 | 12.4 | 12.2 | 11.8 | 11.5 | 11.4 | 11.3 | 11.1 | 11 | 11 | 11.7 | 11.8 |
| 2.6 | 0.27 | 3.07 | 3.34 | 2.62 | 2.85 | 3.1 | 3.25 | 3.51 | 3.72 | 3.97 | 4.28 | 4.49 | 4.87 | 5.39 | 5.8 | 6.11 | 9.13 | 12.4 | 12.4 | 16 | 13.1 | 12.8 | 12.9 | 13.2 | 12.8 | 12.4 | 12.2 | 11.8 | 11.5 | 11.4 | 11.3 | 11.1 | 11 | 11 | 11.7 | 11.8 |
| 3.0 | 0.36 | 3.06 | 3.34 | 2.62 | 2.85 | 3.1 | 3.25 | 3.51 | 3.72 | 3.97 | 4.28 | 4.49 | 4.87 | 5.39 | 5.8 | 6.1 | 9.1 | 12.4 | 12.4 | 16 | 13.1 | 12.8 | 13 | 13.2 | 12.8 | 12.4 | 12.2 | 11.8 | 11.5 | 11.4 | 11.3 | 11.1 | 11 | 11 | 11.7 | 11.7 |
| 3.2 | 0.41 | 3.06 | 3.34 | 2.62 | 2.85 | 3.1 | 3.25 | 3.51 | 3.72 | 3.97 | 4.28 | 4.49 | 4.87 | 5.39 | 5.8 | 6.1 | 9.08 | 12.4 | 12.4 | 16.1 | 13.1 | 12.8 | 13 | 13.2 | 12.8 | 12.4 | 12.2 | 11.8 | 11.6 | 11.4 | 11.3 | 11.1 | 11 | 11 | 11.7 | 11.7 |
| 3.4 | 0.46 | 3.05 | 3.33 | 2.62 | 2.85 | 3.1 | 3.25 | 3.51 | 3.72 | 3.98 | 4.28 | 4.49 | 4.88 | 5.4 | 5.81 | 6.1 | 9.07 | 12.4 | 12.4 | 16.1 | 13.1 | 12.8 | 13 | 13.2 | 12.8 | 12.4 | 12.2 | 11.8 | 11.6 | 11.4 | 11.3 | 11.1 | 11 | 11 | 11.6 | 11.7 |
| 3.6 | 0.52 | 3.05 | 3.33 | 2.62 | 2.85 | 3.1 | 3.25 | 3.52 | 3.72 | 3.98 | 4.29 | 4.49 | 4.88 | 5.4 | 5.81 | 6.1 | 9.04 | 12.4 | 12.4 | 16.1 | 13 | 12.9 | 13 | 13.2 | 12.8 | 12.4 | 12.2 | 11.8 | 11.6 | 11.4 | 11.3 | 11.1 | 11 | 11 | 11.6 | 11.7 |
| 3.8 | 0.58 | 3.05 | 3.33 | 2.61 | 2.85 | 3.1 | 3.25 | 3.52 | 3.73 | 3.99 | 4.29 | 4.5 | 4.88 | 5.41 | 5.82 | 6.11 | 9.06 | 12.4 | 12.4 | 16.1 | 13 | 12.9 | 13 | 13.2 | 12.8 | 12.5 | 12.2 | 11.8 | 11.5 | 11.4 | 11.3 | 11.1 | 11 | 10.9 | 11.6 | 11.6 |
| 4.0 | 0.65 | 3.06 | 3.34 | 2.62 | 2.85 | 3.09 | 3.25 | 3.53 | 3.74 | 4 | 4.31 | 4.51 | 4.89 | 5.42 | 5.83 | 6.12 | 9.06 | 12.3 | 12.4 | 16.1 | 13 | 12.9 | 13 | 13.2 | 12.8 | 12.4 | 12.2 | 11.7 | 11.5 | 11.4 | 11.2 | 11 | 11 | 10.9 | 11.5 | 11.6 |
| 4.2 | 0.72 | 3.07 | 3.34 | 2.62 | 2.85 | 3.09 | 3.25 | 3.54 | 3.75 | 4.01 | 4.32 | 4.52 | 4.9 | 5.44 | 5.84 | 6.13 | 9.07 | 12.3 | 12.4 | 16.1 | 13 | 12.9 | 13 | 13.2 | 12.8 | 12.4 | 12.2 | 11.7 | 11.5 | 11.4 | 11.2 | 11 | 11 | 10.9 | 11.5 | 11.6 |
| 4.4 | 0.80 | 3.08 | 3.33 | 2.63 | 2.85 | 3.09 | 3.26 | 3.55 | 3.76 | 4.02 | 4.34 | 4.54 | 4.91 | 5.45 | 5.86 | 6.15 | 9.09 | 12.3 | 12.4 | 16.1 | 13 | 12.8 | 13 | 13.2 | 12.8 | 12.4 | 12.2 | 11.7 | 11.5 | 11.3 | 11.2 | 11 | 10.9 | 10.8 | 11.5 | 11.6 |
| 4.6 | 0.88 | 3.11 | 3.34 | 2.63 | 2.85 | 3.09 | 3.26 | 3.56 | 3.77 | 4.04 | 4.35 | 4.56 | 4.92 | 5.47 | 5.88 | 6.16 | 9.12 | 12.3 | 12.4 | 16.1 | 13 | 12.8 | 12.9 | 13.2 | 12.7 | 12.4 | 12.1 | 11.6 | 11.4 | 11.3 | 11.1 | 10.9 | 10.9 | 10.8 | 11.4 | 11.4 |
| 4.8 | 0.97 | 3.14 | 3.35 | 2.64 | 2.86 | 3.09 | 3.28 | 3.58 | 3.79 | 4.05 | 4.37 | 4.58 | 4.93 | 5.49 | 5.89 | 6.18 | 9.16 | 12.3 | 12.4 | 16.1 | 13 | 12.8 | 12.9 | 13.2 | 12.7 | 12.3 | 12.1 | 11.6 | 11.4 | 11.2 | 11.1 | 10.9 | 10.8 | 10.7 | 11.3 | 11.4 |
| 5.0 | 1.06 | 3.21 | 3.37 | 2.66 | 2.88 | 3.11 | 3.29 | 3.6 | 3.81 | 4.08 | 4.44 | 4.61 | 4.95 | 5.51 | 5.92 | 6.2 | 9.21 | 12.4 | 12.4 | 16 | 13 | 13 | 12.8 | 13.2 | 12.6 | 12.2 | 12 | 11.5 | 11.3 | 11.1 | 10.9 | 10.8 | 10.7 | 10.6 | 11.2 | 11.3 |
| 5.2 | 1.16 | 3.19 | 3.38 | 2.68 | 2.88 | 3.1 | 3.32 | 3.62 | 3.85 | 4.11 | 4.43 | 4.66 | 4.98 | 5.54 | 5.96 | 6.24 | 9.29 | 12.5 | 12.4 | 15.9 | 12.9 | 13.2 | 12.7 | 13.1 | 12.5 | 12.1 | 11.9 | 11.4 | 11.2 | 11 | 10.9 | 10.7 | 10.6 | 10.5 | 11.2 | 11.3 |
| 5.4 | 1.27 | 3.22 | 3.4 | 2.7 | 2.92 | 3.13 | 3.35 | 3.66 | 3.9 | 4.16 | 4.49 | 4.72 | 5.02 | 5.59 | 6.02 | 6.3 | 9.4 | 12.5 | 12.3 | 15.8 | 12.9 | 13.4 | 12.5 | 13 | 12.3 | 12 | 11.7 | 11.2 | 11 | 10.9 | 10.7 | 10.5 | 10.5 | 10.4 | 11.2 | 11.3 |
| 5.6 | 1.38 | 3.26 | 3.42 | 2.75 | 2.98 | 3.14 | 3.37 | 3.7 | 3.98 | 4.24 | 4.57 | 4.79 | 5.12 | 5.65 | 6.1 | 6.38 | 9.52 | 12.6 | 12.3 | 15.7 | 13 | 13.7 | 12.3 | 12.9 | 12.1 | 11.7 | 11.5 | 11.1 | 10.8 | 10.7 | 10.6 | 10.4 | 10.4 | 10.3 | 11.2 | 11.3 |
| 5.8 | 1.50 | 3.52 | 3.44 | 2.81 | 3.06 | 3.28 | 3.47 | 3.77 | 4.08 | 4.33 | 4.68 | 4.87 | 5.24 | 5.74 | 6.23 | 6.49 | 9.61 | 12.7 | 12.4 | 15.3 | 12.8 | 13.9 | 12.1 | 12.6 | 11.8 | 11.5 | 11.3 | 10.8 | 10.6 | 10.5 | 10.3 | 10.4 | 10.4 | 10.2 | 11.1 | 11.2 |
| 6.0 | 1.62 | 3.84 | 3.48 | 3.07 | 3.3 | 3.52 | 3.72 | 4 | 4.23 | 4.52 | 4.81 | 5.03 | 5.56 | 5.83 | 6.38 | 6.62 | 9.62 | 12.7 | 12.4 | 15 | 12.7 | 14.2 | 12.2 | 12.3 | 11.5 | 11.2 | 11 | 10.6 | 10.3 | 10.2 | 10.3 | 10.4 | 10.4 | 10.2 | 11.1 | 11.2 |
| 6.2 | 1.75 | 4.21 | 3.63 | 3.49 | 3.73 | 3.98 | 4.21 | 4.51 | 4.83 | 5.09 | 5.39 | 5.72 | 6.05 | 6.24 | 6.66 | 6.92 | 9.63 | 12.7 | 12.4 | 14.6 | 12.7 | 14.4 | 12.4 | 11.9 | 11.2 | 10.9 | 10.7 | 10.3 | 10 | 10.1 | 10.2 | 10.4 | 10.3 | 10.2 | 11.1 | 11.3 |
| 6.4 | 1.89 | 4.67 | 3.97 | 3.99 | 4.24 | 4.56 | 4.88 | 5.18 | 5.55 | 5.85 | 6.12 | 6.57 | 6.91 | 7.17 | 7.62 | 7.99 | 9.69 | 12.7 | 12.4 | 14.4 | 12.7 | 14.7 | 12.6 | 11.5 | 10.8 | 10.5 | 10.3 | 9.99 | 9.95 | 10 | 10.2 | 10.3 | 10.3 | 10.2 | 11.5 | 11.6 |
| 6.6 | 2.04 | 5.22 | 4.35 | 4.51 | 4.81 | 5.24 | 5.56 | 5.88 | 6.31 | 6.76 | 7 | 7.49 | 7.79 | 8.24 | 8.83 | 9.22 | 9.82 | 12.6 | 12.3 | 14.6 | 12.6 | 15 | 12.9 | 11 | 10.5 | 10.2 | 10.1 | 9.93 | 9.88 | 10 | 10.1 | 10.3 | 10.3 | 10.2 | 12 | 12.1 |
| 6.8 | 2.19 | 5.8 | 5.04 | 5.08 | 5.48 | 5.86 | 6.33 | 6.7 | 7.14 | 7.6 | 8.08 | 8.53 | 8.78 | 9.46 | 9.99 | 10.5 | 11 | 12.7 | 12 | 14.7 | 12.5 | 15.4 | 13.3 | 10.8 | 10.5 | 10.3 | 10.2 | 10.1 | 10.1 | 9.97 | 10.1 | 10.3 | 10.3 | 10.1 | 12.6 | 12.7 |
| 7.0 | 2.35 | 6.34 | 5.82 | 5.74 | 6.19 | 6.64 | 7.07 | 7.56 | 8 | 8.51 | 9.01 | 9.52 | 10 | 10.6 | 11.1 